Inferring Histories of Accumulation Rate, Ice Thickness, and Ice Flow from Internal Layers in Glaciers and Ice Sheets

Michelle R. Koutnik

A dissertation submitted in partial fulfillment of
the requirements for the degree of

Doctor of Philosophy

University of Washington

2009

Program authorized to offer degree: Earth and Space Sciences

University of Washington
Graduate School

This is to certify that I have examined this copy of a doctoral dissertation by

Michelle R. Koutnik

and have found that it is complete and satisfactory in all respects,
and that any and all revisions required by the final
examining committee have been made.

Chair of the Supervisory Committee:

_____
Edwin D. Waddington

Reading Committee:

_____
Edwin D. Waddington

_____
Howard B. Conway

_____
Dale P. Winebrenner

Date: _____

In presenting this dissertation in partial fulfillment of the requirements for the doctoral degree at the University of Washington, I agree that the Library shall make its copies freely available for inspection. I further agree that extensive copying of this dissertation is allowable for scholarly purposes, consistent with "fair use" as prescribed in the U.S. Copyright Law. Request for copying or reproduction of this dissertation may be referred to ProQuest Information and Learning, 300 North Zeeb Road, Ann Arbor, MI 48106-1346, 1-800-521-0600, to whom the author has granted "the right to reproduce and sell (a) copies of the manuscript in microform and/or (b) printed copies of the manuscript made from microform."

Signature _____

Date _____

University of Washington

Abstract

Inferring Histories of Accumulation Rate, Ice Thickness, and Ice Flow from Internal Layers in Glaciers and Ice Sheets

Michelle R. Koutnik

Chair of Supervisory Committee:
Professor Edwin D. Waddington
Earth and Space Sciences

Spatial and temporal variations in past accumulation, ice thickness, and ice flow of polar ice sheets are weakly constrained on Earth, and are fundamental unknowns on Mars. On Earth, the spatial and temporal histories of accumulation and ice-sheet flow are necessary to recreate ice-volume and sea-level histories, and are important to properly interpret ice-core chemistry. On Mars, accumulation and ice-flow histories are necessary to decipher the connection between climate and ice-mass formation, evolution, and observable structure.

Internal layers in ice sheets on Earth and on Mars have been observed with ice-penetrating radar. These layers preserve information about how the ice sheet responded to past spatial and/or temporal changes in accumulation rate and ice flow, and present-day internal-layer shapes observed by radar are the most accessible remaining record of this past information. Deeper layers contain information from further in the past, making them highly valuable, but they are more difficult to decipher.

In this work, an inverse problem is solved to infer transients in accumulation rate, ice-sheet thickness, and ice flow from the shapes of deep internal layers. While some details of these histories can be recovered from ice cores, ice cores represent conditions at only a single point. However, the approach presented here is more robust in combination with ice-core data. If internal layers are dated, for example by an intersecting ice core, then radar-observed internal layers provide both spatial and temporal information. Each layer represents a past surface of a particular age that has been subsequently buried by accumulation and also modified by ice flow.

In this work, the goal of solving this inverse problem is to find a set of model parameters (e.g. accumulation-rate history) that have the minimum variation required to explain the data (e.g. internal-layer shapes). The process of internal-layer formation is described with a 2.5-D thermomechanical ice-flow flowband model. Estimates of the data are matched to measured values within their uncertainties, and to an expected tolerance. We seek an accumulation pattern that is spatially smooth, and a parameter set that is consistent with characteristic values of the parameters. This dissertation presents this inverse approach, and discusses applications to data from Antarctica and from Mars.

Table of Contents

List of Figures

List of Tables

Acknowledgements

This work would not have been possible without the insight, guidance, and continuous support I have received from Ed Waddington. Ed has given me the instruction, the focus, and the inspiration required to complete this dissertation. I also acknowledge the tremendous support of my committee, Twit Conway, Dale Winebrenner, Ken Creager, and Gerard Roe; I sincerely appreciate their significant contributions. I thank Tom Neumann for his work on the steady-state version of this problem, and for providing necessary data for West Antarctica.

There isn't the space to acknowledge everyone that has contributed to the educational and personal aspects of my time in graduate school, and the impact they have had on my life. I will just briefly acknowledge a few people, but I recognize that there are many others. I must start by acknowledging Bruce Murray, who showed me how fun it is to pursue answers to questions about the world (or other worlds). I have learned much from Shane Byrne and Oz Pathare. I thank Shawn Marshall for introducing me to glaciology, and for inspiring my path in graduate school.

I acknowledge all of my past and present officemates: Bob Hawley, Steve Price, Joe Macgregor, Al Rasmussen, Jessica Lundin, Twila Moon, Hans Christian Steen-Larsen, Asbjørn Persson, and Huw Horgan. I shared in this graduate program with truly remarkable people. In addition to my officemates, I acknowledge Ginny Catania, Michele Koppes, Claire Todd, Julia Jarvis, Lora Koenig, Erin Whorton, Kat Huybers, Summer Rupper, Jelte Harnmeijer, Tom Neumann, Ben Smith, Andy Ganse, and TJ Fudge, among many others. I thank Mike Town, Louise Leahy, Paul Hezel, Ruschle Dadic, and Gina Schmalze for their support.

An outstanding aspect of the University of Washington has been the diversity of research projects and the diversity of opportunities. I thank Twit Conway for showing me the way up to Blue Glacier (again and again), and I thank Al Rasmussen for his major role in motivating this work. I thank Erin Pettit and Ron Sletten for giving me firsthand experience with different projects in different parts of the world. I thank Gerard Roe for making it possible to share a special part of the world with undergraduate students, and I also thank Peter Colding-Jorgensen for his support with this adventure. I appreciate everything that I have learned from Charlie Raymond, Kenny Matsuoka, Steve Warren, Eric Steig, David Battisti, Ron Merrill, Bernard Hallet, and Ian Joughin.

I am indebted to my family and friends for their support. Natalie, Annie, Brooke, Max, Zoe, Elizabeth, Zac, Carolyn, Jacob, Becky, Lisa, Brendan, Jodi, Forest, and all of the other wonderful people I have met in Seattle. Most of all I thank my Mom, Dad, and sister for everything they have taught me, and for everything they have inspired me to pursue.

I dedicate this to my Grandma.

Chapter 1

Introduction

1.1. Motivation and goals

Glaciers and ice sheets evolve in response to climate, but they are also an important component of the Earth system that affect climate. The interplay between ice, air, ocean, and land is complicated by feedback relationships among these systems, and also by dynamic behavior that may arise internal to each component. For example, more snowfall across an ice sheet may cause it to thicken, which may alter atmospheric circulation, or may increasse the calving flux of icebergs and affect ocean circulation. For the large ice sheets, dynamic behavior can include fast-flow instabilities (e.g. ice streams) and ice-sheet response to ice-shelf changes. This relatively unstable ice-sheet behavior is exhibited today, where glaciers have changed speed in Greenland (e.g. Joughin and others, 2004a; Rignot and Kanagaratnam, 2006) and in Antarctica (e.g. Bamber and Rignot, 2002), and the disintegration of massive ice shelves in Antarctica has resulted in the speedup of outlet glaciers there (e.g. Rignot and others, 2004). While this action is concentrated near ice-sheet margins, ice-sheet interiors also respond to this forcing.

Although observations are advancing our understanding, the physics governing these processes are still not well resolved, and therefore our ability to accurately predict the initiation of and response to these

instabilities is limited. A challenge remains, that the volume-adjustment timescales of large ice sheets can be thousands of years, and we are trying to understand past and future ice-sheet behavior.

Information about ice and climate history over longer timescales can be obtained from ice cores. Deep ice cores in Greenland (e.g. NGRIP members, 2004) and in Antarctica (e.g. Petit and others, 1999; EPICA members, 2004) have provided a proxy of regional and global climate changes over tens to hundreds of thousands of years. Ice-sheet flow centers, called ice divides, are target sites for drilling an ice core, because there has generally been less spatial and temporal gradients in ice flow than at off-divide sites. However, ice divides may have moved through time, and assumptions about these transients must be made in order to properly interpret ice-core records. These transients may have been significant, as many different proxies (e.g. ocean-sediment cores, cave records, coral records) show that there have been significant changes ice volume, air temperature, and sea level; variations in ice thickness and ice-divide position of ice-sheet interiors can be due to local forcing (e.g. changes in local accumulation), regional forcing (e.g. changes in ice streams), or global forcing (e.g. changes in mean sea level, see e.g. Clark and Mix, 2002).

The motivation for this dissertation is to improve understanding of ice-sheet history. In particular, I focus on the transient behavior of ice sheets in the vicinity of ice divides (in the central regions of an ice sheet) in response to local changes in accumulation, and in response to regional or global changes in ice flux. While valuable information can be recovered from ice cores, they represent conditions only at a single point.

In this dissertation I show how we can build a spatial and temporal picture of changes in accumulation and ice flow in the central portions of ice

sheets. A consistent estimate of these changes is critical to properly interpret climate history from an ice core, and it is important to predicting how ice sheets may evolve in the future.

An exciting dimension of this dissertation is that the questions, data sets, and methods that I develop for Terrestrial ice also pertain to Martian ice. New insight into the ice and climate histories on Mars is bolstered by terrestrial experience, and the foundation from which I construct an approach to infer ice and climate histories on Earth is bolstered by Martian experience.

In this dissertation, I use the fact that internal layers have been shaped by spatial and temporal histories of ice flow and accumulation, and that present-day layer shapes contain a record of these histories. Deeper radar-detected layers contain information from farther back in time, making them valuable archives. However, the shapes of such deep layers have been subjected to more strain from spatial and temporal gradients in ice flow and accumulation, making them more complicated to interpret. The goal of this dissertation is to show how these histories of ice flow and accumulation can be inferred from internal layers, and to demonstrate the capability of this new approach in preparation for application with emerging ice-sheet data.

The spatial scales of ice sheets, the timescales involved in their evolution, and the diffusive nature of ice flow create a challenge to understand ice-sheet response to change. Ice-flow models are powerful tools to predict ice-sheet behavior, but they require estimates of initial conditions and boundary conditions that are often unknown. In addition, quantitative measurements may not be available. Inverse methods allow us to use ice-flow models and ice-sheet data together, to investigate ice-sheet behavior (e.g. Truffer, 2004; Waddington and others, 2007; Eisen, 2008). This

dissertation presents a new inverse-theory approach to infer histories of accumulation and ice dynamics from internal layers. The methods presented here are generally applicable, but I focus on questions related to the history of central West Antarctic Ice Sheet (WAIS) and to the history of the Martian Polar Layered Deposits (PLD). Here I outline the motivation for these applications.

1.1.1. Central West Antarctica

The site of the WAIS Divide ice core in central West Antarctica was targeted because the relatively high accumulation rate there (compared to other parts of Antarctica) means that the ice core can be accurately dated for at least the past ~40,000 years. The ice core will have higher resolution than other Antarctic cores, and will be ideal for comparing to ice-core records from Greenland (e.g. Morse and others, 2002). Emerging evidence supports that the ice divide at this site has migrated over time (Neumann and others, 2008), and Conway & Rasmussen (2009) showed that the divide is migrating today due to flux changes near the margin. However, the millennial history of ice-divide migration is an open question. The ice core was drilled ~24 km from the present-day divide in order to minimize the impact of ice-divide migration on the stratigraphy, and yet be close enough to the divide so that the stratigraphy is not disturbed by flow. The affects of divide migration and ice thickness changes on particle-path trajectories through the ice sheet are critical to understand in order to properly interpret and date the ice core. Here I constrain the histories of accumulation and ice flow in order to support analyses of the WAIS Divide ice core, in an effort to help understand the history of West Antarctica.

1.1.2. Martian Polar Layered Deposits

Past and present accumulation and ablation rates for the Martian PLD must be known in order to decipher the connection between climate and PLD formation, evolution, and observable structure. While present-day ice flow on Mars may have an insignificant influence on the shape of the PLD, it has been proposed that ice flow was more active in the past (e.g. Clifford, 1987; Fisher, 2000; Pathare and Paige, 2005). Winebrenner and others (2008) showed that the shape of present-day inter-trough topography along flowlines across Gemina Lingula, North PLD (see map in Appendix A) matches the shape of an ice mass that has flowed. This evidence for past ice flow of at least part of the Martian North PLD requires that conditions such as the ice temperature or the basal-ice constitutive properties were very different from their present-day values. Here I seek to understand the ice-flow and climate history of the Martian PLD using available data to constrain the range of plausible conditions that could facilitate ice flow.

1.2. Background

1.2.1. Radar layers

Ice-penetrating radar profiles are windows to the interior of glaciers and ice sheets. These views inside the ice display the bed topography, and also internal layers. Each reflection is caused by variations in dielectric properties, density, or impurity concentration (e.g. Fujita and others, 1999), and is assumed to be a surface of constant age (an isochrone). Different radar frequencies are used to image internal layers at different depths and deeper layers can be better imaged using lower frequencies. Recent radar development has made it possible to obtain detailed images of the deepest

layers in Greenland and Antarctica, several kilometers beneath the ice (e.g. Laird and others, In Press).

This is an extraordinary time in Mars' polar science; detailed radar profiles of the Martian ice caps have revealed the bed topography and the internal structure there for the first time. There are currently two satellite radar systems, the Mars Advanced Radar for Subsurface and Ionosphere Sounding (MARSIS; e.g. Picardi and others, 2005; Plaut and others, 2007) and the Shallow Subsurface Radar (SHARAD; e.g. Seu and others, 2007; Phillips and others, 2008). MARSIS operates between 1.3- to 5.5-MHz with a 1-MHz bandwidth, and a spatial resolution of ~10 km (e.g. Picardi and others, 2005). SHARAD has a 20-MHz center frequency with a 10-MHz bandwidth, and a spatial resolution of 3-6 km (e.g. Phillips and others, 2008).

1.2.2. Ice flow

Experimental work by Glen (1995) provided a physical relationship between applied stress and strain rate in ice; this is often called 'Glen's law' or the flow law. The flow law is a power-law relationship, where the flow exponent depends on the dominant creep mechanism. In this work, we consider that ice flows primarily by dislocation creep, with a flow-law exponent n=3; this is the value traditionally used for ice-flow studies, and generally produces a good fit to observations. Ice flow is temperature dependent. The temperature-dependent ice viscosity follows an Arrhenius relationship; the ice viscosity is often referred to as the ice-softness parameter or the fluidity parameter. Ice flow also depends on crystal size and on crystal orientation. Since Glen's law assumes that ice is isotropic, and this is not always an appropriate assumption, a scalar enhancement

factor can be included in the flow law to account for the effects of anisotropy (e.g. Paterson, 1994, pg. 99).

1.2.3. Ice-flow models

Use of ice-flow models provides a means to understand glacier and ice-sheet behavior because an ice-flow model should run faster than it would take for an actual ice mass to evolve. Ice-flow models in combination with laboratory analyses of ice cores are needed to infer the correct climate history, because climate information that is recorded in the ice has been affected by the history of ice flow (e.g. Paterson, 1994, pg. 276-288). However, ice-flow modeling is nontrivial because only the simplest cases have analytical solutions. For most problems, the solution must be calculated numerically, meaning that the governing equations must be cast in a numerical form. Finite-difference, finite-volume, and finite-element methods are all commonly used in glaciology (e.g. Van der Veen, 1999; Hooke, 2005, pg. 288). Here I employ the finite-volume method (e.g. Patankar, 1980).

To find a numerical solution, it is often necessary, or desirable, to make simplifying assumptions. A common assumption in ice-flow modeling is the "Shallow Ice Approximation" (SIA, e.g. Hutter, 1983, pg. 256; Paterson, 1994, pg. 262), which applies in cases where the ice thickness is much smaller than the characteristic horizontal length scales over which thickness or stress change significantly. If the characteristic horizontal length scale is the lateral extent of the ice cap, then derivatives of velocities and stresses with respect to x (horizontal axis) are generally much smaller than derivatives with respect to z (vertical axis). Here I use the SIA.

However, in principle the inverse problems could also be solved using full-stress solutions to the momentum conservation equations.

1.2.4. Inverse problems

In an inverse problem, the existing data have resulted from a known process that depends on some unknown parameters or boundary conditions that we wish to find. That is, an inverse problem needs a forward algorithm and an inverse algorithm. Based on a guess of the unknown parameter values, the forward algorithm generates a realization of observable quantities. The inverse algorithm evaluates the fit of the modeled observables to the actual data, and assesses whether any physical constraints imposed on the problem have been satisfied, in order to infer the best set of unknown parameter values. In general, setting up an inverse problem is a powerful tactic to solve problems in solid-earth geophysics (e.g. Menke, 1989; Parker, 1994; Gubbins, 2004) and in physical oceanography (e.g. Wunsch, 1996), among other fields. However, solving inverse problems is a relatively new frontier in glaciology; here I contribute to this growing body of work.

1.3. Structure and synopsis of the dissertation

The tools that I have integrated and developed to infer changes in ice flow and accumulation can be used in many applications. However, the strengths and weaknesses of these tools must be understood before we can draw robust conclusions. The chapters in this dissertation address methodology and implementation for terrestrial and Martian ice.

1.3.1. Inferring mass-balance patterns and topography on Mars

Internal layers are necessary to accurately infer mass-balance patterns because the ice-surface shape only weakly reflects spatial variations in mass balance. Additional rate-controlling information, such as the layer age, the ice temperature, or the ice-grain sizes and ice-crystal fabric, can be used to infer the absolute rate of mass balance. An inverse problem is solved to infer mass balance from the shapes of internal layers. The solution to the inverse problem is the best set or sets of unknown boundary conditions or initial conditions that, when used in the calculation of ice-surface elevation and internal-layer shape, will generate appropriate predictions of observations that are available. Internal layers can also be used to infer Martian paleo-surface topography from a past era of ice flow, even though the topography may have been largely altered by subsequent erosion. Chapter 2 shows that accumulation rates and surface topography have been successfully inferred from internal layers in Antarctica. Using synthetic data, the ability of this method to solve the corresponding inverse problem to infer accumulation and ablation rates, as well as the surface topography, for Martian ice is demonstrated. If past ice flow has affected the shapes of Martian internal layers, this method is necessary to infer the spatial pattern and rate of mass balance.

1.3.2. Response timescales for Martian ice masses

The shape of the Martian North Polar Layered Deposits (PLD) reconstructed by Winebrenner and others (2008) is used to estimate pairs of mass-balance rate and ice temperature that could generate their reconstructed shape. For any ice mass, the flow rate depends on the mass-

balance rate, on the near-basal ice temperature, and on any flow enhancement due to impurities in the ice or variations in the physical properties of the ice. Therefore, pairs of mass-balance rate and ice temperature (plus any flow enhancement) can generate identical ice-surface topography. Without additional information to constrain the actual rate of mass balance, the actual ice temperature, or the actual ice-flow constitutive properties, another means to constrain the plausible range of ice-flow rates is needed. The volume-response timescale for an ice mass is the time for an ice mass to accumulate or shed enough mass approach a new steady-state shape following a climate change (e.g. Johannesson and others, 1989). Chapter 3 shows that the volume response timescale can be used to eliminate implausible combinations of mass-balance rate and ice temperature or ice-flow enhancement that take too long to adjust.

1.3.3. Transient ice flow using a limited-domain model

Some of the spatial information about ice-sheet history that is sought from data in the vicinity of an ice divide can be inferred by solving an inverse problem. However, computational efficiency is required when solving inverse problems that involve many iterations of the ice-flow model, or when using a higher-resolution model. Limiting the model domain to include only the relevant portions of the ice sheet is a way to reduce computation time. It is also advantageous to limit the model domain when assimilating data that are available only in limited locations on the ice sheet. When the domain is limited, we do not need to make estimates of observable quantities in regions where parameter values and boundary conditions are unconstrained. However, limiting the domain of a transient ice-flow model is not trivial. Chapter 4 presents a new method to accurately

calculate transient ice flow using a limited-domain model. This new method incorporates additional information to ensure that the limited domain evolves consistently with the full domain within which it exists.

1.3.4. Inferring transients in accumulation rate, ice-sheet thickness, and ice flow from internal layers

Chapter 5 describes a method to infer histories of ice flow, ice-sheet thickness, and accumulation rate from the shapes of internal layers. Present-day internal-layer shapes observed by radar are the most accessible remaining record of this past information, and an inverse problem can be solved to infer this information. The new aspect of this work is to incorporate a transient forward algorithm, using the ice-sheet evolution calculation described in Chapter 4. Waddington and others (2007) solved the inverse problem to infer a steady-state accumulation pattern from internal layers using a steady-state forward algorithm, and here this approach is extended to infer transient histories from deeper layers. The goal in solving this inverse problem is to find a set model parameters (e.g. accumulation-rate history) that have the minimum variation required to explain the data (e.g. internal-layer shapes). To assess the capability of this new approach, parameter values can be prescribed to generate synthetic data, then the synthetic data can be used to infer these parameter values. Chapter 5 demonstrates how local accumulation variations and external-flux variations (e.g. from sea-level changes leave distinct imprints on internal-layer structure, and how these histories can be inferred by solving an inverse problem.

1.3.5. Inferring histories of accumulation and ice dynamics for Central West Antarctica

In preparation for an application to data from the West Antarctic Ice Sheet (WAIS) Divide ice-core site, Chapter 6 describes the available data and the motivation for this work. Neumann and others (2008) found that the accumulation pattern may have been the same over the past 8 kyr, but the accumulation rate was at least 30% higher from 5-3 kyr ago. Conway and Rasmussen (2009) found that the present-day ice divide is migrating due to variations in ice dynamics, rather than by variations in local accumulation. The WAIS Divide is dynamically influenced by ice streams on the Ross-Sea side and the Amundsen-Sea side. Given the recent speed up of Thwaites and Pine Island glaciers on the Amundsen-Sea side, and the recent stagnation of Kamb Ice Stream (e.g. Joughin and Tulaczyk, 2002) on the Ross-Sea side, it is evident that dynamical changes can be significant. Given the extent of present-day divide migration, the ice-flow history at this site is especially critical to properly interpret ice-core chemistry.

Chapter 2

A Method to Infer Past Surface Mass Balance and Topography from Internal Layers in Martian Polar Layered Deposits

This chapter is published under the same title with authors M. Koutnik, E. Waddington, and D. Winebrenner in *Icarus* **204**(2), 458-470. The comments of two anonymous reviewers improved the manuscript.

Internal layers in ice masses can be detected with ice-penetrating radar. In a flowing ice mass, each horizon represents a past surface that has been subsequently buried by accumulation, and strained by ice flow. These layers retain information about relative spatial patterns of accumulation and ablation (mass balance). Internal layers are necessary to accurately infer mass-balance patterns because the ice-surface shape only weakly reflects spatial variations in mass balance. Additional rate-controlling information, such as the layer age, the ice temperature, or the ice-grain sizes and ice-crystal fabric, can be used to infer the absolute rate of mass balance. To infer mass balance from the shapes of internal layers, we solve an inverse problem. The solution to the inverse problem is the best set or sets of unknown boundary conditions or initial conditions that, when used in our calculation of ice-surface elevation and internal-layer shape, generate appropriate predictions of observations that are available. We also show that internal layers can be used to infer Martian paleo-surface topography from a past era of ice flow, even though the topography may have been largely altered by subsequent erosion. We have successfully inferred accumulation rates and surface topography from internal layers in Antarctica. Using synthetic data, we demonstrate the ability of this method to solve the corresponding inverse problem to infer accumulation and ablation rates, as well as the surface topography, for Martian ice. If past ice flow has affected the shapes of Martian internal layers, this method is necessary to infer the spatial pattern and rate of mass balance.

2.1. Introduction

The spatial pattern and rate of accumulation and ablation (mass balance) over an ice cap (i.e. mass exchange with the atmosphere) must be known in order to infer the ice-flow history. On Earth, rates of accumulation can be determined by drilling an ice core, measuring the thickness of datable layers, and correcting for strain thinning where necessary, but this represents mass-balance conditions at only the single point of origin of each ice-core sample. Internal layers, which in almost all terrestrial cases are isochrones, contain information about mass-balance patterns in both space and time. The large body of radar data from terrestrial ice sheets has greatly increased our understanding of terrestrial ice-sheet evolution and climate (e.g. Paren and Robin, 1975; Morse and others, 1998; Conway and others, 1999; Fahnestock and others, 2001b).

Past and present accumulation and ablation rates are fundamental unknowns for the Martian Polar Layered Deposits (PLD). This information is necessary if we are to decipher the connection between climate and PLD formation, evolution, and observable structure. Internal-layer shapes must be known if we want to determine past mass-balance patterns, because the surface topography is relatively insensitive to spatial variations in mass balance. Fortunately, internal layers in the North and South PLD have been imaged successfully by radar (e.g. Picardi and others, 2005; Plaut and others, 2007; Seu and others, 2007; Phillips and others, 2008).

While present-day ice flow on Mars may have an insignificant influence on the shape of the PLD, it has been proposed that ice flow was more important in the past (e.g. Clifford, 1987; Fisher, 2000; Pathare and Paige, 2005), and Winebrenner and others (2008) showed that the shape of present-day inter-trough topography along lines following surface gradients (i.e. “flowlines”) across Gemina Lingula (also referred to as Titania Lobe;

Pathare and Paige, 2005), North PLD matches the shape of an ice mass that has flowed. We consider an era of past ice flow as a time when the influence of ice flow was comparable to the influence of mass balance in shaping the internal layers and the ice-surface topography. In this paper, we assume that past ice flow affected the shapes of internal layers and the surface topography of the Martian PLD. Under this assumption, an approach that accounts for the effect of ice flow on the internal-layer shape and depth must be used to infer the mass-balance pattern from internal layers; we demonstrate such a method here. In addition, we emphasize that the shapes of internal layers alone cannot be used to determine whether an ice mass has flowed or not; this is discussed more fully in Section 2.3.3. Depending on the spatial pattern of accumulation and ablation, identical layer shapes can be generated in an ice mass where flow is significant and in an ice mass where flow is insignificant relative to other processes. Conversely, flowing ice sheets with similar surface topography but different accumulation patterns can have dramatically different internal-layer architecture.

Using terrestrial glaciological experience and methods that have been applied to terrestrial ice sheets, we show that an inverse method can potentially infer mass-balance patterns during that era of flow, from internal-layer shapes on Mars. To demonstrate this method, we generate synthetic internal layers based on a prescribed spatial mass-balance distribution, and then we attempt to infer the mass-balance pattern from these synthetic layers. The *relative mass-balance pattern* can be successfully inferred from the shapes of internal layers; however the layer age, the ice temperature, the ice velocity, or the ice-grain sizes and ice-crystal fabric must be known to constrain the *absolute mass-balance rate*. We solve different inverse problems to infer mass balance by assuming that

different combinations of information are available. In the first inverse problem, we infer only the relative spatial pattern of mass-balance from the shape of an internal layer with no rate information. This problem could potentially be solved with data currently available for Mars. Then we solve three different inverse problems to infer the relative spatial pattern and the absolute rate of mass-balance in a flowing ice mass. We use (1) the ice-surface topography and ice temperature, (2) the shape of an internal layer, the ice-surface topography, and ice temperature, or (3) the shape of an internal layer, the ice-surface topography, and ice-rheological parameters. Finally, we also solve an inverse problem using internal layers to infer surface topography from a time in the past when ice flow significantly shaped the surface; this is an important problem to solve with Martian internal layers because much of that topography has been significantly eroded to form the present-day surface.

2.1.1. Internal-layer structure and depth

In a flowing ice mass, the depth variations of an individual internal layer are controlled by the spatial pattern of mass balance, and by ice flow. Waddington and others (2007) discussed how to diagnose the appropriate strain regime of a particular layer. Shallow layers (with a depth of at most a few percent of the ice thickness, or in the upper tens of meters in a terrestrial ice sheet), are not significantly altered by ice flow, and the net accumulation at each site can be inferred from the ice-equivalent layer depth divided by the layer age; this is called the Shallow Layer Approximation (SLA). For shallow layers, the mass-balance pattern alone determines the internal-layer structure and depth. If the influence of mass-balance on the shapes of internal layers was always more important than

the influence of ice flow, the SLA would be appropriate for layers at all depths. However, in a flowing ice mass, as the depth to the layer increases, accumulated strain due to ice flow becomes more important, and this simple SLA relationship between layer depth and the mass-balance pattern breaks down. For intermediate layers (in the upper 10%-20%, or to a depth from 10-100 meters in a terrestrial ice sheet), the impact of accumulated vertical strain on the depth of the layer can be estimated using a 1-D model of vertical ice flow; this is called the Local Layer Approximation (LLA). However, this local strain correction also can become invalid for deeper layers. Deeper, older layers reflect conditions further in the past, but they have been more affected by horizontal gradients in strain rate and accumulation. Therefore, their information is highly valuable but more difficult to interpret. Waddington and others (2007) demonstrated that it is necessary to use formal inverse methods, incorporating 2-D ice flow, to correctly determine the accumulation pattern recorded by deeper layers in terrestrial ice caps. We cannot rule out that ice flow was important in shaping topography and internal structure across the PLD, especially for Gemina Lingula, North PLD (Winebrenner and others, 2008). Therefore, we expect that an inverse method must be used to infer spatial patterns and rates of mass-balance from deeper layers in Martian ice.

On terrestrial glaciers, and parts of the large terrestrial ice sheets, snow typically accumulates at higher elevations (the accumulation zone). Ice flow redistributes the excess mass to lower elevations where it ablates (the ablation zone). The equilibrium line demarcates the two zones. Internal horizons represent past ice-sheet surfaces, which have been subsequently buried, and the thickness of ice between any two horizons has been displaced and strained by ice flow. On Earth and Mars, we assume that each individual horizon is an isochrone, i.e. a surface of constant age.

The horizons are observed with ice-penetrating radar, and at different depths there are different distances between each pair of horizons. In this paper we refer to each horizon as a 'layer', but we note that a layer also has a thickness. The shape and depth of an individual layer are influenced by the rate of accumulation or ablation, gravitational forces, internal stresses, ice-rheological parameters (which depend on the ice temperature), bedrock topography, and unconformities.

2.1.2. Necessary Data

Internal layers have been observed across the Martian PLD by the Mars Advanced Radar for Subsurface and Ionosphere Sounding (MARSIS; e.g. Picardi and others, 2005; Plaut and others, 2007) and by the Shallow Subsurface Radar (SHARAD; e.g. Picardi and others, 2005; Phillips and others, 2008). The shapes of continuous internal layers along putative flow lines will be the primary data when we apply our method to Mars in the future. We also use the PLD surface geometry, which is available from the Mars Orbiter Laser Altimeter (MOLA), and the ice thickness from the radars. Currently, the internal-layer ages, the ice velocity at the time of flow, the ice temperature at the time of flow, the ice-crystal fabric, and the ice-grain size are not known for the PLD. However, if any of this information becomes available, or can be reasonably estimated, then we can incorporate it as part of the inverse problem.

2.2. Methods

Inference of mass-balance patterns from internal layers is an inverse problem, which can be solved using geophysical inverse theory (e.g. Menke

1989; Parker 1994; Aster and others 2005). An inverse problem is one where the existing data have resulted from a known process that depends on some unknown parameter values or boundary conditions that we wish to find. In the Martian problem, the data are the shapes of individual internal layers and at least parts of the elevation profile of the ice surface, and the unknowns are the layer ages, the mass-balance pattern, and the ice temperature. An inverse problem needs a forward algorithm and an inverse algorithm. We calculate the shapes of layers and the surface topography with the forward algorithm. Then the unknown parameters can be found by minimizing a performance index in the inverse algorithm. The performance index is a number representing how well the observable quantities calculated by the forward algorithm match the data to an expected tolerance while, in this case, finding a spatially smooth mass-balance pattern. Any simplifications made in the forward algorithm, or constraints included in the inverse algorithm, must be considered when interpreting the solution.

In Section A2.1 we describe our particular forward algorithm, and in Section A2.2 we outline our particular inverse algorithm. The forward algorithm is a steady-state flowband model that calculates ice-surface elevation and internal-layer shapes (Waddington and others, 2007). A flowband is illustrated in Figure 2.1. This is a 2-D model that also accounts for width variations; therefore it is considered to be 2.5-D. There are many unknowns regarding the Martian PLD, and for this reason we start with a simple, steady-state forward model. As shown in Figure 2.1, the model domain does not need to include an ice-sheet terminus or an ice divide; it can be defined over a limited domain. The surface-profile prediction depends on the ice flux entering the domain, the mass-balance profile, the ice thickness at one point in the domain, and the constitutive properties of the ice. Layer prediction in this forward calculation requires the ice-surface

profile, which is either known or calculated, and depends on the layer age, the ice flux entering the domain, and the mass-balance pattern. The forward algorithm can include only a surface calculation, only a layer calculation, or both a surface calculation and a layer calculation (see Section A2.1). Therefore, our unknown model-parameter set may consist of the layer age, the ice flux entering the domain, the spatial pattern of mass balance, the ice thickness at one point in the domain, and the ice-softness parameter (see Equation A2.1.5). The inverse algorithm uses a Gradient solution method (e.g. Parker, 1994; Aster and others, 2005) to find physically reasonable values of these unknown parameters (see Section A2.2). The preferred parameters generate an internal layer and an ice surface that fits the data at an expected tolerance determined by data uncertainties.

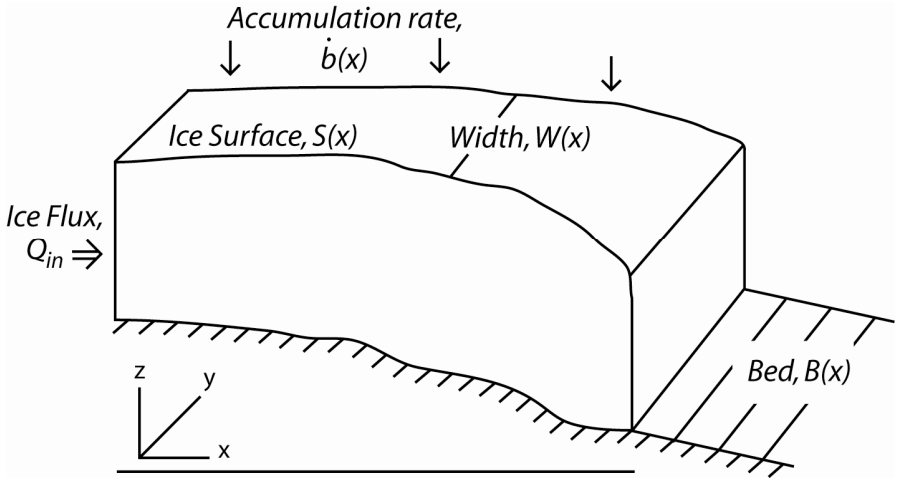

Figure 2.1. Geometry of a flowband with width variations. The ice-surface elevation (at least at a single point), flowband width, and bed geometry are required inputs to the forward algorithm. The flowband domain can be limited in horizontal extent.

This general method can be modified based on site-specific conditions and/or data availability. Following Waddington and others (2007), we illustrate this method using data from Antarctica. In preparation for using this method with Martian radar data, we generate synthetic Martian layers, and then we investigate the ability of the inverse procedure to infer a known synthetic mass-balance pattern from those synthetic layers.

2.3. Results

Depending on which data are available, and which calculations are included in the forward algorithm, different quantities must be assumed, and different information can be inferred with this inverse approach. The simplest problem uses a forward algorithm that includes only a kinematic layer calculation, assuming that the surface topography is known, to infer the relative mass-balance pattern from an undated internal layer. We show that if the layer age is known, or if the ice velocity or the accumulation rate during the era of flow is known, we can also infer the absolute mass-balance rate using a forward algorithm that includes only a kinematic calculation. In principle, data that are currently available for Mars could be processed along flowlines so that some of the inverse problems here could be solved. The other problems further motivate challenges for future laboratory experiments and missions.

Using steady-state continuity from Equation A2.1.1, and using the depth-averaged horizontal velocity in Equation A2.1.6, Equation 2.1 shows how, for any ice-sheet profile defined by the ice thickness $H(x)$ and surface slope dS/dx, the accumulation rate $\dot{b}(x)$ and the ice-temperature-dependent softness parameter $A(T(x))$ always occur in a ratio

$$\left[\frac{\dot{b}(x)}{A(T(x))}\right] = \frac{1}{x}\frac{2}{n+2}(\rho g)^n \left|\frac{dS}{dx}\right|^{n-1}\left(-\frac{dS}{dx}\right)H^{n+2}(x) \qquad (2.1)$$

Higher accumulation rates $\dot{b}(x)$ can always trade off against greater ice softness *A(T(x))* through higher temperature, to produce the same surface shape, and therefore the same layer shape with a younger layer age. We discuss ways in which accumulation rate and ice temperature may be untangled.

2.3.1. Mass Balance and Topography in Antarctica

Waddington and others (2007) solved the inverse problem to infer the relative spatial pattern and absolute rate of accumulation at Taylor Mouth, a flank site near Taylor Dome, Victoria Land, Antarctica. At Taylor Mouth, additional data were available beyond the surface topography and internal-layer shapes observed with radar. Bed elevation was also measured by radar, and flowband width was found by interpolating velocities between measurement points and finding the distance between two nearby flow lines. A 100-meter ice core intersects the flow line, and the average accumulation rate at the core site was known. A strain network in this area provided velocity data at the ice surface.

The forward algorithm in this previous application to Taylor Mouth (Waddington and others 2007) included only a kinematic layer calculation. The unknown parameter set consisted of the ice flux entering one end of the flowband, the spatial pattern of accumulation (there is no ablation area near this site), and the age of the layer. Use of only a kinematic forward algorithm was justified because the surface elevation at Taylor Mouth has been approximately in steady-state over the past few thousand years. Therefore, the dynamic calculation of surface topography could be excluded

to simplify the problem. Since the surface topography is known, and because a dynamic calculation was excluded in the forward algorithm, rate information was included only through the surface-velocity measurements and the one accumulation-rate measurement. At Taylor Mouth, these rate-containing data were sufficient to constrain the magnitude of accumulation rate.

2.3.1.1. Inferring Mass Balance from an Undated Layer

To show the sensitivity of the Taylor Mouth solution (Waddington and others 2007) to rate information from measurements of surface-velocity and accumulation-rate, and to prepare for Martian applications where rate information is unavailable, we now solve the Taylor Mouth inverse problem using only internal-layer data. In this problem, the mass-balance rate is determined by the layer age. If the internal layer is undated, and if no additional rate-controlling data exist, we can infer only the relative mass-balance pattern. To express this result, we represent the spatial pattern of accumulation, $\dot{b}(x_i)$ at spatial positions x_i, as a nondimensional spatial pattern of accumulation, $\tilde{\dot{b}}(x_i)$, having root-mean-square amplitude, i.e.

$$\frac{1}{L}\int_0^{x=L} \tilde{\dot{b}}^2(x)dx = 1 \tag{2.2}$$

multiplied by the magnitude B of the accumulation rate, giving

$$\dot{b}(x_i) = B\tilde{\dot{b}}(x_i)\,. \tag{2.3}$$

By representing the mass-balance pattern $\dot{b}(x_i)$ in this way, we can compare the values of B that correspond to solutions using different combinations of rate-controlling data (e.g. the layer age or the ice temperature).

Figure 2.2a shows different accumulation-rate solutions corresponding to different guesses of the layer age, inferred using only an internal layer as data, and using the known modern surface topography. Particles can follow the same paths and reach the same depths over a longer time when accumulation rate is low, or over a shorter time when accumulation rate is high. The central result from this test is that similar spatial patterns can be inferred, regardless of the accumulation-rate magnitude. Figure 2.2b shows B/B_{ref}, the scaling factor B divided by the scaling factor of a reference solution B_{ref} (here taken to be the solution from Waddington and others 2007), corresponding to the solutions in Figure 2.2a.

On Mars, we are likely to know only the layer shape. It is unlikely that we will know the layer age, and velocities and accumulation rates from the regime in which the layers formed cannot be measured. However, by exploring the sensitivity of the Antarctic solution, we found that useful information about the relative spatial variability in mass balance can still be inferred, even if the absolute rate of accumulation cannot be recovered.

2.3.1.2. Inferring Surface Topography

We can also infer the shape of the ice-surface topography from the shape of an internal layer. This will be useful for the PLD, where the surface shape at the time of flow has been subsequently eroded, or largely obliterated. We demonstrate this using data from Taylor Mouth, Antarctica.

If the surface topography is unknown, and is being solved for as part of the inverse problem, we still have to estimate the surface topography for the first iteration of the forward algorithm. As the inferred mass-balance pattern is iteratively updated in the inverse algorithm, the inferred surface

topography is also updated, using Equation A2.1.7, and this updated surface is used in the subsequent iteration for the mass-balance pattern. The unknown parameter set consists of the ice flux entering one end of the flowband Q_{in}, the spatial pattern of accumulation $\dot{b}(x)$, the age of the layer *Age*, and the ice thickness at one location along the flowband H_0. In the absence of rate-controlling information (e.g. layer age, ice velocity), we have shown that we cannot determine the absolute rate, B, of mass balance.

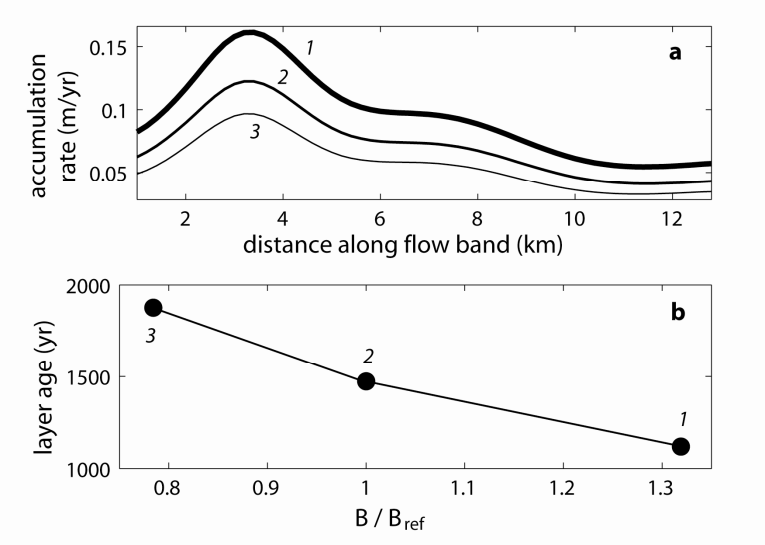

Figure 2.2. **a**. The accumulation-rate solution for the Taylor Mouth inverse problem using an undated internal layer and no rate-controlling data. The dark gray line shows the solution with an initial guess at the layer age that was 25% lower (resulting in a higher accumulation rate) than the layer age inferred from Waddington and others (2007), and the light gray line shows the solution with an initial guess at the layer age that was 25% higher (resulting in a lower accumulation rate). **b.** The numbered points correspond to the numbered solutions in the above panel. The accumulation-rate magnitude B equals unity for the correct accumulation rate. Without additional rate information, the same internal layer can be generated with an older age and a lower accumulation rate, or a younger age and higher accumulation rate.

Using data from Taylor Mouth, Antarctica, we demonstrate our ability to infer the ice-surface topography by performing two tests. First, we infer ice-surface topography from the shape of an undated internal layer, an estimate of elevation at one point on the ice surface, and the known ice temperature (referred to as test 1). We estimate the ice-surface elevation at the furthest upstream point along the flowband and assume that we know this value within 5 m. In this problem, with no additional rate-controlling data, the ice temperature determines the inferred mass-balance rate and the length of the ice mass (the maximum thickness is specified).

In the second test (referred to as test 2) we infer ice-surface topography from the shape of an undated internal layer and at least two points on the ice surface. We assume that the ice temperature is unknown, and the greater the horizontal distance between the two known surface-elevation points, the better we can infer the ice-surface profile. We show that we can infer a surface with the correct shape, even if the inferred rates are incorrect. At the first iteration of the forward algorithm we guess that the ice-surface has a uniform elevation along the flowband. We guess that the ice-softness parameter $\tilde{A}(x)$ is five times greater than the original value, so that the deformation rates are five times larger. The inferred mass-balance pattern together with the inferred ice-surface shape generate an internal layer that has the appropriate balance between smoothness and fit to the data, where the data are fit with a root-mean-square mismatch consistent with data uncertainties (see Section A2.2).

Figure 2.3a shows that the solution from the inverse problem is similar to the actual ice surface at Taylor Mouth (dotted line). Figure 2.3b compares the mismatches of test 1 and test 2 against the actual ice surface, normalized by a reasonable estimate of the measurement uncertainty of 5 meters. This test with Taylor Mouth data shows that the surfaces found by

solving these inverse problems have the same shape as the measured surface; this is a significant result. The inferred values are within one standard deviation of the point(s) on the surface that are known, and at most within two standard deviations elsewhere along the profile. Knowledge of the ice temperature, especially if there are spatial variations in ice temperature, gives a slightly better solution. However, since ice-temperature information is not currently available for Mars, it is important that we can infer the shape of the surface topography from an internal layer and two points on the ice surface; in Section 2.3.4.5 we discuss a test to reconstruct paleo-surface topography using synthetic data for Mars.

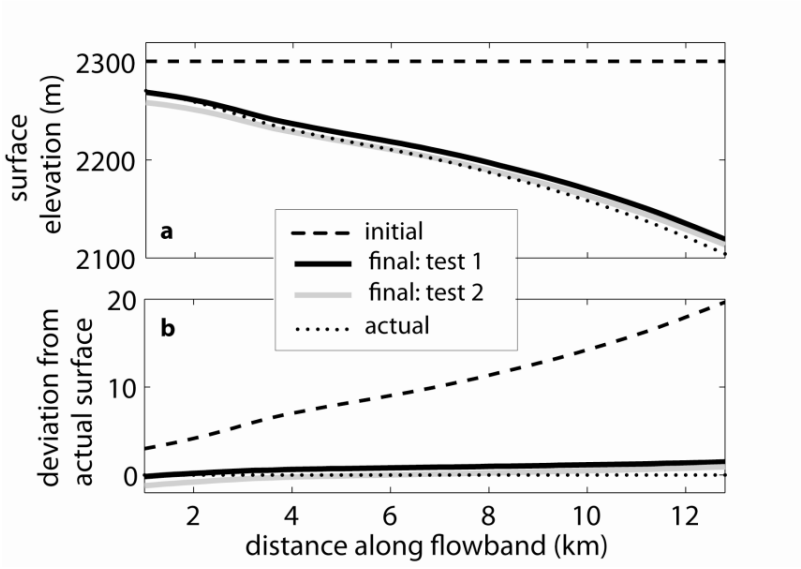

Figure 2.3. a. Comparison between the actual ice-surface topography at Taylor Mouth, Antarctica (dotted line), initial guess of ice-surface topography (dashed line), and the best estimate of ice-surface topography found by solving the inverse problem using an internal layer, the ice-surface elevation at one point, and a known ice temperature (test 1; black-solid line), and using an internal layer and two points on the ice surface (test 2; gray-solid line). **b.** The actual ice surface is subtracted from itself (dotted line), from the ice-surface topography estimated at the initial iteration (dashed line), and from the ice surface found by solving the inverse problem (black and gray solid lines), all nondimensionalized by the uncertainty of 5 m in the measured surface elevation.

2.3.2. Synthetic Data for Mars

To demonstrate the usefulness of our inverse approach, we solved inverse problems with synthetic "data" that we generated for Mars. Using our forward algorithm with prescribed maximum ice thickness, ice-softness parameter, mass-balance pattern, layer age, and input ice flux at the upstream end of the flowband, we calculated the associated ice-surface profile and generated shapes of synthetic internal layers. Then we used these synthetic data with our inverse method to infer a model-parameter set that included a characteristic ice thickness, the ice-softness parameter, the mass-balance pattern, the layer age, and the input ice flux. In order to see how well our inverse procedure worked, we compared the inferred set of model parameters to the known values that we used to generate the synthetic data.

The following assumptions were made in all our tests for the PLD. The modeled PLD were assumed to be pure ice, which restricts the value of the softness parameter A_0 (in Equation A2.1.5). The exponent in the constitutive relationship for ice flow, Equation A2.1.4, had a value of $n = 3$, as inferred by Winebrenner and others (2008) for Martian ice. An exponent of $n = 3$ is typical for terrestrial ice sheets and applies for deformation primarily by dislocation creep (e.g. Paterson, 1994, pg. 85). The temperature at depth was approximated by a uniform gradient using a surface temperature of 170 K (e.g. Pathare and Paige, 2005) and a basal heat flux of 0.025 Wm^{-2} (e.g. Clifford 1987; Grott and others, 2007). The maximum ice thickness and bed topography used to generate synthetic data resemble conditions on the present-day North PLD (e.g. Phillips and others, 2008), as does our chosen mass-balance rate of ~0.5 mm yr^{-1} (e.g. Laskar and others, 2002). Present-day ice temperatures (e.g. Pathare and Paige, 2005) make ice flow very slow, but any value of ice temperature could have

been used. The surface geometry for each mass-balance pattern came from a steady-state surface calculation based on ice dynamics using Equation A2.1.7. The ice-divide thickness was chosen to be 2 km. We assume a uniform flowband width, which is a simplification, and the flowband width could be estimated by tracking the divergence of adjacent flow paths along the surface of the actual topography, as done by Winebrenner and others (2008).

Using our estimate of surface temperature, heat flux, and mass-balance rate, and because the steady-state model does not allow for past ice-temperature transients, the resulting length of the flowband is approximately 20 km, and we can solve the inverse problems using only a limited portion of this full length. Compared to modern flowband lengths of ~100 km or more across the PLD, these lengths are very short because near-basal ice at the present-day temperature of ~180 K (e.g. Pathare and Paige, 2005) requires very steep slopes to achieve equilibrium with the present-day mass balance of ~0.5 mm yr^{-1} (e.g. Laskar and others, 2002). Present-day ice is so cold that ice-flow rates are insignificant with the existing low surface slopes (e.g. Hvidberg, 2003; Greve and others, 2004; Greve and Mahajan, 2005), and conditions must have been different in the past for ice flow to shape the observed topography (Winebrenner and others, 2008; Koutnik and others, 2008). The bed topography was chosen to be flat, but any topography can be used in the model. We used an isothermal temperature distribution, and we assigned an age of 1 Myr to the synthetic data layer. To make the inverse problem more realistic, we added red noise to our synthetic layer and used the perturbed layer as the data. We set the standard deviation, $\sigma_i^{(d)}$, on the layer data to be 3 m because we applied red noise with an amplitude of 3 m, and chose a correlation length of 600 m. Our initial guess at the layer age was several percent higher than the true

age of the synthetic data; any initial guess could be used. The initial guess of the accumulation rate was the layer depth divided by our initial guess of the layer age (SLA, see Section 2.1.1). We focused our study near the ice divide, where no ice flux enters the domain (i.e. $Q_{in} = 0$).

2.3.3. Internal-Layer Shapes

Internal-layer shapes can be generated for any mass-balance pattern and flow regime. For example, Fisher (2000) generated internal-layer shapes for the "accublation" model (Fisher, 1993, Fisher, 2000). The accublation mass-balance pattern has alternating zones of accumulation and ablation to account for the presence of troughs on the North PLD landscape. In the accublation model, the shapes of both the ice surface and the internal layers were significantly affected by the mass-balance pattern. However, it is also possible for different mass-balance patterns to result in similar surface profiles, yet have very different internal-layer shapes (see Figure 2.5).

While the mass-balance pattern directly shapes the internal layers, the surface shape is relatively insensitive to details of the mass-balance pattern. The ice flux $q(x)$, given by Equation A2.1.2, is proportional to the integral of the mass-balance pattern. The surface slope, given by Equation A2.1.7, is smooth because it depends on the mass-balance pattern only through the nth-root of the ice flux, $q(x)^{1/n}$. The surface slope is integrated to get the ice-surface topography, which further reduces the influence of mass-balance variability on the ice-surface topography.

2.3.3.1. Synthetic Mass-Balance Patterns

We generate steady-state internal layers over a limited part of the domain using several different mass-balance patterns to emphasize the variation of internal-layer shapes. Figure 2.4 shows layers generated with a synthetic mass-balance pattern with linearly decreasing accumulation transitioning into linearly increasing ablation as elevation decreases.

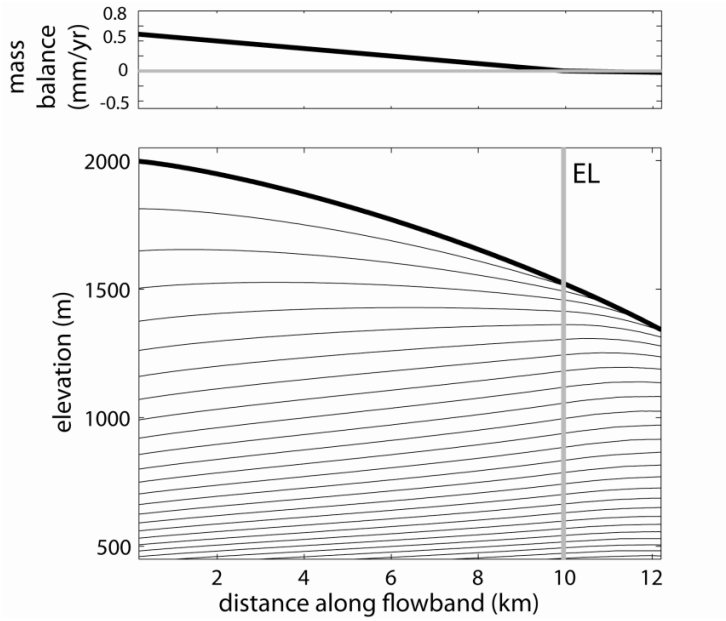

Figure 2.4. Lower panel shows synthetic internal layers from the prescribed mass-balance pattern shown in the top panel. The mass balance decreases linearly with decreasing surface elevation, as net accumulation transitions into net ablation. The layers intersect the surface in the ablation zone. The accumulation and ablation zones are separated at the equilibrium line (EL).

The equilibrium line marks the point of balance between net accumulation and net ablation. Layers near the ice divide in this accumulation zone can have simple, nearly horizontal shapes. Since the transition from net accumulation to net ablation is continuous, the internal layers trend

gradually toward the surface, and can intersect the surface in the ablation zone. In this example, layers also trend towards the surface in the accumulation zone because the accumulation rate decreases with decreasing surface elevation. Even though the magnitude of ablation is small, ablation has a significant impact on the layer shape.

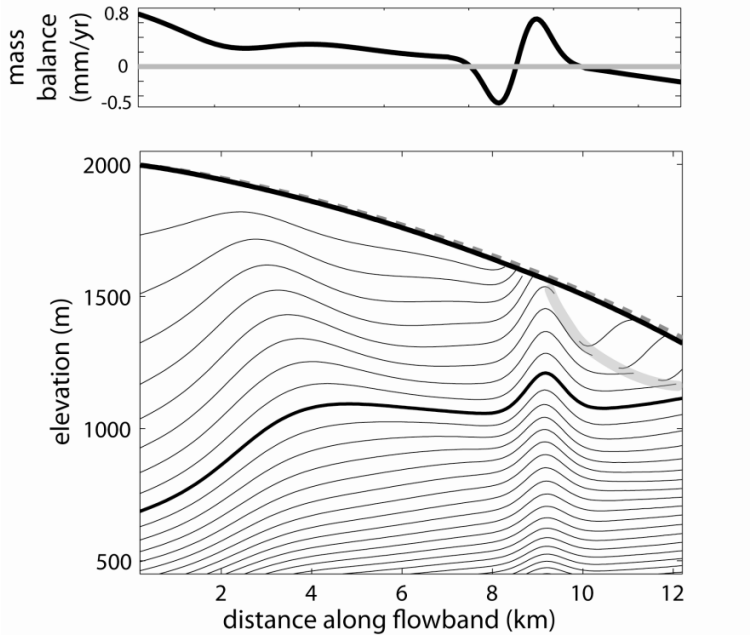

Figure 2.5. Lower panel shows synthetic internal layers from the prescribed mass-balance pattern shown in the top panel. The mass balance varies on short spatial scales and the layers intersect the surface in the ablation zones. The bed is at zero meters, and layers are shown at equal age intervals. The unconformity, highlighted by the gray band, develops in steady state. The gray-dashed line is the ice-surface topography from Figure 2.4. The shapes of the internal layers depend strongly on the mass-balance pattern, while the shape of the ice surface does not. The bold layer is used in the inverse problem we solve in Section 2.3.4.4 and Figure 2.9.

Figure 2.5 shows layers generated with a more complicated mass-balance pattern that fluctuates on smaller spatial scales. The internal-layer shapes reflect these smaller-scale variations in mass balance, but as expected, the ice surface is insensitive to these details. The gray-dashed

line in Figure 2.5 shows the ice surface generated with the mass-balance pattern from Figure 2.4. While the internal-layer shapes associated with the different mass-balance patterns in Figures 2.4 and 2.5 are very different, the ice-surface profiles are nearly the same. We use the mass-balance pattern in Figure 2.5 to illustrate how complex layer structures, including unconformities, can form in a steady state. In Section 2.3.4.3 we infer the mass-balance pattern using the internal layer shown in bold in Figure 2.5. In Section 2.4.2 we discuss this unconformity, highlighted with a gray band in Figure 2.5, which develops due to localized ablation followed by renewed accumulation in the direction of flow.

In addition to the mass-balance patterns used in Figures 2.4 and 2.5, in Section 2.3.3.2 we also generated internal layers using the idealized mass-balance pattern of a zone of uniform accumulation and a zone of uniform ablation. Figures 2.4-2.6 show that internal layers in a flowing ice mass can also have very simple shapes; folded or faulted layer shapes are not required. In terrestrial ice sheets, folded layers can be found near the base of the ice, where bed topography, shear stress, and subtle transients in the flow direction can have a large influence on the layer shapes (e.g. Hooke, 2005, pg. 361). Variations in ice rheology (e.g. Thorsteinsson and others, 2003), movement of the ice divide (e.g. Waddington and others, 2001; Jacobson and Waddington, 2005), and advance and retreat of the ice margin (e.g. Hudleston, 1976) can also cause folded layers. Waddington and others (2001) noted that folds may be clearly identifiable only for a very short time before they overturn, which is another reason that it is rare to observe folds in terrestrial ice sheets. Layers that exhibit faulting have experienced brittle-type deformation, which is not indicative of the creep-type deformation that is associated with ice flow. Cold temperatures promote brittle behavior, and it is possible that faults are indicators of colder ice

temperatures, whereas unfaulted layers may be indicative of warmer ice temperatures. These general features of internal layers in a flowing ice mass should be considered when interpreting internal structure across the Martian PLD.

2.3.3.2. Gemina Lingula, North PLD

Winebrenner and others (2008) found that the inter-trough topography of flowbands across Gemina Lingula, North PLD, closely resembled ice-surface topography generated with a simple steady-state ice-flow algorithm. They interpreted these inter-trough regions to be areas where surface topography has survived from an earlier era in which mass movement due to ice flow balanced mass exchange at the surface. Their algorithm assumed that the mass-balance pattern consisted of a zone of uniform accumulation and a zone of uniform ablation (Paterson, 1972). As explained in Section 2.3.3, this is not a restrictive assumption, because surface shape is relatively insensitive to details of the mass-balance distribution. By seeking the model topography that best fits the actual inter-trough topography, they could estimate the boundary between accumulation and ablation zones (the equilibrium line) when the ice was flowing.

Figure 2.6 shows the internal-layer shapes corresponding to this idealized mass-balance pattern of a single zone of uniform accumulation and a single zone of uniform ablation. We cannot put a scale on this relative mass-balance pattern, because the dimensional scaling factor B (see Section 2.3.1.1) depends on additional assumptions about the layer ages or the ice temperature. Figure 2.6 demonstrates that layers in a flowing ice mass can have simple, nearly horizontal shapes that are continuous across a broad

accumulation region. In the ablation zone, layers intersect the surface. Due to the discontinuity in mass balance, the layers have a discontinuous slope at the equilibrium line, but the shape of the ice-sheet surface is smooth.

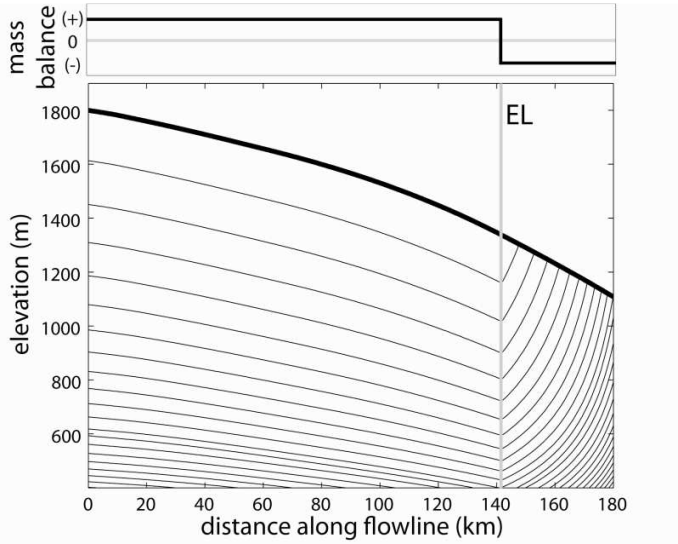

Figure 2.6. Prediction of internal layers along a flowband on Gemina Lingula, North PLD, based on the surface topography and the idealized mass-balance pattern inferred by Winebrenner and others (2008). The mass-balance pattern consists of a zone of uniform accumulation and a zone of uniform ablation, separated by the Equilibrium Line (EL).

2.3.4. Past Surface Mass Balance and Topography for Mars

We demonstrate how well we can infer the model parameters by solving five different inverse problems using a uniform accumulation pattern to generate synthetic internal-layer data. In these inverse problems, in addition to the relative spatial pattern, we can infer the absolute rate of mass balance because the surface-elevation data, ice temperature, and rheological parameters may each provide rate information. For most of the inverse problems that we solve, we used a

limited domain with a simple mass-balance pattern of uniform accumulation so that the results from these different inverse problems could be easily compared. However, any mass-balance pattern could be used. In Section 2.3.4.3, we show the results of an additional test to infer information from an internal layer generated using a mass-balance pattern that included an ablation zone; this test was done only for the case in which the data comprise only surface topography and an undated internal layer. The parameter values inferred in Sections 2.3.4.1-2.3.4.4 are compared in Table 2.1. The inferred mass-balance patterns are compared in Figure 2.7.

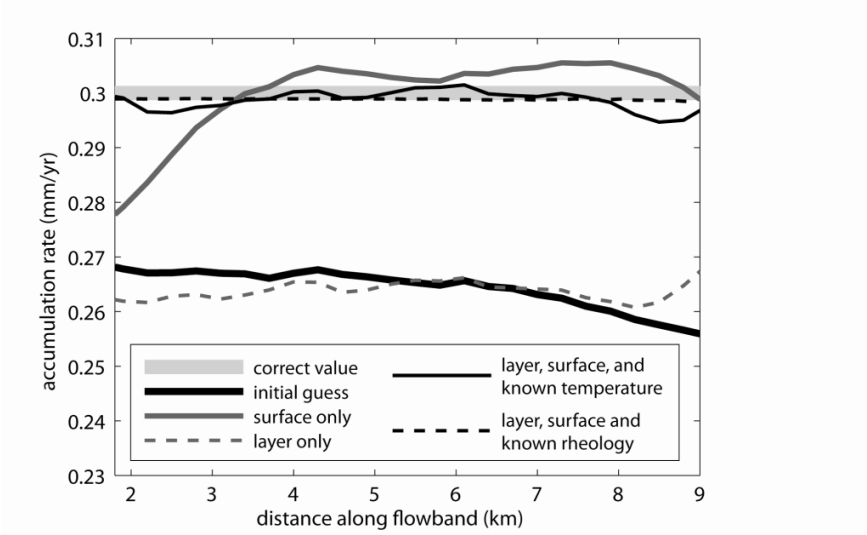

Figure 2.7. The spatial patterns of accumulation from four different inverse problems are compared to each other, to the initial guess, and to the correct values (light-gray curve). Using only undated internal-layer data (gray-dashed curve) we recover the correct spatial pattern, but the wrong magnitude. Using only the surface-elevation data (dark-gray curve) we recover an accumulation-rate profile with the correct average value, but the wrong spatial pattern. Using internal-layer data and surface-elevation data, in addition to either a known ice temperature (thin solid-black curve) or known ice rheological parameters (black-dashed curve) we can recover the actual spatial pattern and rate of accumulation.

Inverse Problem	**All Model Parameters**	**Layer Age, *Age* (Myr)**	**Nondimensional accumulation-rate magnitude, B/B_{ref}**	**Input Flux, Q_{in} (m^3/yr per m width)**
Correct values of the parameters	---	1.0	1.0	0.3
Undated internal layers only	Q_{in}, Age, $\dot{b}(x)$	1.13	0.88	0.261
Ice surface and known ice temperature	Q_{in}, $\dot{b}(x)$, S_{in}, $A(T)$	---	1.02	0.28
Undated internal layers, ice surface, known ice temperature	Q_{in}, Age, $\dot{b}(x)$ S_{in}, $A(T)$	1.0016	0.99	0.256
Undated internal layers, ice surface, known ice rheology	Q_{in}, Age, $\dot{b}(x)$ S_{in}, $A(T)$, K	1.002	0.98	0.35

Table 2.1. The layer age, nondimensional accumulation-rate magnitude B (Section 2.3.1.1) divided by the accumulation-rate magnitude for the correct solution B_{ref}, and the input flux for four synthetic inverse problems are compared to the correct values of the model parameters.

2.3.4.1. Inferring Mass Balance from an Undated Internal Layer

In our first inverse problem, we attempt to infer the relative spatial pattern of mass balance $\tilde{\dot{b}}(x)$, as in Equation 2.3, using a forward algorithm that adopts the synthetic surface and calculates only the internal-layer shape. This inverse problem could be solved with Martian internal layers tracked along putative flowlines. This test is similar to the Antarctic example (Section 2.3.1.1), where the lack of data containing rate

information makes it difficult to constrain the layer age; the initial guess at the layer age determines the rate of accumulation B inferred. In this test, the initial guess at the accumulation pattern differed from the known pattern, and the initial guess at the layer age was several percent higher than the known age (any age guess could be used). Even though we cannot find the correct rate, as shown in Section 2.3.1.1, the pattern of accumulation in the solution is a much better approximation of the true accumulation-rate pattern than our initial guess was, as shown in Figure 2.7.

2.3.4.2. Inferring Mass Balance from Surface Topography

In our second inverse problem, we attempt to infer the relative spatial pattern $\tilde{\dot{b}}(x)$ and the absolute rate of mass balance B from the ice-surface elevation $S(x)$ alone. As discussed in Section A2.1, the surface calculation uses ice dynamics and contains rate information through the temperature-dependent ice softness parameter (Equation A2.1.5). Figure 2.7 illustrates, as we anticipated, that details of the inferred mass-balance pattern are unlike the actual pattern. Using the surface data alone is not very informative about the spatial pattern of mass balance, even when the mass-balance pattern is very simple.

2.3.4.3. Inferring Mass Balance with a Known Ice Temperature

In our third inverse problem, we attempt to infer both the relative spatial pattern $\tilde{\dot{b}}(x)$ and the absolute rate of mass balance B from the internal-layer shape and the ice-surface shape, assuming that the ice temperature at the time of flow is known. The results shown in Figures 2.7

and 2.8 used the same ice temperature that was used to create the synthetic data.

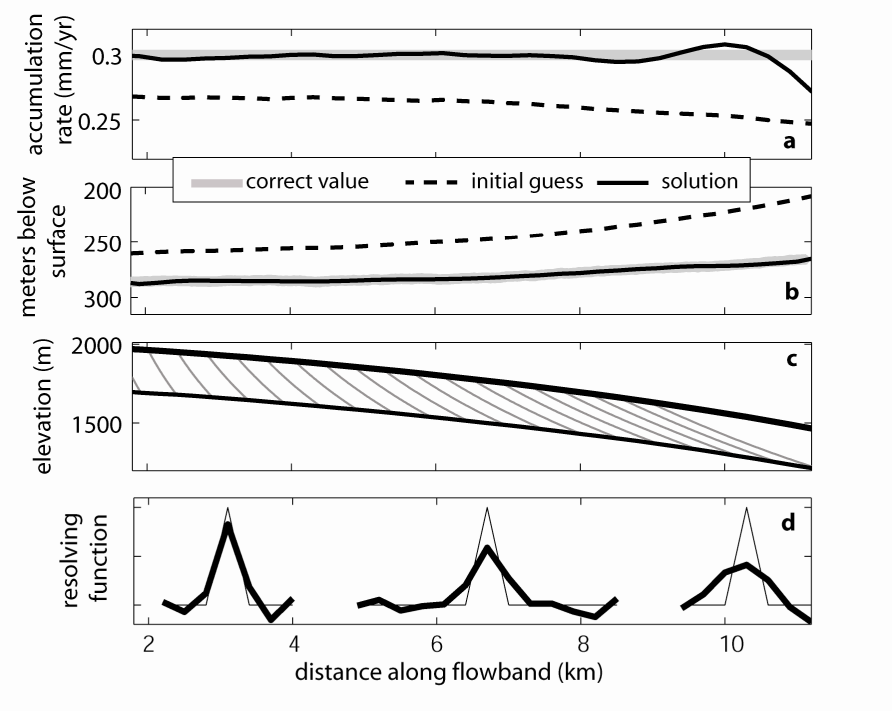

Figure 2.8. Results for the inverse problem using an internal layer, the ice-surface shape, and a known ice temperature; a portion of this solution is also shown in Figure 2.7. **a)** The correct mass-balance pattern was a uniform accumulation rate of 0.3 mm/yr. **b)** The synthetic data layer and the layer predicted by the forward algorithm using the model parameters found by solving the inverse problem. **c)** Paths of particles whose end points create a modeled layer. **d)** The resolving function (bold line) shows the best ability of the solution to recover the single-node perturbation (thin line).

Using the internal layer and the ice-surface elevation as data, the inverse algorithm generates a model-parameter set that is very similar to the actual parameter values; the values are listed in Table 2.1. Figure 2.8a shows the mass-balance solution compared to the known mass-balance pattern and an initial estimate of the mass-balance pattern from the Shallow Layer Approximation (SLA; Section 2.1.1) based on a poor estimate

of the layer-age parameter. Figure 2.8b shows the internal-layer solution compared to the synthetic layer data, and to the initial guess of the layer calculated using an initial guess of the accumulation rate estimated from the SLA. Figure 2.8c shows the paths of particles moving through the ice to form the internal layer, and Figure 2.8d shows the resolving functions for this inverse problem.

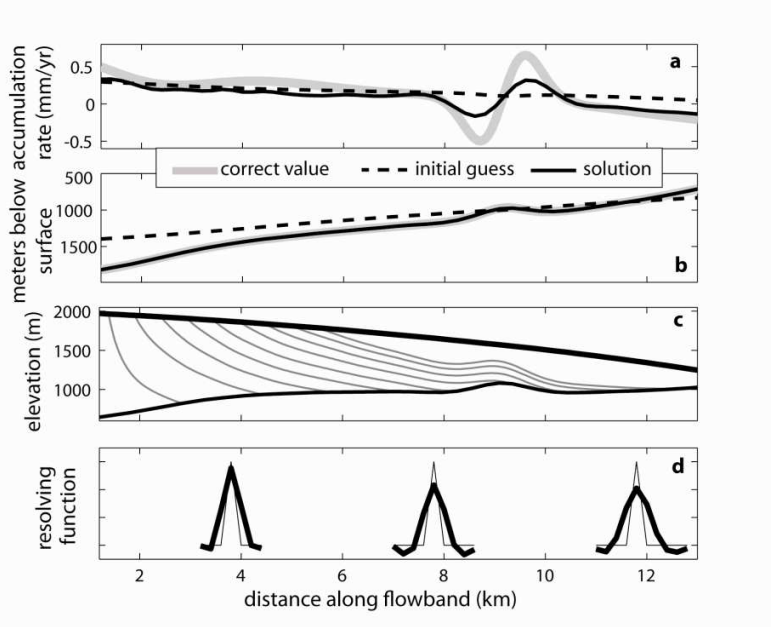

Figure 2.9. Results for the inverse problem using an internal layer, the ice-surface shape, and a known ice temperature. **a)** The correct mass-balance pattern varied on short spatial scales and included a zone of ablation. The initial guess was the depth of the layer divided by the estimated layer age. **b)** The synthetic data layer and prediction by the forward algorithm using the model parameters found by solving the inverse problem. **c)** Paths of particles whose end points create a modeled layer. **d)** The resolving function (bold line) shows the best ability of the solution to recover the single-node perturbation (thin line).

Resolving functions, which indicate the ability of an inverse algorithm to resolve structure in the model parameters (see Section A2.2), show that structure in the spatial variability of accumulation can be better

resolved closer to the divide. The spread of the resolving functions increases due to increasing length of particle paths further from the divide. Figure 2.8c (and Figure 2.9c) shows the paths of particles starting on the surface as they move through the steady-state velocity field and map out an internal layer of a particular age. Particle paths near the downstream end of the domain extend farther, and the particles can move through larger changes in accumulation and strain rate, effectively integrating information about the mass-balance pattern as they move. In addition, we desire a spatially smooth accumulation-rate solution, and we enforce this smoothness criterion in the inverse algorithm (Equation A2.2.1). Therefore, only weighted averages of accumulation rate over the width of the resolving function can be inferred.

We also generated synthetic internal-layer data with a mass-balance pattern, shown in Figure 2.5, which varied on shorter spatial scales, and included an ablation zone. If an internal layer intersects the surface in the ablation zone, information about this mass-balance pattern can be inferred from that layer only over the upstream area where the internal layer exists. Figure 2.9a shows the mass-balance solution compared to the known mass-balance pattern, and to the initial guess from the Shallow Layer Approximation (SLA).

Figure 2.9b shows the internal-layer solution compared to the synthetic layer data and the initial guess at the layer using an accumulation rate estimated from the SLA. Figure 2.9c shows the paths of particles moving through the ice to form the internal layer, and Figure 2.9d shows the resolving functions. Figure 2.9 demonstrates that we can infer a mass-balance pattern that varied on short spatial scales; we can also recover information about the pattern of ablation from the shape of an internal layer as it trends towards the surface. The individual influences of ice

temperature and mass-balance rate are uncoupled by assuming that the ice temperature is known. For any estimate of ice temperature on Mars, the ice-surface topography and the internal-layer shape can be used to recover the corresponding absolute rate of mass balance.

2.3.4.4. Inferring Mass Balance with Known Ice Rheology

In our fourth inverse problem, we attempt to infer the relative spatial pattern $\tilde{b}(x)$ and the absolute rate of mass balance B from the internal-layer shape and the ice-surface shape, assuming that the ice temperature is *unknown*. If both the layer age and the ice temperature are unknown, additional information must be used to uniquely determine the accumulation-rate magnitude and deformation rate, in order to infer the correct values of accumulation and ice temperature (see Equation 2.1). We demonstrate that including a third rate factor through a more general constitutive relation for strain rate may allow us to resolve both mass-balance rate and ice temperature in some circumstances.

Glen's flow law (Glen, 1955; Equation A2.1.4) describes ice flow by a non-linear constitutive relationship between strain rate and deviatoric stress, where deformation occurs primarily by dislocation creep. The flow-law exponent, n, is typically assumed to have a value of 3. However, under different temperature and stress conditions, and for different ice-grain sizes, deformation of ice may be influenced by, or even controlled by, processes other than dislocation creep. The mechanisms of dislocation creep, grain-boundary-sliding-limited creep, and basal-slip-limited creep, can have unique flow-law exponents n, ice-grain-size exponents p, and activation energies for creep Q (Goldsby and Kohlstedt, 1997, Goldsby and Kohlstedt, 2001; Durham and others, 2001). In addition, the shape of an ice sheet

differs when different mechanisms are dominant (e.g. Pettit and Waddington, 2003).

The stress and grain-size conditions for the different regimes in which each mechanism is dominant can be illustrated with a "deformation map" (e.g. Goldsby, 2006). Goldsby and Kohlstedt (2001) proposed a generalized flow law that explicitly accounted for several of these deformation processes. Pettit and Waddington (2003) proposed a simpler modified flow law (discussed in Appendix 2.3) which we use here to illustrate how the existence of multiple deformation regimes can be exploited to extract rate information. The constitutive relation in Equation A2.3.1, which is a generalized version of Equation A2.1.4, can account for a range of dominant deformation processes in terrestrial ice sheets, by blending n=3 processes with n=1 processes, and it can be incorporated easily into an ice-flow model. This modified flow law (Pettit and Waddington, 2003) has a second rate factor because there can be different activation energies for creep when n=1 or when n=3, producing different temperature dependencies for n=1 and n=3 processes. When the temperature, stress, and grain size fall in a regime where both terms in the Pettit and Waddington (2003) flow law have similar magnitudes, i.e. near a boundary in a deformation map, we show that the additional rate factor can allow us to separate the individual influences of accumulation rate and ice temperature in the inverse problem, and therefore to infer both accumulation rate and ice temperature uniquely.

Using the flow law in Equation A2.3.1, expressed in the form of Equation A2.3.2, we solve an inverse problem with both Γ (defined by Equation A2.3.3) and k (defined by Equation A2.3.4) as model parameters. The parameter Γ, which corresponds to *A(T),* given by Equation A2.1.5, contains one rate factor in $A_{01}\exp(-Q_1/RT)$, and k incorporates another rate

factor through $A_{02}\exp(-Q_2/RT)$, where Q is the activation energy for creep and R is the gas constant. Incorporating only one additional model parameter, the crossover stress k, instead of solving for all the rheological parameters and coefficients directly, is the simplest way to demonstrate the influence of an additional rate factor. We generated an internal layer and ice surface with k equal to 3×10^5 Pa, using the same accumulation rate, ice thickness, and temperature from the previous synthetic tests (Section 2.3.3). In the inverse problem with only two rate factors (in the temperature-dependent softness parameter *A(T)* from Equation A2.1.5, and the accumulation rate) we could not infer the correct value of the layer age and the ice temperature when both values were unknown. Many different pairs of these values could also fit the data, and the pair selected by our inverse procedure depended on our initial guesses. However, in the inverse problem with three rate factors, we can better infer the correct values of the layer age and the ice temperature in some cases when both terms in Equation A2.3.2 make comparable contributions to the strain rate $\dot{\varepsilon}_{ij}$. Table 2.1 and Figure 2.7 show the results. The spatial pattern best matches the correct value because the crossover stress used to make the synthetic data leaves a distinct imprint on the ice-surface shape. In this case, the inferred ice-softness parameter Γ differs by ~1% from the correct value and the crossover stress k differs by less than 3% from the correct value, compared to initial guesses that differed by 10%.

To use this additional rate factor as a constraint when solving inverse problems with Martian radar data, it would be most accurate to use a generalized flow law such as that of Goldsby and Kohlstedt (2001). This requires that we know the ice-grain size (e.g. Barr and Milkovich, 2008) in the target area at the era of flow of the PLD and the activation energies, grain-size exponents, and ice-softness parameters associated with this fully

mechanism-based constitutive relationship. Not all of this information is currently available, but our synthetic tests provide another reason why they would be valuable to obtain. This is a challenge for future laboratory experiments and missions. Our synthetic test indicates that including an additional rate factor can help to constrain the timing in some cases, if the ice-rheological parameters are known, and if the ice mass is in a regime where at least two of the most important terms in the flow law (e.g. Equation A2.3.2) have a similar magnitude.

2.3.4.5. Inferring Paleo-Surface Topography

In our fifth inverse problem, we attempt to infer the surface topography during an era of ice flow. We have shown in Section 2.3.1.2 that we can successfully solve this inverse problem using data from Antarctica. The surface topography across most of the PLD has been significantly altered by trough formation, and there might not be many locations where inter-trough surface topography from a past era of ice flow is still intact (Winebrenner and others 2008). We show how internal layers can be used to reconstruct ice-surface topography across the PLD if we can assume that there was an era of ice flow.

As in Section 2.3.1.2, we perform two tests of this inverse problem. First we assume that we know the elevation of one point on the ice surface and we know the ice temperature. Second, we assume that we know the elevation at two or more points on the ice surface and we do not know the ice temperature. In the first test, the surface generated with this inferred mass-balance pattern closely matched the original surface used to generate the synthetic internal-layer data. In the second test, we assume that the ice temperature is unknown, but at least two points on the ice surface are

available. We find that this information about the thickness at different elevations along the flowband length allow us to reconstruct surface topography when the ice temperature is unknown. However, inferring the correct mass-balance rate B still requires correct ice-temperature information, or other rate-controlling information.

This inverse problem to infer surface topography using just two elevation-data points on the ice surface can be solved using Martian internal layers tracked along putative flowlines across the PLD. Even if rate-controlling information were unavailable for the PLD, the shape of the past topography can be inferred from internal layers.

2.4. Discussion

2.4.1. Implications of ice flow

Based on our understanding of terrestrial ice masses, we expect that Martian ice experiences flow at some rate. The real question is how significant this flow might be in relation to other processes. If ice flow has a minor influence on PLD structure, then both the internal-layer shape and surface shape are determined by the mass-balance pattern. This is similar to the situation in the upper tens of meters in terrestrial ice sheets and to terrestrial ice caps that have stagnated (e.g. Meighen Ice Cap; Paterson, 1969) or have recently built up (e.g. Hans Tausen Ice Cap; Hvidberg and others, 2001). A terrestrial ice mass whose slope is determined by the mass-balance pattern alone can take on a much broader range of surface shapes than an ice mass whose slope is determined by a balance between surface mass exchange and ice flow. The two different mass-balance patterns shown in Figure 2.4 and in Figure 2.5 generate very differently-shaped

internal layers, but, as shown in Figure 2.5, they produce nearly-identical surfaces.

The inverse method that we used in this paper assumes steady state, so that ice flow, at some rate, has an influence on the topography and on the shapes of internal layers. If an episode of ice flow shaped the North PLD, as proposed by Winebrenner and others (2008), then our steady-state method is appropriate to infer information about the most recent episode of ice flow. Even in the case of transient flow, transient ice-surface topography resembles steady-state ice-surface topography, but the internal-layer shapes will be different. In the future, we could extend this method using a time-dependent forward algorithm and multiple internal layers, to infer spatial and temporal patterns of accumulation while allowing for transient ice-surface topography. However, as we have demonstrated here, some fundamental unknowns about the Martian PLD can be determined with this simple, steady-state approach.

2.4.2. Unconformities

Unconformities on various scales have been identified visually in troughs and scarps across the North and South PLD with imagery (e.g. Murray and others, 2001; Tanaka, 2005; Fortezzo and Tanaka, 2006; Kolb and Tanaka, 2006; Tanaka and others, 2008). Subsurface unconformities have also been detected with radar observations (e.g. Seu and others, 2007; Milkovich and Plaut, 2008; Putzig and others, 2009). While unconformities limit the amount of information that we can infer directly from the shape of a deeper internal layer, understanding the cause and timing of these breaks in the stratigraphic record is necessary in order to accurately decipher the history of the PLD and the climate record archived within these deposits.

Figure 2.5a shows that an unconformity can develop in steady-state flow when ice moves through multiple zones of accumulation and ablation. Ice is removed in the ablation zone, but ice is deposited on the erosional surface when it moves into the adjacent downstream accumulation zone. This causes spatial gaps in layers of the same age, and causes younger ice to be deposited directly onto much older ice.

2.5. Conclusions

We can successfully solve the inverse problem to infer the spatial variability in mass balance using the shapes of internal layers. Waddington and others (2007) applied this method to Antarctica, and here we have shown that it is possible to infer spatial patterns of accumulation and ablation, and possibly also the rates of accumulation and ablation, for Mars. While the mass-balance pattern can be inferred, the layer age, the ice velocity, the ice temperature, or the grain size and the crystal fabric must be known before the correct magnitude of the mass-balance rate can be inferred, because steady-state ice-surface topography and layer shapes are, in general, consistent with a wide range of pairs of ice temperature and mass-balance rate magnitude. The ice velocity or ice temperatures necessary in this inverse problem are the values during an era when ice flow closely equilibrated with surface mass balance to produce the surface topography and internal-layer architecture; because the North PLD is probably stagnant today, present-day ice temperatures and accumulation rates are probably not relevant. Therefore, estimating the age of the layer when flow stopped, or determining the ice-grain sizes and conducting laboratory experiments to find the activation energies, ice-softness

parameters, and exponents for the flow law on Mars could lead to more appropriate constraints on the mass-balance rate.

Internal layers are necessary to resolve spatial variations in mass balance because surface topography alone retains little of this information. The ice-surface topography can also be inferred from the shape of an internal layer, because there is an ice-surface shape that is consistent with a given mass-balance pattern that together will generate a given internal layer. If the ice temperature at the time of flow is known, then the internal-layer shape and one point on the ice surface can be used to reconstruct the topography. If the ice temperature is unknown, but the internal-layer shape and at least two points widely separated on the ice surface are known, we can also reconstruct the correct topography; this is a problem we can solve with data currently available for Mars. To solve this problem we require internal layers from radar observations that follow putative flowlines. Reconstructed topography across the PLD could be compared to the shape of the present-day ice surface in areas of the PLD that have been significantly altered by trough formation and other sublimation or deposition processes. Inferring surface topography, mass-balance patterns, and possibly rates and ice temperatures associated with an era of significant ice flow, would be a valuable step towards deciphering the climate history recorded in the PLD.

A2.1. Forward Algorithm

The basis of this algorithm is steady-state continuity (e.g. Paterson, 1994, pg. 256),

$$\frac{1}{W(x)}\left(\frac{\partial q(x)}{\partial x}\right) = \dot{b}(x) - \dot{m}(x) \qquad \text{(A2.1.1)}$$

Along-flow gradients in the volumetric flux of ice $q(x)$, in a flowband with surface profile, $S(x)$, bedrock profile, $B(x)$, and width, $W(x)$, must balance the rate of surface accumulation or ablation, $\dot{b}(x)$, and any basal melting, $\dot{m}(x)$. A time-dependent problem would allow the surface elevation to change over time to accommodate an imbalance in this equality. By integrating Equation A2.1.1 from the boundary where ice flux is specified, the ice flux can be represented kinematically by

$$q(x) = q_{in} + \int_{x_{in}}^{x} (\dot{b}(\zeta) - \dot{m}(\zeta))W(\zeta)d\zeta \qquad \text{(A2.1.2)}$$

where q_{in} (in $m^3\ yr^{-1}$; we use Earth years) is the ice flux entering at one end of the flowband domain ($x=x_{in}$). An equivalent ice flux can also be represented dynamically, where the flux of ice passing through a cross-sectional area $W(x)\times H(x)$, is related to the depth-averaged horizontal velocity $\bar{u}(x)$ in that cross-section by

$$q(x) = W(x)H(x)\bar{u}(x) \qquad \text{(A2.1.3)}$$

and $\bar{u}(x)$ is calculated from the applied gravitational stress together with the constitutive relation for ice. The ice thickness $H(x) = S(x) - B(x)$.

The forward algorithm has two components. The first component generates a steady-state ice surface, calculated by equating the ice fluxes, $q(x)$, in Equation A2.1.2 (kinematic flux) and Equation A2.1.3 (dynamic flux). The surface calculation is a dynamic calculation because it incorporates the constitutive relation for strain rate. The second component

of the forward algorithm generates internal layers using a kinematic particle-tracking calculation.

In the dynamic calculation, the depth-averaged horizontal velocity comes from the Shallow Ice Approximation (SIA, e.g. Hutter, 1983 pg. 256; Paterson, 1994, pg. 262). The SIA is a simplifying assumption that applies in cases where the ice thickness is much smaller than the characteristic horizontal length scales over which thickness or stress change significantly. If the characteristic horizontal length scale is the lateral extent of the ice cap, then derivatives of velocities and stresses with respect to x (horizontal axis) are generally much smaller than derivatives with respect to z (vertical axis). Using the SIA, a constitutive relationship for ice flow (Glen 1955) is,

$$\dot{\varepsilon}_{xz} = A(T(x,z))\tau_{xz}^{n} \qquad \text{(A2.1.4)}$$

where $\dot{\varepsilon}_{xz} = (1/2)\,\partial u/\partial z$ is the simple-shear strain rate along a horizontal plane, $T(x,z)$ is the ice temperature, τ_{xz} is the shear stress along a horizontal plane, and based on laboratory experiments n typically has a value of 3 for dislocation creep (e.g. Paterson, 1994, pg. 85), and $A(T(x,z))$ is the temperature-dependent softness parameter (in $Pa^{-n}\ yr^{-1}$; e.g. Paterson 1994, pg. 86):

$$A(T) = A_0 \exp(-Q/RT) \qquad \text{(A2.1.5)}$$

where A_0 is the temperature-independent ice-softness parameter, Q is the activation energy for creep, and R is the universal gas constant. Using the flow law in Equation A2.1.4 and writing shear stress as $\tau_{xz} = -\rho g(S-z)\,dS/dx$ using the SIA, and integrating strain rate over depth to get velocity, and integrating again to get the depth-averaged horizontal velocity,

$$\bar{u}(x) = \frac{2\tilde{A}(x)}{n+2}(\rho g)^{n}\left|\frac{dS}{dx}\right|^{n-1}\left(-\frac{dS}{dx}\right)H^{n+1}(x) \qquad \text{(A2.1.6)}$$

where ρ is density, g is gravitational acceleration, *S(x)* is ice-surface elevation, *H(x)* is ice thickness, and $\tilde{A}(x)$ is an effective isothermal softness parameter. The effective isothermal softness parameter is found by equating a depth-averaged ice velocity using a temperature-dependent softness parameter *A(T(x,z))*, with depth-varying temperature *T(x,z)*, with the depth-averaged ice velocity for an isothermal column at temperature *T(x)*, as in Equation A2.1.6, and solving for the effective isothermal temperature *T(x)*, and corresponding softness parameter $\tilde{A}(x)$ required to give the same depth-averaged velocity and ice flux.

By representing depth-averaged velocity $\bar{u}(x)$ in terms of ice flux and ice thickness using Equation A2.1.3, and representing ice thickness as the difference between the surface and the known bed elevations, *H(x)* = *S(x)* – *B(x)*, Equation A2.1.6 can be rearranged to produce a nonlinear ordinary differential equation for the steady-state ice surface *S(x)*,

$$\frac{dS(x)}{dx} = -\left(\frac{(n+2)q(x)}{2\tilde{A}(x)(\rho g)^n W(x)(S^{n+2}(x) - B^{n+2}(x))} \right)^{1/n} \qquad \text{(A2.1.7)}$$

The ice flux, *q(x)*, is found kinematically using Equation A2.1.2. The ice-surface elevation at one point along the flowband is required as an initial condition to solve Equation A2.1.7.

In the calculation used here, the paths of particles starting on the surface are tracked through space and time by integrating the velocity field, given below. We represent the horizontal velocity, *u(x,z)*, in terms of its depth-averaged value, $\bar{u}(x)$, and a non-dimensional shape function, $\phi(x, \hat{z})$, which captures variations with depth (Reeh, 1988),

$$u(x, z) = \bar{u}(x)\phi(x, \hat{z}) \qquad \text{(A2.1.8)}$$

where $\hat{z}$ is the normalized non-dimensional height above the bed,

$$\hat{z} = \frac{z - B(x)}{S(x) - B(x)} \qquad \text{(A2.1.9)}$$

The choice of the appropriate shape functions $\phi(x,\hat{z})$ from a thermomechanical calculation can depend on the particular inverse problem being solved. Here we chose to use shape functions for an isothermal, parallel-sided slab (e.g. Paterson, 1994, pg. 251).

We invoke mass conservation to find the vertical velocity. Since ice is incompressible,

$$\frac{\partial w}{\partial z} = -\left(\frac{\partial u}{\partial x} + \frac{\partial v}{\partial y}\right) \tag{A2.1.10}$$

where u is the horizontal velocity along the flowband, v is the velocity transverse to the central flow line in the flowband as required to make flow tangential to the flowband width, and w is the vertical velocity. In a flowband, the transverse strain rate (e.g. Paterson, 1994, pg. 257) is,

$$\frac{\partial v(x,z)}{\partial y} = \frac{1}{W(x)}\frac{dW}{dx}u(x,z) \tag{A2.1.11}$$

The vertical velocity is,

$$w(x,z) = -[\dot{b}(x)\psi(x,\hat{z}) - \dot{m}(x)(1-\psi(x,\hat{z}))] + \tag{A2.1.12}$$
$$u(x,z)\left[(1-\hat{z})\frac{dB}{dX} + \hat{z}\frac{dS}{dx}\right] - \bar{u}(x)H(x)\int_0^{\hat{z}}\frac{\partial\phi(x,\hat{\zeta})}{\partial x}d\hat{\zeta}$$

where

$$\psi(x,\hat{z}) = \int_0^{\hat{z}}\phi(x,\hat{\zeta})d\hat{\zeta} \tag{A2.1.13}$$

is called the vertical-velocity shape function, and $\phi(x,\hat{z})$ is called the horizontal-velocity shape function in Equation A2.1.8.

The calculated horizontal and vertical velocity fields are then integrated over time to obtain the paths of particles that started on the ice surface. A layer of a particular age is found by connecting the end points of particle paths calculated over a time span equal to the age of the layer. A

sequence of steady-state layers subject to the same mass-balance pattern can be generated using a sequence of layer ages.

A2.2. Inverse algorithm

For a particular inverse problem with an associated forward algorithm, different inversion procedures should yield similar solutions. Different procedures may have different advantages and disadvantages affecting the accuracy, uniqueness, stability, and computation time. We chose an inverse procedure that is computationally fast and converges on a single solution that satisfies our criterion for an appropriate match to our data.

In an inverse problem, the observable quantities (e.g. internal layers) may not contain enough information to discriminate against accumulation-rate solutions that are physically unreasonable on other grounds. Because observations contain errors, we do not want to fit these data exactly; a solution found by minimizing only the mismatch between the data and the forward-algorithm prediction could overfit the data. To find a physically reasonable solution, we stabilize, or regularize, the inverse algorithm. As part of this regularization, we require that the mass-balance pattern vary smoothly along the flowband, because variability on small spatial scales is unexpected. Because roughness is penalized, any variability in the solution is clearly required by the data. We also require a solution that fits the data with a root-mean-square mismatch consistent with data uncertainties. The solution to this problem is a "model", i.e. a vector of the model parameters (e.g. mass-balance rate at discrete points) that we seek. Obtaining a smooth

model that fits the data at an expected tolerance can be achieved by minimizing a performance index I_p given by

$$I_p = \|m\|^2 + v(\|d\|^2 - T^2) \qquad \text{(A2.2.1)}$$

In this application, the squared model norm, $\|m\|^2$, contains the square of the curvature of the accumulation-rate profile integrated along the flowband. For model parameters that do not fall in this spatial sequence, the model norm incorporates deviations of the inferred values of these parameters from expected values, in which we have a known confidence. Penalizing large values of $\|m\|^2$ prevents the solution from exhibiting roughness in the accumulation-rate profile or deviating too far from expected values of the other parameters. The squared data norm, $||d||^2$, is the sum of squared mismatches between the N_d observations, $o_i^{(d)}$, and the forward-algorithm predictions of the same observable quantities, $o_i^{(m)}$, normalized by the standard deviations $\sigma_i^{(d)}$ of the data:

$$\|d\|^2 = \sum_{i=1}^{N_d} \left[\frac{(o_i^{(m)} - o_i^{(d)})}{\sigma_i^{(d)}} \right]^2 \qquad \text{(A2.2.2)}$$

The factor v is a trade-off parameter, which is adjusted until the solution produces a data norm that equals a defined tolerance, $T \sim \sqrt{N}$, which is based on the statistical uncertainties N of the data (Parker, 1994, pg. 124). The data-mismatch criterion,

$$\|d\|^2 - T^2 = 0 \qquad \text{(A2.2.3)}$$

is then satisfied. This value of v sets the most appropriate trade-off between smoothness and fit. A smaller value of v puts more emphasis on a smooth model, whereas a larger value of v puts more emphasis on closely fit data (Parker, 1994).

Our inverse method performs a local search for the most-likely solution by finding the minimum of I_p in the model space that is most

accessible from the initial guess of the parameter set. This steepest-descent approach locates only one solution, and that solution may be only a local minimum. To address this issue, we can start from multiple initial guesses of the parameter set. In addition, most inverse problems are nonlinear, making them more difficult to solve. Our problem is nonlinear because predictions of the data by the forward algorithm are nonlinear functions of the model parameters. We address this complication by linearizing our problem. This means that instead of solving for the solution directly, we iteratively solve for corrections to trial values of the unknown parameters. The parameter values are guessed at the first iteration, and are then adjusted in subsequent iterations as the inverse algorithm minimizes the performance index (Equation A2.2.1). The forward algorithm makes predictions of the data using estimates of the model parameters from the previous iteration. For any given value of the trade-off parameter v, a solution is found when adjustments to the model parameters become small. We then adjust the value of v and repeat the solution procedure until the solution also satisfies the data-mismatch criterion (Equation A2.2.3).

Formal inverse theory allows us to investigate our ability to infer unknown parameters; this ability is known as the resolving power. The preferred solution from our regularized algorithm minimizes the performance index I_P in Equation A2.2.1, and fits the data at an expected tolerance, satisfying Equation A2.2.3. However, we still do not know whether we have found the best values and spatial variability of the parameters. It is important to assess the ability to resolve those parameters before making physical inferences from the preferred solution. Parker (1994, pg. 200-213) showed that, when using a regularized algorithm, the inferred structure is a version of the true structure that has been smoothed by a set of narrowly peaked model-resolving functions. The half-width of

the resolving function at each spatial position gives the physical scale over which meaningful structure can be resolved. Features with shorter spatial extent than this cannot be resolved with confidence from these data and this algorithm.

A2.3. Modified flow law

The modified flow law from Pettit and Waddington (2003), in tensor notation, is

$$\dot{\varepsilon}_{ij} = \left[\frac{E_1 A_{01}}{d^{P1}} e^{(-Q_1/RT)} + \frac{E_2 A_{02}}{d^{P2}} e^{(-Q_2/RT)} (\tau_{eff}^2) \right] \tau_{ij} \qquad \text{(A2.3.1)}$$

where $\dot{\varepsilon}_{ij}$ is the strain-rate tensor, E_1 and E_2 are the two enhancement factors, A_{01} and A_{02} are the two temperature-independent softness parameters, d is the average grain diameter, exponents P_1 and P_2 express grain-size dependencies, Q_1 and Q_2 are the activation energies for creep, R is the gas constant, τ_{ij} is the deviatoric-stress tensor, and τ_{eff} is the effective deviatoric stress (τ_{eff}^2 is the second tensor invariant of τ_{ij}). The first term in Equation A3.1 is linear in the deviatoric stress τ_{ij}, while the second term is a non-linear (Glen) term with n=3. When the coefficient of τ_{eff}^2 in the second term is extracted as a common factor on the left-hand side of Equation A2.3.1, the strain rate $\dot{\varepsilon}_{ij}$ can be expressed as,

$$\varepsilon_{ij} = \Gamma[k^2 + \tau_{eff}^2]\tau_{ij} \qquad \text{(A2.3.2)}$$

where k is called the crossover stress because it is the deviatoric stress at which the linear and non-linear terms contribute equally to the strain rate; Γ is given by

$$\Gamma = \frac{E_2 A_{02}}{d^{P2}} e^{(-Q_2/RT)} \tag{A2.3.3}$$

and k is given by

$$k = \left[\frac{E_1 A_{01}}{E_2 A_{02}} \frac{d^{P2}}{d^{P1}} e^{-\frac{Q_1 - Q_2}{RT}} \right]^{1/2} \tag{A2.3.4}$$

Pettit and Waddington (2003) showed that a linear constitutive relationship produces an ice divide with a more-rounded (less-peaked) shape. In order to successfully resolve an unknown mass-balance rate and an unknown ice temperature using the additional rate factor in Equation A2.3.1, the ice sheet must have been in a regime where the linear and the non-linear terms in Equation A2.3.1 have similar magnitudes.

Chapter 3

Response Timescales for Martian Ice Masses and Implications for Past Climate and Ice Flow

On Earth and Mars, ice masses experience changes in precipitation, temperature, and radiation. In an attempt to equilibrate to a new climate state, ice masses will adjust in length and in thickness. When ice flow is equilibrated by mass exchange at the surface, the response toward a new equilibrium has a characteristic timescale. A flowing ice mass also has a predictable shape, which is a function of ice temperature, ice rheology, and surface mass-exchange rate. We show that the present-day geometry of Martian ice masses could be indicative of past climate conditions on Mars. We use the current topography across Gemina Lingula, North Polar Layered Deposits to infer characteristics of past ice temperatures, or past climate conditions, in which ice-flow rates were more significant than today. A range of plausible mass-balance rates and plausible volume response timescales associated with a range of near-basal ice temperatures and a range of ice-flow enhancement factors can generate the characteristic geometry of an ice mass that has been shaped by flow.

3.1. Introduction

On Earth, a valuable archive of past-climate information can be accessed directly by drilling an ice core. However, it is important to recognize that ice-surface topography and the shapes of internal layers are also informative about terrestrial ice-sheet and climate histories. It is likely that the Polar Layered Deposits (PLD) of Mars play a role similar to the terrestrial ice sheets, by archiving information about past Martian climate. Even though a Martian ice core has not yet been recovered, topographic data, radar observations, and images of the Martian PLD are accessible, and these data can be informative about the ice and climate histories on Mars.

Winebrenner and others (2008) used a simple ice-flow model to infer parameters (i.e. PLD geometry, mass-balance pattern) that generated excellent reconstructions of the inter-trough Mars Orbiter Laser Altimeter (MOLA) topography along flowbands across Gemina Lingula, North PLD. Their inferred parameters relate to an era of ice flow across Gemina Lingula, when mass exchange at the surface (accumulation and ablation) was approximately balanced by ice flow, i.e. the ice mass was in, or near, steady state, and the troughs dissecting the present-day surface were filled with ice. For any ice mass, the ice-flow rate depends on the mass-balance rate and on the near-basal ice temperature and any flow enhancement due to impurities in the ice or variations in the physical properties of the ice. Therefore, pairs of mass-balance rate and ice temperature (plus any flow enhancement) can generate identical ice-surface topography. We use the ice-surface shape reconstructed by Winebrenner and others (2008) to estimate pairs of mass-balance rate and ice temperature that would generate their reconstructed shape. However, without additional information to constrain the actual rate of mass balance, the actual ice

temperature, or the actual ice-flow constitutive properties, we need another way to constrain the plausible range of ice-flow rates. We use the volume-response timescale for an ice mass, which is the time for an ice mass to accumulate or shed enough mass approach a new steady-state shape following a climate change (e.g. Johannesson and others, 1989), to narrow the range of plausible mass-balance rate and ice-temperature pairs by eliminating implausible combinations that take too long to adjust.

3.2. Background and theory

Since the accumulation rate, the ablation rate, and the ice temperature during the postulated era of significant ice flow on Mars are all unknown, Winebrenner and others (2008) used a nondimensionalized model to infer parameter values that would generate ice-surface topography that matched the MOLA data at specific locations along flowbands across Gemina Lingula. While Ivanov and Muhlemen (2000) showed that the present-day surface topography across Planum Boreum, North PLD could have been dominantly shaped by ice sublimation, their results were inconclusive across Gemina Lingula; this result is consistent with Winebrenner and others (2008), where Winebrenner and others (2008) noted that Gemina Lingula could have been shaped by a near balance between ice flow and mass balance, but their results were inconclusive across Planum Boreum. The model used by Winebrenner and others (2008) assumed a simple mass-balance pattern that consisted of a zone of uniform accumulation c and a zone of uniform ablation a, separated at the equilibrium line R (Paterson, 1972). The parameter values they inferred were the flow law exponent n (see Equation 1), the ratio of accumulation rate to ablation rate (c/a), the maximum ice thickness H, and the flowband

length L. While they found that there was smooth spatial variation in parameter values that they inferred independently for 51 flowbands, this variation was small and is not central to the results presented here, and we use parameter values associated with only one characteristic flowband.

3.2.1. Ice flow and ice-surface topography

The relationship between shear strain rate and shear stress for ice (the flow law) has been determined from laboratory experiments (e.g. Glen, 1955):

$$\dot{\varepsilon}_{xz} = EA(T(x,z))\tau_{xz}^{n} \tag{3.1}$$

where $\dot{\varepsilon}_{xz}=(1/2)\,\partial u/\partial z$ is the simple-shear strain rate along a horizontal plane, E is the dimensionless ice-flow enhancement factor, $T(x,z)$ is the ice temperature, τ_{xz} is the shear stress along a horizontal plane, and based on laboratory experiments n typically has a value of 3 for dislocation creep (e.g. Paterson, 1994, pg. 85), and $A(T(x,z))$ is the temperature-dependent softness parameter for ice I_h (in $Pa^{-n}\ yr^{-1}$; e.g. Paterson, 1994, pg. 86) follows an Arrhenius relationship:

$$A(T) = A_0 \exp\left(\frac{-Q}{R_0 T}\right) \tag{3.2}$$

where Q is the activation energy for creep ($Q \sim 60$ kJ mol^{-1} for temperatures below -10^{o} C), A_0 is the temperature-independent ice-softness parameter ($A_0 \sim 4 \times 10^{-4}$ $kPa^{-3}\ s^{-1}$ for a flow-law exponent n=3, and $Q \sim 60$ kJ mol^{-1}, calculated based on values from Paterson, 1994, pg. 97), and R_0 is the universal gas constant (R_0 = 8.314 J $mol^{-1}\ K^{-1}$). The ice-flow enhancement factor E can account for variations in the physical properties of ice that enhance or retard the deformation rate (e.g. Paterson, 1994, Ch. 5).

In the Paterson (1972) model for ice-surface topography, the maximum ice thickness H is related to length L through,

$$H^{2+(2/n)} = KL^{1+(1/n)} \tag{3.3}$$

where K is given by,

$$K = \frac{2(n+2)^{1/n}}{\rho g}\left(\frac{c}{2EA(T)}\right)^{1/n}\left(\frac{a}{c+a}\right)^{1/n} \tag{3.4}$$

where ρ is density, and g is gravity. We assume the density of pure ice with ρ=917 kg m^{-3} and Martian gravity g=3.72 m s^{-2}. From Equations 3 and 4, the ablation rate a is

$$a = \left(\frac{H^2}{L}\right)^{n+1} \frac{(\rho g)^n}{2^n (n+2)} 2EA(T) \frac{(1+(c/a))}{(c/a)}. \tag{3.5}$$

Using the flow law exponent n, the accumulation-to-ablation ratio (c/a), the maximum ice thickness H, and the flowband length L inferred by Winebrenner and others (2008) for one typical flowband across Gemina Lingula, we can calculate the accumulation rate c and the ablation rate a for any combination of ice temperature T and ice-flow enhancement factor E.

3.2.2. Volume response time

The response of ice masses to small perturbations can be estimated using linearized kinematic wave theory (e.g. Nye, 1960; Johannesson and others, 1989; Hooke, 2005, ch. 14). From this fundamental theory, Jóhannesson and others (1989) showed that the volume response time for an ice mass to evolve from an initial (datum) state to a new steady state after a change in climate can be approximated by

$$\tau_V = \frac{H}{|a(L)|} \tag{3.6}$$

where H is the maximum ice thickness and $a(L)$ is the ablation rate at the terminus, both in the datum state. The volume response time is the e-folding time needed for the ice mass to accumulate (or ablate) enough ice to reach a new steady-state shape. An ice mass of any ice thickness, with any ice temperature and any ice-flow enhancement, has a corresponding mass-balance rate and volume response timescale. See Appendix F for additional details.

3.3. Results

To constrain the conditions necessary to facilitate ice flow, we constrain the plausible range of mass-balance rates and the plausible range of volume response timescales associated with pairs of ice temperature and ice-flow enhancement. The ice temperature that we prescribe is the near-basal ice temperature, because this is the value that is important for ice deformation. Near-basal ice temperature can be simply related to the surface temperature using Fourier's law of heat conduction in 1-D (e.g. Paterson, 1994, pg. 206),

$$Q = -K(T)\frac{\partial T}{\partial z} \tag{3.7}$$

where Q is the heat flux (in mWm^{-2}), K is the conductivity (in $Wm^{-1}K^{-1}$), T is the temperature (in K), and z is the depth (in m). The conductivity is a function of temperature (e.g. Paterson, 1994, pg. 205), given by

$$K(T) = 9.828 * \exp(-0.0057 * T) . \tag{3.8}$$

Figure 3.1 shows the surface temperature required to produce near-basal temperatures from 200-270 K for different values of Martian heat flux. We

compare surface temperatures associated with heat fluxes of 5 – 50 mW m^{-2} (where a value of 20-30 mW m^{-2} is often assumed, e.g. Clifford, 1987; Grott and others, 2007), and a total ice thickness of 1900 m. For example, if the heat flux is 20 mW m^{-2}, and the near-basal ice temperature is 230 K, the surface temperature would be ~215 K.

In our calculation of mass-balance rate and volume-response time, we consider near-basal ice temperatures from 180-260 K, and we consider ice-flow enhancement factors from E = 1-100; the range of E is chosen based on terrestrial experience, and the physical significance of E is discussed in Section 3.4.1. All rates are given in Earth years.

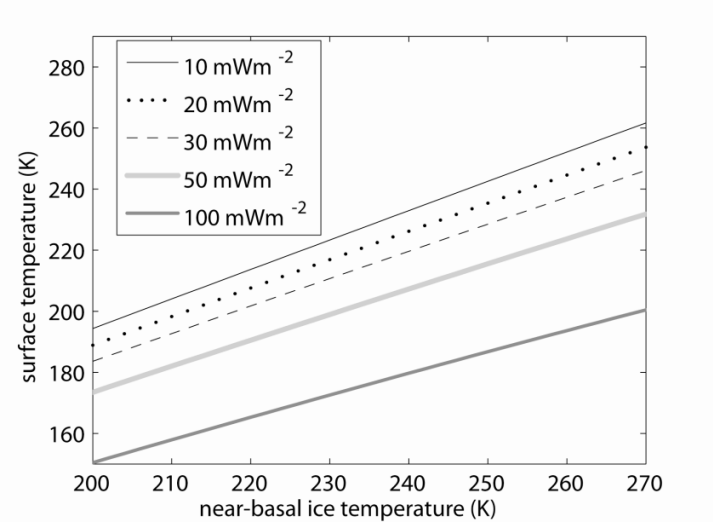

Figure 3.1. Required surface temperature to produce near-basal ice temperature for a plausible range of basal heat fluxes, calculated using Equation 3.7, where thermal conductivity is a function of ice temperature (Equation 3.8).

3.3.1. Geometry of a flowing ice mass

An ice mass that has been shaped by ice flow has a surface slope that can be well predicted by an ice-flow model (e.g. Paterson, 1994; Winebrenner and others, 2008). In order for a stagnant ice mass to achieve the surface shape of a flowing ice mass, a very specific, and persistent, spatial pattern of mass balance is required at each point along the entire profile length; this specific mass-balance pattern must vary with elevation, and an atmospheric mechanism on Mars that would produce this pattern has not yet been identified. In comparison, the shape of a flowing ice mass reflects the integral of the spatial pattern of mass-balance along the profile length.

While the present-day inter-trough topography of Gemina Lingula has the shape characteristic of a flowing ice mass, the actual history of ice flow is unknown. Winebrenner and others (2008) were able to match the inter-trough MOLA topography with their ice-flow model and their inferred parameter values, but we do not know if the present-day thickness of Gemina Lingula is the same as the ice thickness during the era of flow. It is possible that the characteristic shape of a flowing ice mass could be maintained if subsequent accumulation or ablation was extremely uniform. To incorporate this possibility, we use the ratio of inferred ice thickness to inferred length H/L from Winebrenner and others (2008) to calculate the mass-balance rate and the volume response time associated with an ice mass of any thickness or of any length that has this H/L ratio; our results do not apply to a specific ice thickness, but the apply to a specific ice thickness to length ratio.

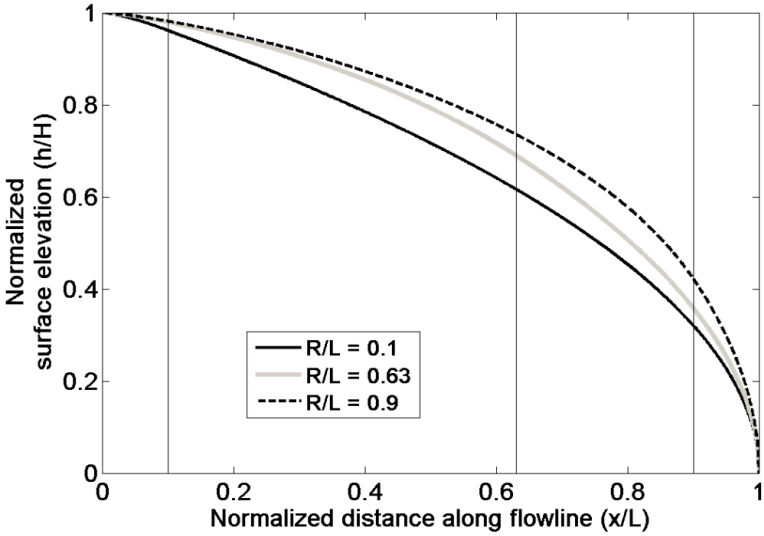

Figure 3.2. Ice-surface shapes generated using a Paterson (1972) model (Equation 1), and three different mass-balance distributions. At the equilibrium-line position R/L the zone of uniform accumulation transitions to the zone of uniform ablation. R/L=0.63 was inferred by Winebrenner and others (2008) for a characteristic profile along Gemina Lingula, North PLD. The vertical lines highlight equilibrium-line positions.

Although the ice-surface shape is sensitive to the flow-law exponent, this parameter was determined to be n=3 by Winebrenner and others (2008). For ice masses with the same maximum thickness H and length L, the surface shape is sensitive to differences in the integral of the mass-balance pattern along the profile. This is shown in Figure 3.2, which compares the normalized shapes of three different ice masses that have uniform width and the same ice thickness and length, but were generated using three different mass-balance patterns. In the Paterson (1972) model, the mass-balance pattern is characterized by the ratio of accumulation rate to ablation rate c/a, and the zone of uniform accumulation and the zone of uniform ablation are separated at the equilibrium-line position R. If the length L and the equilibrium-line position R are known, c/a = (L-R)/R. Therefore, if the equilibrium line R=0.1L, the accumulation zone is much

smaller than the ablation zone, and the ice mass will be thinner along the profile length compared to an ice mass with an equilibrium line R=0.9L, where the accumulation zone is much larger than the ablation zone. As shown in Figure 3.2, these differences in equilibrium-line position R/L (or the corresponding mass-balance distribution c/a) result in significantly different surface shapes; the maximum difference in surface elevation along the profile between the R=0.1L and the R=0.9L surfaces is greater than 10%.

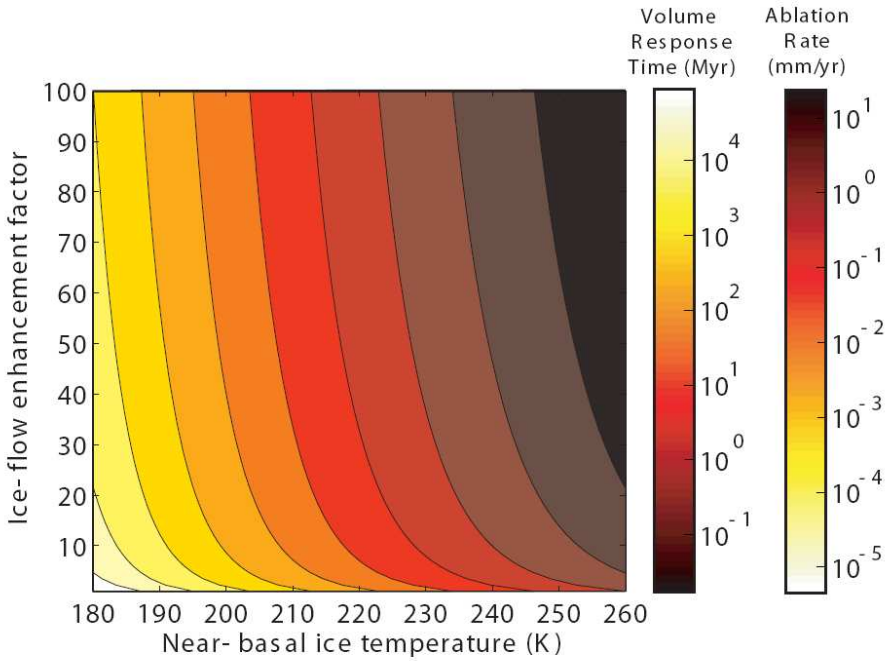

Figure 3.3. Contours of volume response time (from Equation 3.5) and ablation rate (from Equation 3.4) for all pairs of near-basal ice temperature T=180-260 K, and ice-flow enhancement factor E=1-100 and an ice mass with maximum thickness H=2 km. For H=1 km, multiply these values by 0.5. For H=3 km, multiply these values by 1.5.

Using different mass-balance patterns (i.e. R/L=0.1 or R/L=0.9) we calculated the mass-balance rates (Equation 3.5) and the volume response times (Equation 3.6) and found that the differences in these values were relatively small compared to the spread in these values over the range of possible ice temperatures. In addition, Winebrenner and others (2008) used their inferred mass-balance ratio c/a, together with their inferred ice thickness H, length L, and flow-law exponent n, to generate surface shapes that matched the inter-trough MOLA data to within ~1% along the flowband for most profiles included in their study. This quality of fit to the data, compared to the differences in surface shape of order 10% that can result from major differences in the mass-balance pattern (Figure 3.2), indicates that the mass-balance ratio associated with the reconstructed topography across Gemina Lingula has been suitably resolved. This justifies using the inferred mass-balance ratio c/a=0.56 from Winebrenner and others (2008).

3.3.2. Mass-balance rate and response time

To calculate the mass-balance rate and the volume response time, we use the mass-balance ratio c/a=0.56, the geometric ratio of thickness to length H^2/L=11.4 (from H= 1900 m and L~316.67 km), and the flow law exponent n=3 inferred by Winebrenner and others (2008) from a typical flowband along Gemina Lingula. We calculate the ablation rate using Equation 3.5, and we calculate the volume response time using Equation 3.6 for an ice mass with a maximum ice thickness of 1 km, 2 km, or 3 km. The ablation rate required for steady state scales linearly with the ice-flow enhancement factor, and the ice-softness parameter $A(T)$ follows an Arrhenius relation (Equation 3.3).

Figure 3.3 shows the ablation rate a required for steady state (where the accumulation rate $c = 0.56a$) and the volume response time τ for all pairs of ice temperature T=180-260 K and enhancement factor E=1-100 for an ice mass with maximum thickness H=2 km. For all pairs of ice temperature and enhancement factor, and assuming that the ice mass has a thickness to length ratio H^2/L=11.4, an ice mass with H=1 km has a volume response time that is 0.5 times the value at H=2 km (a thinner ice mass responds faster), and an ice mass with H=3 km has a volume response time that is 1.5 times the value at H=2 km (a thicker ice mass responds slower).

3.3.3. Constraining the accumulation rate

Based on observational estimates of modern accumulation rates (e.g. Laskar and others, 2002; Milkovich and Head, 2005; Fishbaugh and Hvidberg, 2006) and modern ablation rates (e.g. Pathare and Paige, 2005), as well as model-based estimates of past mass-balance rates (e.g. Levrard and others, 2004), the polar mass-balance rate on Mars has likely been on the order ~0.1-1 mm/yr over at least the past 10 Myr. With an accumulation rate of ~0.1-1 mm/yr and E=1, the near-basal ice temperature must have been ~240-260 K to produce topography similar to that along Gemina Lingula. Alternatively, with a near-basal ice temperature of ~180 K, the ice-flow enhancement factor must be ~20,000 to equilibrate a mass-balance rate of 0.1 mm/yr, and ~210,000 to equilibrate a mass-balance rate of 1 mm/yr. While a near-basal ice temperature of 180 K is plausible, we know of no way to make water ice at least ~20,000 times softer. If Martian ice flow was ever near equilibrium with mass balance, and if ice flow was not substantially enhanced, the ice temperature required to equilibrate a mass-balance rate ~0.1-1 mm/yr is one argument for warmer ice.

Near-basal ice temperature (K)	Ice-flow enhancement factor	Ablation rate (mm/yr)	Volume response time
180	1	4.7×10^{-6}	425 Byr
215	100	0.3	6.2 Myr
230	50	1.4	1.4 Myr
250	50	17.6	113 kyr

Table 3.1. Calculated values for select pairs of near-basal ice temperature and ice-flow enhancement factor, corresponding to an ice mass with ice thickness H=2 km. For an ice mass following H^2/L=11.4, if H=1 km, multiply these values by 0.5. For H=3 km, multiply these values by 1.5.

3.3.4. Constraining the volume response time

In addition to limiting the range of plausible ice temperatures based on the plausible range of mass-balance rates, we further constrain the ice temperature using the physically-based characteristic volume response timescale for an ice mass, given by Equation 3.5. By putting upper bounds on plausible response times, we put lower bounds on the past mass-balance rate and the past ice temperature, and/or the enhancement factor. Figure 3.3 shows that volume response times associated with near-basal ice temperatures less than ~200 K, without any ice-flow enhancement, are physically implausible; these temperatures imply response times that are older than the age of the planet. The ice-flow enhancement factor is a scaling factor. Ice temperature effects flow following an Arrhenius relation (Equation 3.2), and therefore can have a more significant effect on ice softness. Table 3.1 highlights pairs of values from Figure 3.3.

3.4. Discussion

3.4.1. Variations in basal-ice temperature

Surface temperatures at the North Pole, subject to orbital-parameter variations over the past 10 Myr, have been calculated (e.g. Pathare and

Paige, 2005; Levrard and others, 2007; Schorghofer, 2008), and the annual-average surface temperature at 80-90º N was always below ~180 K. Pathare and Paige (2005) showed that the summertime maximum temperature at the North Pole was ~220 K, and could even reach ~270 K depending on the perihelion configuration, obliquity, and eccentricity. Despite these relatively warm summertime temperatures, the annual-average temperature is very low, due in part to the cold wintertime temperatures and the cold-trapped CO_2 frost cover that presently has a 7 mbar frost-point temperature of 148 K (Kieffer and others, 1976). Annual-average surface temperatures would be higher if there was a reduction in the extent or duration of seasonal CO_2 deposition across the North PLD. Surface warming would be further enhanced if there was a decrease in surface albedo from the formation of a dust-lag deposit, which must have been present if the North PLD survived the last period of high obliquity from 4-10 Ma (e.g. Mischna and Richardson, 2005; Levrard and others, 2007). A simple estimation using the Stefan-Boltzman Law indicates that an albedo change from 0.6 (minimum value for a snow surface; e.g. Paterson 1994, pg. 59) to 0.3 (typical value for a soil-type surface) can yield a change in surface temperature (in degrees Kelvin) of more than 10%. However, to affect the rate of ice flow, changes in surface temperature must propagate to the near-basal ice, and this deep ice can warm only by diffusion. The length of the diffusion time for an ice sheet ~2 km thick can range from ~10-100 ka depending on the thermal conductivity. Larsen and Dahl-Jensen (2000) showed that if this time is comparable to the length of an obliquity cycle, there would have been a delay before the surface temperature during a given obliquity period propagated to the base. Therefore, an orbital state with minimal variation would best promote warmer ice. On Mars, orbital states with minimal variation have occurred every ~2-3 Myr in the past 20

Myr and have lasted for ~300 Kyr (e.g. Laskar and others, 2002). The near-basal ice can also be warmed by variations in basal heat flux. While spatial variations in terrestrial heat-flux can be surprisingly substantial (e.g. Fahnestock and others, 2001a; NGRIP members, 2004), on Mars, Phillips and others (2008) estimate that the crustal heat flux beneath the North PLD is as low as 8 mWm^{-2} (previous estimates of ~20 mWm^{-2} have been used, e.g. Grott and others, 2007). To warm the near-basal ice of a 2 km thick ice mass to 230 K, a heat flux of ~95 mWm^{-2} is required if the surface temperature is 170 K, and a heat flux of ~45 mWm^{-2} is required if the surface temperature is 200 K (using Fourier's Law, Equation 3.7). The ice temperature near the base of an ice mass is the value important for ice flow because shear strain rates are largest there (see also Section A3.3).

3.4.2. Variations in basal-ice properties

In the absence of a significant change in the near-basal ice temperature, it is possible that there were also changes in the properties of ice that enhanced ice flow (see also Section A3.4). Including an ice-flow enhancement factor in the ice-flow law could account for variations in the physical properties of ice, such as grain size, crystal orientation, and impurity content that can enhance or retard deformation rate (e.g. Paterson, 1994, Ch. 5). When these variations are concentrated in the basal layer of a glacier or ice sheet, their effect on ice flow can be especially significant (e.g. Knight, 1997).

There is the potential for CO_2 or CO_2 clathrate to be a constituent of the PLD (e.g. Ross and Kargel, 1998, pg. 32). The Phoenix lander found perchlorate in the surface soil at ~68° S (e.g. Hecht and others, 2009), and even though the distribution and mode of formation of the perchlorate remains unknown, there is the potential for percholorate to be a constituent

of the PLD. Perchlorate is highly water soluble, and could depress the freezing point as much as 70° C for a brine mixture (Hecht and others, 2009). In addition, Delory and others (2006) report that Martian dust storms may generate strong enough electrostatic fields to dissociate CO_2 and H_2O, to eventually form hydrogen peroxide (H_2O_2) that subsequently falls out of the Martian atmosphere. Dust storms of all scales are omnipresent on Mars, and the largest dust storms typically occur during perihelion, when Southern hemisphere summer temperatures are relatively high (e.g. Martin and Zurek, 1993). If hydrogen peroxide snow, or any other chemical constituent, is entrained in Northern hemisphere winter precipitation, this could change the hardness, and therefore the deformation rate of the PLD ice relative to pure H_2O ice.

3.5. Conclusions

Warmer near-basal ice temperatures, most likely in combination with enhanced ice flow, are required for near-equilibrium ice flow to generate topography with the shape characteristic of topography across Gemina Lingula, North PLD in a plausible amount of time, and with a plausible rate of mass balance. We do not propose a specific mechanism, or combination of mechanisms, that could warm the ice or enhance the flow, but we present a range of combinations of ice temperature and ice-flow enhancement that can inform future analyses of PLD geometry, internal structure, and ice rheology. Any history of ice flow requires conditions that are very different from the present day.

A3.1.

Inferred parameter	Value
Maximum ice thickness, H	1900 m
Flowband length, L	320 km
Equilibrium line position, R	203 km
Ratio of accumulation to ablation, c/a	0.56
Flow law exponent, n	3

Table A3.1. Values for a typical flowband on Gemina Lingula, North PLD (from Winebrenner and others 2008).

A3.2. Present-day Polar Layered Deposits

The present-day mean annual surface temperature of the North PLD is ~170 K (e.g. Pathare and Paige, 2005; Levrard and others, 2007; Schorghofer 2008), the present-day ablation rate is estimated to be ~0.2 mm/yr (e.g. Pathare and Paige, 2005), and the present-day accumulation rate is estimated to be ~0.5-0.6 mm/yr (e.g. Laskar and others, 2002; Milkovich and Head, 2005). For a surface temperature of 170 K, and assuming a heat flux of 20 mWm^{-2}, the ice temperature at a depth of 1900 m ~180 K. Using these values, Figure A3.1 shows the surface shape of a steady-state flowing ice mass calculated from Equation 3.3 with a maximum ice thickness of 1900 m, a surface temperature of 170 K, an accumulation rate of 0.5 mm/yr**,** and with a mass-balance ratio c/a=0.56. This surface shape is compared to the MOLA topography along a profile across Gemina Lingula, and, unlike the results from Winebrenner and others (2008), these

surfaces are very different. Present-day Martian surface temperature is too cold, and the mass-exchange rates are too high (even though the actual values are physically very low) to develop the present-day topography across Gemina Lingula. In order for ice flow to be significant at very cold temperature, and to equilibrate this rate of accumulation, the surface slopes have to be very high. It has already been shown that present-day ice flow has an insignificant affect on the surface topography, and that Martian ice must have been warmer to flow at a significant rate (e.g. Greve and others, 2004; A. Pathare, personal communication); Figure A3.1 emphasizes this result.

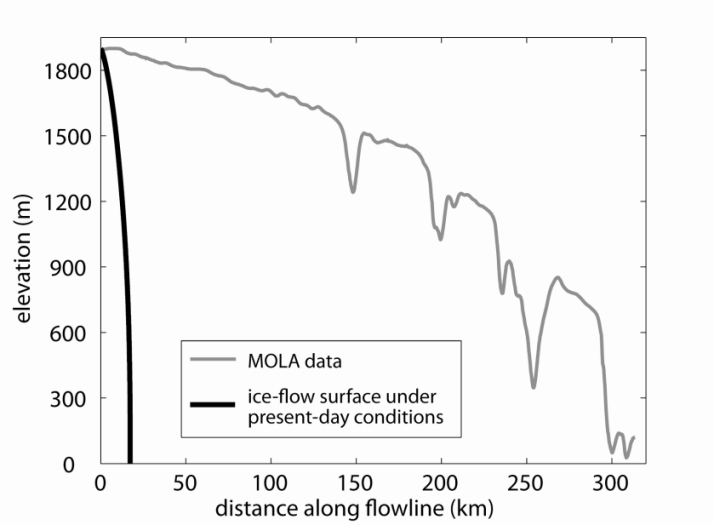

Figure A3.1. Thick black line shows the steady-state ice surface calculated with a surface temperature T=170 K, an accumulation rate c=0.5 mm/yr, and an ablation rate a=0.2 mm/yr. The thin gray line shows the present-day MOLA topography along the study flowband on Gemina Lingula, North PLD. The surface slopes must be very high for ice flow to balance the relatively high mass flux for ice at 170 K.

A flowing ice mass has a predictable surface slope, and this corresponds to a characteristic relationship between ice thickness and basal shear stress. For terrestrial ice sheets, the ice thickness is ~1-4 km, and the length is ~100-200 km (L~200 km in Antarctica), giving H/L~0.01-0.02. However, any mass of material that does not flow following the constitutive relation given by Equation 3.1 is unlikely to have a similar relationship between maximum ice thickness and length. For example, the North polar sand erg, Olympia Undae, has a maximum thickness of ~1 km and a half width of ~250-350 km (e.g. Byrne and Murray, 2002), giving H/L~0.003-0.004.

Figure A3.2 compares different estimates of ice thickness and length for terrestrial ice masses (shown in black) and Martian ice masses (shown in gray). The points represent actual values for PLD and terrestrial ice sheets and ice caps, and the lines are model fits to these points that are associated with an ice temperature specified to fit these points. As shown in Figure A3.1, an ice mass in steady-state with present-day surface temperature and mass fluxes does not match the geometry of the PLD. The ice thickness and length point values for the North and South PLD domes are estimated from the central portions of the PLD excluding the chasmata, and they do not follow this curve. Instead, the PLD domes have a thickness-length relationship similar to that of Greenland and Antarctica. The North/South PLD-dome curve (2) is generated with a near-basal ice temperature of ~210 K, consistent with a volume response timescale of ~100 Myr. The Greenland curve (3) is generated with a near-basal ice temperature of ~260 K, an accumulation rate of 10 cm/yr, and an ablation rate of 20 cm/yr, which are consistent with present-day values (e.g. Paterson 1994, pg. 346; Ohmura and others, 1999). The ice-thickness and length relationship for Gemina Lingula does not fit along the curve for the PLD domes. The Gemina

Lingula curve (4) is generated with a near-basal ice temperature of ~240 K, a mass-balance rate ~0.1 mm/yr, and a volume response time of ~18 Myr.

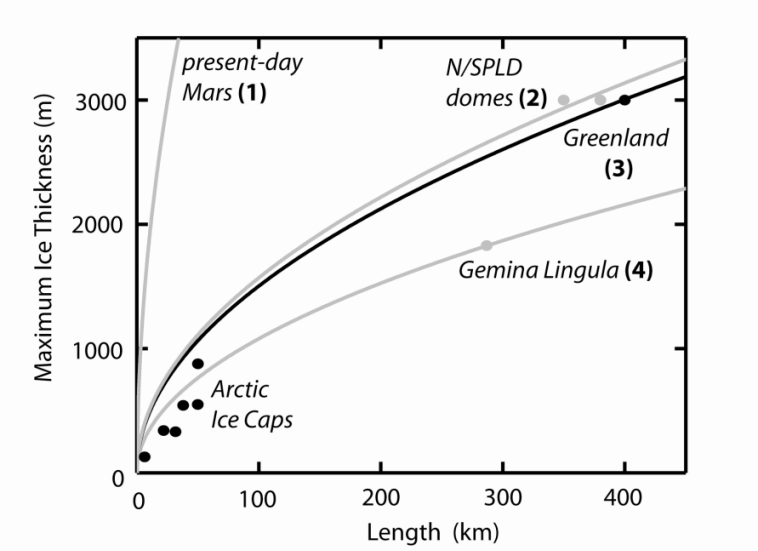

Figure A3.2. Comparison of maximum ice thickness and length for terrestrial ice masses (shown in black) and for martian ice masses (shown in gray). The curves are generated with prescribed values of near-basal ice temperature T, accumulation rate c, and ablation rate a. The curve for present-day Mars (1) is calculated with T=170 K, c=0.5 mm/yr, and a=0.2 mm/yr. The point estimates for the North and South PLD domes, are estimated from the central portions of the PLD to the margin (excluding the chasma). The North/South PLD-dome curve (2) is calculated with T=210 K, c=0.01 mm/yr, and a=0.05 mm/yr (c and a are consistent with a response time of 100 Myr for the study flowband on Gemina Lingula). The Greenland curve (3) is calculated with T=260 K, c=10 cm/yr, and a=20 cm/yr. The Gemina Lingula curve (4) is calculated with T=230 K, c=0.01 mm/yr, and a=0.05 mm/yr (c and a are consistent with a response time of 100 Myr).

While the relationship between thickness and length for the Planum Boreum and for the Planum Australe portions of the PLD *may* indicate that these surfaces are consistent with past ice flow, Winebrenner and others (2008) find that trough formation or sublimation and deposition may have significantly modified the surface of these portions of the PLD, and the

inverse problem to recover information about the ice-flow history cannot be solved with the same approach. However, even if the shape of the topography from a past era of ice flow has been significantly modified, if it is known that there was a history of ice flow, it is possible that we can use the shapes of radar-detected internal layers to reconstruct the ice-surface topography (Koutnik and others, 2009).

A3.3. Ice temperature

Albedo is important because surface temperature depends on the fraction of incoming shortwave radiation from the sun that is absorbed by the surface. Mischna and Richardson (2005) showed that the polar ice caps must be insulated at high obliquity in order to avoid completely subliming away, and that the polar contribution to the global water budget is limited at high obliquity. Levrard and others (2007) also found that the North PLD ice was unstable at high obliquity (~30-35º), whenever the absorbed insolation was greater than 300 Wm^{-2}. Unless an efficient dust-lag deposit formed to protect the North PLD, the north-polar ice would quickly sublimate and redeposit in the midlatitudes during the high-obliquity conditions from 4-10 Myr ago, because the seasonal sublimation rates during high obliquity are an order of magnitude greater than the seasonal accumulation rates. High-obliquity conditions with a mean value ~41.8º are statistically preferred over the last 5 Byr, but the solution for the chaotic obliquity is nonunique (Laskar and others, 2004). Unless the entire North PLD are less than ~4 Myr old, protection of at least some portion of the North PLD from higher insolation 4-10 Myr ago, and possibly for many millions or billions of years, must have occurred. We know that a dust

deposit has effectively protected the South PLD from complete sublimation during high obliquity because the surface exposure age of the South PLD is 30-100 Myr (e.g. Plaut and others, 1988; Herkenhoff and Plant, 2000; Koutnik and others, 2002), and the present-day South PLD surface has a very low thermal inertia (e.g. Paige and Keegan, 1994; Vasavada and others, 2000). The South PLD has also received ~4-11% more insolation on an annual average over the past 20 Myr (from calculations by Laskar and others 2004). However, the nature of the preserved cratering record, where the floors of craters greater than ~800 m in diameter have viscously relaxed (e.g. Pathare and others, 2005), but the crater rims have been maintained (e.g. Koutnik and others, 2002; Pathare and others, 2005), attests to the efficiency of the lag deposit in preserving the underlying ice. If the sublimation rate at the South Pole was ~0.2 mm/yr, a rim height of ~10 m would be removed in less than 50,000 years, which has not been the case. The thickness of the lag deposit is minimally ~5 mm (e.g. Skorov and others 2001), but could be ~50 cm (e.g. Paige and Keegan, 1994; Ellehoj, 2007); the lag deposit could also be thicker, as the actual thickness is unknown. The state of the South PLD is an indication that the dust-lag deposit has potentially protected the underlying ice for millions of years; this means that the South PLD surface, at least in the summertime, could have maintained a low albedo for millions of years. Even though the South PLD received more insolation than the North PLD over the past 20 Myr, and the South PLD surface has been covered by a dark-albedo lag deposit over that time, there is no evidence that these effects have warmed the ice. The ice temperature is determined by the long-term average surface temperature and basal heat flux. As long as CO_2 frost at ~148 K covers the PLD surface in the wintertime, the annual-average temperature will always be low relative to the summertime maximum temperature, regardless of enhanced

summertime warming from increased insolation or decresed albedo. However, if the extent or the duration of wintertime frost cover was reduced for at least hundreds of thousands of years, the near-basal ice temperature could become warmer.

Terrestrial heat-flux variations can be surprisingly large. For example, basal melting was found at the base of the North Greenland Ice-Core Project (NGRIP) site that required a heat flux of ~130 mWm^{-2} (e.g. Fahnestock and others, 2001a; NGRIP members, 2004; Buchardt and Dahl-Jensen, 2007), which is approximately twice the expected value. On Mars, the present-day planetary heat flux was been estimated at ~20 mWm^{-2} (e.g. Clifford 1987; Grott and others 2007), but the actual value of heat flux and the spatial variation in heat flux, especially in the past, is not well known. Presently, Mars' internal dynamics are assumed to be inactive, and this is supported by radar observations that show a lack of deflection of the crust beneath the North PLD (e.g. Picardi and others 2005; Phillips and others 2008). Based on these observations, Phillips and others (2008) estimate that the crustal heat flux beneath the North PLD is ~8 mWm^{-2}.

What heat flux is required to warm the basal ice to 230 K? For a specified surface temperature, and using Equation 3.7, we can calculate the heat flux at a depth of 2 km that is required to achieve an ice temperature of 230 K at this depth. For a surface temperature of 170 K, a heat flux 95 mWm^{-2} is required to reach 230 K at 2 km depth, and for a surface temperature of 200 K, a heat flux 45 mWm^{-2} is required. If there was a region of higher heat flux in the geologically recent martian past, it is presumed to be due to a transient tectono-thermal or volcanic event (e.g. Clifford 1987; Benito and others, 1997;Anguita and others, 2000; Fishbaugh and Head, 2002; Hovius and others, 2008). We do not address the plausibility or timing of such a thermal event here, but a heat flux of

approximately 50-100 mWm^{-2} may be possible if thermal heat-flux transients occurred on Mars.

A3.4. Ice rheology

In our calculations, we assumed that deformation occurred entirely by creep, and that there was no sliding at the base. However, a water- or till-lubricated base could cause sliding that could significantly quicken the rate of ice flow. While a mechanism to facilitate sliding of the PLD cannot be ruled out (e.g. Fisher and others, 2009), we focus our discussion on mechanisms to enhance the rate of internal deformation. In addition to the ice temperature, the rate of ice deformation is also controlled by the physical properties of ice, such as grain size, crystal orientation, and impurity content, which can enhance or retard deformation (e.g. Paterson 1994, Ch. 5). The influence of these properties on ice flow can be especially significant in the basal layer of a glacier or ice sheet (e.g. Knight 1997). We briefly review the primary ways that variations in ice properties affect the rate of ice deformation on Earth, and we consider how these mechanisms may be relevant to ice deformation on Mars.

The flow law for ice used to calculate the depth-averaged horizontal velocity in Equation 3.1 includes an enhancement factor E, which on Earth typically accounts for changes in the creep rate for anisotropic ice compared to isotropic ice at the same stress and temperature. Ice crystals subject to strain in excess of 10% develop a preferred orientation that facilitates glide along basal planes in the direction of the applied stress (for simple shear), and the c-axes will typically align close to vertical (e.g. Paterson 1994, pg. 99). Therefore, development of ice fabric makes the ice easier to shear, but

harder to compress. Most terrestrial ice masses are anisotropic to some degree in some places, but ice sheets are often considered to be isotropic to simplify theoretical studies of ice-sheet behavior. While sophisticated flow laws that incorporate enhancement from anisotropy have been developed (e.g. Azuma, 1994), a multiplicative enhancement factor is a simple way to account for any mechanism, including anisotropy, that changes the flow rate. The enhancement factor represents enhancement in the dominant strain-rate component.

Analysis of ice cores has shown that anisotropy can change the creep rates by an order of magnitude (e.g. Paterson 1994, pg. 99), and therefore it is important to account for this effect. Thorsteinsson and others (1997) analyzed the variation in crystal size and crystal fabric in the Greenland Ice Core Project (GRIP) ice core, and how differences between glacial and inter-glacial periods have a marked impact on the properties of the ice and the pattern of deformation. For example, glacial ice has a higher impurity content, which slows crystal growth and leads to finer-grained ice that can deform more rapidly, and the opposite is true for inter-glacial ice (e.g. Thorsteinsson and others, 1997).

Therefore, while crystal fabric plays a role in either enhancing or retarding ice deformation, the impurity content of the ice is also important. An impurity can replace a water molecule in the ice crystal, fit within the crystal lattice, or exist at the ice-crystal grain boundaries (e.g. Paterson 1994, pg. 88). From analyses on the Vostok, Antarctica ice core, Petit and others (1999) reported that aerosol fallout (both dust and chemical impurity) increased during cold periods. From analyses on the EPICA Dome C ice core, Lambert and others (2008) found that dust concentration increased by ~25 times during glacial periods. They attributed this to an increase in the source of dust from South America, and because of an increase in

atmospheric transport of dust when the hydrological cycle is reduced. For terrestrial ice sheets, the overall dust content is still low, and dust has a relatively minor influence on ice rheology. However, sand-sized impurities, particularly those entrained in the near-basal ice, can have a major influence on the rheology. For example, Hooke and others (1972) found that the creep rate of ice containing fine-grain sand decreased exponentially as a function of sand content for temperatures greater than -10° C and for high sand concentrations, but results were inconclusive for lower sand concentrations (e.g. Paterson, 1994, pg. 88). The strength of ice with a high sand content can also be less than the strength of clean ice, increasing the creep rate (e.g. Cuffey, 2000; Fitzsimons and others, 2001). This agrees with tunnel-closure observations, which detected localized enhanced deformation of the debris-rich basal layers of Taylor Glacier, Antarctica (e.g. Fitzsimons and others, 1999; Samyn and others, 2005). It also agrees with modeling of the observed strain rates at Taylor Glacier (Whorton and others, In Preparation), with basal ice from the Byrd, Antarctica ice core (e.g. Gow and others 1968), and with studies of the basal ice at Meserve Glacier, Antarctica (e.g. Paterson 1994, pg. 287).

Carbon dioxide (CO_2) ice precipitates out of the Martian atmosphere, and it has been proposed PLD (e.g. Ross and Kargel 1998, pg. 32) that it might be present in the. While it is likely that it is only a relatively minor constituent of the PLD (e.g. Nye, 2000), CO_2 ice or clathrate hydrate, if present, could influence the rate of ice flow. Durham and others (2000) demonstrated that CO_2 ice is weaker than water ice, but that clathrate hydrate is stronger, and also has a lower conductivity.

Li and others (2009) showed that sulfuric acid (H_2S0_4) reduces the strength of ice proportional to the square root of the sulfuric acid concentration. Notably, Li and others (2009) found that sulfuric acid was

more effective at softening the ice at lower temperature; they showed results for -10° C compared to -20° C. Soluble impurities, such as HF and HCl, at concentrations of only a few parts per million, can increase the creep rate by a factor of 10 (Paterson 1994, pg. 88) because the impurities cause point defects in the crystal structure. These experimental results that indicate ice can be significantly softened with even minor impurity content are typically valid at ice temperatures above the eutectic point; at temperatures below the eutectic point the impurities may provide only limited ice-flow enhancement.

Chapter 4

An Efficient Model of Transient Ice Flow Using a Spatially Limited Domain

To develop a computationally efficient ice-flow model that can assimilate data that exist over only a portion of an ice sheet, it is advantageous to limit the model domain. A limited-domain model is particularly well suited as part of the forward algorithm in a computationally intensive inverse problem, and as part of an investigation of transient ice flow near an ice divide (near ice-core sites). We present a way to accurately model the evolution of a limited-domain ice sheet that crosses an ice divide, and has no termini. In a limited-domain model, accurately calculating ice-sheet evolution in response to spatial and temporal changes in ice flow and climate depends on accurately calculating the ice flux crossing the limited-domain boundaries. Simple extrapolations or estimations of ice flux at the limited-domain boundaries can be numerically or physically incorrect, resulting in incorrect ice-sheet evolution. We develop a new approach to provide boundary-value information to our limited-domain model without conventionally "nesting" the limited model in a full model. We show that evolution of only part of an ice sheet can be consistent with the full ice sheet within which it exists.

4.1. Introduction

Numerical ice-flow models are widely used to solve problems in glaciology that cannot be solved analytically (e.g. Van der Veen, 1999; Hooke, 2005, pg. 288), and ice-flow models can generate realizations of ice-sheet behavior that exceed our observational capabilities. To make these models more realistic, we can use an ice-flow model in combination with any available information about past and present ice-sheet geometry, ice-sheet internal structure, and climate variables that, for example, can be determined from ice-penetrating radar (e.g. Conway and others, 1999; Vaughan and others, 1999), from ice cores (e.g. NGRIP members, 2004), or from glacial-geological reconstructions (e.g. Denton and Hughes, 2002; Stone and others, 2003). Ice divides are regions of the ice sheet where a variety of these geophysical and paleoclimatic data have often been collected at the same site. Ice-flow models are needed in combination with laboratory analyses of ice-core samples to infer the correct climate history, because climate information that is recorded in the ice has been affected by the history of ice flow (e.g. Paterson, 1994, pg. 276-288). While an ice-core site is chosen because the history of ice flow there is usually simpler to decipher than at other sites on an ice sheet, the ice-divide thickness and the ice-divide location can change due to spatial and temporal changes in accumulation rate and ice dynamics. These spatial changes influence particle-path trajectories through the ice, and the spatial dimension should be included in an ice-flow model that is used to interpret an ice-core record where ice-divide variations may have been significant.

Some of the spatial information about ice-sheet history that is sought from data in the vicinity of an ice divide can be inferred by solving an inverse problem. However, computational efficiency is required when solving inverse problems that require many iterations of the ice-flow model,

or when using a higher-resolution model. Limiting the model domain to include only the relevant portions of the ice sheet is a way to reduce computation time. It is also advantageous to limit the model domain when assimilating data that are available only in limited locations on the ice sheet. When the domain is limited, we do not need to make estimates of observable quantities in regions where parameter values and boundary conditions are unconstrained. However, limiting the domain of a transient ice-flow model is not trivial. Accurate calculation of the boundary values in the limited model requires additional information to ensure that the limited domain evolves consistently with the full domain within which it exists.

In practice, additional information can be provided to the limited model by embedding the limited-domain (regional) model in a full-domain (global) model. There are at least two approaches to embedding a limited domain in a full domain. In a commonly used embedding approach, the limited-domain boundary values are provided directly from calculations performed within a full model that is solved jointly with the limited model; this is referred to as a "nested" model. In our new approach, the limited-domain boundary values are provided from calculations performed within a limited model that rely on information about the behavior characteristics of the full model rather than specifically on its detailed evolution; we refer to this case simply as a "limited-domain" model.

4.1.1. "Nested" ice-flow model

Nesting (embedding) schemes are common in numerical models of physical processes; for example, a regional climate model that is driven by the lower-resolution output of a global climate model (e.g. IPCC, 2007, Ch. 11; Salathe and others, 2007). In ice-sheet modeling, higher resolution

and/or higher-order physics that are important in specific regions of an ice sheet are often nested into a full ice-flow model with coarser resolution and/or simplified physics. For example, there have been numerous models of ice-sheet evolution in which regions of fast ice flow, or regions requiring higher-order physics, are nested into a 3-D thermomechanically coupled model of the entire ice sheet (e.g. Marshall and Clarke, 1997; Fastook, 2005; Huybrechts and others, 2007); these modifications result in global ice-sheet evolution that is more realistic, while remaining more computationally tenable compared to a global model at the resolution of the nested component. In addition to directly incorporating sub-grid physics into a global model, global calculations may also provide necessary boundary values for the regional model. For example, Gagliardini and Meyssonnier (2002) used a global ice-flow model to calculate lateral boundary conditions for their regional anisotropic flow model. The limited model and the full model can have different spatial and/or temporal resolution, but they are calculated in step with each other, and therefore ice-sheet evolution within both models is always consistent.

4.1.2. "Limited-domain" ice-flow model

We define a limited-domain ice-flow model as any ice-flow model whose spatial domain includes only a limited (regional) portion of an ice sheet. In the problem of transient ice flow, as an ice sheet experiences spatial and temporal changes in accumulation and in flow, the ice thickness must change in order for the ice sheet to conserve mass. To solve the mass-conservation equation for ice-sheet evolution (Equation 4.1), the ice thickness must be known or estimated as an initial condition at the first timestep. Then, the calculation of ice-thickness evolution depends on the

calculation of ice flux through the domain, which depends on the ice thickness, the surface slope, and basal conditions (e.g. Section A4.1). In a full-domain model, there is a zero-flux boundary condition or a calving condition at the terminus, and the ice thickness can be calculated everywhere. However, in a limited-domain model, the ice flux crossing the limited-domain boundaries is unknown. As discussed in Section 4.2.1, improperly calculating the boundary flux can lead to numerically driven ice-sheet transients and unphysical ice-sheet behavior.

Our strategy to deal with this boundary-flux problem is analogous to problems where information is known about the behavior of the boundary forcing, but the actual boundary values are unknown. For example, Cuffey and others (1995) estimated air-temperature forcing in central Greenland using a calibrated $\delta^{18}O$ record; these transfer functions were then used to prescribe the necessary temperature forcing in different applications (e.g. Cuffey and Clow, 1997; Marshall and Cuffey, 2000).

4.1.3. Synopsis

We introduce our new approach to efficiently calculate physically realistic ice-sheet evolution with a limited domain; in Section A4.1 we present the details of our solution for ice-sheet evolution within a 2.5-D limited-domain flowband. Our approach can be summarized in three steps, which are discussed in detail in Section 4.2.2.1 – Section 4.2.2.3. The first step is to embed the limited model in a full model that includes an ice sheet terminus. By including a terminus, the boundary condition at the end of the domain is known. If the limited domain includes an ice divide, or begins near an ice divide, we embed the limited model in a full domain that extends off both sides of the divide and includes two termini. The second

step is to characterize the behavior of the full ice sheet. We do this by calculating the response of the full ice sheet to an impulsive perturbation in accumulation. This impulse-response function provides information about how the full model would respond to a change in volume over time. The third step is to use the response functions evaluated at the limited-domain boundaries to determine how much flux to enter in to or discharge out of the limited domain. This enables the limited-domain model to adjust to any volume change at a glaciologically realistic rate that is compatible with a full ice-sheet model experiencing the same climate changes. In Section 4.3.2.3 we discuss how to incorporate changes in ice-flow and climate forcing that originate outside the limited domain. These externally forced changes (e.g. changes in sea level) will affect ice-sheet evolution in the limited domain, and we must consider how to inform the limited model about these external changes. Our approach is a general formulation that could be applied to transient ice-flow problems using ice-flow models of varying complexity.

4.2. Boundary conditions for a limited-domain model

To calculate ice-thickness evolution we solve the mass-continuity equation (e.g. Paterson, 1994, pg. 256):

$$\frac{\partial h(x,t)}{\partial t} = -\frac{1}{W(x)}\left(\frac{\partial q(x,t)}{\partial x}\right) + \dot{b}(x,t) \tag{4.1}$$

where $h(x,t)$ is the ice thickness, $W(x)$ is the flowband width, $q(x,t)$ is the ice flux, and $\dot{b}(x,t)$ is the accumulation rate. A flowband model is a 2-D model that also accounts for width variations; therefore it is considered to be 2.5-D. We solve this conservation equation numerically using an implicit approach (e.g. Patankar, 1980); details are given in Section A4.2. To solve for ice-

thickness evolution, we need to calculate the ice flux *q(x,t)*. The accumulation-rate history $\dot{b}(x,t)$ is prescribed, or can be inferred as part of an inverse problem if internal-layer data are available.

We use the Finite (Control)-Volume Method (FVM; Patankar, 1980; Versteeg and Malalasekera, 1995) discretization scheme. Using the FVM, the model domain is divided into discrete volumes. Ice thickness is calculated at finite-volume center points, and ice flux is calculated at finite-volume edges. In this paper, we discuss a generic problem with a limited domain that crosses an ice divide, and therefore has two unknown boundary conditions.

4.2.1. Incorrect boundary conditions

There is no physical basis for any generic extrapolation scheme from inside the limited domain when we want to calculate the value of ice flux *q(x,t)* crossing the limited-domain boundaries, that adequately approximates the flux crossing this point in a full ice sheet. This includes extrapolating the ice flux from upstream values, which can be very inaccurate because this extrapolation assumes that flux variations are spatially linear. If variations in accumulation are not spatially linear (or do not combine to be spatially linear), then the linear extrapolation is incorrect. We cannot assume spatial linearity of accumulation and flow-band width for a transient problem. However, a higher-order extrapolation is also inadequate. The correct boundary-flux treatment on each side of the domain requires information from both sides of the domain.

In pursuit of the most-accurate estimation of the value of ice flux crossing the limited-domain boundaries, we identify other estimations that are also incorrect. For example, ice flux can be determined dynamically

from Equation A4.1.2 using the depth-averaged velocity $\bar{u}(x,t)$ and ice thickness *H(x,t)* across the flowband width *W(x)*. In a finite-volume formulation, the dynamic flux crossing a limited-domain edge is dependent on the ice thickness and surface slope evaluated there. A way to evaluate the ice thickness and surface slope at a finite-volume edge would be to quadratically extrapolate the ice thickness and to linearly extrapolate the surface slope from neighboring quantities. Instead of using neighboring values of ice flux to extrapolate the ice flux crossing the limited-domain boundaries, we could extrapolate the upstream ice thicknesses and surface slopes, and calculate the flux dynamically. Unfortunately, some extrapolations will under-predict the flux and some extrapolations will over-predict the flux at this boundary, and the limited-domain model is unable to hold steady state under a constant climate. Figure 4.1a shows four points on an initial ice surface that are then tracked under steady-state forcing conditions. Figure 4.1b shows how the ice thickness changes at each point, and Figure 4.1c shows how the ice flux changes over time; however there should be no time variation in the ice thickness and the ice flux under steady-state forcing.

These variations originate at the limited-domain boundary because of the poor representation of ice flux there. The ice thickness will continue to evolve until the extrapolation matches a different steady-state solution, resulting in a solution that has migrated for strictly numerical reasons. This migration is physically possible because there are infinitely many surface profiles that have the same flux profile, and the numerical calculation determines the solution. If the value of flux is not calculated adequately for a limited-domain model with an unknown span, the surface can migrate to another solution; a model with a known span does not have this problem.

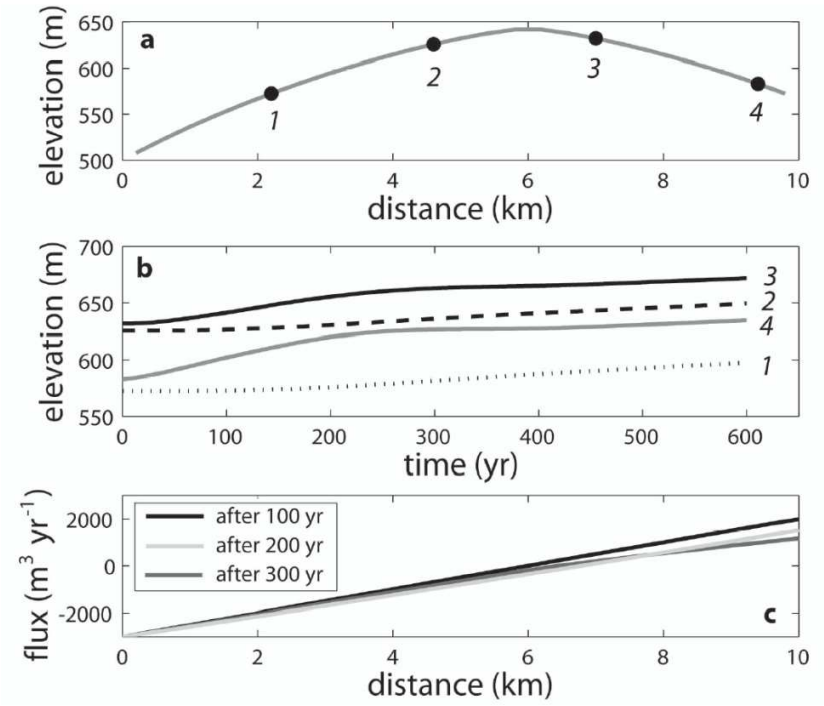

Figure 4.1. An example of a limited-domain model that does not hold steady state when the boundary flux at the right margin is calculated dynamically. **a)** Steady-state-ice-surface profile that crosses an ice divide. The labeled points 1-4 correspond to the time evolution of ice thickness in panel b. **b**) Evolution of ice thickness for four points on in a limited-domain model, under steady-state conditions (no change in forcing). The ice thickness changes because the ice flux at the limited-domain boundary on the right side of the divide is incorrect. **c)** Evolution of the ice-flux profile after 100, 200, and 300 years, driven by an incorrect value at the right-side boundary, under steady-state conditions.

Instead of using a direct extrapolation of ice flux, or a dynamic calculation based on an extrapolation of ice thickness and slope, we could estimate the flux crossing the last downstream finite-volume edge with a kinematic calculation. The kinematic flux (Equation A4.1.1) is calculated by integrating the continuity equation (Equation 4.1). The accumulation rate $\dot{b}(x,t)$ is known, and the rate of ice-surface change at the current timestep $\dot{h}(x,t_i)$ can be estimated from the known value of $\dot{h}(x,t_{i-1})$ at the previous

timestep. Calculating the boundary flux kinematically would allow the limited-domain model to retain information about the original steady-state surface. While this boundary condition is more physically based, and would allow the model to hold steady state, it is not physically realistic. To retain information about the initial steady-state solution, the kinematic calculation forces any additional mass that enters the domain in a given timestep to be exported instantaneously. However, instantaneous export is not glaciologically realistic. To address these concerns, we present a new approach to calculate the boundary flux in a limited-domain model that is accurate and achieves our physical expectation of real ice-sheet behavior.

4.2.2. Physically-based boundary condition

4.2.2.1. Embed the limited model in a full model

We embed our limited-domain model in a full-domain model in order to calculate impulse-response functions for the full domain; we do this at the start of the calculation, and we do not need to embed the limited domain at each timestep. Analytical solutions of steady-state ice-surface profiles can be good approximations to actual ice-sheet surfaces (e.g. Paterson, 1994, pg. 244). Therefore, it is reasonable to embed our limited domain in a simple full model that captures the essential behavior of a full ice sheet. A simple full-domain model is also computationally efficient. The shape of the full-domain model is matched to the shape of the limited-domain model over the horizontal extent of the limited domain, but the shape of the full model is extended to include a terminus. An analytical ice-sheet surface that could be used to extend a limited-domain model is discussed in Appendix 4.3, and

a steady-state surface equation that can be solved numerically is given by Equation A4.2.8; any ice-surface model could be used for the full domain.

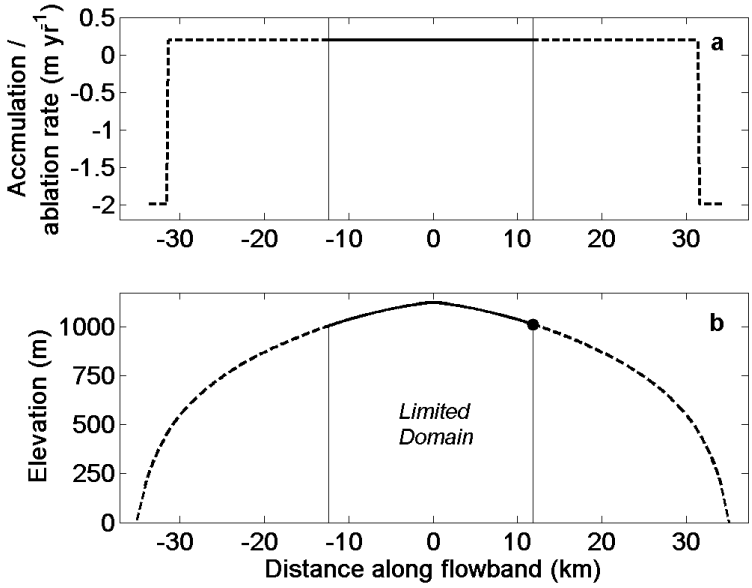

Figure 4.2. a) The accumulation and ablation rates used to generate a full-domain surface profile using a Paterson (1972) model. The Paterson (1972) model assumes that the mass balance consists of a zone of uniform accumulation c and a zone of uniform ablation a, given by the ratio c/a; we pick c/a=0.1, and there is an ablation rate of ~1 m yr^{-1} across the wedge-shaped termini. **b)** Ice-surface profile for a limited domain that crosses an ice divide (solid line), and for the corresponding full domain (dashed line) within which it is embedded. The marked location at the right-side boundary of the limited domain relates to subsequent figures.

To facilitate physical terminus behavior (i.e. ice-sheet length changes in response to accumulation changes) in our numerical calculations with our simple full-domain model, we replace the terminus with a wedge shape, and conserve mass across the wedge (e.g. Nye, 1963; Hooke, 2005, pg. 376); this allows the terminus to advance and retreat. Our wedge-terminus formulation in a finite-volume scheme is discussed in Section A4.3. If the

limited-model domain is focused near an ice divide, the terminus will be far from the limited-domain region of study, and the solution for ice-sheet evolution will be relatively insensitive to the numerical treatment of terminus dynamics.

The solid curve in Figure 4.2a shows a limited domain that crosses an ice divide with a maximum thickness of ~1000 m, a limited extent of 25 km, and an average accumulation rate of 20 cm/yr. The dashed curve shows the extension of this limited surface to a full domain that includes a terminus. As discussed in Section A4.3, our full-domain surface is from an analytical ice-surface model with a zone of uniform accumulation c and a zone of uniform ablation a (Paterson 1972), and we use the mass-balance ratio c/a=0.1. For the specific limited domain shown in Figure 4.2a, and for this specific full-model extension (we note that any extension could be used), the full model crosses an ice divide and is ~60 km long, with an average accumulation rate of 20 cm yr^{-1}, an average ablation rate of ~2 cm yr^{-1}, and an ablation rate across the terminus wedge of ~2 m yr^{-1}.

4.2.2.2. Response functions for the full model

To characterize the behavior of the full model within which the limited model is embedded, we solve for the ice-thickness evolution of the full-domain model in response to an impulsive perturbation in accumulation. Using our implicit numerical scheme (Section A4.2) to calculate ice-thickness evolution with the full-domain model, we first confirm that the analytically-derived full-domain surface holds steady state in this numerical calculation, and then we can calculate the ice-thickness response of the full-domain to an impulsive perturbation in accumulation. The impulse-response function for ice thickness h_1 is the evolution of ice

thickness at any single point along the full-domain surface, from the time of the impulsive perturbation until the time when the surface has returned to a new steady state. As shown by Nye (1960), ice-thickness response and ice-flux response can be related using kinematic-wave theory. For small perturbations (denoted with '1') from the datum state (denoted with '0'), the ice-flux response function q_1 at any position x can be given by a series expansion,

$$q_1 = \left(\frac{\partial q}{\partial h}\right)_0 h_1 + \left(\frac{\partial q}{\partial \alpha}\right)_0 \alpha_1 \quad . \tag{4.2}$$

The coefficients of ice thickness h and surface slope α are

$$c_0(x) = \left(\frac{\partial q}{\partial h}\right)_0 = (n+2)\frac{q_0}{\alpha_0} \tag{4.3}$$

$$D_0(x) = \left(\frac{\partial q}{\partial \alpha}\right)_0 = n\frac{q_0}{\alpha_0} \tag{4.4}$$

where n is the exponent in the flow law. The quantity c_0 is the kinematic-wave velocity per unit width, in units (m yr^{-1}). The quantity D_0 is the kinematic-wave diffusivity per unit width, in units (m^2 yr^{-1}). The surface slope $\alpha = \partial h / \partial x$; surface slope is positive on the left side of the ice divide, and is negative on the right side of the ice divide.

Following Nye (e.g. 1960), this perturbation theory applied to ice sheets assumes that the impulsive accumulation-perturbation term is spatially uniform. However, in our case the response function is used to characterize the behavior of a full ice sheet, and actual changes in accumulation are likely to be nonuniform. Therefore, we explore the sensitivity of ice-sheet evolution to spatially nonuniform perturbations (Section 4.3.1). The accumulation pattern for the impulse-response calculation is given by the sum of the steady-state pattern $\dot{b}_0(x)$ and a perturbation $\dot{b}_1(x,t)$

$$\dot{b}(x,t) = \dot{b}_0(x) + \dot{b}_1(x,t)\,. \tag{4.5}$$

We need only the ice-thickness response at the limited-domain boundaries to calculate the ice-flux response at these positions, and the solid black curve in Figure 4.2b shows the ice-thickness impulse-response function and the ice-flux impulse-response function at the limited-domain boundary on the right side of the ice divide, as marked in Figure 4.2a. Since this is a numerical calculation, we must define the full-adjustment time of ice volume (when the ice surface has returned to steady state after the impulsive perturbation). The impulse-response function is defined as the ice-sheet response from the time of the perturbation to the time when the ice thickness returns to within our chosen threshold of 10^{-6} meters of the initial steady-state value (see Appendix J). It is the shape of the response function that is used in our calculation of a physically-based boundary condition.

4.2.2.3. Boundary values for the limited model

The boundary condition for our limited-model calculations is the time series of ice flux at each limited-domain boundary. Therefore, we convert our ice-thickness impulse-response functions at the limited-domain boundaries to ice-flux impulse-response functions at the limited-domain boundaries using Equation 4.2. We need the response functions at the limited-domain boundaries x_{LD} only, and the datum-state values of ice flux q, ice thickness h, and surface slope α are the values at each limited-domain boundary at the timestep t_0 when the limited-domain has been embedded in the full domain to calculate (or recalculate) the response functions there. In our finite-volume formulation, the limited-domain boundary x_{LD} can be on the left side of the ice divide at the western finite-volume edge $x_w{}^1$, or on the

right side of the ice divide at the eastern finite-volume edge x_e^{end}. The equations given below are identical for each boundary, but flux to the left side of the divide is negative, and flux to the right side of the divide is positive; the ice flux is equal to zero at the ice divide.

The steady-state ice flux is given by

$$Q(x_{LD},t_0) = Q^0(x_{LD}) = Q_{in}(x_o,t_o) + \int_{x_{div}(t_0)}^{x_{LD}} \dot{b}_0(\zeta_{LD})d\zeta \tag{4.6}$$

where the integration limits in Equation 4.6 start from the ice-divide position in steady state (at the first timestep) $x_{div}(t_0)$; this describes the steady-state flux at the limited-domain boundary, and we want to calculate changes in ice flux relative to this steady-state value. Ice-sheet evolution within the limited domain is driven directly by ice-flow and climate changes that occur within the limited domain. It is also driven indirectly by externally-forced changes that occur outside the limited domain. The change in the amount of global ice volume within the limited domain over a timestep Δt, given by $\Delta\dot{V}(x,t)$, is the change in kinematic ice flux due to changes in the accumulation rate (Equation 4.5), giving

$$\Delta\dot{V}^{\dot{b}}(x_{LD},t) = \int_{x_{div}(t_0)}^{x_{LD}} (\dot{b}(\varsigma,t) - \dot{b}_0(\varsigma))W(\zeta)d\varsigma = \int_{x_{div}(t_0)}^{x_{LD}} (\dot{b}_1(\varsigma,t))W(\zeta)d\varsigma\,. \tag{4.7}$$

The ice flux is negative on the left side of the ice divide, so the change in boundary flux is negative when a positive volume is added. The ice flux is positive on the right side of the ice divide, so the change in boundary flux is positive when a positive volume is added. However, the ice divide may also migrate, and therefore we must also calculate the change in ice volume from ice-divide migration. Changes in ice flux due to ice-divide migration are

found by integrating the steady-state ice flux from the steady-state ice-divide position at time t_0, to the new divide position at time t

$$\Delta \dot{V}^{div}(x_{LD},t) = \int_{x_{div}(t_0)}^{x_{div}(t)} \dot{b}_0(\zeta_{LD})d\zeta \tag{4.8}$$

Equation 4.8 accounts for the fact that some amount of the steady-state flux might move across a different limited-domain boundary as the divide migrates over each timestep; if the divide moves to the left of the steady-state divide position, more flux goes out the right boundary of the limited domain, and vice versa. Since the ice flux is negative on the left side of the divide, the change in the value of ice flux from changes in ice volume due to divide migration is positive if the divide moves to the left, and it is negative if the divide moves to the right. On the right side, the change in the value of ice flux from changes in ice volume due to divide migration is positive if the divide moves to the left, and it is negative if the divide moves to the right.

The time-variation of ice thickness $h_1(x_{LD},t)$, and of surface slope $\alpha_1(x_{LD},t)$, at the limited-domain boundaries x_{LD} in response to an impulsive perturbation in accumulation are calculated with the full-domain model. Using these values, the ice-flux response function $q_1(x_{LD},t)$ can be calculated from Equation 4.2,

$$q_1(x_{LD},t) = \left(\frac{\partial q(x_{LD},t_0)}{\partial h(x_{LD},t_0)}\right) h_1(x_{LD},t) + \left(\frac{\partial q(x_{LD},t_0)}{\partial \alpha(x_{LD},t_0)}\right)_0 \alpha_1(x_{LD},t) \tag{4.9}$$

$$= c_0(x_{LD},t_0)h_1(x_{LD},t) + D_0(x_{LD},t_0)\alpha_1(x_{LD},t).$$

We evaluate the kinematic-wave velocity $c_0(x_{LD},t_0)$ and the kinematic-wave diffusion coefficient $D_0(x_{LD}, t_0)$ at the limited-domain boundaries (Nye 1960; Hooke 2005, pg. 373-375) in the steady (datum) state. The time variation of ice flux at each limited-domain boundary is the ice-flux impulse-response function $q_1(x_{LD},t)$, which we call $F_{LD}(t)$. For example, Figure 4.4a

and Figure 4.4b show the ice-flux impulse-response functions corresponding to the geometry in Figure 4.2b. The impulse-response function characterizes a particular geometry, and corresponds to a particular accumulation-rate perturbation. In Section 4.3.1 we discuss how the response function changes as a function of accumulation-rate perturbation and ice-sheet geometry, and in Section 4.4.1 we discuss the utility of any particular response function.

In a kinematic calculation for the boundary flux (Section 4.2.1), the change in volume $\Delta V(x,t)$ over each timestep is exported or accumulated completely over each timestep. As we discussed in Section 4.2.1, and is supported by the duration of the impulse-response function, for example in Figure 4.2b, instantaneous adjustment is not physically realistic. For realistic ice-sheet evolution across the limited-domain boundaries, we form a vector of volume perturbations over time by multiplying the scalar value of volume change $\Delta \dot{V}^{b}(x_{LD},t)$ (Equation 7) or $\Delta \dot{V}^{div}(x_{LD},t)$ (Equation 8) at each timestep with the impulse-response function $\dot{F}^{b}_{LD}(t)$ or $\dot{F}^{div}_{LD}(t)$, formulated from Equation 9. The impulse-response functions associated with changes in accumulation $\dot{F}^{b}_{LD}(t)$, and the impulse-response function associated with changes in divide position $\dot{F}^{div}_{LD}(t)$ may not be the same. As discussed in Section 4.3.1, the impulse-response function depends on the spatial pattern of the perturbation. For a given impulse-response function, the flux of ice crossing the limited-domain boundary due to accumulation-rate perturbations $\Delta \dot{Q}^{b}(x_{LD},t)$ at a particular time t is the convolution of volume-perturbation functions for that timestep and all applicable previous timesteps:

$$\Delta \dot{Q}^{b}(x_{LD},t) = \Delta \dot{V}^{b}(x_{LD},t) * \dot{F}^{b}_{LD}(t) = \int_{-\infty}^{t_i} \Delta \dot{V}^{b}(x_{LD},\tau)\dot{F}^{b}_{LD}(t-\tau)d\tau . \qquad (4.10)$$

A similar equation is used to calculate the changes in ice flux due to ice-divide migration $\Delta Q^{div}(x_{LD},t)$,

$$\Delta Q^{div}(x_{LD},t) = \Delta V^{div}(x_{LD},t) * F_{LD}^{div}(t) = \int_{-\infty}^{t_i} \Delta V^{div}(x_{LD},\tau) F_{LD}^{div}(t-\tau) d\tau. \tag{4.11}$$

Figure 4.3b illustrates that the volume added or removed from the domain over time is determined by convolving the volume-perturbation time series (the change from the steady-state value), illustrated in Figure 4.3a**,** with the appropriate impulse-response function. At any timestep, the change in ice flux from the known steady-state value is the sum of the changes in ice flux from all applicable previous timesteps. Contributions from previous timesteps are included until the entire volume perturbation has been accounted for, which occurs when the value of the impulse-response function goes back to zero or when the duration of the model calculation is reached. In the simple scenario depicted in Figure 4.3, the change in the rate of input ice flux that has to be exported through each boundary could be due to a change in accumulation, a change in ice-divide position, or a change in external forcing. The ice-flux boundary condition $q(x_{LD},t)$ at the limited-domain boundaries x_{LD} on the left side and on the right side of the divide at each timestep t is given by the sum of the steady-state ice flux $Q^0(x_{LD})$ (Equation 4.6), with the change in ice flux due to accumulation perturbations $\Delta Q^{\dot{b}}(x_{LD},t)$ (Equation 4.7), and with the change in ice flux due to ice-divide migration $\Delta Q^{div}(x_{LD},t)$ (Equation 4.8), and with the change in ice flux due to external forcing $\Delta Q^{ext}(x_{LD},t)$ (see Section 4.3.2.3

and Section 4.4.2), giving

$$q(x_{LD}, t_i) = Q^0(x_{LD}) + \Delta Q^{\dot{b}}(x_{LD}, t) + \Delta Q^{div}(x_{LD}, t) + \Delta Q^{ext}(x_{LD}, t) \quad (4.12)$$

These four terms account for the total flux crossing the limited-domain boundary on the left side of the divide or on the right side of the divide at any time t_i.

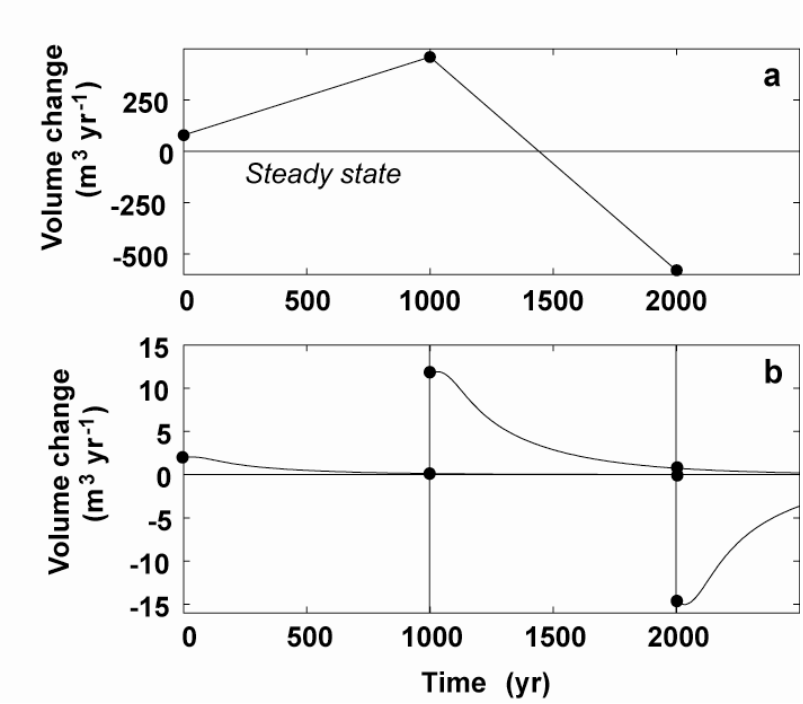

Figure 4.3. **a)** Example change in ice volume from steady state, which may be due to changes in accumulation (Equation 7), changes in ice-divide position (Equation 8), or changes in external forcing. **b)** The change in ice volume at each timestep is scaled by a response function, and added to or removed from the limited domain over multiple timesteps. The actual change in ice volume at any timestep is the convolution of changes in ice volume from all applicable previous timesteps with the impulse-response function. In this illustration, the convolution value is the sum of changes in ice volume (marked with a dot) at each timestep (marked with vertical lines).

4.3. Results

We have described a new approach to calculate a physically-realistic value for the flux crossing the boundaries of a limited-domain model. The accuracy of the solution from our limited-domain model depends on the suitability of the impulse-response functions. In practice, the full-domain model is used only to calculate impulse-response functions that are required for the limited-domain boundary-flux calculation. However, ice-sheet evolution in the limited-domain model with the correct boundary flux must be consistent with ice-sheet evolution in the full-domain model within which it is embedded. The full-domain solution and the limited-domain solution should be equivalent, and we show how this can be achieved.

Unless stated otherwise, the standard limited-domain model we use in our tests has a maximum initial ice thickness H of 1000 m, crosses an ice divide with a limited-domain length L= 25 km, has a mean accumulation rate $\dot{b}$=20 cm yr^{-1}, has a uniform flowband width $W(x)$, and has ice flux leaving the left-side boundary Q_{in}= -2500 m^3 yr^{-1}; ice flux on the left side of the divide is negative, because the surface slopes there are positive. The ice-divide position is the spatial location with the highest surface elevation.

4.3.1. Impulse-response functions

Following the linearized kinematic-wave theory that was applied to glaciers by Nye (e.g. 1960), the accumulation-rate perturbation $\dot{b}_1(x,t)$ in Equation 4.5 has a small magnitude and has a spatially uniform distribution. An impulse-response function can well characterize the response of glaciers and ice sheets to changes in climate (e.g. Hooke 2005, pg. 373-375). We use the impulse-response function not only to gain a characteristic understanding of ice-sheet response time, but the shape of the

impulse-response function is the primary information supplied to the limited model to facilitate realistic ice-sheet evolution. In this case, the response function to a spatially uniform impulse of accumulation can well describe the evolution of a limited domain to spatially uniform perturbations, but the actual accumulation perturbations may not be spatially uniform. In addition, the impulse-response functions are calculated for specific limited-domain geometry, and this geometry may change over time. We must quantify the utility of a given impulse-response function to properly characterize ice-sheet behavior as the limited model evolves to different ice-sheet geometries and experiences different accumulation-rate perturbations. Since we aim for the most efficient calculation of ice-thickness evolution, it is an advantage to recalculate the response function only when necessary.

Four impulse-response functions $F_{LD}(t)$ are required in a limited-domain model, and they may all be different. The impulse-response functions control volume perturbations across the limited domain, and these perturbations may be attributable to accumulation variations or to divide migration. For a limited domain that crosses an ice divide, accumulation-rate perturbations are transported across both the left-side boundary and across the right-side boundary. To properly control volume perturbations due to changes in accumulation, we use separate impulse-response functions $F_{LD}^{\dot{b}}(t)$ for each boundary. Another impulse-response function $F_{LD}^{div}(t)$ is also required to control volume perturbations due to changes in divide position, we again use separate impulse-response functions $F_{LD}^{div}(t)$ for each boundary. We explore the sensitivity of the solution for ice-sheet evolution with the limited-domain model to the four impulse-response functions used in the problem.

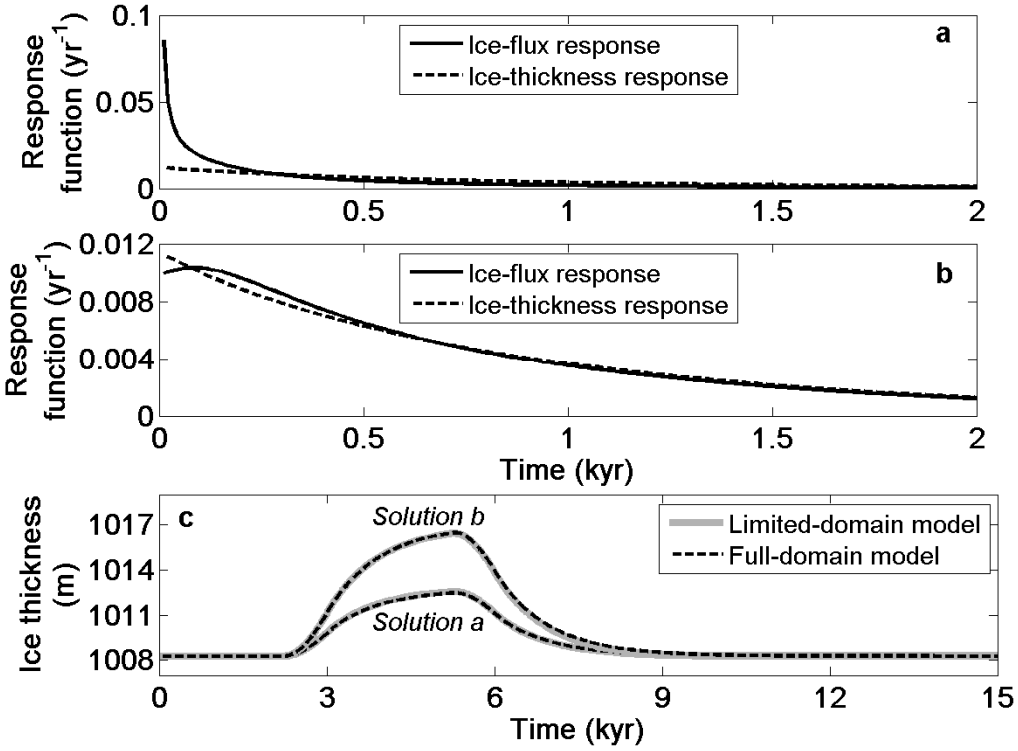

Figure 4.4. Response functions and ice-sheet evolution for the right-side boundary of the limited domain in Figure 4.2b. The ice-thickness response function is calculated by solving the continuity equation (Equation 4.1) with an implicit numerical scheme (Appendix 4.2). The ice-flux response function is calculated using this ice-thickness response function and kinematic wave theory (Section 4.2.3.2). **a)** Impulse-response functions to a uniform accumulation perturbation that spans only the extent of the limited domain. **b)** Impulse-response functions to a uniform accumulation perturbation that spans the full domain. **c)** Evolution of divide thickness in response to a step change in accumulation rate. Solutions from the limited-domain model (gray lines), using impulse-response functions from **a)** and from **b)**, are the same as the solutions from a full model; using the correct impulse-response functions in the limited model can yield correct ice-sheet evolution.

4.3.1.1 Sensitivity to the extent of the accumulation perturbation

The extent over which the accumulation perturbation is distributed over the full domain will affect the response of the ice sheet. Figure 4.4a shows the response functions associated with a uniform perturbation that is

restricted to the extent of the limited domain, and Figure 4.4b shows the response functions associated with a uniform perturbation that covers the entire span of the full domain; all response functions are for the right-side boundary of the limited domain shown in Figure 4.2b. The ice-flux response function is calculated from the ice-thickness and surface-slope evolution using Equation 4.9.

If the accumulation perturbation is restricted to a limited portion of the ice sheet, the local surface slope changes are initially larger than if the entire ice sheet is responding directly to the accumulation perturbation. Therefore, the ice-flux response function in Figure 4.4a is different from the ice-flux response function in Figure 4.4b because the slope term in Equation 4.9 depends on the extent of the impulsive perturbation.

Figure 4.4c shows that correct ice-sheet evolution can be achieved if the correct response function is used in the limited-model calculations. If actual volume perturbations in the limited domain are restricted to the extent of the limited domain, the response functions in Figure 4.4a will be appropriate. In reality, we expect that actual spatial and temporal variations in accumulation rate will occur over the full span of the ice sheet, and will not be restricted to the arbitrary extent of the limited-domain model. In the subsequent sensitivity tests and results shown here, we use response functions associated with an accumulation perturbation that was distributed over the entire span of the full model.

4.3.1.2 Sensitivity to the distribution of the perturbation

The spatial pattern of the impulsive perturbation in accumulation over an ice sheet will affect the response time. For example, as shown in Figure 4.5, a spike in accumulation that is spatially concentrated near the

ice divide will be discharged from the limited domain at a faster rate than a spatially uniform perturbation with the same volume. It is important to consider the sensitivity of the impulse response function to the perturbation used to calculate the response function, because actual ice-volume perturbations across the limited domain may not be spatially uniform.

We compare the shape of the impulse-response functions associated with accumulation perturbations $\dot{b}_1(x,t)$ across the entire span of the full domain that are (a) spatially uniform, (b) linearly varying across the domain, and (c) a delta function at the divide. A delta function can be represented as the limit of a Gaussian distribution (e.g. Arfken and Weber, pg. 81),

$$\delta = \frac{a}{\sqrt{\pi}} \exp(-x^2 a^2), \tag{4.13}$$

where a is the width of the Gaussian distribution, and $a \to 0$ in the definition of the delta function. We evaluate Gaussian functions with a=1/2 and a=1/10 (by definition, a=1/10 is a narrower spike). Figure 4.5a displays the shapes of the four accumulation perturbations, and Figure 4.5b shows the response curves for the limited-domain boundary. Each accumulation perturbation adds the same ice volume impulsively over the full domain. By definition, the impulse-response function integrates to unity over the full response time (in this case when the ice thickness at the limited-domain boundary has returned to within 10^{-6} of the steady-state value). The volume response time τ is an e-folding time, which is the time to reach $(1-e^{-1})$ of the new equilibrium value. Figure 4.5b shows that the re-equilibration of the ice sheet to a narrow spike in accumulation is very different from the re-equilibration of the ice sheet to a uniformly distributed accumulation perturbation. In Figure 4.5c we show the evolution of surface elevation at the limited-domain boundary in response to an accumulation history that

increases as a step function by 5% from the steady-state value at t=1500 years and returns to the initial steady-state value at t=5500 years. The thickness response is influenced by the response function used to calculate this solution. When the actual accumulation perturbation is spatially uniform, but an impulse-response function derived from a spatially restricted spike perturbation is used to characterize ice-sheet behavior, ice added to the domain is evacuated too quickly.

In reality it is unlikely that the spatial pattern of accumulation perturbations will be so spatially restricted. Ice-sheet evolution is determined primarily by long-term average changes in accumulation rate, and not by localized, even if large in magnitude, excursions in the accumulation rate. Therefore, to calculate the impulse-response function used to control actual ice-volume perturbations due to changes in accumulation $F_{LD}^{\dot{b}}(t)$ within the limited-domain model we use a spatially uniform accumulation-rate perturbation $\dot{b}_1(x,t)$. However, changes in ice input directed toward one boundary or the other due to ice-divide migration are better characterized by a spike function. Under steady-state accumulation forcing (i.e. with no accumulation perturbation), divide migration can redirect some of this accumulation toward one boundary or another. Therefore, to calculate the impulse-response function used to scale actual ice-volume changes due to divide migration $F_{LD}^{div}(t)$ within the limited-domain model we use an accumulation-rate perturbation $\dot{b}_1(x,t)$ that is a function with a=1/10 centered at the initial divide.

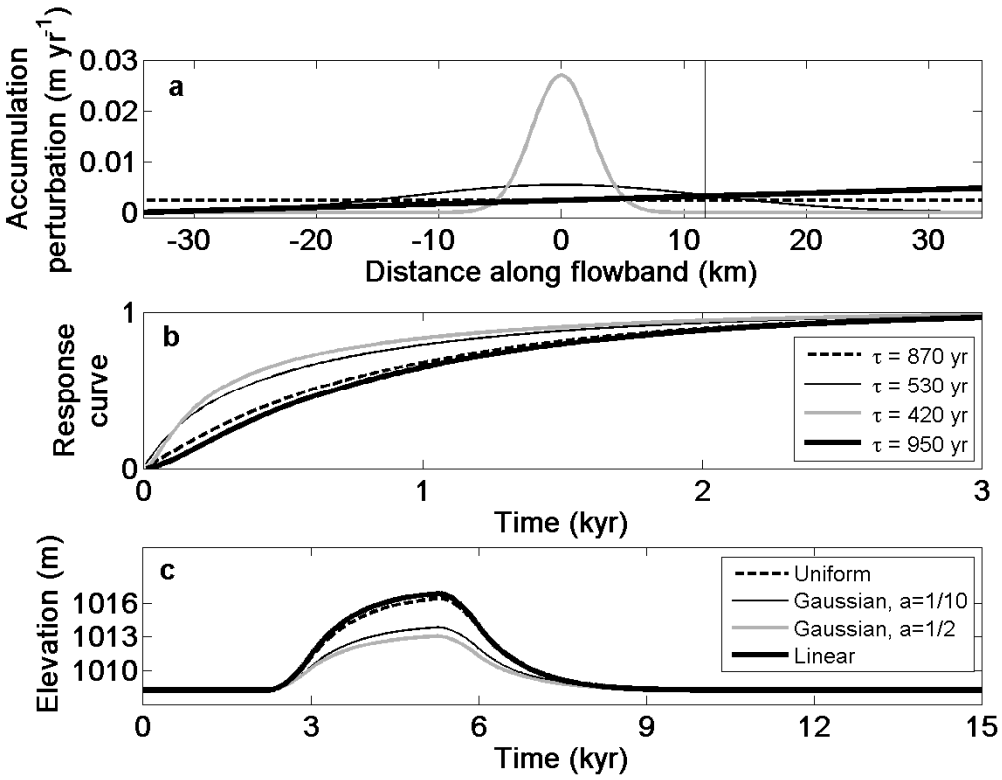

Figure 4.5. a) Accumulation perturbations that are spatially uniform (dashed line), linearly varying (thick solid line), a Gaussian function (Equation 4.13) with α=1/2 (thin line), and a Gaussian function with α=1/10 (gray line); these are examples of the perturbation term $\dot{b}_1(x,t)$ in Equation 4.5, and all perturbations add the same ice volume in one timestep. The vertical line marks the position of the limited-domain boundary on the right side of the ice divide, as in Figure 4.2b. **b)** Response curves associated with response functions associated with the impulsive perturbations in **a)**. The volume response time τ is an e-folding time, the time to reach (1-1/e) of the new equilibrium. **c)** Ice-sheet evolution from the limited-domain model in response to a step change in uniformly distributed accumulation, using the different response functions that characterize uniform and nonuniform perturbations.

4.3.1.3. Sensitivity to ice-sheet geometry

Jóhannesson and others (1989) showed that the volume response time for an ice sheet can be estimated as the ratio of the maximum ice thickness to the ablation rate at the terminus, i.e. the impulse-response function is

dependent on the ice thickness. The response function is associated with specific ice-sheet geometry, and in this case it is the full domain in which limited-domain model is embedded. However, in a transient problem, the ice thickness and the ice-divide position can change. Our impulse response functions should produce longer response times for thicker ice sheets.

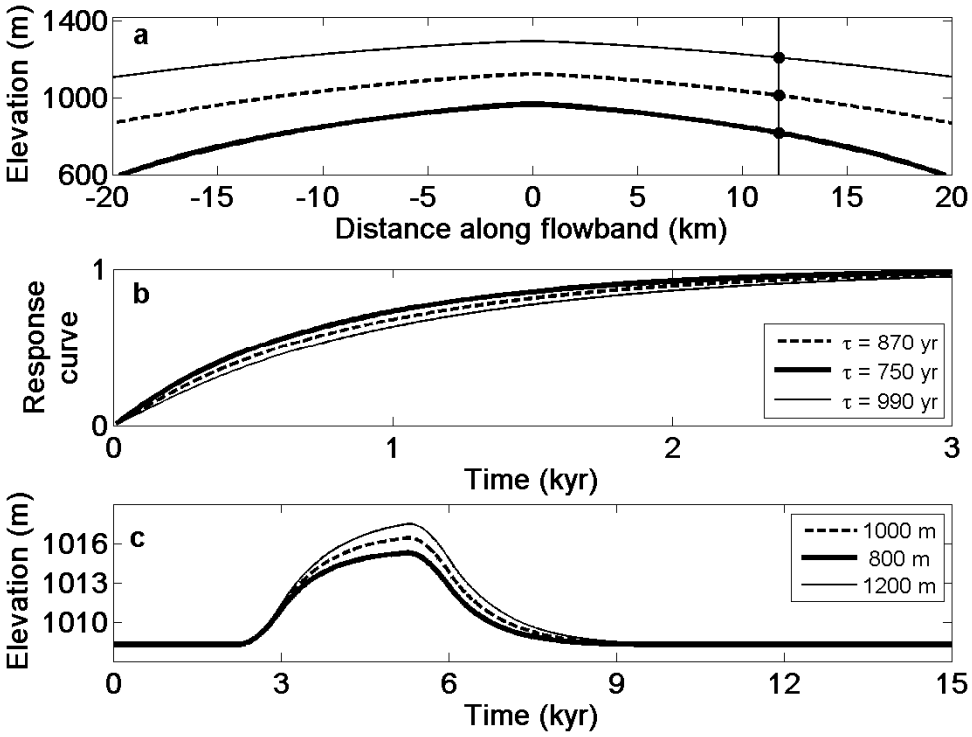

Figure 4.6. Ice-sheet surfaces generated with an ice thickness at the left side of the limited domain of 800 m (thick line), 1000 m (dashed line), and 1200 m (thin line). The ice divide is at 0 km along the flowband. The dots mark the spatial location of the time-varying response functions shown below. **b)** Response curves for impulse-response functions calculated from a uniform accumulation perturbation across a full model in which each ice-sheet surface in **a)** was embedded. The volume response time τ is an e-folding time, the time to reach (1-1/e) of the new equilibrium. **c)** Ice-sheet evolution from a limited-domain model that is ~1000 m thick, in response to a step change in uniformly distributed accumulation, using response functions that characterize a ~800 m thick ice sheet and a ~1200 m thick ice sheet. The dashed line shows the correct solution, a thicker ice sheet has a longer response time, and a thinner ice sheet has a shorter response time.

We calculate impulse-response functions associated with ice sheets of different ice thicknesses. Figure 4.6b shows the response curves for ice thicknesses of 1000 m, 800 m, and 1200 m, shown in Figure 4.6a. We calculate the evolution of our standard 1000-meter thick ice sheet in response to a step 5% increase in accumulation rate, but we use impulse-response functions for an ice sheet that is 200 m thicker (at 1200 m), and for an ice sheet that is 200 m thinner (at 800 m) than the standard ice sheet. Figure 4.6c shows that ice-thickness evolution is sensitive to the ice-sheet geometry from which the impulse-response function is calculated. In Section 4.4.1 we discuss how to assess the range of applicability of a specific response function, and how to estimate when the response function must be recalculated because the ice-sheet geometry has changed.

4.3.2. Efficient transient calculations

Our limited-domain calculations require appropriate impulse-response functions. For efficiency, we do not update the impulse-response functions throughout the calculation for ice-sheet evolution. We assume that an impulse-response function generated with a spatially uniform accumulation perturbation is appropriate to control volume discharges due to accumulation variations $F_{LD}^{\dot{b}}(t)$, and we use an impulse-response function generated with a Gaussian-function accumulation perturbation to control volume discharges associated with ice-divide migration $F_{LD}^{div}(t)$. Given the other sources of uncertainty in the ice-thickness solution that we seek, we show that this is a reasonable procedure.

While the primary purpose of the full-domain model is to calculate the impulse-response functions required to properly calculate the limited-domain boundary flux, we can also use the solution for ice-sheet evolution

from the full-domain model to test our limited-domain solution. In Section A4.3 we show that the full-domain model exhibits ice-sheet evolution that is consistent with our physical expectation. Therefore, we can require that the limited-domain model exhibit the same behavior as the full-domain model. In tests of ice-sheet evolution with the limited-domain model, we must prescribe the accumulation-rate history $\dot{b}(x,t)$. We must also prescribe the history of externally forced changes in ice flux on the left side of the divide $\Delta Q_{ext}^{L}(t)$, and on the right side of the divide $\Delta Q_{ext}^{R}(t)$. The accumulation-rate and external-forcing histories, together with the impulse-response functions, contain all of the information about ice-sheet evolution that is required by the limited-domain model calculations.

4.3.2.1. Ice-thickness evolution and ice-divide migration

If the correct impulse-response functions are used, the ice sheet can thicken and thin in exactly the same way as a full-domain model for small perturbations. If an impulse-response function associated with a spatially uniform perturbation is used to scale ice-volume perturbations that are not strictly uniform, the ice sheet will thicken and thin in a similar, but not exactly the same, way to a full-domain model. Figure 4.7 shows that if there are no mass-balance perturbations outside the limited domain, the ice-sheet history can be well reproduced by using information from the impulse-response functions alone. As illustrated in Figure 4.7a, the accumulation-rate history for this test varies in space and time across the limited domain, but remains at the steady-state values elsewhere. Figure 4.7b and Figure 4.7c show that using one set of impulse-response functions does not exactly capture the behavior of the full domain. However, the results are similar. We argue that this is a simplified test, and that the errors accrued by not

recalculating the impulse-response functions are minor compared to other uncertainties; this is discussed in more detail in Section 4.4.1.

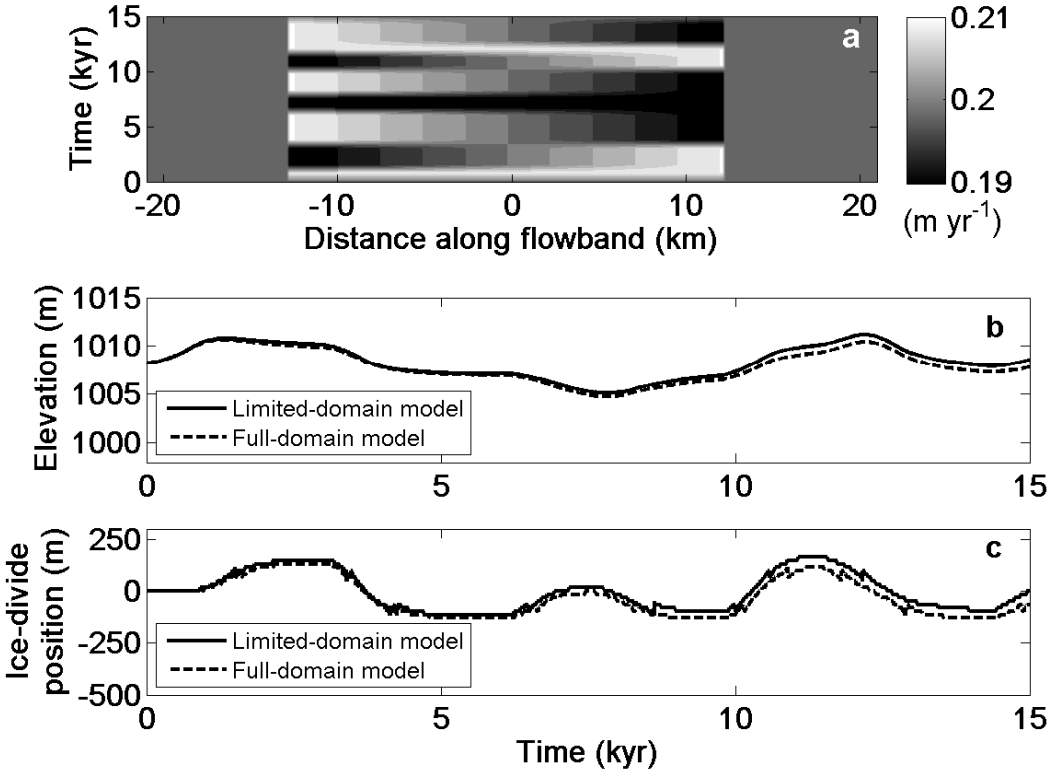

Figure 4.7. a) Accumulation-rate history that changes in space and time across the extent of the limited domain, but is constant outside the limited domain. This accumulation-rate history over the full domain is used to calculate ice-sheet evolution in the full-domain model; the portion covering the limited domain is used to calculate ice-sheet evolution in the limited-domain model. The limited model uses response functions from an accumulation perturbation that extends over the limited domain only. **b)** Ice-thickness evolution at the right-side boundary of the limited domain (as in Figure 4.2b). **c)** Ice-divide position from the limited-domain model and from the full-domain model. The solutions from the limited model and from the full model are not identical because the impulse-response function cannot provide information about proper ice-divide migration.

A realistic full-domain ice sheet will experience changes in ice flow and climate across its entire extent. Therefore, a more realistic test is to prescribe accumulation-rate variations across the full domain, and compare the solutions for ice-sheet history from the limited-domain model and from the full-domain model. Figure 4.8a shows an accumulation history that changes from a spatially uniform pattern, to a pattern that has a strong spatial gradient across the divide; the variation across the limited domain is the same as in Figure 4.7a. In this case, external forcing is a significant driver of divide migration.

Figure 4.8b and Figure 4.8c confirm our expectation that when external forcing is significant, the impulse-response functions alone cannot provide enough information to facilitate accurate ice-sheet evolution. If the impulse-response functions are generated with a spatially uniform impulsive perturbation that spans the entire full domain (as in Figure 4.4b), the solution in Figure 4.8 is better approximated than if the impulse-response functions are generated with an impulsive perturbation that spans the limited domain only (as in Figure 4.4a, and in Figure 4.7). However, if the influence of external forcing on the boundary is not adequately described by spatially uniform mass balance outside the limited domain, additional information is required; this is demonstrated by the mismatch in Figure 4.8b and Figure 4.8c.

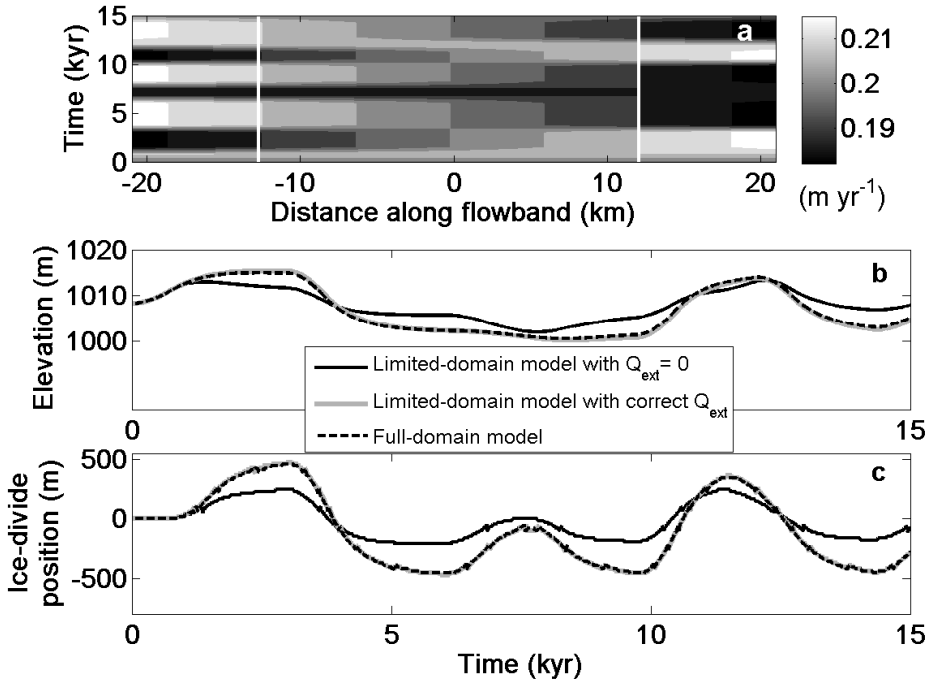

Figure 4.8. a) Accumulation-rate history that changes in space and time across the full domain. This history is used to calculate ice-sheet evolution in the full-domain model; the portion covering the extent of the limited domain (bounds shown with white lines) is used to calculate ice-sheet evolution in the limited-domain model. The limited-domain model uses response functions from an accumulation perturbation that extends over the full domain. **b)** Ice-thickness evolution at the right-side boundary of the limited domain (as in Figure 4.2b). **c)** Ice-divide position from the limited-domain model and from the full-domain model. The solutions from the limited model and from the full model are identical if the correct external-flux forcing Q_{ext} is known.

4.4. Discussion

4.4.1. Utility of the impulse-response functions

We must establish over what timescales and over which ice-sheet geometries the impulse-response function is valid. For efficiency, we propose that the impulse-response functions are not recalculated for

accumulation perturbations with different spatial distributions, and are recalculated only when changes in ice thickness have been significant. In the case of the evolution of large ice sheets, we propose that the threshold for a significant ice-thickness change be determined by the point when the time $(1-e^{-1})$ to export additional ice volume has changed by more than 10%. The volume response time could be tabulated for many ice sheets with different ice thicknesses. As ice thickness is changing in the limited-domain calculation of ice-sheet evolution, this look-up table could be used as a proxy to determine when a given ice thickness would result in a volume response time that is significantly different. Crossing this ice-thickness threshold implies that the impulse-response functions should be recalculated for this geometry.

4.4.2. Inferring external forcing

On glacial-interglacial timescales, ice-sheet interiors will change in ice thickness due to local changes in accumulation and ice flux, but also in response to externally forced global changes in ice volume. In particular, ice-sheet margins respond directly to changes in sea level by advancing or retreating. These changes in ice-sheet span influence the overall ice-sheet geometry, and therefore changes at the margin drive changes in the interior. The impulse-response function we have presented is associated with a full ice sheet with a specific geometry, and it is used to regulate volume perturbations that originate within the limited domain. Since the limited domain does not have any information about global changes in ice volume, these externally-forced changes at the limited-domain boundary $\Delta Q^{ext}(x_{LD},t)$ must be prescribed differently than our treatment of volume

perturbations due to accumulation variations and ice-divide migration; we prescribe this information through the $\Delta Q^{ext}(x_{LD},t)$ term in Equation 4.12.

The correct value of $\Delta Q^{ext}(x_{LD},t)$ at the limited-domain boundaries x_{LD} over time t must come directly from a full-model calculation, or must be estimated using a proxy for the externally forced perturbations (e.g. changes in sea level). However, it may be that the history of external forcing is largely unknown. To infer this value, we could infer the change in ice flux due to external forcing $\Delta Q^{ext}(x_{LD},t)$ at the limited-domain boundaries as part of an inverse problem. In particular, we will use this efficient model for transient ice flow to infer histories of accumulation and ice dynamics from the shapes of radar-observed internal layers. By solving this inverse problem, we can infer histories of ice thickness, ice-divide position, accumulation rate, and external forcing that are consistent with internal-layer architecture and ice-surface topography.

4.5. Conclusions

We have demonstrated how to setup a limited-domain model that can efficiently calculate transient ice flow. This efficient limited-domain model is well suited as part of an inverse problem, and in particular, a problem that is focused near an ice divide. There are two key insights that promote efficiency and accuracy in this problem. First, rather than calculate ice-sheet evolution using a limited model that is always nested in a full model, we embed the limited model only at limited points in the calculation. Second, we use the full model only to provide information about characteristic behavior of this full ice sheet, not to provide exact values of the required boundary conditions. The behavior of a full ice sheet is characterized using impulse-response functions. We have illustrated how

the impulse response of an ice sheet depends on the spatial distribution of the accumulation perturbation, in addition to the ice-sheet geometry. In the calculation of ice-sheet evolution with a limited-domain model, different impulse-response functions should be used to realistically control changes in ice volume that may be due to changes in accumulation rate or to changes in ice-divide position.

A4.1. Ice-sheet flowband model

We use a flowband model, which is a 2.5-D representation of ice flow, where the boundaries are defined by two nearby flowlines and the volume is bounded vertically beneath these flowlines.

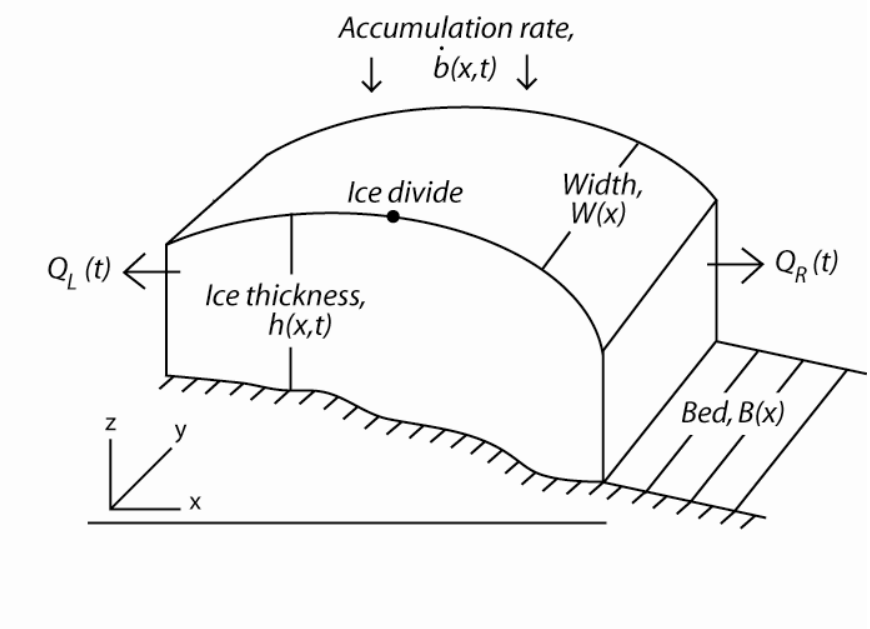

Figure A4.1. Geometry of an ice-sheet flowband with a limited domain. The flux leaving the domain on the left side $Q_L(t)$ and on the right side $Q_L(t)$ are calculated, and the spatial and temporal history of accumulation rate $\dot{b}(x,t)$ is prescribed as a boundary condition. For this model, the bed topography and the width function do not change in time.

Figure A4.1 illustrates the geometry of a flowband. Horizontal variations in the bed topography $B(x)$ and in the flowband width $W(x)$ are specified. We assume that glacial-isostatic, tectonic, or erosional processes are not changing the bed topography over time. In reality, the flowband width and the bed topography could change over time, but as a first-order assumption we assume that the flowband width and the bed topography are

constant over time. The ice thickness $h(x,t)$ is related to the ice-surface elevation by $h(x,t) = S(x,t)-B(x)$. If a steady-state surface calculation is performed to estimate the initial ice surface, the ice-surface elevation at one point at the first timestep $S_0(t_0)$ and the ice flux entering the domain at the first timestep $Q_0(x_0)$ are both required initial conditions. The boundary conditions include the spatial and temporal accumulation rate $\dot{b}(x,t)$ and the externally-forced change in ice flux $Q_{LD}^{ext}(t)$. These values must be known, be estimated, or be solved for as a part of an inverse problem (e.g. Waddington and others, 2007).

By integrating Equation 4.1 from the boundary at x_0 where ice flux is specified, the ice flux at the end of the domain x_{end} can be represented kinematically by

$$q(x,t) = Q_0(t) + \int_{x_0}^{x_{end}} (\dot{b}(\chi,t) - \dot{h}(\chi,t) - \dot{m}(\chi,t))W(\chi)d\chi\,, \qquad \text{(A4.1.1)}$$

where $Q_0(t)$ is the time variation of ice flux entering at one end of the flowband domain, $\dot{h}(x,t)$ is the rate of change in ice thickness, and $\dot{m}(x,t)$ is the basal melt rate.

Dynamically, the flux of ice passing through a cross-sectional area $W(x)\times h(x,t)$ at any point x and at any time t, is related to the depth-averaged horizontal velocity $\bar{u}(x,t)$ in that cross-section by

$$q(x,t) = W(x)h(x,t)\bar{u}(x,t)\,. \qquad \text{(A4.1.2)}$$

We can calculate $\bar{u}(x,t)$ using the Shallow Ice Approximation (SIA; e.g. Hutter, 1983, pg. 256-332; Paterson, 1994, pg. 262); the SIA is a simplifying assumption that can be applied in cases where the ice thickness $h(x,t)$ is much smaller than the horizontal span of the ice sheet. Therefore, derivatives of velocities and stresses with respect to x are generally much smaller than derivatives with respect to z. The constitutive relationship for ice flow (Glen, 1955) using the SIA is,

$$\dot{\varepsilon}_{xz} = A(T(x,z,t))\tau_{xz}^{n} \tag{A4.1.3}$$

where $\dot{\varepsilon}_{xz}$ is the simple-shear strain rate along a horizontal plane, *A(T(x,z,t))* is the temperature-dependent ice-softness parameter, τ_{xz} is the component of the shear-stress tensor acting horizontally along a horizontal plane, and we choose the flow law exponent *n=3* (e.g. Paterson, 1994, pg. 85). The component of the strain-rate tensor along a horizontal plane is

$$\dot{\varepsilon}_{xz} = \frac{1}{2}\left(\frac{\partial u}{\partial z} + \frac{\partial w}{\partial x}\right) \tag{A4.1.4}$$

Following the SIA, the derivatives of velocities with respect to x are negligible, giving $2\dot{\varepsilon}_{xz} \approx \partial u / \partial z$ (e.g. Paterson, 1994, pg. 262). Using the flow law given by Equation A4.1.3 for the SIA, and assuming that the temperature is uniform with depth for each position in x (*T(x,z,t)=T(x,t)*), the depth-averaged horizontal velocity can be found by integrating $\partial u / \partial z$ twice over depth z,

$$\bar{u}(x) = \frac{2A(T(x,t))}{n+2}(\rho g)^{n}\left|\frac{dS}{dx}\right|^{n-1}\left(-\frac{dS}{dx}\right)h(x)^{n+1} \tag{A4.1.5}$$

where ρ is density, g is gravitational acceleration, *S(x,t)* is the ice-surface elevation, and *h(x,t)* is the ice thickness.

If the ice temperature is not uniform with depth at each location, we can solve for an effective isothermal softness parameter $\tilde{A}(x,t)$ that gives the same depth-averaged velocity and ice flux as a depth-varying-temperature-dependent softness parameter *A(T(x,z,t))*. We calculate the effective isothermal value by equating the depth-averaged ice velocity $\bar{u}(x,t)$ with *A(T(x,z,t))*,

$$\bar{u}(x,t) = 2A_0\left(\rho g \frac{\partial S(x,t)}{\partial x}\right)^{n} h(x)^{n+1}\int_0^1\int_0^{\hat{z}} \exp\left(-\frac{Q}{RT(\hat{\varsigma},t)}\right)(1-\hat{\varsigma})^{n}\, d\hat{\varsigma}d\hat{z}\,, \tag{A4.1.6}$$

to the depth-averaged velocity $\bar{u}(x,t)$ from Equation A4.1.5, and solving for *A(T(x,t))*, given as here as $\tilde{A}(x,t)$,

$$\tilde{A}(x,t) = (n+2)\int_0^1\int_0^{\hat{z}} A(T(x,\varsigma,t))(1-\hat{\varsigma})^n \, d\hat{\varsigma}d\hat{z} \,. \qquad \text{(A4.1.7)}$$

where $\hat{z}$ is a nondimensional elevation given by

$$\hat{z} = \frac{z - B(x)}{S(x,t) - B(x)} \,. \qquad \text{(A4.1.8)}$$

Using Equation A4.1.5 for the depth-averaged velocity, but with the effective isothermal softness parameter from Equation A4.1.7, and then by representing average velocity $\bar{u}(x,t)$ in terms of ice flux *q(x,t)* and ice thickness *h(x,t)* using Equation A4.1.2 and *h(x,t) = S(x,t) - B(x)*, we can rearrange this equation to formulate a nonlinear ordinary differential equation for a steady-state ice surface,

$$\frac{dS_0(x,t_0)}{dx} = \left[\frac{(n+2)q(x,t_0)}{2\tilde{A}(x,t_0)(\rho g)^n W(x)(S_0(x,t_0) - B(x))^{n+2}} \right]^{1/n} \qquad \text{(A4.1.9)}$$

We use this ice-surface profile $S_0(x,t_0)$ as the required initial condition to solve for the ice-thickness evolution *h(x,t)* that we find by solving Equation 1; therefore, all the values used in this calculation are for the first time, $t=t_0$.

A4.2. Numerical solution using the Finite-Volume Method

We use numerical methods to solve the mass-conservation equation for ice flow (Equation 4.1). The background on numerical methods applied to glaciological problems is rich (e.g. Van der Veen, 1999, pg. 218), but we discuss only the methods we have chosen to use in this work. Solving an equation numerically is done by replacing the values represented by a

continuous function, in this case in Equation 4.1, by values at discrete points. We use the Finite-Volume Method (FVM; e.g. Patankar, 1980; Versteeg and Malalaskera, 1995), also known as the Control-Volume Method, to discretize the domain. The set of individual volumes fill the domain. In the FVM, each volume in the domain has a finite size, and is defined by a volume-center point and two edge points, as illustrated and described in Appendix G. In the FVM solution of the mass-continuity equation (Equation 4.1), we evaluate the ice thickness at each volume center and we evaluate the flux across each volume edge (west and east along the horizontal domain from each center point). Ice flux is calculated at the finite-volume western edge x_w and the eastern edge x_e, but it is a function of ice thickness and surface slope that are calculated at finite-volume center points x_P. Therefore, in order to evaluate the ice flux, the ice thickness and surface slope must be evaluated at the finite-volume edges, and this relationship is discussed further in Appendix G. However, at the first western finite-volume edge x_w^1 and the last eastern finite-volume edge x_e^{end}, no information exists outside the limited domain to interpolate the ice thickness and slopes at the limited domain boundaries, and values extrapolated from inside the limited domain are inadequate. As discussed in Section 4.2.1, this is why we need a careful treatment of the calculated flux across the limited-domain boundary. Discretization using the FVM is discussed further in Appendix G, and how to address the nonlinear dependence of the ice flux on the ice thickness is discussed in Appendix I.

Here we use a fully-implicit timestepping scheme, which is described in detail in Appendix H. In Appendix H we also compare a fully-explicit scheme, a Crank-Nicolson (semi-implicit scheme), and a fully-implicit scheme. Following Patankar (1980, pg. 57), we use a fully-implicit scheme, but we verify that our fully-implicit solution matches an appropriately time-

stepped fully-explicit solution. In addition, we invoke underrelaxation to stabilize our procedure to solve a nonlinear problem that has been linearized between iterative calculations of updates to the solution values. As described by Patankar (1980, pg. 67), underrelaxation is a way to slow down convergence of the solution by using a weighted contribution of values from previous iterations.

The problem is nonlinear because the ice flux $q(x,t)$ in Equation 4.1, calculated dynamically using Equation A4.1.2 with Equation A4.1.5, is a nonlinear function of ice thickness $h(x,t)$ and surface slope $dS(x,t)/dx$; the ice thickness and surface slope are the values we are trying to find. The solution for ice-thickness evolution must satisfy Equation 4.1, and the treatment of the nonlinearity is discussed further in Appendix I. We use an iterative procedure, and we stop iterations when changes in the solution are smaller than a threshold value (e.g. Patankar, 1980, pg. 47; Waddington, 1982, pg. 239; Van der Veen, 1999, pg. 226); here we use a threshold value of 10^{-6}, and the choice of this value is discussed further in Appendix J.

A4.3. Full-domain model

As sketched in Figure 4.2a, the full-domain surface is extended from the limited-domain surface. Any full domain could be used to embed the limited domain, but here we use a simple analytical ice-sheet surface in which the mass-balance distribution is given by a zone of uniform accumulation c over part of the domain, and a zone of uniform ablation a over the rest of the domain. The two zones are separated at the equilibrium line R; this is the Paterson model (Paterson, 1972; Paterson, 1994, pg. 245),

and this model is discussed further in Appendix E. The ablation rate depends on the size of the ablation zone, expressed as the position of the equilibrium line R (or equivalently the ratio c/a of the accumulation rate to the ablation rate). Since the ablation rate influences the ice-sheet response time, we prescribe a ratio of accumulation rate to ablation rate c/a that gives a realistic rate of ablation. Our limited-domain model crosses an ice divide, and must be embedded in a full domain that extends off both sides of the divide.

The calculation of the full-domain surface shape from the analytical Paterson (1972) model requires the length of the full domain. If the full-domain length cannot be estimated from a map of the ice-sheet study site, the full length L on either side of the divide could be calculated by matching the full-domain surface to the limited-domain surface h_{LD} at the limited-domain-boundary position x_{LD} on either side of the divide for the ice-sheet model used to represent the full domain. For the Paterson (1972) model, this is given by

$$L = \frac{x_{LD} - x_0}{\left[\left(1-\left(h_{LD}/H_0\right)^{2+(2/n)}\right)/(1+c/a)^{1/n}\right]^{1+(1/n)}} \qquad \text{(A4.3.1)}$$

where x_0 is the position of the ice divide, H_0 is the thickness at the ice divide, and c/a is the ratio of accumulation rate to ablation rate.

In a model that includes an ice-sheet terminus, as the distance along the flowline approaches the total length of the flowline, the ice flux and the ice thickness will approach zero at the terminus. This means that the velocity at the terminus will also approach zero (e.g. following Equation A4.1.5). As pointed out by Nye (1960; 1963), this resulted in the non-physical situation of an immobile terminus; the terminus should be able to advance and retreat. To address this problem in our discretized model, the region near the terminus can be replaced by a wedge with a defined angle to

the surface and a discrete area (e.g. Nye, 1963; Waddington, 1982, pg. 247). Mass conservation and the flow law are satisfied separately in the wedge.

Figure A4.2 sketches the finite-volume geometry for our wedge-shaped terminus, which is implemented on both sides of the divide. We cut off the full-domain surface at a finite-volume edge point close to the terminus, which we call x_L^c on the left side of the divide, and x_R^c on the right side of the divide. The surface slope at the cut-off point is the slope of the wedge surface, and can be defined by the surface slope between the upstream finite-volume center points. The surface slope at the cut-off point on the right side of the divide x_R^c (Figure 4.2b) is:

$$\frac{dS(x_R^c)}{dx} = \frac{S_P^c - S_W^c}{dx_w} = m_R \tag{A4.3.2}$$

where S_P^c is the last finite-volume center point used at the position x_R^c, and S_W^c is the center point upstream of S_P^c. Analogously, the surface slope at the cut-off point on the left side of the divide x_L^c is:

$$\frac{dS(x_L^c)}{dx} = \frac{S_E^c - S_P^c}{dx_e} = m_L \tag{A3.3}$$

where S_P^c is the last finite-volume center point used at the position x_L^c, and S_E^c is the center point upstream of S_P^c. Note the difference in subscript between w (edge-point value) and W (center-point value). Using these slopes, we can evaluate the equation for a line, $y=mx+b$, at $y=S(x_R^c)$ for the y-intercept b_R:

$$b_R = S_P^c - m_R x_P^c \tag{A4.3.4}$$

and $y=S(x_L^c)$ for the y-intercept b_L:

$$b_L = S_P^c - m_L x_P^c \tag{A4.3.5}$$

Using these y-intercepts b_L and b_R, we can again solve the equation for a line to calculate the wedge lengths L_{wedge} at the termini where the ice thickness goes to zero, where $y=0$. The length of the wedge on the right side of the divide is:

$$L_{wedge}^{R} = -(b_R / m_R) - x_w^c \tag{A4.3.6}$$

The length of the wedge on the left side of the divide is:

$$L_{wedge}^{L} = x_e^c + (b_L / m_L) \tag{A4.3.7}$$

A wedge is in steady-state when the ice flux entering the wedge from upstream at either $x=x_L^c$ or $x=x_R^c$ is removed by ablation on the wedge. The ice flux (in m^3 yr^{-1}) entering the domain is ablated over the area of the wedge (in m^2), defining an ablation rate (in m yr^{-1}). The ice flux entering the wedge is calculated dynamically using Equation A4.1.2.

To solve for ice-thickness and length changes within either wedge, we define the volume in the wedge at any timestep as

$$V = \frac{1}{2} h(x_w^c) L_{wedge} W_{wedge} \tag{A4.3.8}$$

where L_{wedge} is the wedge length given by Equation A4.3.6 or Equation A4.3.7, and W_{wedge} is the flowband width at the terminus. The change in volume of the wedge from time t to time $t+\Delta t$ can be defined by

$$\delta V = V(t+\Delta t) - V(t) = \delta V_{flux} - \delta V_{balance} \tag{A4.3.9}$$

where δV_{flux} is the change in volume due to changes in ice flux, and $\delta V_{balance}$ is the change in volume due to changes in accumulation or ablation (balance). This conservation equation must be satisfied in order to solve for ice thickness in the wedge at a future timestep $h(x_P^c,\ t+\Delta t)$. Since the change in volume due to changes in ice flux $\delta V_{flux} = V_{flux}(t+\Delta t) - V_{flux}(t)$ is a nonlinear function of the ice thickness $h(x_P,\ t+\Delta t)$ at the timestep $t+\Delta t$, we use an iterative scheme to find the correct values at a future timestep. The

estimate of ice thickness at $t+\Delta t$ used in the flux calculation to calculate ice thickness at $t+\Delta t$ is iteratively updated until the mass-conservation equation (Equation 4.1) is satisfied. In the conservation equation for the wedge (Equation A4.3.8), the total volume change δV is also a function of the wedge length L_{wedge} $(t+\Delta t)$, which is a function of the ice-surface elevation at the future timestep $S(x_L^c,\ t+\Delta t)$ and $S(x_R^c,\ t+\Delta t)$, which are the values we are solving for. We use a similar iterative scheme to that for the nonlinearity (Appendix I) to find the correct value of wedge length L_{wedge} $(t+\Delta t)$. In this formulation, if the ice flux entering the wedge does not equal the amount of ice lost by ablation, the terminus will advance or retreat.

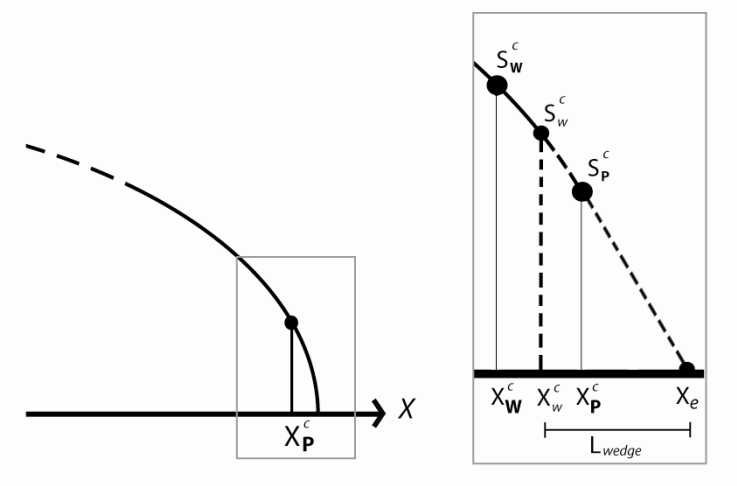

Figure A4.2 Sketch of wedge terminus in the full-domain model, for the right side of the ice divide (a similar wedge is emplaced on the left side of the divide). The full domain is cut off at a point that we call x_P^c at some distance before the actual terminus, at x_e. The terminus position at x_e is defined from the upstream slope between the cut-off point and next upstream finite-volume center point, in this case x_W^c. The wedge is highlighted with dashed lines, and extends from the last western finite-volume edge x_w^c to the last eastern finite-volume edge x_e, with a length L_{wedge}.

In our formulation, the wedge terminus is always represented by one grid cell at the end of the domain. While Lam and Dowdswell (1996) suggested that an adaptive-grid scheme could be used at the terminus in order to best represent ice-sheet behavior in the numerical model, we are solving for this full-domain model in response to small perturbations only, and therefore the simple regridding treatment presented here is adequate. However, this is a consideration when we use this full-domain model to validate the solution from our limited-domain model. In addition, before we can use the full-domain model to validate the limited-domain model, we check that the evolution of our full-domain model is similar to the evolution that is characteristic of an ice sheet with the same geometry and mass-balance distribution.

Jóhannesson and others (1989) characterized volume response timescales for ice masses in response to small perturbations, which are discussed further in Section 4.4.1 and Appendix F. Jóhannesson and others (1989) also showed that the evolution of ice volume in response to a step-change in mass balance is well approximated by the curve $(1-\exp(t/\tau_v))$, where $\tau_V = -H_{\max}/\dot{b}_{term}$ is the volume response time calculated from the maximum ice thickness $H_{\max}$ and the ablation rate at the terminus $\dot{b}_{term}$. Hooke (2005, pg. 373-374) showed that this exponential behavior can be derived from the kinematic-wave equation (Appendix F), and that it characterizes the response of a steady-state ice mass to a uniform, step change in accumulation as it approaches a new steady state. To validate our full-domain model, we compare the $(1-\exp(t/\tau_v))$ curve to the response of the full model.

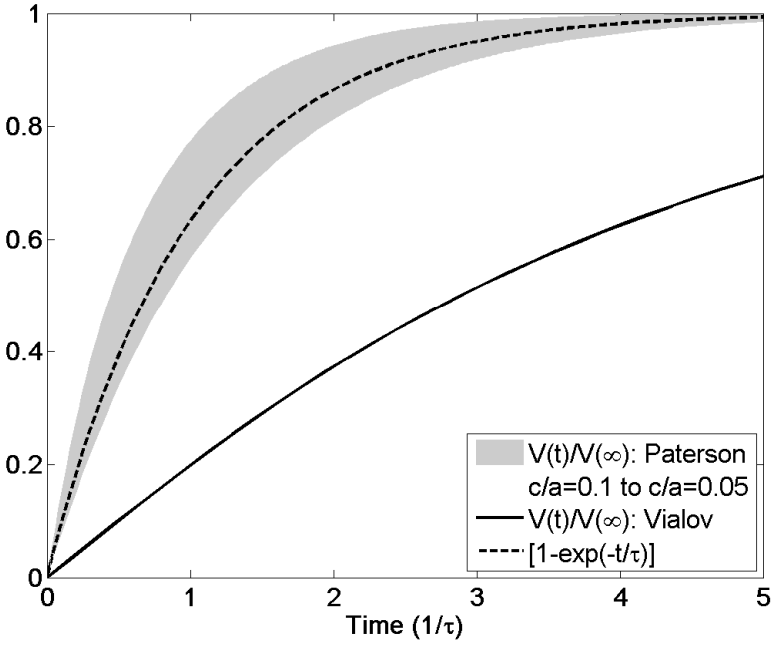

Figure A4.3 Ice-volume evolution *V(t)* in a full-domain model that has been extended from the limited model in Figure 4.2a using a Paterson (1972) model (gray band), or a Vialov (1958) model (solid line), compared to a theoretical expectation for long-term ice-volume evolution (dashed line, e.g Jóhannesson and others, 1989). The gray band shows the solutions for a Paterson model with a mass-balance ratio of c/a=0.1 to c/a=0.05; different mass-balance distributions influence the rate of ablation at the terminus. Time is given as a ratio of the volume response time $\tau = H_{\max} / \dot{b}_{term}$, where $H_{\max}$ is the maximum ice thickness and $\dot{b}_{term}$ is the ablation rate at the terminus.

We prefer to embed the limited domain in a Paterson-model surface profile, compared to a Vialov-model profile, because the Paterson model gives a magnitude of ablation at the terminus that is more physically realistic. The mass-balance distribution in a Paterson model determines the rate of ablation at the terminus, which influences the volume response time. We find that an ablation rate with a comparable order of magnitude to the accumulation rate results in ice-sheet evolution that best matches our

theoretical expectations (following e.g. Jóhannesson and others, 1989). Figure A4.3 shows the evolution of the geometry in Figure 4.2a in response to a step-change in accumulation, extended using both a Paterson (1972) model and a Vialov (1958) model. The evolution of ice volume for a full model with a Paterson extension, shown in Figure A4.3 with a gray band representing c/a in the range 0.05-0.1, gives a better fit to the $(1-\exp(t/\tau_v))$ curve. While embedding the limited domain in a Paterson model results in a more physical evolution of ice volume, both extensions conserve mass, allowing the limited domain to hold steady state and to return to the same steady state after a perturbation.

Chapter 5

A Method to Infer Transients in Accumulation Rate, Ice Thickness, and Ice Flow from Internal Layers

Ice-sheet internal layers preserve information about how the ice sheet responded to past spatial and temporal changes in accumulation rate, ice-sheet thickness, and ice flow, and present-day internal-layer shapes observed by radar are the most accessible remaining record of this past information. To infer transients in accumulation rate, ice-sheet thickness, and ice flow from the shapes of internal layers, we solve an inverse problem. We present a new algorithm to solve this inverse problem, and we address the capabilities of this new approach. While some details of the accumulation history and the ice-flow history can be recovered from an ice core, ice cores are temporal measurements that provide limited spatial information. However, the solution to this inverse problem is better constrained in combination with ice-core data. If internal layers are dated, for example by an intersecting ice core, then radar-observed internal layers provide both spatial and temporal information about accumulation rate, ice thickness, and ice flow.

5.1. Introduction

Internal layers of glaciers and of ice sheets have been imaged with ice-penetrating radar (e.g. Paren and Robin, 1975). Internal layers are assumed to be isochrones, horizons of constant age, and they have distinct chemical properties that cause a radar reflection. Each layer represents a past surface of a different age that has been subsequently buried by accumulation and also displaced and strained by ice flow. Ice-sheet internal layers preserve information about how the ice sheet responded to past spatial and temporal changes in accumulation rate and ice flow, and present-day internal-layer shapes are the most accessible remaining record of this past information. Deeper layers contain information from further in the past, making them highly valuable. However, deep layers have also likely been subjected to greater spatial and temporal gradients in strain rate, making them more difficult to decipher. To infer transients in ice flow, ice-sheet thickness, and accumulation rate from the shapes of radar-observed internal layers, we solve an inverse problem. While some details of these histories can be recovered from ice cores, ice cores represent conditions at only a single point. However, utilizing internal layers with our inverse approach is more robust in combination with ice-core data. In particular, if the internal layers are dated, for example by an intersecting ice core, then radar-observed internal layers provide both spatial and temporal information.

The spatial and temporal histories of ice-sheet flow and of accumulation are necessary to recreate ice-volume and sea-level histories. In addition, understanding large-scale evolution of ice sheets over long timescales is critical in order to properly interpret ice-core chemistry and to properly date an ice core, especially in portions of the core where annual-

layer counting is no longer reliable. For example, we can infer the accumulation rate at the location and time where each piece of ice in the ice core originated on the ice surface to convert chemical concentrations into fluxes from the atmosphere, or we can infer temporal changes in accumulation and ice thickness at one location on the surface to test general circulation model (GCM) simulations of past climate. These spatial and temporal histories are necessary to properly date an ice core with occluded gases because the difference between the age of the gas and the age of the ice at pore close off depends on accumulation rate (e.g. Sowers and others, 1989). Histories of accumulation and ice flow are imprinted upon internal-layer architecture, and we present an inverse approach to recover this information.

5.1.1. Previous work

Recent studies have advanced our understanding of the general relationships among internal-layer shape, accumulation, and ice flow (e.g. Parrenin and others, 2006; Hindmarsh and others, 2006; Parrenin and Hindmarsh, 2007; Leysinger-Vieli and others, 2007; Martin and others, 2009). Understanding the relationship between internal-layer shapes and ice-sheet history helps us to make appropriate assumptions when inferring information from the layers.

Incorporating internal-layer shapes as a constraint in ice-flow models is informative about ice-sheet history (e.g. Nereson and Raymond, 2001; Nereson and Waddington, 2002; Martin and others, 2006). In addition, numerous colleagues have inferred spatial patterns of accumulation directly from the shapes of internal layers (e.g. Pinglot and others, 2001; Spikes and others, 2004), and by using an ice-flow model (e.g. Morse and others, 1999;

Vaughan and others, 1999; Nereson and others, 2000; Fahnestock and others, 2001b; Baldwin and others, 2003; Siegert, 2003; Leysinger-Vieli and Gudmundsson, 2004; Siegert and Payne, 2004). For internal layers whose shapes have not been affected by spatial gradients in strain rate or in accumulation, the previous studies to infer accumulation rates from internal layers directly, or by using a 1-D vertical strain correction, have been successful. However, these assumptions cannot always be made.

Waddington and others (2007) presented a quantitative metric to define a "deep" internal layer, whose shape has been affected by spatial gradients in strain rate or accumulation rate; an internal layer that is shallow compared to the total ice thickness, can be deep in this context. As the depth to the layer increases to a larger fraction of the total ice thickness, accumulation-rate estimates based on depth variations alone, or that have been corrected using a 1-D flow model, are no longer appropriate. Waddington and others (2007) demonstrated that in most cases properly recovering information from deep layers is an inverse problem, in which 2-D ice flow must be incorporated to determine the correct histories of mass balance and ice dynamics; it is imperative to account for the cumulative vertical strain experienced by particles moving through the ice to map out deep internal layers.

Previous work by Waddington and others (2007), and corroborated by Steen-Larsen and others (In Press) with a different inverse approach, established that steady-state spatial patterns of accumulation can be inferred from the architecture of deep internal layers by solving an inverse problem. The next step is to use internal layers, and other available data, to infer spatial *and* temporal patterns of accumulation and ice flow. The time-dependent problem is especially relevant for inferring accumulation patterns from the deepest internal layers observed by radar, where a

steady-state assumption is no longer valid. As detailed images of the deepest internal layers are being collected (e.g. Laird and others, In Press), the ability to infer histories of accumulation and ice flow from these data is a mounting imperative. However, solving this time-dependent inverse problem is computationally intensive, and it is necessary to use a time-dependent ice-flow model and an inverse algorithm that are computationally fast. Chapter 4 showed how to reduce computation time in an ice-flow model by limiting the model domain to include only the relevant portions of the ice sheet. In addition, Waddington and others (2007) demonstrated that a gradient inverse method is an efficient and robust way to solve an inverse problem.

5.1.2. Solving an inverse problem

In an inverse problem, the existing data have resulted from a known process that depends on some unknown parameter values or boundary conditions that we wish to find. An inverse problem needs a forward algorithm and an inverse algorithm. Based on a guess of the unknown parameter values, the forward algorithm generates a realization of observable quantities. The inverse algorithm evaluates the fit of the modeled observables to the actual data, and assesses if any physical constraints imposed on the problem have been satisfied, in order to infer the best set of unknown parameter values. The same inverse problem could be solved with different forward algorithms and with different inverse algorithms, both of which could be developed with different assumptions. Any simplifications made in the forward algorithm, or constraints included as part of the inverse algorithm, must also be considered when interpreting the solution.

In the language of inverse theory, a problem that consists of a finite number of data points and a finite number of model parameters is called a *discrete* inverse problem (also called a parameter estimation problem); compared to a *continuous* inverse problem where the data and the model parameters are continuous functions (e.g. Aster and others, 2005, pg. 2). Continuous inverse problems can often be effectively discretized, which can make their solution more accessible. For a discrete and linear system, an inverse problem can be stated in a general algebraic form as

$$\mathbf{G}(\mathbf{p}) = \mathbf{G}\mathbf{p} = \mathbf{d} \tag{5.1}$$

where **G** is a matrix operator (e.g. a differential equation), **p** refers to the vector of model parameters, and **d** refers to the vector of data parameters. However, linear inverse problems can still be difficult to solve.

If the matrix **G** in Equation 5.1 is *rank deficient*, this means that there exists a nontrivial null space that can complicate finding a unique solution (e.g. Aster and others, 2005, pg. 233). For a *discrete ill-posed problem*, the singular-value decomposition (see Section A5.3) of **G** yields a singular-value spectrum that decays gradually to zero, the condition number (the ratio of the largest singular value to the smallest singular value) is large and finite, and the left and right singular vectors of **G** exhibit more variability (i.e. sign changes) as the index number i of G_i increases (e.g. Aster and others, 2005, pg. 73; Hansen, 1987). Our problem is a discrete ill-posed inverse problem, and therefore we focus on techniques to stabilize the inverse algorithm and find a unique solution. Most geophysical inverse problems are also ill-posed, and the techniques we discuss here are generally applicable.

Stabilization can be achieved through *regularization*. One way to regularize the problem is to use a coarser discretization to reduce the number of parameter values, or to utilize singular value decomposition

(SVD; e.g. Aster and others, 2005, pg. 55) and truncate the set of singular values. However, valuable information can also be lost in these stabilizing processes. In particular, it is difficult to determine at which point to truncate the singular values, especially if the singular-value set does not transition abruptly from nonzero to near-zero values (e.g. Menke, 1989, pg. 123). While a truncated SVD solution may still be necessary (e.g. Eisen, 2008), we rely primarily on stabilization through the commonly used damped least-squares solution procedure called *Tikhonov regularization*, which minimizes both prediction error and solution error (e.g. Aster and others, 2005, pg. 89; Section A5.3). We incorporate a priori information so that the solution that does not overfit noisy data.

5.1.3. Inverse problems in glaciology

The spatial scales of ice sheets, the timescales involved in their evolution, and the diffusive nature of ice flow creates a challenge for the glaciological community, which relies on measurable quantities to understand glaciological processes. Ice-flow models are powerful tools to predict ice-sheet behavior, but they require estimates of initial conditions and boundary conditions that are often largely unknown. In addition, desirable information about glaciers and ice sheets is often intensive or impossible to obtain. Therefore, inverse methods can be an ideal complement to use with ice-flow models and with data from glaciers and ice sheets (e.g. Truffer, 2004; Waddington and others, 2007; Eisen, 2008). In general, setting up an inverse problem is a powerful tactic to solve problems in solid-earth geophysics (e.g. Menke, 1989; Parker, 1994; Gubbins, 2004), and also in physical oceanography (e.g. Wunsch, 1996), among other fields. However, solving inverse problems is a relatively new frontier in glaciology.

As discussed by Aster and others (2005, pg. 11), issues regarding solution existence, solution uniqueness, and stability must be considered for every inverse problem; these issues are especially relevant to inverse problems in glaciology.

A well-known glaciological inverse problem is the inference of basal-ice velocity from surface-velocity measurements. This problem is an example of an *ill-posed* (or *ill-conditioned*) geophysical inverse problem. The degree of ill-posedness is defined by the degree to which a small change in a measurement value can result in a large change in the parameter values (e.g. Aster and others 2005, pg. 12; Hansen 1987). In addition, problems that do not have a definitive solution, for example because they are defined by an inexact model, are inexorably ill-posed (e.g. Wunsch 1996, pg. 11). Both of these types of ill-posedness can complicate stably finding a unique solution. With respect to the ill-posed basal-ice velocity inverse problem, different algorithms have been employed to successfully find an approximate solution. These have included a force-balance method (e.g. van der Veen and Whillans, 1989), a control method (e.g. Macayeal, 1993; Joughin and others, 2004b), an analytical power-series expansion (Bahr 1994), a gradient inverse method (Truffer, 2004), a transfer-function approach (Raymond and Gudmundsson, 2005), a Monte-Carlo method (Chandler and others, 2006), and an accelerated iterative scheme (Maxwell and others, 2008). These different algorithms have different advantages and disadvantages between accuracy, uniqueness, stability, and computation time, and the appropriate algorithm must be chosen based on the goal of solving the inverse problem. For example, the goal may be to analyze the statistics of possible solution sets, or to find a solution with the minimum structure required to fit the data.

We describe our forward and inverse algorithms to solve the inverse problem to infer ice-sheet and accumulation-rate histories from internal layers. Our forward algorithm describes the process of ice-sheet evolution and internal-layer structure. Our inverse algorithm is a gradient method that finds updates to the unknown parameter values by minimizing a performance index. The performance index is a number representing how well the predictions of observable quantities calculated by the forward algorithm match the data to an expected tolerance while, in this case, finding a spatially smooth accumulation pattern and a parameter set that is consistent with physically characteristic values of the parameters. Our goal in solving this inverse problem is to infer the smoothest set of model parameters that is required to explain the data. See Table 5.1 for a list of possible incorporated data values, and see Table 5.2 for a list of possible unknown model parameters in our problem.

5.2. Forward Algorithm

We describe our forward algorithm, which is a 2.5-dimensional thermomechanical ice-flow model used to make predictions of observable quantities, in particular the shapes of internal layers. At present, it is too computationally intensive to use a 3-dimensional ice-flow model and, for the problem that we aim to solve, this extra dimensionality adds unnecessary complexity. We desire a computationally efficient forward algorithm, so we utilize all numerical approximations and physical simplifications that are appropriate. For example, our model domain includes only a limited portion of the ice sheet (Chapter 4), and we use the Shallow Ice Approximation (SIA; e.g. Hutter, 1983, pg. 256-332; Paterson, 1994, pg. 262). In addition,

the ice-temperature distribution can be prescribed, or it can be thermomechanically coupled to the ice flow. The appropriate forward algorithm depends on the site conditions of each specific application, and the goal of solving the inverse problem.

Our forward algorithm solves for ice-sheet surface topography, an ice-velocity field, and an ice-temperature field, and integrates the velocity field to map out internal layers of a specified age. This algorithm generates realizations of all data values that may be incorporated as part of the inverse problem (see Table 5.1). Here we give a generic description of the governing equations for our 2.5-dimensional flowband model. In Section A5.1 we discuss specific assumptions that we make regarding the ice-velocity field, and in Section A5.2 we discuss specific initial conditions and boundary conditions that we use the applications of our algorithm.

5.2.1. Ice-surface evolution

Ice-thickness evolution is found by solving the mass-continuity equation (e.g. Paterson, 1994, pg. 256). In a flowband, this is given by

$$\frac{\partial h(x,t)}{\partial t} = -\frac{1}{W(x)}\left(\frac{\partial q(x,t)}{\partial x}\right) + \dot{b}(x,t) \tag{5.2}$$

where $h(x,t)$ is the ice thickness, $W(x)$ is the flowband width, $q(x,t)$ is the ice flux, and $\dot{b}(x,t)$ is the accumulation rate. The ice thickness $h(x,t) = S(x,t) - B(x)$, where $S(x,t)$ is the ice-surface elevation, and we assume that the bed topography $B(x)$ does not change in time. Any numerical scheme and any physical parameterizations may be invoked to solve this equation. However, the computational cost must be minimized when calculating ice-surface evolution as part of an inverse problem, especially for long calculation times, and for higher-resolution calculation domains.

We solve this conservation equation numerically using an implicit approach with a finite-volume numerical scheme (e.g. Patankar, 1980); details are given in Chapter 4. The calculation of ice-thickness evolution depends on the calculation of ice flux through the domain, which depends on the ice thickness and the surface slope. In a full-domain model, there is a zero-flux boundary condition at the terminus, and by knowing this boundary condition the ice thickness can be calculated everywhere. However, in a limited-domain model, the ice flux crossing the limited-domain boundaries is unknown. Improperly calculating the boundary flux can lead to numerically driven ice-sheet transients and unphysical ice-sheet behavior. Chapter 4 describes a new approach to efficiently calculate physically realistic ice-sheet evolution with a limited domain. We do this by characterizing the behavior of a full ice sheet using impulse-response functions, and we use these response functions to calculate actual flux transients at the boundaries of our limited domain.

5.2.2. Kinematic and dynamic descriptions of flow

By integrating Equation 5.2 from the boundary at x_0 where ice flux is specified to the end of the domain x_{end}, the ice flux can be represented kinematically by

$$q(x,t) = Q_0(t) + \int_{x_0}^{x_{end}} (\dot{b}(\chi,t) - \dot{h}(\chi,t) - \dot{m}(\chi,t))W(\chi)d\chi\,, \qquad (5.3)$$

where $Q_0(t)$ is the time variation of ice flux entering at one end of the flowband domain, $\dot{h}(x,t)$ is the rate of change in ice thickness, and $\dot{m}(x,t)$ is the melt rate. Dynamically, the flux of ice passing through a cross-sectional area $W(x)\times h(x,t)$ at any point x and at any time t, is related to the depth-averaged horizontal velocity $\bar{u}(x,t)$ in that cross-section by

$$q(x,t) = W(x)\int_{B(x)}^{S(x,t)} u(x,\zeta,t)\,d\zeta = W(x)h(x,t)\bar{u}(x,t)\,. \tag{5.4}$$

We represent depth z through $\hat{z}$, a non-dimensional height above the bed,

$$\hat{z} = \frac{z - B(x)}{S(x,t) - B(x)} \tag{5.5}$$

For flexibility, we represent the horizontal velocity $u(x,\hat{z},t)$ in terms of the depth-averaged horizontal velocity $\bar{u}(x,\hat{z},t)$, and a non-dimensional function as

$$u(x,\hat{z},t) = \bar{u}(x,t)\phi(x,\hat{z},t) \tag{5.6}$$

where $\phi(x,\hat{z},t)$ is called the horizontal-velocity shape function. In a flowband, the strain rate transverse to the direction of flow is

$$\frac{\partial v(x,\hat{z},t)}{\partial y} = \frac{1}{W(x)}\frac{dW}{dx}u(x,\hat{z},t) \tag{5.7}$$

The vertical velocity then follows from incompressibility (e.g. Paterson 1994, pg. 255)

$$\frac{\partial w}{\partial z} = -\left(\frac{\partial u}{\partial x} + \frac{\partial v}{\partial y}\right) \tag{5.8}$$

Integrating Equation 5.8 over depth z, gives an expression for the vertical-velocity field

$$\begin{aligned} w(x,\hat{z},t) = &-\left(\dot{b}(x,t) - \dot{h}(x,t)\right)\psi(x,\hat{z},t) \\ &+ u(x,\hat{z},t)\left((1-\hat{z})\frac{dB}{dx} + \hat{z}\frac{dS}{dx}\right) \\ &- \bar{u}(x,\hat{z},t)h(x,t)\int_0^{\hat{z}} \frac{\partial\phi(x,\hat{\zeta},t)}{\partial x}\,d\hat{\zeta} \end{aligned} \tag{5.9}$$

where $\psi(x,\hat{z},t)$ is called the vertical-velocity shape function, and is defined as

$$\psi(x,\hat{z},t) = \int_0^{\hat{z}} \phi(x,\hat{\zeta},t)\,d\hat{\zeta} \tag{5.10}$$

The horizontal-velocity shape function and the vertical-velocity shape function $\psi(x,\hat{z},t)$ are defined according to the depiction of ice dynamics used in each specific application of this algorithm. For example, in Section A5.1 we define horizontal-velocity shape functions using the Shallow Ice Approximation (SIA), and using a shape-function parameterization for divide flow from Nereson and Waddington (2002).

5.2.3. Constitutive relationship

The constitutive relationship for ice flow describes the specific mechanical relationship between strain rate and applied stress in ice. The commonly used flow law (Glen, 1955; Paterson 1994, pg. 259) relates deviatoric stress and strain rate, assuming that ice is incompressible and that the ice-crystal distribution is isotropic. This so-called Glen's law is

$$\dot{\varepsilon}_{ij} = A(T)\tau_{eff}^{n-1}\tau_{ij} \tag{5.11}$$

where strain rate $\dot{\varepsilon}_{ij}$ and applied stress τ_{ij} are tensors where i and j can have values from 1 to 3, τ_{eff} is the effective shear stress, n is the flow-law exponent, and $A(T)$ is the temperature-dependent ice-softness parameter. The individual components of the strain-rate tensor are given by

$$\dot{\varepsilon}_{ij} = \frac{1}{2}\left(\frac{\partial u_i}{\partial x_j} + \frac{\partial u_j}{\partial x_i}\right) \tag{5.12}$$

where u_i and u_j are different components of the velocity field in different directions x_i and x_j. The flow law exponent n=3 for dislocation creep (e.g. Paterson, 1994, pg. 85). The temperature-dependent ice-softness parameter (in $Pa^{-n}\ yr^{-1}$; e.g. Paterson 1994, pg. 86) follows an Arrhenius relationship, given by

$$A(T(x,\hat{z},t)) = A_0 \exp(-Q/RT(x,\hat{z},t)) \tag{5.13}$$

where A_0 is the temperature-independent ice-softness parameter (see e.g. Paterson 1994, pg. 97), Q is the activation energy for creep, and R is the universal gas constant.

5.2.4. Thermomechanical flow calculation

The ice-temperature field $T(x, \hat{z}, t)$ can be prescribed, or calculated independently of the ice-flow field. However, in reality the thermodynamics and the mechanics of ice flow are coupled because ice-viscosity is temperature dependent, and the contribution of advection to the ice-temperature field depends on the ice-flow field (e.g. Paterson, 1994, pg. 216; Hooke, 2005, pg. 303). Conservation of energy is given by

$$\frac{\partial T}{\partial t} = -u_i \frac{\partial T}{\partial x_i} + \frac{1}{\rho c} \frac{\partial}{\partial x_i} \left(k \frac{\partial T}{\partial x_i} \right) + \frac{\sigma_{ij} \dot{\varepsilon}_{ij}}{\rho c} \tag{5.14}$$

where T is temperature, t is time, u_i is the component of velocity in the x_i direction, ρ is density, c is specific heat capacity, k is thermal conductivity, σ_{ij} is the stress-tensor component in the ij direction, and $\dot{\varepsilon}_{ij}$ is the strain-rate tensor component in the ij direction. Specific heat capacity c and thermal conductivity k are a function of temperature, we follow the formulations given by Paterson (1994, pg. 205).

In a numerical model of thermomechanical ice flow, the mechanical calculation requires an estimate of the thermal field, and iterative updates to these coupled fields are calculated in order to find an ice-temperature and an ice-sheet evolution that are thermally and mechanically consistent; here we follow the standard iterative approach to couple our thermal and mechanical models (e.g. Van der Veen, 1999, pg. 231; Hooke 2005, pg. 303). At each timestep t_i in the numerical model for ice-surface evolution, an ice-temperature field $T_i^0(x, \hat{z}, t)$ is estimated, and the ice-surface topography

$S_i^0(x,t)$ and the ice-flow field $\boldsymbol{u}_i^0(x,\hat{z},t)$ are calculated. Then, an ice-temperature field $T_i^1(x,\hat{z},t)$ is calculated using this ice-surface topography $S_i^0(x,t)$ and this ice-flow field $\boldsymbol{u}_i^0(x,\hat{z},t)$. Unless the temperature distribution is well-known at the first iteration, the difference between $T_i^0(x,\hat{z},t)$ and $T_i^1(x,\hat{z},t)$ will be significant, so that when $T_i^1(x,\hat{z},t)$ is used to recalculate the ice-surface topography $S_i^1(x,\hat{z},t)$ and the ice-flow field $\boldsymbol{u}_i^1(x,\hat{z},t)$, these fields will be different from their values in the first iteration. The ice-temperature field, the ice-surface topography, and the ice-flow field are iteratively updated until the difference in the temperature field $(T_i^j(x,\hat{z},t) - T_i^{j-1}(x,\hat{z},t))$ between iteration j and iteration *j-1* becomes small; we choose a temperature difference threshold of 10^{-6} °C. See Figure K1 for a flowchart depiction of this iterative process.

Our model of thermomechanically-coupled flow uses a finite-volume thermal calculation from Price and others (2007). If thermomechanical coupling is not utilized, the ice temperature can be isothermal at a prescribed ice temperature, or temperature variations with depth can be calculated using Fourier's Law describing the linear relationship between a prescribed surface temperature and a prescribed geothermal flux (e.g. Van der Veen 1999, pg. 178). If the ice-temperature field is not isothermal, an effective isothermal ice-softness parameter $\tilde{A}(T(x,t))$ is calculated (see Section A5.1) for use in the ice-flow calculations.

5.2.5. Internal-layer calculation

To generate internal layers, we track particles through time by integrating the velocity field. Each particle starts at the surface $S(x_i)$ at time $t=t_0$, and the position of each particle i can be given by the material derivative

$$\frac{dx_i}{dt} = u\big(x_i(t), z_i(t)\big), \qquad \frac{dz_i}{dt} = w\big(x_i(t), z_i(t)\big) \tag{5.15}$$

where u is the horizontal velocity and w is the vertical velocity, and (x,z) are the particle position and particle depth at any time t. The coupled differential equations given by Equation 5.15 are integrated numerically. A layer of any given age is constructed by joining the endpoints of particle paths at the time equal to the age of the layer.

Table 5.1. Possible set of incorporated data values

Data value	Size	Symbol
Internal-layer shapes	$N_{layers} \times N_h$	$h_d(x,z)$
Modern ice-surface topography	N_S	$S(x,t_0)$
Modern accumulation rate	$N_{\dot{b}}$	$\dot{b}(x,t_0)$
Modern surface velocity	N_u	$u(x,t_0)$

Table 5.2. Possible set of unknown model parameters

Model parameter	Size	Symbol
Accumulation-rate history	$N_t \times N_x$	$\dot{b}(x,t)$
External-flux history	$N_t \times [\, N_x{}^1 \, N_x{}^{end} \,]$	$Q_{ext}(x,t)$
Ice flux entering the domain at initial timestep	1	Q_0^{in}
Ice thickness at first spatial node at initial timestep	1	S_0^{in}
Temperature-independent ice-softness parameter	1	A_0
Average geothermal flux	1	Q_{geo}

5.3. Inverse Algorithm

The inverse algorithm used here is a gradient (steepest-descent) solver that uses Tikhonov regularization to stabilize the algorithm and to find a physically meaningful solution. This inverse algorithm follows Waddington and others (2007), where they solved a steady-state version of this inverse problem, to infer a steady-state accumulation pattern from an internal layer. A gradient solver is well-suited for our transient problem because it is computationally fast and it is designed to converge upon a single, though robust, solution (e.g. Parker, 1994; Aster and others, 2005). This algorithm performs a local search for the most-likely solution by finding the minimum of I_p in the model space that is most accessible from the initial guess of the parameter set. While this steepest-descent approach locates only one solution, and that solution may be only a local minimum, we can start from multiple initial guesses of the parameter set to search other parts of the model space. The steady-state results from Waddington and others (2007) using a gradient inverse algorithm were corroborated by Steen-Larsen and others (In Press) using a Monte Carlo inverse algorithm that performed a complete search of the model space; the results of these previous studies give us confidence that this inverse algorithm is appropriate to solve this problem.

5.3.1. Regularization

Regularization is a way to stabilize ill-posed inverse problems, where a relatively insignificant change in the measurement can lead to a significant change in the solution (e.g. Aster and others 2005, pg. 73; Hansen 1987). In an inverse problem, the observable quantities (e.g.

internal layers) may not contain enough information to discriminate against solutions (e.g. the spatial and temporal history of accumulation rate) that are physically unreasonable on other grounds. In addition, because the observations contain errors, we do not want to fit these data exactly; a solution found by minimizing only the mismatch between the data and the forward-algorithm prediction could overfit the data (e.g. Parker, 1994).

The solution to an inverse problem is a "model", i.e. a vector of the model parameters (e.g. mass-balance rate at discrete points) that we seek. The model parameter set is size N_p number of parameters, and all spatial and temporal parameters are defined at discrete points. It is desirable to find a solution (set of model parameters) that minimizes a combination of prediction error and length of the solution vector. Generally speaking, this can be described by minimizing a performance index I_p given by

$$I_p = \|\mathbf{p}\|^2 + v\|\mathbf{d}\|^2 \tag{5.16}$$

where $\|\mathbf{p}\|^2$ is the squared model norm (see Section 5.3.4), and $\|\mathbf{d}\|^2$ is the squared data norm (see Section 5.3.5). The factor v is a positive trade-off parameter, where the best value of v gives an appropriate balance between fitting the data (minimizing the prediction error), and finding a smooth model (minimizing the solution length). In this case, the underdetermined part of the problem has been damped, and the solution to this problem is called a *damped least squares solution*; this approach is also referred to as *Tikhonov regularization* (e.g. Aster and others, 2005).

As discussed in Section 5.3.1, to minimize the solution error we chose a model norm $\|\mathbf{p}\|$ that minimizes the roughness of model parameters that occur in a spatial sequence (i.e. the accumulation-rate pattern at any time), and/or in a temporal sequence (i.e. the accumulation-rate history at any point), and that minimizes the variation in model parameters from estimations of their given characteristic values within a given tolerance.

However, the data have uncertainties, and we do not want to strictly minimize the prediction error. Obtaining a smooth model that fits the data at an expected tolerance can be achieved by minimizing a performance index I_p given by

$$I_p = \|\mathbf{p}\|^2 + v(\|\mathbf{d}\|^2 - T^2) \tag{5.17}$$

where T is a defined tolerance, which is commonly assumed to be based on the statistical uncertainties N of the number of data (Parker, 1994, pg. 124),

$$T \sim N_d^{1/2}\left[1 - \frac{1}{4N_d} + \frac{1}{32N_d^2} + O(N_d^{-3})\right] \tag{5.18}$$

We want to find the vector of model parameters p and the value of the trade-off parameter v that minimize the performance index in Equation 5.17. The N_p+1 number of equations,

$$\frac{\partial I_p}{\partial m_j} = 0 \qquad \frac{\partial I_p}{\partial v} = 0 \tag{5.19}$$

can be solved simultaneously, where p_j represents each model parameter in the set. In this case, the trade-off parameter v is a Lagrange multiplier (e.g. Menke, 1989, pg. 56; Aster and others, 2005, pg. 276). The solution will minimize the model norm $\|\mathbf{p}\|$, and satisfy the data-mismatch criterion,

$$\|\mathbf{d}\|^2 - T^2 = 0 \tag{5.20}$$

where the appropriate value of v sets the most appropriate trade-off between smoothness and fit. A smaller value of v puts more emphasis on a smooth model, whereas a larger value of v puts more emphasis on closely fit data (Parker, 1994). We follow the solution procedure used by Waddington and others (2007); details are given in Section A5.3.

5.3.2. Linearized problem

In a nonlinear inverse problem, the forward algorithm predictions of the observable quantities are nonlinear functions of the model parameters. Our problem is nonlinear because estimates of internal layers are nonlinear functions of the accumulation-rate history and our other parameter values; this can be seen more explicitly in the analytical expressions given in Appendix N. A nonlinear problem is not as straightforward to solve as a linear problem, but we address this problem by assuming that values of the unknown parameters can be approximated by a linear expansion in the vicinity of their trial values; this is how we linearize the problem. Instead of solving for the unknown parameter values p directly (as in Equation 5.1), corrections $\Delta\mathbf{p} = \mathbf{p} - \mathbf{p}^{est}$ to trial values of the unknown parameters $\mathbf{p}^{est}$ are found (e.g. Menke 1989, pg. 152). In a linear problem,

$$\mathbf{G}(\mathbf{p}) \approx \mathbf{G}(\mathbf{p}^{est}) + \mathbf{G}(\mathbf{p} - \mathbf{p}^{est}) . \tag{5.21}$$

Using this form of **G**(**p**) in Equation 5.1, gives

$$\mathbf{G}(\Delta\mathbf{p}_{n+1}) = \mathbf{d} - \mathbf{G}(\mathbf{p}^{est}) . \tag{5.22}$$

In a linearized problem, matrix **G** is a Jacobian matrix, expressing how changes in each model parameter p_j affect the value of each modeled observable o_i^m,

$$G_{ij} = \left.\frac{\partial G_i}{\partial p_j}\right|_{p_j = p_j^{est}} \tag{5.23}$$

In Equation 5.22, $\mathbf{d} - \mathbf{G}(\mathbf{p}^{est})$ are the residuals between the actual data values **d** and the model estimates of the data values calculated using the estimate of the model parameters $\mathbf{p}^{est}$. Each parameter value p_j^n is guessed at the first iteration n, and then is iteratively adjusted by finding Δp_{n+1}^j that

further minimizes the performance index (Equation 5.17). The updated parameter set is given by

$$p_{n+1}^{j} = p_{n}^{j} + \Delta p_{n+1}^{j} \tag{5.24}$$

For any given value of the trade-off parameter v, this iterative procedure is stopped (i.e. a solution is found) when adjustments to the model parameters Δp_{n+1}^{j} from one iteration to the next iteration insignificantly change the value of the performance index (i.e. do not further reduce the value to zero). This cutoff criterion is preferable to simply stopping the iterative procedure when the parameter changes become small (e.g. Gubbins 2004, pg. 131). Once we have a converged solution for one value of v, we repeat the solution procedure for different values of v, and find the solution corresponding to the value of v that satisfies the data-mismatch criterion (Equation 5.20).

In a linearized ill-posed problem, instability in the solution procedure means that the solution will not converge; changes in the performance index between iterations for a given value of v do not stably approach the cutoff criterion. Stabilization techniques for linearized ill-posed inverse problems are the same as the techniques for linear ill-posed problems (e.g. Tikhonov regularization). However, regularization of a linear problem damps the underdeterminancy of the problem by directly minimizing the prediction error and the solution error, whereas regularization of a nonlinear problem damps the iteratively calculated parameter-value updates Δp_{n+1}^{j} by minimizing the prediction error and solution error (e.g. Gubbins 2004, pg. 131). If Tikhonov regularization alone does not stabilize the problem, the singular values can also be truncated if there is a natural break in distribution between larger and smaller values (e.g. Eisen 2008).

Due to the nonlinearity of this problem, both in the forward algorithm and in the inverse algorithm, several iteration loops must be performed in order to calculate the final set of model parameters, which is the solution to

the inverse problem. The outermost loop of the inverse problem is to find the value of the trade-off parameter v; a full solution must be found for each sampled value of the trade-off parameter, and we seek the trade-off parameter that satisfies the data-mismatch criterion in Equation 5.20. Since the nonlinear inverse problem has been linearized to solve for changes in the parameter values Δp_{n+1}^{j}, rather than the parameter values directly, the next loop iterates until further changes in the parameter values insignificantly change the value of the performance index. In the forward algorithm, an iteration is required on the nonlinearity in the implicit solution for the ice-surface evolution $S(x,t)$. If the forward algorithm is thermomechanically coupled, there is an additional iteration to find a consistent thermal and mechanical solution in the forward algorithm. See Appendix K for flowcharts of all calculations in the forward and inverse algorithms.

5.3.3. Model parameters

In an inverse problem, the unknown model parameters are the set of unknown values that are required in the forward algorithm. For example, unknown initial conditions or boundary conditions are part of the parameter set. Generally speaking for this problem, the model parameter set could include the ice flux entering the domain at the initial timestep $Q_{in}(t_0)$, the ice flux across the limited domain due to forcing from outside of the domain $Q_{ext}(t)$, the piecewise bilinear spatial and temporal pattern of accumulation rate $\dot{b}(x,t)$, the spatial and temporal pattern of basal melt rate $\dot{m}(x,t)$, the ice-surface elevation at one location at the initial timestep $S_{in}(t_0)$, the temperature-independent ice-softness parameter A_0, and the spatial and temporal variation in geothermal flux $Q_{geo}(x,t)$. The values that must be

included in the model parameter set will depend on which values are unknown at each site where this inverse problem is being solved. Any of these parameters can be excluded from the set of model parameters if they are known and can be prescribed, or if they are not necessary in the forward calculation.

5.3.4. Model norm

In this inverse problem to infer histories of accumulation, ice thickness, and ice flow from internal layers (introducted in Section 5.1), we expect the accumulation-rate solution $\dot{b}(x,t)$ to be spatially smooth, so we chose the model norm $\|p\|$ to be the curvature of the accumulation-rate solution integrated along the flow band (i.e. the roughness of the accumulation-rate solution). Other model norms could be used in this problem, and we discuss possibilities in Section 5.6.4.

The accumulation history $\dot{b}(x,t)$ is piecewise bilinear, and the second derivative is zero everywhere except the (x_j, t_j) nodes, where it can be infinite. For this reason, following Waddington and others (2007), we estimate roughness by attributing a uniform curvature to each x-interval that joins the midpoints of the two linear segments upstream (x_{j+1}, t_j) and downstream (x_{j-1}, t_j) from the position (x_j, t_j). We calculate curvature based on these values in the vicinity of each point (x_j, t_j) using a centered-difference approximation for the derivative,

$$c_j = c(\hat{x}_j, t) = \frac{dm(\hat{x}_j, t)}{d\hat{x}_j} = 2\left(\frac{m_{j+1}(t) - m_{j-1}(t)}{\hat{x}_{j+1} - \hat{x}_{j-1}} \right) \tag{5.25}$$

where $\hat{x}_j$ is the normalized position, and $\hat{x}_j = x_j / L_c$, where L_c is a characteristic length scale. The upstream surface slope is given by a backward difference,

$$m_{j-1}(t) = \frac{L_c}{\dot{b}_c}\left(\frac{b_j(t) - b_{j-1}(t)}{\hat{x}_j - \hat{x}_{j-1}}\right) \tag{5.26}$$

where L_c is the characteristic length scale, and $\dot{b}_c$ is the characteristic accumulation rate that are used to normalize the slope. The downstream surface slope is given by a forward difference,

$$m_{j+1}(t) = \frac{L_c}{\dot{b}_c}\left(\frac{b_{j+1}(t) - b_j(t)}{\hat{x}_{j+1} - \hat{x}_j}\right) \tag{5.27}$$

Equations 5.25, 5.26, and 5.27 give the non-dimensional curvature in the j^{th} spatial interval as

$$c_j = 2\frac{L_c^2}{\dot{b}_c}\frac{1}{\Delta\hat{x}_j}\left[\frac{\dot{b}_{j+1}}{\Delta\hat{x}_{j+1}} + \frac{\dot{b}_{j-1}}{\Delta\hat{x}_{j-1}} - \frac{\dot{b}_j}{(\Delta\hat{x}_{j+1} + \Delta\hat{x}_{j-1})}\right] \tag{5.28}$$

At the spatial edges of the domain, where Equation 5.28 is undefined, we minimize the difference between the slope at each edge of the domain and the slope of the adjacent value within the domain.

The model norm should include contributions from all model parameters p_j. So, for model parameters that do not fall in a spatial sequence, we incorporate deviations of the estimates of these parameters from a given characteristic value, within a given tolerance. For any parameter p_j that is not accumulation rate,

$$c_j = \frac{p_j^c - p_j}{\delta p_j^c} \tag{5.29}$$

where p_j^c is an estimate of the characteristic value of the parameter, and δp_j^c is the characteristic acceptable deviation in this estimate. The model norm used in Equation 5.17 is then given by,

$$\|p\|^2 = \sum_{j=1}^{N_p} (w_j^c)^2 c_j{}^2 \tag{5.30}$$

where $(w_j^c)^2$ are positive non-dimensional weights corresponding to each type of model parameter. If the model parameter is a value of accumulation rate, the weight w_j is the length over which each segment is integrated Δx_j divided by the average segment distance $\overline{\Delta x}$.

5.3.5. Data norm

The squared data norm $\|d\|^2$ is the sum of squared mismatches between the observations o_i^d, and the forward-algorithm predictions of the same observable quantities o_i^m, normalized by the standard deviations σ_i^d of the data. The data norm used in Equation 5.17 is then given by,

$$\|d\|^2 = \sum_{i=1}^{N_d} \left[\frac{(o_i{}^m - o_i{}^d)}{\sigma_i{}^d} \right]^2 \tag{5.31}$$

The data norm includes residuals between all existing data and their corresponding predictions from the forward algorithm, where N_d is the number of data values. In this problem, the primary data are the shapes of internal layers imaged with ice-penetrating radar. Additional data may include the modern ice-surface topography, the modern ice-surface velocity, or the modern accumulation-rate (see Table 5.1). These modern data provide rate control, and it is important that these data are available. While internal-layer shapes at all depths directly provide valuable spatial information, these layers must be dated by an intersecting ice core to provide accurate temporal information. Accurate dating is especially important when inferring information from deeper layers, where present-day rate control is a less-effective constraint on the problem. The amount

and types of data included in the problem depend on site-specific data availability.

5.4. Results with synthetic data

To assess the capability of our new algorithm to infer histories of accumulation rate and ice flow, we first solve the inverse problem using synthetic data. We generate synthetic data by prescribing parameter values, we perturb the data with red noise, and then we try to infer the original parameter values using this synthetic data set. While this is a simple test, especially because the forward algorithm used to estimate the data is the same algorithm that we used to generate the data. However, the procedure allows us to explore the sensitivity of our algorithm. Comparing the inferred parameter values to the known parameter values shows how well we can recover each parameter value for a given test.

In the three tests performed here (see Sections 5.4.2-5.4.4), we assume that the layer ages are known (e.g. from an ice core). Figure 5.1a illustrates the site conditions used in our synthetic tests. The ice thickness, bed topography, and magnitude of accumulation are similar to values near the West Antarctic Ice Sheet (WAIS) Western Divide (e.g. Neumann and others, 2008; Conway and Rasmussen, 2009). We assume that the ice temperature does not change in time (i.e. there is no thermomechanical coupling), but that temperature variations with depth are prescribed as the present-day values calculated by Neumann and others (2008) for WAIS Divide, with a geothermal flux of 70 mW m^{-2} (Figure 5.1b).

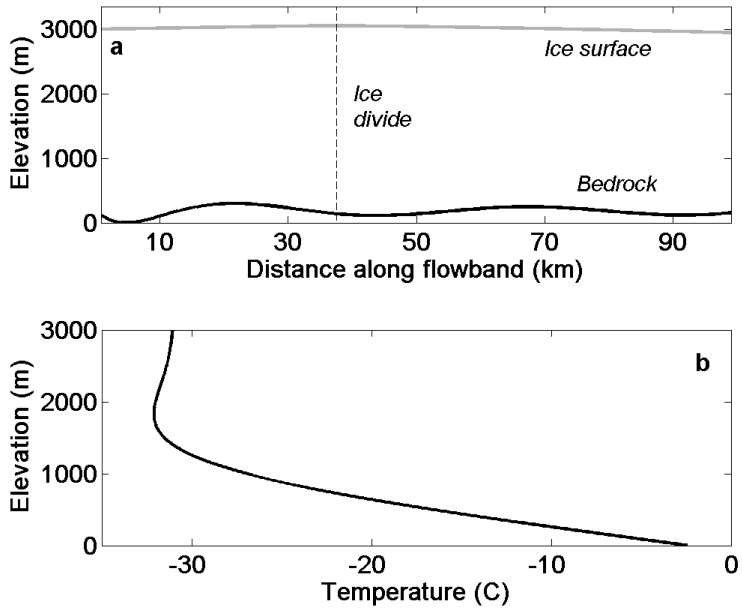

Figure 5.1. **a)** Synthetic geometry of a site analogous to the West Antarctic Ice Sheet (WAIS) Divide. **b)** Temperature with depth profile for this synthetic site; these values are comparable to modeled values for present-day WAIS Divide from Neumann and others (2008).

We represent the accumulation rate in space and time as a piecewise bilinear function. Our spatial and temporal parameter grid is lower resolution than our spatial and temporal calculation grid. For example, Figure 5.2a shows the parameter grid at Δx=1500 m and Δt=2000 years, and Figure 5.2b shows the calculation grid at Δx=900 m and Δt=200 years. The accumulation-rate solution on the parameter grid is interpolated onto the higher-resolution grid for ice-surface, ice-temperature, and ice-velocity calculations.

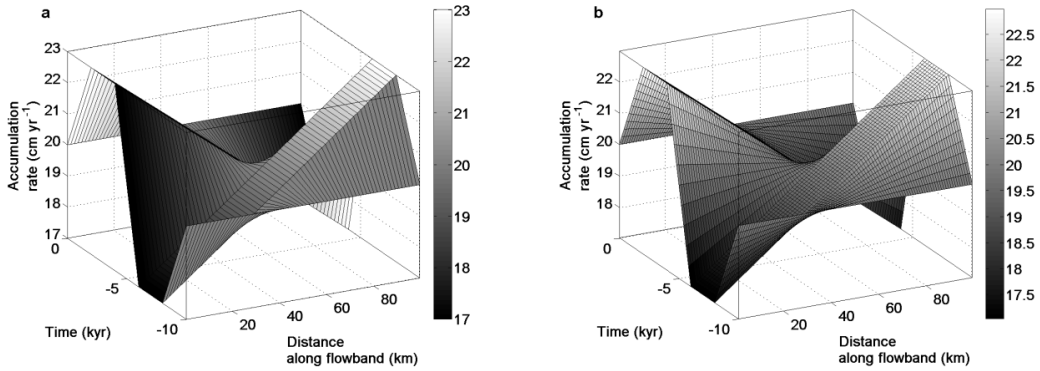

Figure 5.2. Accumulation rate as a piecewise bilinear function of space and time on **a)** the parameter grid with Δt= 2000 yr and Δx=1500 m, and **b)** the calculation grid with Δt= 200 yr and Δx=900 m. The accumulation-rate history is inferred on a coarser grid, and interpolated to a finer grid for calculations with the forward algorithm.

5.4.1. Imprint of ice-sheet transients on internal layers

The primary data for our inverse problem are the shapes and locations of internal layers. If we are to recover realistic histories of accumulation rate and of ice flow, these histories must have left a distinct imprint on the internal-layer architecture. We perform synthetic tests with two different accumulation-rate histories. One history has only a change in the accumulation rate, and one history has only a change in external-flux forcing, but they both drive a similar history of divide migration. Figure 5.3 shows internal layers generated with these two different histories. Layers shown with a solid line were generated by an accumulation history that varies linearly in time across the ice divide. Layers shown with a dashed line were generated by an accumulation history that is uniform over all time, but has prescribed external-flux changes that force the same history of divide migration exhibited by the linearly varying accumulation history. The deepest layer shown in Figure 5.3 is 10 kyr.

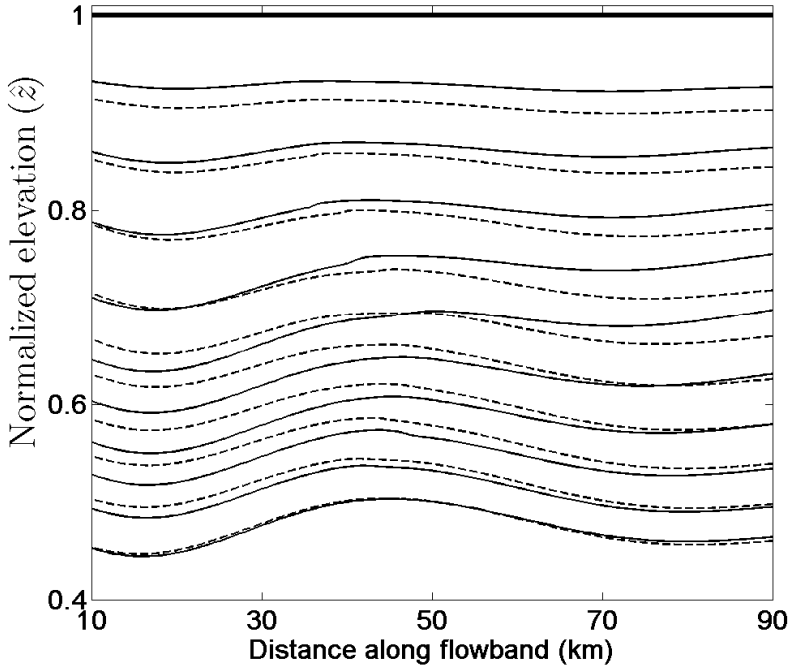

Figure 5.3. Internal-layer shapes for two different accumulation-rate and ice-flow histories. The solid lines are layers generated with a mass-balance history that varies linearly in time, with no external-flux forcing. The dashed lines are layers generated with a mass-balance history that is uniform in space and time, but divide-migration is driven by variations in external-flux forcing. The layers span 10 kyr and are separated by 1 kyr in age.

5.4.2. Spatial and temporal variation in accumulation

In the first test, we generate synthetic internal-layer data, ice-surface velocity data, and accumulation-rate data using an accumulation history that varies linearly over time, with no variation in external-flux forcing; there is no change in $Q_{ext}(t)$, but there are changes in the flux on the left side of the limited domain $Q_L(t)$ and on the right side of the domain $Q_R(t)$ due to local accumulation-rate changes. These synthetic data are used to solve the

inverse problem for these known histories of accumulation and ice flow, and Figure 5.4 shows the results of this test.

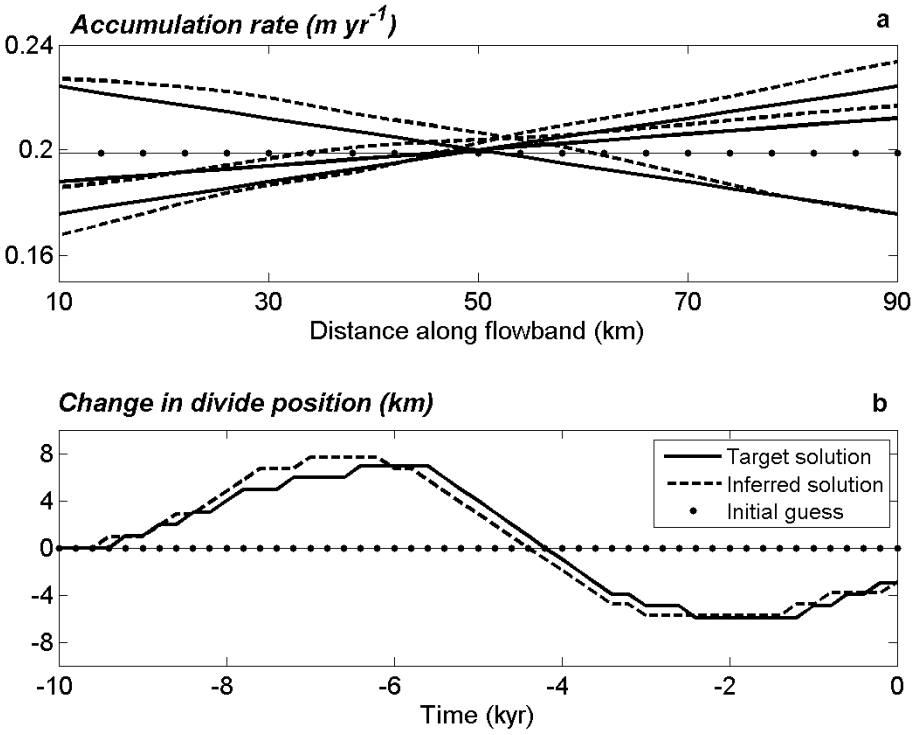

Figure 5.4. Solid lines represent the target solution, dashed lines represent the solution inferred by solving the inverse problem, and dotted lines represent the initial guess. **a)** The accumulation rate at three times (-9 kyr, -6 kyr, -4 kyr). **b)** The change in ice-divide position associated with this accumulation forcing.

The inferred history of accumulation well approximates the target history, and this provides a history of divide migration that also well approximates the target history. We initially guessed that there were no variations in external flux, and we imposed a constraint to seek a solution with minimum external-flux variability. Since the data could be fit and the constraints

could be satisfied without external-flux variations, we found a solution that properly attributed divide migration to accumulation-rate variations.

5.4.3. Temporal variation in external-flux forcing

While variations in the spatial pattern of accumulation can drive divide migration, we expect that externally forced changes in ice flux will be the primary control on longer-term variations in ice-divide position. For example, Conway and Rasmussen (2009) found that the present-day WAIS Western Divide is undergoing dynamically forced migration toward the Ross Sea. Ice sheets can experience significant changes in ice flux at their margins, especially if the ice-sheet margins are marine based. This has occurred most notably at glacial-interglacial transitions, and in particular from the last glacial maximum to the present, when sea-level was more than 100 meters lower than it is today (e.g. Lambeck and Chappell, 2001). Ice-divide position is influenced by changes in margin geometry that can affect flow at the center of the ice sheet, and also by changes in ice-stream activity.

In the second test, we generate synthetic internal-layer data, ice-surface velocity data, and accumulation-rate data using an accumulation history that does not vary in space or time, but does have variations in external flux. These synthetic data are used to solve the inverse problem for these known histories of accumulation and ice flow, and Figure 5.5 shows the results of this test. We start from an initial guess with no flux variation, but set a high tolerance on our initial guess so that the external-flux history can vary if dictated by the data. Figure 5.5 shows that the imprint of external flux on internal-layer shapes is distinct enough that we can recover changes in divide position when these layer shapes are used in

an inverse problem. However, divide migration can be attributed to local accumulation-rate variations, or to external-flux variations. If the data do not provide enough information to properly attribute divide migration to the correct forcing, we must use constraints to find the best history that can reproduce the data. In the results shown in Figure 5.5, we used a constraint that the accumulation rate should be spatially smooth.

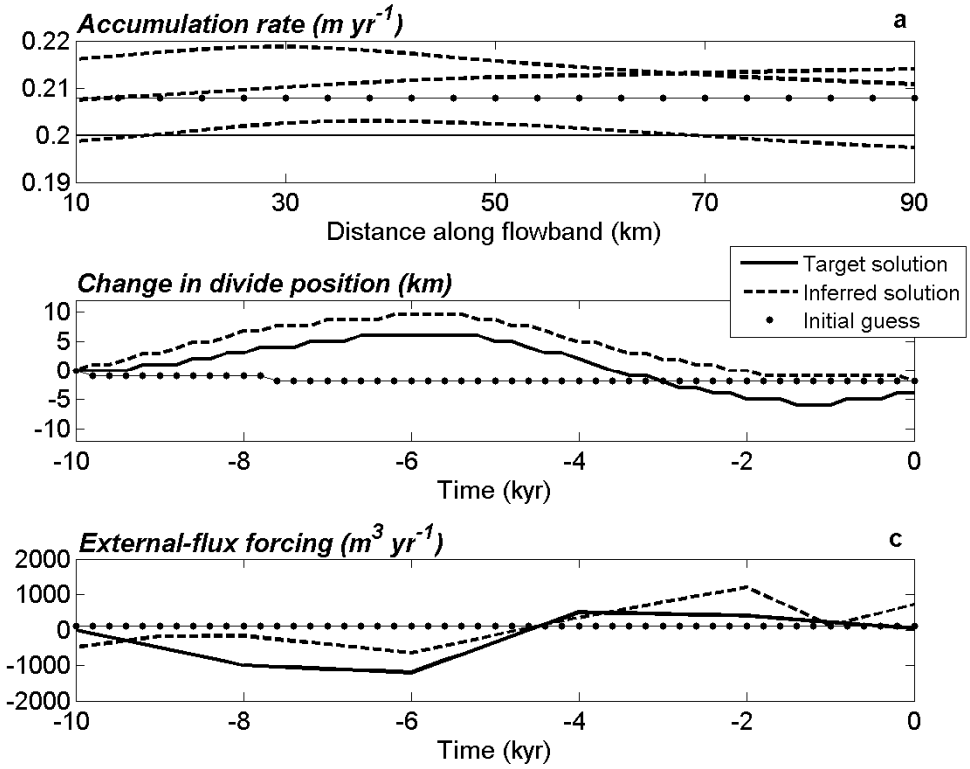

Figure 5.5. Solution to the inverse problem with constant accumulation forcing, and divide migration from external-flux variations. Solid lines represent the target solution, dashed lines represent the solution inferred by solving the inverse problem, and dotted lines represent the initial guess. **a)** The accumulation rate at three times (-9 kyr, -6 kyr, -4 kyr); the target accumulation is constant. **b)** The change in ice-divide position. **c)** The change in external flux on the left side of the divide.

Figure 5.5 shows that some variation in the rate and pattern of accumulation over time can also fit the data and satisfy the constraints. We apply an additional constraint to better infer the actual accumulation and external-flux histories.

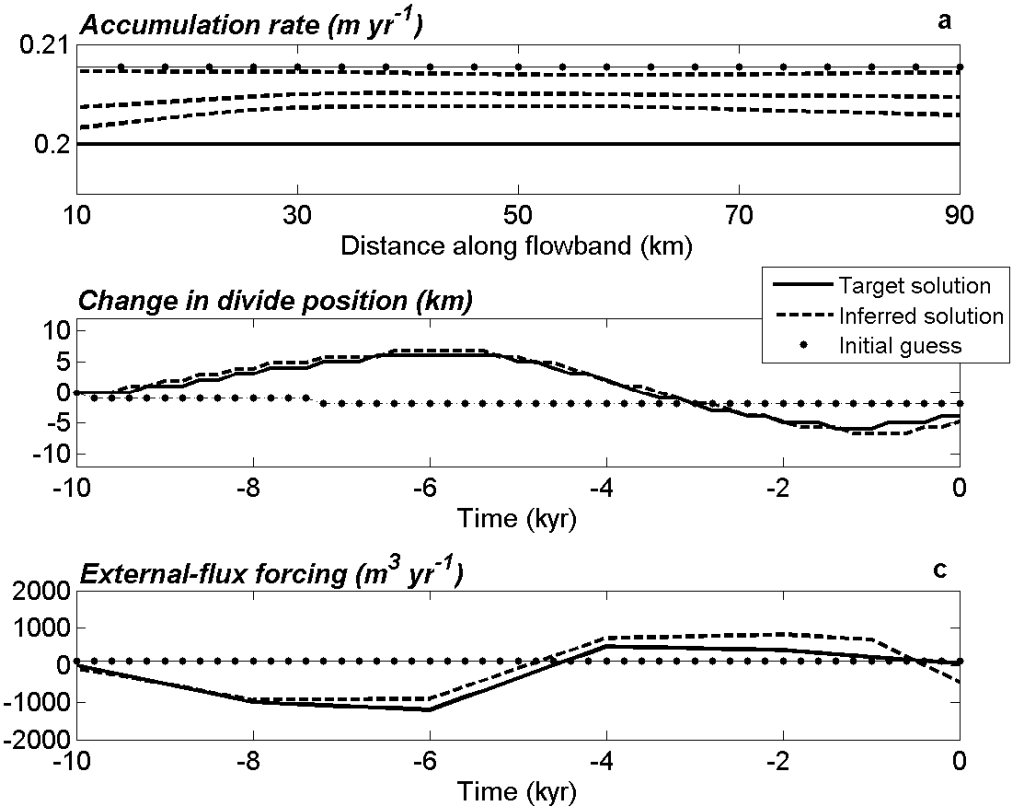

Figure 5.6. Solution to the inverse problem with a constant accumulation history, but divide migration forced by external-flux variations. Black lines represent the target solution, dashed lines represent the solution inferred by solving the inverse problem, and dotted lines represent the initial guess. **a)** The accumulation rate at three times (-9 kyr, -6 kyr, -4 kyr); the target accumulation is constant. **b)** The change in ice-divide position. **c)** The change in external flux on the left side of the divide.

Figure 5.6 shows the results of a test where we use a constraint that the accumulation rate should be spatially smooth and also should be temporally smooth. By penalizing solutions that exhibit accumulation-rate variations in both space and time, we can infer the correct histories of external-flux forcing and of accumulation forcing.

5.4.4. Variations in accumulation and external-flux forcing

In the third test, we generate synthetic internal-layer data, ice-surface velocity data, and accumulation-rate data using an accumulation history that varies in space and time, and with external-flux forcing that varies in time. These synthetic data are used to solve the inverse problem for these known histories of accumulation and ice flow, and Figure 5.7 shows the results of this test. In this test, we constrained accumulation rate to be spatially smooth.

As part of the accumulation-rate history in Figure 5.7a, the spatial pattern of accumulation may vary linearly through time, but also may vary as a sine function. We used the constraint that the accumulation rate should be spatially smooth, but Figure 5.7b shows that there must be some spatial variation in accumulation in order to fit the data. A smoothed version of the actual accumulation history can still fit the data. This accumulation history, and the well-reproduced history of external-flux forcing, give a history of divide position that well approximates the actual history (Figure 5.7c).

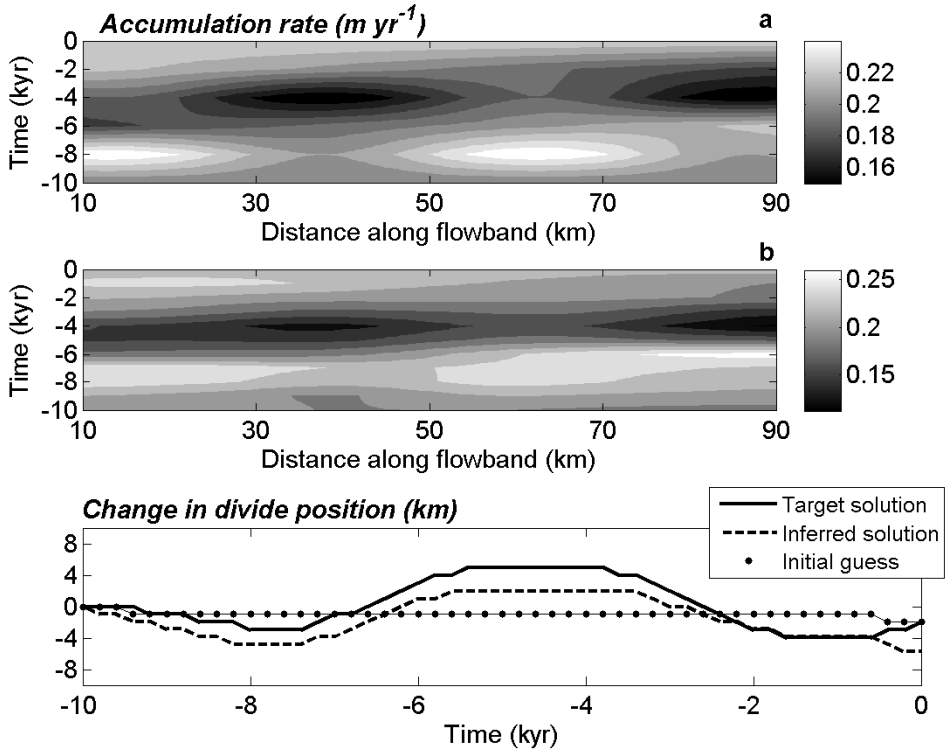

Figure 5.7. Solution to the inverse problem where accumulation-rate varies in space and time, and external flux varies in time. **a)** Actual accumulation-rate history. b) Inferred accumulation-rate history. **c)** Change in divide position associated with changes in accumulation and changes in external flux.

5.5. Results with data from Taylor Mouth, Antarctica

5.5.1. Steady-state results

Waddington and others (2007) solved the inverse problem to infer a steady-state pattern of accumulation using an internal layer, a modern accumulation-rate measurement, and modern ice-velocity measurements from Taylor Mouth, a flank site off Taylor Dome, Antarctica. The internal layer used by Waddington and others (2007) was undated. In addition to

solving for the spatial pattern of accumulation, the layer age and the ice flux entering the flowband were treated as unknown parameters in their inverse problem. There were four ice-velocity measurements and one accumulation-rate measurement available. The internal layer that they used had an inferred age of ~1660 years, and was ~100-200 m below the surface (the shallowest layer shown in Figure 5.8). Waddington and others (2007) reported that the accumulation rate in this area has been roughly in steady-state over the past 6,000 years. Therefore, we expect that an accumulation-rate pattern inferred using other internal layers with ages less than ~6,000 years should be similar to the stready-state pattern inferred by Waddington and others (2007) from the ~1660 year-old layer.

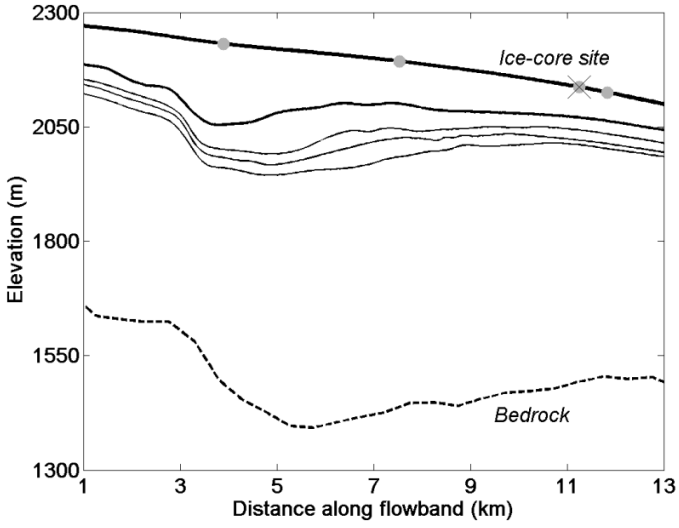

Figure 5.8. Internal layers and ice-sheet geometry at Taylor Mouth, Antarctica. Gray dots mark the location of surface-velocity measurements. An accumulation-rate estimate is available at the ice-core site. The shallowest layer (bold) was used in the steady-state problem solved by Waddington and others (2007).

First, we solve the inverse problem three additional times using the steady-state forward algorithm from Waddington and others (2007) with three

additional internal layers that span ~3000 years. Figure 5.8 shows these additional internal layers and the surface and bed topography of this profile from Taylor Mouth. Figure 5.9a shows the inferred steady-state pattern of accumulation from each layer, found by solving the inverse problem using one internal layer at a time and using the same surface-velocity measurements and the one accumulation-rate measurement at this site, as given by Waddington and others (2007).

5.5.2. Transient results

Next we solve an inverse problem using a transient forward algorithm and all four internal layers from Taylor Mouth (Figure 5.8) together to find an accumulation history that is consistent with all four layers. We use the layer ages inferred by solving the steady-state inverse problem using each layer individually.

Figure 5.9b shows the accumulation-rate history found by solving an inverse problem using a transient ice-flow model and all four internal layers. In this test, we constrained the accumulation rate to be spatially smooth. This solution shows spatial and temporal variability in accumulation that is not exhibited in the accumulation patterns inferred by solving four separate steady-state inverse problems. This occurs because few data are available and minimal constraints were applied to constrain this transient problem. For example, no layers are available from 1660 years to the present, and there are no reliable modern accumulation-rate measurements. The few data available can be fit with an accumulation history that varies through time, and without additional constraints an accumulation history that changes in time is not penalized. In addition, in a transient problem there can be trade-offs between accumulation variations

and ice-thickness variations. Those tradeoffs can lead to a solution with more structure than the solution to the steady-state problem.

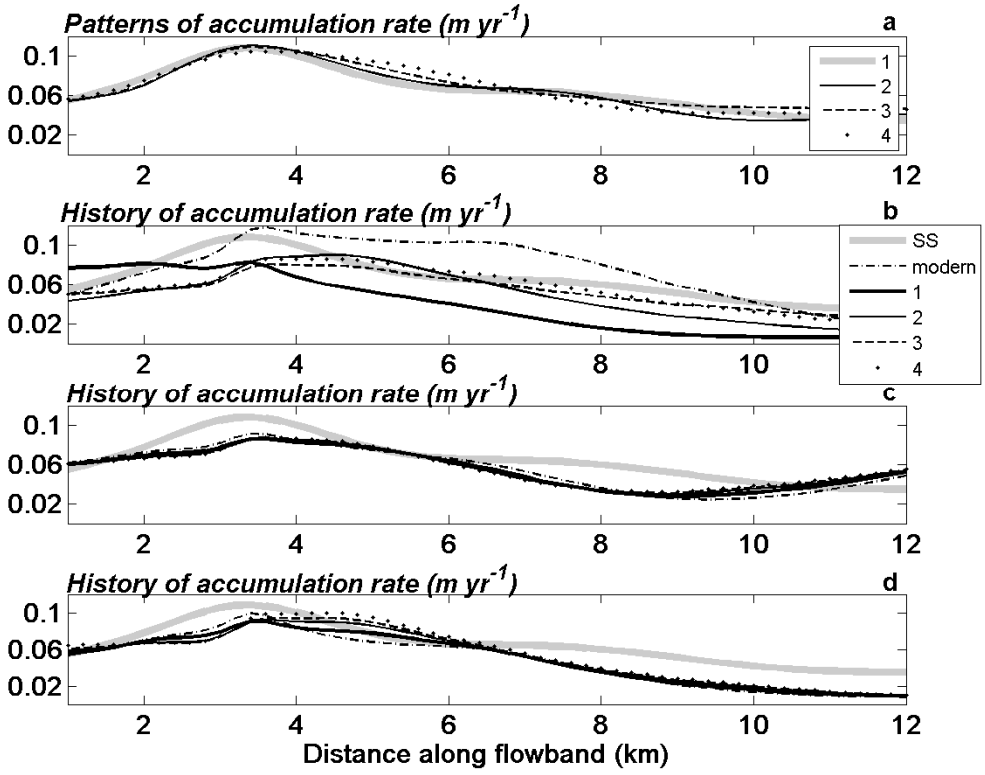

Figure 5.9. Results from solving inverse problems using data from Taylor Mouth. **a)** Four patterns of accumulation, found by solving four separate steady-state inverse problems (following Waddington and others 2007). **b)** History of accumulation rate found by solving a transient inverse problem with all layers. 'SS' is the steady-state solution for layer 1 from panel a, and 'modern' is the present-day pattern. **c)** Transient solutions constrained to produce a temporally smooth accumulation history. **d)** Transient solutions using a known initial ice thickness, and constrained to produce a temporally smooth accumulation history.

Figure 5.9c shows the accumulation-rate history found by solving a transient inverse problem using all four internal layers, and constraining the accumulation rate to be temporally smooth. This additional constraint

is warranted in this case because we expect that these few data come from an ice sheet in steady state, and because we seek the minimum variation in accumulation that is required to fit the data. By imposing an additional constraint, a solution with less temporal variability is found. However, the ice-sheet thickness still changes in time. This leads to a spatial pattern that differs from the steady-state solutions.

Figure 5.9d shows the accumulation history found by solving a transient inverse problem using all four internal layers, constraining the accumulation rate to be temporally smooth, and assuming that the ice thickness initial condition (S_0^{in}) is known. Compared to Figure 5.9b and Figure 5.9c, a different accumulation rate is found. This demonstrates that available data and imposed constraints influence the solution. Especially in the case where few data are available to constrain a transient problem, the *a priori* information imposed on the problem is very important.

5.6. Discussion

5.6.1. Initial estimate of parameter values

To solve the inverse problem, all parameter values must be estimated at the first iteration; the iteration loop on the nonlinearity in this problem is discussed in Section 5.3.2, and illustrated in a flowchart in Appendix K. The initial ice flux entering the domain Q_{in} at the first node, the initial ice-surface elevation at the first node S_0^{in}, the ice-flux forcing external to the limited domain $Q_{ext}(x,t)$, the temperature-independent ice-softness parameter A_0, and the geothermal flux Q_{geo} are all estimated using any knowledge of these parameters at each specific site. This may come from present-day measurements, or from ice-core measurements. The internal

layers are assumed to be well-dated, and we these values for their initial estimates. If the layer ages were unknown, we could solve for them as part of the inverse problem, but additional data or additional constraints may be necessary to find a unique solution. The accumulation rate at each time node and at each spatial node is initially estimated from a 1-D vertical strain approximation (called the Local Layer Approximation, Waddington and others 2007) using the depth and age of the internal layer.

Unlike a Monte-Carlo algorithm, our gradient algorithm does not search the entire model space to find the best parameter set. There may be multiple minima (i.e. multiple solutions); a gradient method can find only one solution, and a Monte-Carlo method can find multiple solutions. The gradient algorithm has the advantage of being computationally efficient, but it has the disadvantage of possibly being dependent on the initial estimate of the parameter values. For the steady-state version of this problem (Waddington et al., 2007), Steen-Larsen and others (In Press) showed that a gradient algorithm and a Monte-Carlo algorithm gave similar results. While we assume that the gradient algorithm yields a robust result, we can start from different initial estimates of the parameter values in order to express the range in the inferred parameter set due to the dependence of the solution on this initial estimate. This may also identify multiple solutions to the problem, and is a compromise between using only a gradient algorithm and using a Monte-Carlo algorithm; a Monte-Carlo solution to this transient problem is too computationally intensive to perform now with this transient ice-flow model.

5.6.2. Solution sensitivity to unknown parameters

Formal inverse theory allows us to investigate our ability to infer unknown parameters; this ability is known as the resolving power. The preferred solution from our regularized algorithm is a model that minimizes the performance index I_P in Equation 5.17, and fits the data at an expected tolerance, satisfying Equation 5.20. However, we still do not know whether we have found the best parameter values and the most realistic spatial variability of the parameters. It is important to assess the ability to resolve those parameters before making physical inferences from the preferred solution. In a linear problem, model resolution can be straightforward to assess (e.g. Aster and others 2005, pg. 63). However, Parker (1994, pg. 200-213) showed that when using a regularized algorithm, the inferred structure is a version of the true structure that has been smoothed by a set of narrowly peaked model-resolving functions. The half-width of the resolving function at each spatial position gives the physical scale over which meaningful structure can be resolved. Features with shorter spatial extent than this cannot be resolved with confidence from these data and this forward algorithm. The resolving power will depend on the specific problem, but in general we expect that the spatial resolving power will decrease with distance from the divide (Waddington and others 2007), and that the resolving power will decrease back in time.

5.6.3. Additional data

We are solving an inherently ill-posed problem, and utilizing all available data will give the best ability to stably find a unique solution. In particular, additional data that constrain the history of accumulation rate will be the most valuable to this problem. As reported by Spencer and

others (2006), a promising prospect for estimates of past accumulation rates could come from the number-density of bubbles in an ice core. Past accumulation rates may also be available from beryllium-10 measurements (e.g. Raisbeck and others, 1981). However, uncertainties in these estimates may be high. We can establish the precision required for these data to provide useful constraints to this inverse problem.

While we are target deep layers because they contain information from further in the past, shallow layers are important because they describe the modern accumulation-rate *pattern*. As shown in Figure 5.9b, if there is a significant temporal gap between the youngest layer and the present day, the accumulation history during this time may be poorly constrained. In addition, the resolving power of our algorithm decreases with distance from the divide because particle-path lengths increase with distance from the divide (Waddington et al., 2007). Modern accumulation-rate, ice-thickness, or ice-velocity data that exist away from the divide are stronger constraints on the solution.

5.6.4. Additional regularization

While penalizing large values of $\|p\|^2$ given by Equation 5.30 does help to prevent the solution from exhibiting roughness that is not required by the data, in a transient problem we may need an additional constraint. In our transient problem, information about the accumulation history and the ice-thickness history comes primarily from dated internal layers. The internal layers alone may not be able to properly attribute temporal changes that may be required to fit the data; temporal changes in accumulation and temporal changes ice thickness can have a similar affect on internal-layer structure and depth. In addition to penalizing spatial or temporal

roughness of the accumulation-rate solution, we could penalize deviations from an average value, or strictly require that global parameter values (e.g. input flux Q_{in}, ice-thickness value S_{in}, temperature-independent ice-softness parameter A_0) cannot deviate from their characteristic values within a given tolerance.

Since the imposed constraints influence the solution, it is important to apply spatial and/or temporal constraints at locations or at times that they are expected to apply. For example, a temporally smooth accumulation history may be expected in the past few thousand years of the Holocene, but not during the last glacial-interglacial transition. If *a priori* information is limited, we advocate imposing as many constraints necessary to find a physically meaningful solution. Seeking the minimum structure that is required to fit the data will help to avoid overfitting the data.

The solution reflects a balance between fitting the data and finding a smooth model, and that balance is weighted by the trade-off parameter (Equation 5.17). We expect a trade-off parameter that is order one. Therefore, the value of the trade-off parameter indicates whether the constraints are oversmoothing (or undersmoothing) information that is actually reflected in the data. For example, if a trade-off parameter must be much larger (or smaller) than unity to find a solution that fits the data, solutions using different constraints should be investigated.

Regularization by solving a damped least-squares problem (Tikhonov regularization) may not be enough to stabilize the problem and find a unique solution. This is discussed generally in Section A5.3, and Parker (1994, pg.160) discusses how to use SVD to assess the reliability of the solution to a given problem. Regularization should sufficiently reduce the influence of nonphysical parameter values, either by damping or removing their contribution to the solution. It is insightful to use the singular vectors

associated with the model space (**V** in Equation A5.3.6, known as the right singular vectors) to analyze effect of regularization.

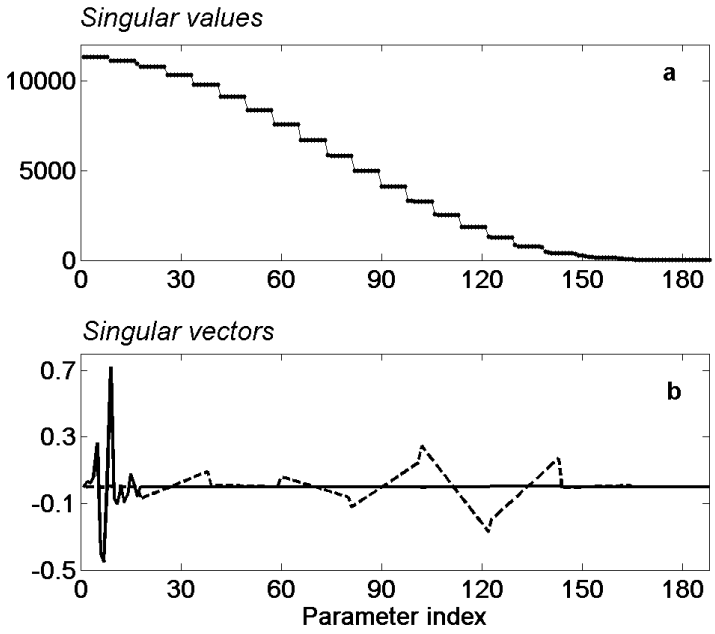

Figure 5.9. a) Singular-value spectrum for a regularized solution. **b)** Two singular vectors associated with small singular values (parameter index 170 and 175). The black line shows noise that contributes nonphysical information about the solution, and the dashed line shows useful information about the solution.

In our problem that has been regularized by Tikhonov regularization, the singular vectors associated with the largest singular values are projections of our smoothness constraint (the model norm). The singular vectors containing the physical structure of our solution is often associated with the smallest singular values, and therefore truncating the singular value set in an already regularized problem could discard useful information about the solution. However, if the problem has not been sufficiently regularized, the singular vectors associated with the smallest singular

values could introduce noise to the solution. Figure 5.10 illustrates this case. The singular-value spectrum is shown in Figure 5.10a, and if no singular values are truncated, both singular vectors shown in Figure 5.10b will contribute to the solution. The spike function (solid line) in Figure 5.10b does not contain physical information about the solution, whereas the singular vector associated with a slightly larger singular value (dashed line) does contain useful information about the solution. Even though the singular value associated with the unphysical singular vector is small, it must be set to zero to remove the influence on the solution.

The magnitude of the singular values is determined by how each contribution to the Jacobian matrix is scaled in the inverse algorithm (see Equation A5.3.3). Finding an appropriate weighting scheme is critical to suitable regularization, and to account for the relative contributions of different physical parameters. For example, Jacobian elements of the partial derivatives of modeled observables with respect to input ice flux $Q_{in}(t_0)$, to ice-surface elevation at one location at the initial timestep $S_{in}(t_0)$, to temperature-independent ice-softness parameter A_0, or to geothermal flux Q_{geo} may be different orders of magnitude, and these parameters can influence every modeled observable. In comparison, changes in an individual spatial and temporal value of accumulation rate $\dot{b}(x_i, t_j)$ will have a limited influence on the set of modeled observables.

5.7. Conclusions

Internal layers are the most accessible archive of the history of accumulation rate, ice thickness, ice-divide migration, and external flux forcing. Using a new inverse approach, we can infer these histories from internal-layer shapes. We present this new method, and demonstrate that

prescribed histories can be inferred from synthetic data. Using data from Taylor Mouth, Antarctica, we highlight the sensitivity of the solution to the data available and to the imposed constraints. To stably find a unique and physically meaningful solution, it is necessary to use *a priori* information to constrain the solution. The constraints should be chosen carefully. If limited *a priori* information is available, we advocate finding a solution with the minimum variation that is required to fit the data and satisfy the constraints.

The solution to this inverse problem is better defined if the internal layers are dated by an intersecting ice core. This approach is well-suited to data in the vicinity of ice divides, and can provide information that is essential to ice-core interpretation and ice-volume reconstructions.

A5.1. Ice-velocity shape functions

We can calculate the average horizontal velocity $\bar{u}(x,t)$ using the Shallow Ice Approximation (SIA; e.g. Hutter, 1983, pg. 256-332; Paterson, 1994, pg. 262); the SIA is a simplifying assumption that can be applied in cases where the ice thickness *h(x,t)* is much smaller than the horizontal span of the ice sheet. Therefore, derivatives of velocities and stresses with respect to *x* are generally much smaller than derivatives with respect to *z*. The constitutive relationship for ice flow (Glen, 1955) using the SIA is,

$$\dot{\varepsilon}_{xz} = A(T(x,z,t))\tau_{xz}^{n} \tag{A5.1.1}$$

where $\dot{\varepsilon}_{xz}$ is the simple-shear strain-rate along a horizontal plane, *A(T(x,z,t))* is the temperature-dependent ice-softness parameter, τ_{xz} is the shear-stress tensor along a horizontal plane, and we choose the flow law exponent *n=3* (e.g. Paterson, 1994, pg. 85). The temperature-dependent ice-softness parameter *A(T(x,z,t))* follows an Arrhenius relationship (e.g. Paterson 1994), given by Equation 5.13.

The components of the strain-rate tensor along a horizontal plane are

$$\dot{\varepsilon}_{xz} = \frac{1}{2}\left(\frac{\partial u}{\partial z} + \frac{\partial w}{\partial x}\right) \tag{A5.1.2}$$

Following the SIA, the derivatives of velocities with respect to *x* are negligible, giving $2\dot{\varepsilon}_{xz} \approx \partial u/\partial z$ (e.g. Paterson, 1994, pg. 262). Using the flow law given by Equation A5.1.1 for the SIA, and assuming that the temperature is uniform with depth for each position in *x* (*T(x,z,t)=T(x,t)*), the depth-averaged horizontal velocity can be found by integrating $\partial u/\partial z$ twice over depth *z*,

$$\bar{u}(x) = \frac{2A(T(x,t))}{n+2}(\rho g)^{n}\left|\frac{dS}{dx}\right|^{n-1}\left(-\frac{dS}{dx}\right)h(x)^{n+1} \tag{A5.1.3}$$

where ρ is density, g is gravitational acceleration, *S(x,t)* is the ice-surface elevation, and *h(x,t)* is the ice thickness.

If the ice temperature is not uniform with depth at each location (*T(x,z,t)* is not equal *T(x,t)*), we can solve for an effective-isothermal value of the ice-softness parameter. The effective isothermal-softness parameter $\tilde{A}(x,t)$ is the isothermal softness parameter required to give the same depth-averaged velocity and ice flux as using a depth-varying-temperature-dependent softness parameter *A(T(x,z,t))*. We calculate the effective isothermal value by using the depth-averaged ice velocity $\bar{u}(x,t)$ with *A(T(x,z,t))*,

$$\bar{u}(x,t) = 2A_0\left(\rho g \frac{\partial S(x,t)}{\partial x}\right)^n h(x)^{n+1}\int_0^1\int_0^{\hat{z}} \exp\left(-\frac{Q}{RT(\hat{\varsigma},t)}\right)(1-\hat{\varsigma})^n\, d\hat{\varsigma}d\hat{z}\,, \quad \text{(A5.1.4)}$$

and equating to the depth-averaged velocity $\bar{u}(x,t)$ from Equation A5.1.3, and solving for *A(T(x,t))*, given as here as $\tilde{A}(x,t)$,

$$\tilde{A}(x,t) = (n+2)\int_0^1\int_0^{\hat{z}} A(T(x,\varsigma,t))(1-\hat{\varsigma})^n\, d\hat{\varsigma}d\hat{z}\,. \quad \text{(A5.1.5)}$$

The ice-velocity field *u(x,z,t)* is calculated from the average velocity and from a velocity shape function (Equation 5.6), where $\phi(x,\hat{z},t) = u(x,\hat{z},t)/\bar{u}(x,t)$. For example, the horizontal velocity shape function for an isothermal temperature field and using the SIA is given by

$$\phi(x,\hat{z}) = \frac{n+2}{n+1}\left(1-(1-\hat{z})^{n+1}\right). \quad \text{(A5.1.6)}$$

However, we target ice-sheet interior sites, and our approach is particularly well suited for use with ice-sheet data that span an ice divide. Therefore, depending on the specific problem, we can also employ shape functions that are appropriate for ice-divide flow. Following Nereson and Waddington (2002), the horizontal velocity shape function is split into two terms,

including a contribution from pure ice-divide flow and a contribution from pure flank (off divide) flow. For our transient problem this is given by

$$\phi(x,\hat{z},t) = \alpha(x)\phi_d(\hat{z},t) + [1-\alpha(x)]\phi_f(\hat{z},t) \qquad \text{(A5.1.7)}$$

As described by Nereson and Waddington (2002), $\alpha(x)$ is a partitioning function that assigns the relative contributions of divide flow and of flank flow across the domain, where $\alpha = 1$ at the divide and decreases to zero away from the divide. Using a Dansgaard-Johnsen description of the velocity shape functions (Dansgaard and Johnsen, 1969) results in a horizontal velocity shape function $\phi(\hat{z},t)$ given by

$$\phi_{f,d}(\hat{z},t) = \frac{1}{1-\left(h_{f,d}/2\right)}\frac{z}{h_{f,d}} \qquad \text{for} \quad z < h_{f,d} \qquad \text{(A5.1.8)}$$

$$\phi_{f,d}(\hat{z},t) = \frac{1}{1-\left(h_{f,d}/2\right)} \qquad \text{for} \quad z \geq h_{f,d} \qquad \text{(A5.1.9)}$$

where h_f is representative of flank flow and h_d is representative of divide flow such that $0 < h_f < h_d < 1$. The vertical velocity shape function is the integral of the horizontal-velocity shape function. In this Dansgaard-Johnsen formulation, following Nereson and Waddington (2002), the vertical velocity shape function is given by

$$\psi_{f,d}(\hat{z},t) = \frac{1}{1-\left(h_{f,d}/2\right)}\frac{z^2}{2h_{f,d}} \qquad \text{for} \quad z < h_{f,d} \qquad \text{(A5.1.10)}$$

$$\psi_{f,d}(\hat{z},t) = \frac{1}{1-\left(h_{f,d}/2\right)}\left(z - h_f/2\right) \qquad \text{for} \quad z \geq h_{f,d} \qquad \text{(A5.1.11)}$$

The appropriate value for h_f and h_d is a site-specific decision; we chose h_f=0.2 and h_d=0.6.

A5.2. Boundary and initial conditions

In our calculation of ice-sheet evolution, the ice-surface profile *S(x)* is required as an initial condition. We estimate this ice-surface profile using a steady-state calculation, which requires the ice thickness at one location in the domain as a boundary condition. This boundary value, which we define at the start of our domain and we refer to as S_0^{in}, is treated as an unknown parameter in our inverse problem.

To calculate the ice-temperature field *T(x,z,t)* in a thermomechanically-coupled problem we must estimate the temperature field in order to calculate ice-surface evolution and the ice-velocity field. The temperature field is iteratively updated with these calculation values until a consistent ice-temperature field, ice surface, and ice-velocity field are found. If the temperature field does not change in time, and therefore is not thermomechanically coupled to the transient ice-flow field, we can still achieve a realistic temperature field by prescribing the boundary conditions of surface temperature and of geothermal flux. From these boundary conditions, the depth variation in ice temperature follows from Fourier's Law of heat conduction (e.g. Van der Veen 1999, pg. 178)

$$T(x,\hat{z}) = T(x,\hat{z}=1) + \frac{Q_{geo}}{K}\Delta\hat{z} \qquad \text{(A5.2.1)}$$

where $\hat{z}=1$ at the surface and $T(x,\hat{z}=1)$ is the surface temperature boundary condition, K is the thermal conductivity (which may be a function of ice temperature, Paterson 1994 pg. 205), Q_{geo} is the geothermal flux, and $\Delta\hat{z}$ is the depth increment. The geothermal flux Q_{geo} is treated as an unknown parameter in our inverse problem. This temperature field is used to calculate the effective-isothermal ice-softness parameter (Equation A5.1.5) in the flow law.

A5.3. Damped least-squares solution

A least-squares solution is one where the inferred model parameters minimize a 2-norm of residuals $r = Gm - d$, and enables an approximate solution be found when an exact solution to Equation 5.1 does not exist; the least-squares solution is considered to be "the next best thing" to an exact solution (e.g. Menke, 1989, pg. 45). However, the standard least-squares solution procedure can fail if multiple solutions exist (e.g. Menke, 1989, pg. 45). In this case, not enough information is available to find a unique solution, and the problem is at least partially underdetermined. The problem may also be ill-posed, making the least-squares solution procedure unstable. As discussed in Section 5.3.1, regularization is used to find a unique solution, and to stabilize the solution procedure. A least-squares solution that has been regularized with Tikhonov regularization is called a damped least-squares solution (e.g. Aster and others 2005, pg. 91). The damped least-squares solution procedure used here is the same procedure used by Waddington and others (2007).

As discussed in Section 5.3.2, we have linearized our otherwise nonlinear problem to find updates to the unknown parameter values **Δp** such that we minimize the performance index I_p, given by Equation 5.17, until Equation 5.20 is satisfied. Following Waddington and others (2007), if the model residuals and data residuals are combined into a single vector **e** of size (N_d + M_p), their respective weights (given by $v^{1/2}$ for the data residuals) combined into a matrix **W** of size (N_d + M_p) × M_p, and the Jacobians (see Section A5.4) are combined into a single matrix **J** of size (N_d + M_p) × M_p, the reformulated performance index I_p is

$$I_p = \sum_{i=1}^{M_p+N_d} W_{ii}^2 e_i^{0\,2} - vT^2 + 2\left(\sum_{k=1}^{M_p} \frac{\partial e_i}{\partial p_k} \Delta p_k\right) + \left(\sum_{i=1}^{M_p+N_d} W_{ii}^2 \sum_{i=1}^{M_p} \frac{\partial e_i}{\partial p_k} \Delta p_k\right)^2 \qquad \text{(A5.3.1)}$$

It follows that the partial deriviative $\partial I_p / \partial p_j$ is

$$\frac{\partial I_p}{\partial p_j} = 2 \sum_{i=1}^{M_p+N_d} W_{ii}^2 e_i^0 \frac{\partial e_i}{\partial p_j} + 2 \sum_{i=1}^{M_p+N_d} \frac{\partial e_i^0}{\partial p_j} \sum_{k=1}^{M_p} \frac{\partial e_i}{\partial p_k} \Delta p_k = 0 \qquad \text{(A5.3.2)}$$

This set of linear equations can be expressed as *normal equations* for the least-squares problem (e.g. Aster and others 2005, pg. 237). From Equation A5.3.2 this is given by

$$\mathbf{J}^T\mathbf{W}^T\mathbf{W}\Delta\mathbf{p} = \mathbf{J}^T\mathbf{W}^T\mathbf{W}\mathbf{J}\mathbf{e} \qquad \text{(A5.3.3)}$$

where $\mathbf{\Delta p}$ is the vector of parameter-value updates that we are solving for:

$$\Delta\mathbf{p} = \left[\mathbf{J}^T\mathbf{W}^T\mathbf{W}\mathbf{J}\right]^{-1}\mathbf{J}^T\mathbf{W}^T\mathbf{W}\mathbf{J}\mathbf{e} \qquad \text{(A5.3.4)}$$

If $\mathbf{A}=\mathbf{WJ}$, $\mathbf{x} = \mathbf{\Delta p}$, and $\mathbf{b}=\mathbf{We}$, Equation A5.3.3 regains the standard normal-equation form

$$\mathbf{A}^T\mathbf{A}\mathbf{x} = \mathbf{A}^T\mathbf{b} \qquad \text{(A5.3.5)}$$

Singular value decomposition (SVD) is an important way to examine and solve a least-squares problem, in particular one that is rank-deficient and/or ill-posed (e.g. Aster and others 2005, pg. 55). In the form of Equation A5.3.5, the SVD of matrix $\mathbf{A}$ yields,

$$\mathbf{A} = \mathbf{U}\Lambda\mathbf{V}^T \qquad \text{(A5.3.6)}$$

where $\mathbf{U}$ are the unit basis vectors that span the data space, $\mathbf{V}$ are the basis vectors that span the model space, and $\mathbf{\Lambda}$ are the singular values. The singular values are ordered by size, largest to smallest, and some of the singular values may be zero; $\mathbf{A}$ is rank deficient if it contains any singular values that are equal to zero, and if there is a sharp transition between nonzero and zero singular values (e.g. Aster and others 2005, pg. 67). The SVD can be used to calculate the generalized inverse of $\mathbf{A}$, which is given by

$$\mathbf{A}^{-1} = \mathbf{V}\Lambda^{-1}\mathbf{U}^T \qquad \text{(A5.3.7)}$$

Unfortunately, even damped, small singular values can still cause instability in the generalized inverse solution. Fortunately, the SVD allows

the singular-value spectrum to be analyzed, and the trivial (but nonzero) singular values can be neglected (i.e. set to zero) to improve stability (e.g. Aster and others 2005, pg. 64; Eisen 2008). If the set of singular values $\mathbf{\Lambda}$ transitions abruptly to zero, it is more obvious where to truncate the singular-value set, but otherwise this cutoff must be chosen. Truncating the singular-value set requires finding a balance between stability and solution accuracy; truncating singular values can eliminate useless information, as well as useful information. We chose to not cutoff additional singular values, but to regularize our problem primarily with our smoothness constraint. Suitable regularization may be sensitive to how the Jacobian matrix $\mathbf{J}$ is weighted using the matrix $\mathbf{W}$; consistent normalization can be critical if the Jacobian is comprised of different physical quantities. In the case where Tikhonov regularization alone is not sufficient, and since truncating singular values is a useful regularization tactic, we discuss this strategy in more detail.

Generally speaking, if $\mathbf{A}$ has size $N \times M$, where N represents the number of data and M represents the number of model parameters. Matix $\mathbf{A}$ can be reduced based on its rank. The rank is the number of non-zero singular values (e.g. Aster and others 2005, pg. 233). In a numerical problem, zero may be determined by machine precision, and it is possible that these very smallest singular values could still introduce noise, and it is good practice to reduce the matrix $\mathbf{A}$ by its rank. As discussed by Eisen (2008), the SVD of $\mathbf{A}$ can also be given by

$$\mathbf{A} = \mathbf{U}_R \Lambda_R \mathbf{V}_R^{\mathrm{T}} \tag{A5.3.8}$$

where $\mathbf{A}$ has been reduced by its rank R. SVD, and this reduced-rank form of $\mathbf{A}$, is highly flexible because it is valid for over-determined ($N > M$) and under-determined ($N < M$) problems. This is accomplished by handling both a possible model null space (if $R < M$ there exists $\mathbf{V}$ spanning $M \times (M\text{-}R)$)

and a possible data null space (if $R < N$ there exists $\mathbf{U}$ spanning $N \times (N\text{-}R)$). If there is a non-trivial data null space, it will not be possible to fit the data exactly. If there is a non-trivial model null space, the model parameters cannot be recovered exactly. Suppressing non-trivial null spaces is a central purpose of regularization, and if this has not been accomplished by Tikhonov regularization alone, we set values in the null spaces of $\mathbf{A}$ to zero. As discussed by Wunsch (1996, pg. 147), setting null-space values to zero further removes structure in the solution that the data do not require. Another way to judge if additional truncation of the singular-value set may be required is if the condition number of the reduced $\mathbf{A}$ remains large; in particular if there is a significant difference in the order of magnitude of the largest singular value and all other singular values. For example, the condition number might be approximately the inverse of the machine precision, indicating that small, but not exactly zero, singular values may influence the solution. In this case the system is nearly linearly dependent and singular values less than a prescribed cutoff value may need to be set to zero.

The prescribed cutoff is best chosen in context of the specific problem onhand, and some suggestions are given by Eisen (2008) and Menke (1989, pg. 123). For example, if there is a distinct break in the distribution between large and small singular values, a truncation point may be obvious. However, in a discrete ill-posed problem, the singular-value spectrum does not exhibit a distinct break in slope, and the truncation point may not be obvious. A meaningful way to determine this cutoff point is to analyze the basis vectors (singular vectors) that span the model space, $\mathbf{V}$ from the SVD of $\mathbf{A}$ using Equation A5.3.6. As illuminated in an example by Parker (1995, pg. 160), assessing if the structure in each singular vector is or is not a meaningful representation of structure in the expected solution set is very

insightful. Fortunately, by nullifying the singular values associated with these unphysical singular vectors, the singular vectors containing meaningful structure can form the solution; the problem is effectively regularized.

In addition to regularization, in some cases it was necessary to use underrelaxation to stabilize the algorithm. Underrelaxation further damps the magnitude of the inferred parameter changes at each iteration; this is similar to the form of underrelaxation used for the implicit ice-surface calculation in Chapter 4. If necessary, we used a relaxation factor of 0.5.

A5.4 Calculation of Jacobian Matrix

To solve our linearized problem, we must calculate a Jacobian that expresses how changes in each model parameter p_j affect the value of each modeled observable o_i^m. The Jacobian matrix is of size $(N_d + M_p) \times M_p$. The partial-derivative components of the Jacobian can be calculated by approximating each derivative numerically, or by formulating analytical expressions that directly relate model parameters to predictions of data values. While we use a strictly numerical calculation here, analytical expressions for some partial derivatives have been derived, and are given in Appendix N.

A derivative can be approximated numerically using a finite-difference scheme, and commonly used difference schemes include the forward difference, backward difference, and centered difference (e.g. Carnahan and others 1969, pg. 35). The order of the difference scheme depends on how many terms from the Taylor expansion are retained. In

general form, a first-order centered-difference derivative of a function *F(x)* is given by

$$\frac{dF(x)}{dx} = \frac{1}{2\delta x}\left(F(x+\delta x) - F(x-\delta x)\right) \qquad \text{(A5.4.1)}$$

where δx is small.

The numerical Jacobian calculation can be highly sensitive to the finite-difference scheme used to approximate the derivative, and higher-order schemes are more computationally expensive. We want to use the simplest difference approximation possible, but we require stability and accuracy in the calculation. In our problem, different approximations of the derivative *and* different perturbation sizes δx can hugely influence the accuracy of the calculation. While a centered-difference approximation requires twice as many calculations as a forward difference or a backward difference, we find that it is much more accurate. Therefore, we use a centered-difference scheme to approximate the derivatives in our Jacobian matrix. We perturb each parameter in turn by adding a small perturbation δp_j, and in a separate calculation by subtracting a small perturbation δp_j, and we calculate a new set of modeled observables corresponding to these two different sets of perturbed parameter values; this requires $2M_p$ calculations of the forward algorithm. We find that the perturbation length used in the numerical calculation is critical for accuracy. Onur and Eyi (2005) derive an optimal perturbation that balances truncation error and computer round-off error. For a nondimensionalized problem where the parameter values are order one, Onur and Eyi (2005) suggest that the optimal perturbation length to be $2\sqrt{\Sigma_M}$, where Σ_M is the machine-working precision. In our case the perturbation length is the fraction of change in each parameter value δp_j. Our double-precision calculations are good to within 2×10^{-52}, and a suitable perturbation length is 2.9×10^{-8}. While the

parameter values in our calculation of the Jacobian matrix are not all order one, we tried a range of perturbation lengths and found that values from 10^{-6} to 10^{-8} gave consistent approximations of the partial derivatives in this problem.

Chapter 6

Inferring Histories of Accumulation Rate, Ice Thickness, and Ice Flow for Central West Antarctica

Tom Neumann, Howard Conway, and Kenny Matsuoka provided the data presented in this chapter.

A deep ice core is currently being drilled in Central West Antarctica. As discussed in Chapter 5, histories of accumulation and ice dynamics are necessary to properly interpret ice-core chemistry, and to develop a depth-age scale for the parts of the core where annual-layer counting is no longer possible. Solving the 2.5-D transient inverse problem is the appropriate way to infer histories from internal-layer shapes, because we expect that spatial and temporal variations in accumulation were significant. Here we describe the context for inferring histories of accumulation rate and ice dynamics in Central West Antarctica, and discuss data available to solve this inverse problem near the WAIS Divide ice-core site.

6.1. Introduction

A deep ice core is currently being drilled in Central West Antarctica; this core is referred to as the West Antarctic Ice Sheet (WAIS) Divide ice core. The high accumulation rates at this site should allow annual-layer counting back ~40 kyr, which will facilitate detailed comparison with Northern Hemisphere ice-core records. The high accumulation rate also means that the age difference between the occluded gas and the surrounding ice will be small, because this delta-age value at pore close-off depth depends on the accumulation rate (e.g. Sowers and others 1989). However, the geothermal flux in this area is poorly known, and the oldest ice at this site may have been lost to basal melting (e.g. Morse and others, 2002; Neumann and others, 2008). In addition, the divide position may have migrated, and the ice core is being drilled ~24 km off the present-day divide to avoid stratigraphic disturbances and complications from divide migration.

As discussed in Chapter 5, histories of accumulation and ice dynamics are necessary to properly interpret ice-core chemistry, and to develop a depth-age scale for the parts of the core where annual-layer counting is no longer possible. In addition, solving the 2.5-D transient inverse problem is the appropriate way to infer histories from internal-layer shapes, because we expect that spatial and temporal variations in accumulation were significant. Here we describe the context for inferring histories of accumulation rate and ice dynamics in Central West Antarctica, and discuss data available to solve this inverse problem near the WAIS Divide ice-core site.

6.1.1. Previous Work

Site-selection criteria for the WAIS Divide ice core are described by Morse and others (2002). A long-term, high-resolution record was desired, and therefore a site with thicker ice, higher accumulation rate, and hopefully lower heat flux was chosen. Morse and others (2002) found that there is a strong spatial gradient in accumulation rate, with values increasing to the North across the divide. Neumann and others (2008) tracked radar layers between the WAIS Divide site and the Byrd ice-core site ~185 km away (e.g. Gow and others, 1968), and using layer dated from the Byrd core they developed a depth-age relationship at WAIS Divide. Then, following Waddington and others (2005), they found suitable combinations of the accumulation-rate history, ice-thickness history, and basal-melting history that could match their derived depth-age relationship within the measurement uncertainty. Neumann and others (2008) used a 1-D model with simplified ice dynamics to calculate histories of accumulation rate and ice dynamics. The deepest layer they used was 8400 years B.P., and they found that the accumulation rate was higher from 3000-5000 years ago and that the divide has been migrating through the Holocene.

Present-day divide migration has been reported by Conway and Rasmussen (2009). They find that the present-day divide is moving towards the Ross Sea at 10 m yr^{-1}, and thinning at ~0.08 m yr^{-1}. Conway and Rasmussen (2009) find that this magnitude of divide migration is driven by ice dynamics, rather than by local accumulation-rate variations. The WAIS Divide is dynamically influenced by ice streams on the Ross-Sea side and the Amundsen-Sea side. Given the recent speed up of Thwaites and Pine Island glaciers on the Amundsen-Sea side, and the recent stagnation of Kamb Ice Stream (e.g. Joughin and Tulaczyk, 2002) on the Ross-Sea side, it is evident that dynamical changes can be significant.

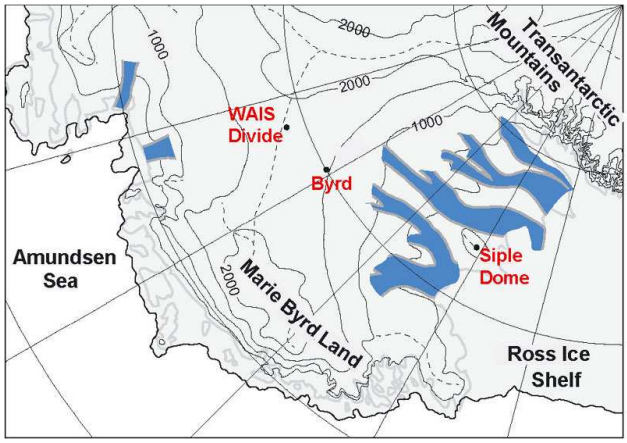

Figure 6.1. Map of West Antarctica highlighting the WAIS Divide ice-core site, the Byrd ice-core site, and the Siple Dome ice-core site. Ross Ice Streams and Thwaites and Pine Island glaciers are outlined. Map from Morse and others (2002).

Siegert and Payne (2004) used internal layers and a 1-D vertical strain model to estimate accumulation rates over the past 16,000 years across Central West Antarctica. However, it is likely that internal-layer depths have been affected by spatial variations in total vertical strain over this time. Siegert and Payne (2004) suggest that the accumulation rate from has been relatively stable over the past 3100 years, but it was lower 6400-16,000 years ago. This result is influenced by the actual ice-thickness history, but is supported by modeling results from Huybrechts (2002), and is consistent with Neumann and others (2008).

6.2. Data

6.2.1. Internal layers

Neumann and others (2008) describe ground-based radar data that were collected during the 2002-03 and 2003-04 field seasons. A 7-MHz

radar was used to detect layers from 30-1000 m below the surface, and a 1-MHz radar was used to detect layers from 300 m below the surface to the bed. The deepest continuous layer is an extremely bright reflection because it has high-acidity content (Hammer and others, 1997), and this so-called "Old Faithful" layer is dated to ~17,500 years B.P. (e.g. Jacobel and Welch, 2005b). In these ground-based radar data, no layers can be continuously traced to the Byrd core between 8400 and 17,400 years. Figure 6.2 shows eight layers detected with the 1-MHz radar, dated from 3500 – 17,345 years B.P. (e.g. Neumann and others 2008).

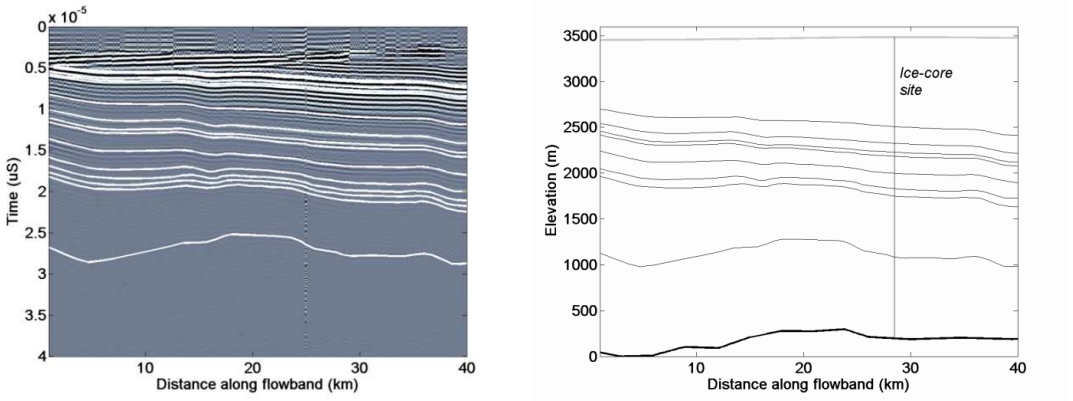

Figure 6.2. Ground-based radar data across the WAIS Divide from Neumann and others (2008). Left panel shows travel-time returns from 1-MHz radar, and white lines highlight continuous internal layers that are traced to the Byrd core. The same internal layers are shown in the right panel, where travel time has been converted to depth, and the ice-sheet geometry and ice-core site are shown for context. The internal layers are dated ~3.5 ka, ~4.3 ka, ~4.6 ka, ~4.85 ka, ~5.95 ka, ~7.2 ka, ~7.8 ka, and ~17.3 ka.

Airborne radar data were collected across the WAIS Divide during the 1999-2000 season. Figure 6.3 shows the locations of the SOAR flight lines in the vicinity of the WAIS Divide ice-core site. One flight line connects to the Byrd core, and other flight lines follow ice-flow lines. The

Center for Remote Sensing of Ice Sheets (CReSIS) at the University of Kansas has collected radar data that target the deepest layers near the WAIS Divide (e.g. Laird and others, In Press). It may be possible to interpolate these data to ice-flow lines, and then to use these high-resolution views of internal layers throughout the depth of the ice sheet.

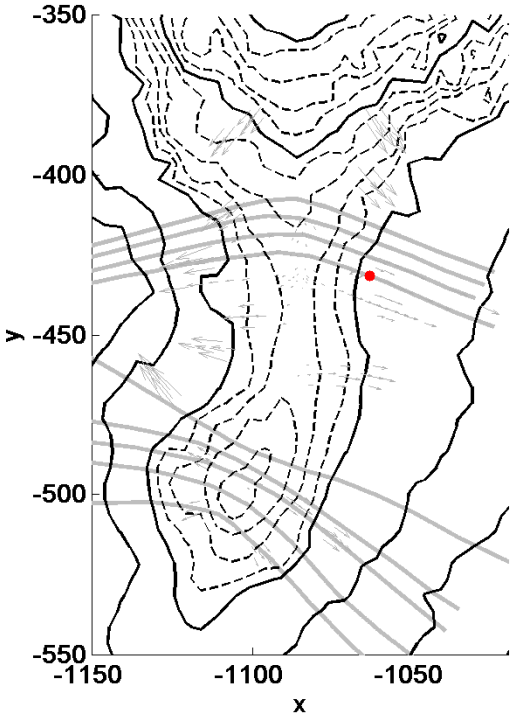

Figure 6.3. Locations of SOAR radar flight lines (thick gray lines) in the vicinity of the WAIS Divide ice-core site (marked with a red dot). Background is surface elevation contours from BEDMAP, ranging from 1650 to 1900 m. Thin gray lines show measured flow vectors, ranging from 0.1 to 5.9 m yr^{-1}. Figure courtesy of K. Matsuoka.

6.2.2. Accumulation-rate measurements

Modern accumulation rates are available from the International Trans-Antarctic Scientific Expedition (ITASE). ITASE core 00-1 is near the

WAIS Divide ice-core site. Neumann and others (2008) used ice-core chemistry from the 105-meter core, which goes back to 1651 AD (Dixon and others 2004), in combination with high-frequency radar to infer spatial variations in the modern accumulation rate. Neumann and others (2008) found that the accumulation rate over the past ~350 years increased from ~25 cm yr^{-1} at the ice-core site to ~35 cm yr^{-1} at ~40 km farther North (towards the Amundsen Sea).

6.2.3. Surface-velocity measurements

Conway and Rasmussen (2009) presented surface-velocity measurements from a Global Positioning System (GPS) network established near the WAIS Divide during the 2002-2003 and 2003-2004 field seasons. The surface-velocity measurements have an uncertainty of 4 cm yr^{-1}. They find that the ice divide is presently migrating toward the Ross Sea at ~10 m yr^{-1}.

6.3. Inferring transients from internal layers

Neumann and others (2008) showed that the accumulation rate across the WAIS Divide has changed over time. They used a time-dependent ice-flow model to infer an accumulation-rate history, but their model used simplified ice dynamics in one dimension. Spatial gradients in accumulation are observed in this area, and the spatial and temporal influence on internal-layer depth should be taken into account. Ultimately the goal is to infer histories of accumulation rate and ice dynamics from internal layers by solving a 2.5-D transient inverse problem. Here we first infer steady-state accumulation patterns from internal layers by solving a

2.5-D steady-state inverse problem. We use the algorithm developed by Waddington and others (2007).

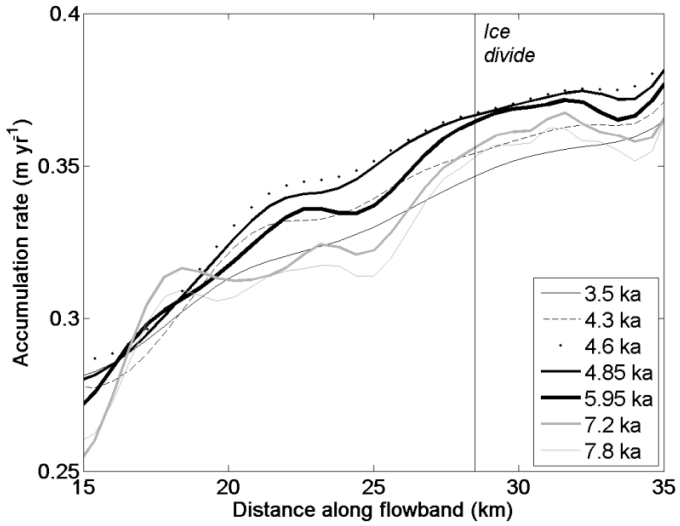

Figure 6.4. Steady-state accumulation-rate patterns inferred by solving seven steady-state inverse problems using internal layers spanning 3.5 ka to ~7.8 ka. The seven internal layers are shown in Figure 6.2.

We use the seven shallowest layers in Figure 6.2 to infer seven different steady-state accumulation patterns; the layers were dated ~3.5 ka to ~7.8 ka. Resolving power decreases further from the divide, so we focus on the internal layers from 15-35 km of a radar line that spans 1-40 km. The ice divide is at ~28.5 km along the flowband. Different steady-state accumulation patterns are inferred from different internal layers. This suggests that the accumulation *rate* has changed over time, and that the accumulation *pattern* has remained roughly the same; this is consistent with Neumann and others (2008). Neumann and others (2008) inferred that accumulation rates have been roughly stable for the past 3,000 years, and

that there was an increase in accumulation rate of at least 30% from 5,000 to 3,000 years ago. We inferred ~6% change in the magnitude of steady-state accumulation from ~3.5 ka to ~7.8 ka. This estimation is not inconsistent with how accumulation transients inferred by Neumann and others (2008) could be averaged over time by a steady-state estimation.

In Figure 6.4, the kilometer-scale spatial variations in the accumulation pattern that we infer by solving seven different steady-state inverse problems reflect kilometer-scale spatial variations in the shape of the internal layers. However, solving separate steady-state problems will give a different history of accumulation than solving a transient problem. Ice-thickness changes and ice-divide position changes are an important part of the history of the WAIS Divide. As we expected, it will be necessary to solve a transient inverse problem to accurately infer transients in accumulation rate and ice dynamics at this site.

6.4. Conclusions and future work

Solving the inverse problem to infer transients in accumulation rate, ice thickness, and ice-divide position will provide valuable, and necessary, constraints on WAIS evolution. Neumann and others (2008) used a 1-D model to infer histories of accumulation and ice dynamics for Holocene layers that were dated by the Byrd ice core. We target deeper layers, which will be dated by annual-layer counting of the WAIS Divide ice core.

Understanding changes in ice volume during the transition from the last glacial period to the present interglacial is central to our understanding of ice-sheet evolution; this is a goal of solving the transient inverse problem

with deep layers from central West Antarctica. This dramatic change in climate led to significant changes in Northern Hemisphere ice volume, but also led to major changes in Antarctica, especially in West Antarctica. While Antarctic ice cores can recover climate histories for many hundreds of thousands of years (e.g. Petit and others, 1999; EPICA members, 2004), we focus on the past ~100,000 years of ice-sheet evolution because there are more data available to constrain this period. We will use our inverse approach to infer histories of accumulation rate, ice thickness, and ice-divide position from internal layers over the past tens of thousands of years. Solutions to an inverse problem to constrain the ice-volume history during the transition from the last glacial maximum (LGM) to the present can be compared to estimates from ice-flow models with prescribed forcing (e.g. Ritz and others, 2001; Huybrechts 2002), and from geologic mapping of terrestrial glacial features (e.g. Ackert and others, 1999; Stone and others, 2003), and mapping of submarine glacial features (e.g. Anderson and others, 2002).

Spatial and temporal gradients in accumulation rate and ice dynamics are significant near the WAIS Divide. Older ice originated further upstream, and as these particle paths traverse significant spatial and temporal gradients, it is no longer appropriate to approximate the total vertical strain using a 1-D model. Our inferred histories will be consistent with the internal structure of the ice sheet, and with present-day measurements. The history of accumulation rate, ice thickness, and ice-divide position are necessary to properly interpret the WAIS Divide ice core, and will provide context for modern changes in ice-sheet flow.

Chapter 7

Synthesis

7.1. Summary

This dissertation presents a method to solve the inverse problem to infer accumulation rates from internal-layer architecture. As part of this inverse problem, a steady-state forward algorithm or a transient forward algorithm could be used. I have demonstrated how a suite of steady-state problems can be formulated, and how they could be solved using radar data across the Martian Polar Layered Deposits (PLD). This application with Martian radar data assumes that past ice flow was important in shaping the internal layers and the ice-surface topography on Mars, and I constrained the necessary conditions for Martian ice to flow at a significant rate. Building from the steady-state inverse problem, I have developed an efficient transient forward algorithm that is well-suited as part of the transient inverse problem to infer histories of accumulation rate, ice thickness, and ice flow. The method I present to solve the transient inverse problem is a valuable new tool that can be used to understand ice-sheet history.

In the process of constructing a numerical model to calculate ice-sheet flow and solve an inverse problem, I have utilized foundational theory in glaciology (e.g. Paterson 1994; Van der Veen 1999; Hooke 2005) and in

inverse theory (e.g. Menke 1989, Parker 1994; Aster and others 2005), as well as foundational theory in numerical methods (e.g. Patankar 1980). The physical equations and physical assumptions necessary to solve this problem have been relayed in this dissertation. However, the effort to find accurate numerical representations and numerical solutions to these equations are also contributions to the field.

A noteworthy aspect of this work is the wide range of questions and data sets to which these theoretical and numerical tools can be applied. While the applications presented here already span Mars to Antarctica, I think this work has the potential to extend much further. We have focused on inferring past accumulation rates, but other parameters, for example the geothermal flux, are also poorly known. In addition to solving this inverse problem with data from different regions and for different parameter values, portions of the forward algorithm could be used independently, or the inverse algorithm could be adapted solve a different inverse problem. Another possibility is that this entire algorithm could be integrated as part of a solution to a larger-scale problem. Specific ideas are discussed in Section 7.4.

7.2. Implications for ice-sheet dynamics

While many 3-D models describe the behavior of large ice sheets to prescribed forcing, there are relatively sparse data available to validate these estimates of ice-sheet evolution. Critical information about ice-sheet history is derived primarily from ice cores, but this information represents only a single point. Internal layers are a powerful data set for understanding histories of ice dynamics because they contain both spatial

and temporal information. Our inverse approach is a new and powerful method for understanding histories of ice dynamics because it assimilates and recovers spatial and temporal information.

Histories of ice-sheet thickness and ice-divide position are necessary to reconstruct ice-volume histories. One of the principal questions facing the glaciology community is how glaciers and ice sheets will contribute to sea-level rise in the coming decades to millennia. Ice sheets respond slower than glaciers and smaller ice caps, but ice-sheet volumes are significantly larger. To gain insight into future ice-sheet behavior, we must understand how ice sheets responded to past climate changes. For example, during the last glacial-interglacial transition, global ice volume was nearly twice the present-day value (e.g. Clark and Mix, 2002). While there are compelling explanations for the evolution of ice-sheet geometries through this transition, specifics are poorly known, and model-based estimates and observational estimates need to be better combined; an inverse approach like the one I have presented in this dissertation is a way to bring together models and observations. In addition, while changing environmental conditions at ice-sheet margins can lead to large and rapid ice-sheet changes there, ice-sheet interiors are also influenced by these changes at the margins. Understanding the evolution of ice-sheet interiors is central to understanding changes in global ice volume and sea level. As we use present-day changes in the flow speed of outlet glaciers to gauge potential ice-sheet behavior, we must take into account the timescales over which this short-term activity can govern global ice-sheet evolution.

Histories of ice-sheet thickness and ice-divide position are necessary to interpret ice-core chemistry. The relationship between oxygen isotopes and surface air temperatures is complicated by changes in ice thickness and ice-divide position, changes in ice flow, and variations in the distribution

and sources of precipitation (e.g. Paterson 1994, pg. 383). Reconstructing the ice-flow history is necessary to develop an accurate depth-age scale for an ice core. In addition, converting chemical concentrations to fluxes from the atmosphere requires the accumulation rate at the time and location of deposition. All of these histories are poorly constrained, but all of these histories can be self-consistently inferred by solving the transient inverse problem. Any bounds on the actual ice-sheet history in the vicinity of ice-core sites could be used directly by the ice-core community. Our inverse approach is more robust in combination with estimates of the age of radar layers that intersect the core, and with any estimates of past accumulation rate that can be made from ice-core analyses (e.g. bubble-number densities or beryllium-10 measurements). Solving inverse problems is a way to answer questions pertinent to both the ice-core community and to the ice-dynamics community.

However, there are challenges to solving any inverse problem. To ensure stability of the solution algorithm, and uniqueness of the solution, we must impose constraints based on *a priori* information. Since there may be limited data available, and there may be limited *a priori* information about the solution, we advocate finding the minimum variation that is required to fit the data and satisfy constraints. Finding the minimum variation will help to avoid overfitting the available data. A smoothed version of the actual history is still valuable to our understanding of ice-sheet history.

7.3. Implications for Mars' polar history

Martian surface topography often evokes terrestrial landscapes, even though the two planets are very different, and the actual evolution of the Martian topography can be difficult to discern remotely. However, radar data across Mars have been revolutionary to our understanding of Martian surface processes. For the PLD, we now have radar delineations of the bed topography and preliminary views of the internal structure. If the PLD have experienced significant ice flow in the past, an inverse approach that accounts for variations in total vertical strain on particle positions through the ice must be used to infer past mass-balance patterns from internal-layer shapes. However, the ice-flow history cannot be determined from internal-layer shapes alone. If the mass-balance history and the ice-flow history are both unknown, internal layer shapes cannot be used to determine the mass-balance history and the ice-flow history. However, as emphasized by Winebrenner and others (2008), a flowing ice mass has a predictable surface shape. The ice surface spatially integrates the mass balance, and the most recent episode of steady-state ice flow can be inferred from present-day ice-surface topography. Then, assuming that the PLD have experienced significant ice flow in the past, an inverse approach can be used to infer past mass balance, as well as past surface topography, from the shapes of internal layers. Inferring past surface topography is important because the modern PLD surface topography has undergone significant erosion, which is concentrated in deeply incising circumpolar troughs. Winebrenner and others (2008) showed that there are few locations with relict topography from which to infer an ice-flow history, and reconstructing topography that is consistent with internal structure would be informative about PLD evolution.

Ice flow at a significant rate on Mars implies that the ice was much warmer than today, and it is likely that significant ice flow also implies that there were variations in the mechanical properties of ice that enhanced the flow. Warmer ice implies warmer surface temperatures, and constraining the ice-flow history is a way to constrain the climate history. The climate that controlled layer formation and evolution is fundamentally unknown, and the PLD chronology is also poorly constrained. Predicting the evolution of the PLD subject to episodes of significant and also insignificant flow, and subject to constraints from present-day surface topography and internal-layer shapes, could be a new way to decipher the ice-flow history of the PLD.

7.4. Future research

The methods presented here use a 2.5-D flowband model, and therefore the data that we need in order to solve this problem must be oriented along a flowline. While most ice-sheet radar data that have been collected do not follow flowlines, radar coverage can be dense across polar ice sheets. On Earth, ice-penetrating radar is critical to identify suitable ice-core sites, and therefore radar data along flowlines often exist in the vicinity of deep ice cores. On Mars, satellite-radar paths are not targeted to follow putative flowlines, but there is a high-density of data at the poles, and some paths are appropriate. For existing radar data on both planets, more effort to accurately project gridded data to align along flow paths would be worthwhile. For future radar-data collection, concerted effort to follow flow paths would benefit studies of ice dynamics.

The two components of this inverse approach, the forward algorithm and the inverse algorithm, require independent assumptions. For example, the governing equations must be represented numerically in the forward

algorithm, and physical expectations about the unknown parameters must be introduced to stabilize the inverse algorithm. These assumptions are well known and often used, but the implications of these approximations in varied applications are often unknown. It is necessary to evaluate these components individually, and also to formally characterize the potential of this inverse approach to answer specific questions. Stemming from this dissertation, there are numerous worthwhile directions and questions to pursue regarding this new method. A few of them are summarized here:

- It is necessary to know what data are required to answer a given question. For example, how many internal layers are necessary to recover centennial-millennial climate variability? The method presented here can determine how large the climate forcing must be in order to be recorded in the ice.

- In addition to radar profiles, this work relies on any available measurements of ice-surface topography, bed topography, modern ice-surface velocity, or modern accumulation rate. While we target deep layers, it may be important to have a shallow layer (i.e. a few hundred years old) available to constrain the recent pattern of accumulation. Constraints on past accumulation are also helpful measurements, and we can quantify what uncertainty is required for these data to be effective in our problem.

- Computing the resolving power and calculating error bars by starting from different initial guesses of the solution should be done for each solution.

- Physical relationships between all the parameter values should be established in order to formalize the weighting scheme used in this inverse algorithm. For example, if individual parameter values can trade off against each other to fit the data, can physical information about how these values should co-vary be imposed to help distinguish the individual influence of each parameter? Or, can the resolving functions be used to weight the influence of each parameter? The effect of additional constraints and of different model norms should be explored.

7.4.1. Specific directions

The high accumulation rates at the WAIS Divide ice-core site may allow layer counting back ~40,000 years. However, deeper layers must be dated using flow models, or distinct horizons must be identified and dated by other means. For example, a strong reflection in the vicinity of the WAIS Divide core site that can be traced for hundreds of kilometers, is dated to ~17,500 years old (e.g. Jacobel and Welch, 2005a), and is a bright reflection because of high acidity (e.g. Hammer and others, 1997). In addition, radars can now image the deepest layers in the ice at high resolution (e.g. Laird and others, In Press); these data may help to constrain the history of the Ross-Amundsen divide. Conway and Rasmussen (2009) showed that the divide is migrating today, but modern measurements cannot determine how long migration towards the Ross Sea has been occurring, or the extent over which the divide has migrated in the past. There is also considerable effort to understand how recent thinning and speed up of Pine Island Glacier (e.g. Shepherd and others, 2001) would affect flow of interior ice.

This inverse approach is well suited to use with data from Greenland and the Arctic ice caps. In the Arctic, higher accumulation rates there mean

that internal layers can be more accurately dated (e.g. Rasmussen and others, 2006). Questions about the pronounced climate variability that punctuated the glacial climate in the Northern Hemisphere, and rapid present-day changes in the Arctic, need to be reconciled with past behavior. There are myriad valuable questions to address with the radar data and ice-core data available across Greenland. For example, isotopic changes in the Camp Century ice core in Northwest Greenland point to an ice thickness change of approximately 800 m since the last glacial period (e.g. Dansgaard and others, 1982), compared to relatively minor thickness changes experienced in central Greenland (e.g. Marshall and Cuffey 2000; Reeh and others, 2002). An independent estimate of ice-thickness changes during this glacial-interglacial transition, and the role of accumulation gradients on ice-sheet evolution during this time are important goals to target (e.g. NGRIP members, 2004). Marshall and Cuffey (2000) showed that divide migration is pronounced during glacial-interglacial transitions, and that the divide may have migrated ~65 km in the past 110 kyr. Using internal layers to solve the inverse problem, we can compare to divide-migration predictions from forward models (e.g. Marshall and Cuffy 2000; Anandakrishnan and others, 1994).

The history of ice volume and ice flow on Mars must be consistent with the history of Mars' climate, and therefore the ice can provide past constraints to help unravel the actual climate history. So far we have targeted questions about the ice-flow history that can be addressed using a steady-state ice-flow model. I think that using internal layers and the ice-surface topography with a transient ice-flow model could constrain plausible histories of ice flow. For example, since orbital variations are so extreme on Mars, and the PLD are stagnant today (assuming that the PLD are pure water ice), it is likely that any history of ice flow included transitions

between flowing and stagnant states; it would be interesting to explore how this type of flow history is imprinted on the shapes of internal layers.

Material in this dissertation provides a springboard for future work. This algorithm could be directly incorporated as part of a larger-scale problem, or it may be possible and fruitful to solve this problem using a 3-D forward algorithm. In addition, it could be insightful to compare solutions to this same problem using other methods. This inverse approach is aligned with the types of data that are available and that are being collected, with our physical understanding of ice flow, and with critical questions facing the glaciology community.

References

Ackert, R.P., D.J. Barclay, H.W. Borns, P.E. Calkin, M.D. Kurz, and others. 1999. Measurements of past ice sheet elevations in interior West Antarctica. *Science*, **286**(5438): 276-280.

Anandakrishnan, S., R.B. Alley and E.D. Waddington. 1994. Sensitivity of the ice-divide position in Greenland to climate change. *Geophysical Research Letters*, **21**(6): 441-444.

Anderson, J.B., S.S. Shipp, A.L. Lowe, J.S. Wellner and A.B. Mosola. 2002. The Antarctic Ice Sheet during the Last Glacial Maximum and its subsequent retreat history: a review. *Quaternary Science Reviews*, **21**(1-3): 49-70.

Anguita, F., R. Babin, G. Benito, D. Gomez, A. Collado, and others. 2000. Chasma Australe, Mars: Structural framework for a catastrophic outflow origin. *Icarus*, **144**(2): 302-312.

Arfken, G.B. and H.J. Weber. 1995. *Mathematical Methods for Physicists.* fourth ed.

Aster, R.C., B. Borchers and C.H. Thurber. 2005. *Parameter Estimation and Inverse Problems.* Elsevier Academic Press.

Azuma, N. 1994. A flow law for anisotropic ice and its applications to ice sheets. *Earth and Planetary Science Letters*, **128**(3-4): 601-614.

Baldwin, D.J., J. Bamber, A.J. Payne and R.L. Layberry. 2003. Using internal layers from the Greenland ice sheet, identified from radio-echo sounding data, with numerical models. *Annals of Glaciology*, **37**: 325-330.

Bamber, J. and E. Rignot. 2002. Unsteady flow inferred for Thwaites Glacier, and comparison with Pine Island Glacier, West Antarctica. *Journal of Glaciology*, **48**(161): 237-246.

Barr, A.C. and S.M. Milkovich. 2008. Ice grain size and the rheology of the martian polar deposits. *Icarus*, **194**: 513-518.

Benito, G., F. Mediavilla, M. Fernandez, A. Marquez, J. Martinez, and others. 1997. Chasma Boreale, Mars: A sapping and outflow channel with a tectono-thermal origin. *Icarus*, **129**(2): 528-538.

Buchardt, S.L. and D. Dahl-Jensen. 2007. Estimating the basal melt rate at NorthGRIP using a Monte Carlo technique. *Annals of Glaciology*, **45**: 137-142.

Byrne, S. and B.C. Murray. 2002. North polar stratigraphy and the paleo-erg of Mars. *Journal of Geophysical Research-Planets*, **107**(E6).

Chandler, D.M., A.L. Hubbard, B.P. Hubbard and P.W. Nienow. 2006. A Monte Carlo error analysis for basal sliding velocity calculations. *Journal of Geophysical Research*, **111**(F04005).

Clark, P.U. and A.C. Mix. 2002. Ice sheets and sea level of the Last Glacial Maximum. *Quaternary Science Reviews*, **21**(1-3): 1-7.

Clifford, S.M. 1987. Polar Basal Melting on Mars. *Journal of Geophysical Research-Solid Earth and Planets*, **92**(B9): 9135-9152.

Conway, H., B.L. Hall, G.H. Denton, A.M. Gades and E.D. Waddington. 1999. Past and future grounding-line retreat of the West Antarctic Ice Sheet. *Science*, **286**(5438): 280-283.

Conway, H. and L.A. Rasmussen. 2009. Recent thinning and migration of the Western Divide, central West Antarctica. *Geophysical Research Letters*, **36**.

Cuffey, K.M. 2000. Methodology for use of isotopic climate forcings in ice sheet models. *Geophysical Research Letters*, **27**(19): 3065-3068.

Cuffey, K.M. and G.D. Clow. 1997. Temperature, accumulation, and ice sheet elevation in central Greenland through the last deglacial transition. *Journal of Geophysical Research-Oceans*, **102**(C12): 26383-26396.

Cuffey, K.M., G.D. Clow, R.B. Alley, M. Stuiver, E.D. Waddington, and others. 1995. Lare Arctic Temperature Change at the Wisconsin-Holocene Glacial Transition. *Science*, **270**(5235): 455-458.

Dansgaard, W., H.B. Clausen, N. Gundestrup, C.U. Hammer, S.F. Johnsen, and others. 1982. A New Greenland Deep Ice Core. *Science*, **218**(4579): 1273-1277.

Dansgaard, W. and S.J. Johnsen. 1969. A flow model and a time scale for the ice core from Camp Century, Greenland. *Journal of Glaciology*, **8**(53): 215-223.

Delory, G.T., W.M. Farrell, S.K. Atreya, N.O. Renno, A.S. Wong, and others. 2006. Oxidant enhancement in martian dust devils and storms: Storm electric fields and electron dissociative attachment. *Astrobiology*, **6**(3): 451-462.

Denton, G.H. and T.J. Hughes. 2002. Reconstructing the Antarctic Ice Sheet at the Last Glacial Maximum. *Quaternary Science Reviews*, **21**(1-3): 193-202.

Durham, W.B., S.H. Kirby and L.A. Stern. 2000. Comparative rheologies of solid H_2O, CO_2, and CO_2 Clathrate Hydrate. *Second International Conference on Mars Polar Science and Exploration*, Rekjavik, Iceland.

Durham, W.B., L.A. Stern and S.H. Kirby. 2001. Rheology of ice I at low stress and elevated confining pressure. *Journal of Geophysical Research-Solid Earth*, **106**(B6): 11031-11042.

Eisen, O. 2008. Inference of velocity pattern from isochronous layers in firn, using an inverse method. *Journal of Glaciology*, **54**(187): 613-630.

Ellehoj, M.D. 2007. Subsurface ice on Mars: A study on ground ice stability and applications. (Masters University of Copenhagen.)

EPICA members. 2004. Eight glacial cycles from an Antarctic ice core. *Nature*, **429**(6992): 623-628.

Fahnestock, M., W. Abdalati, I. Joughin, J. Brozena and P. Gogineni. 2001a. High geothermal heat row, basal melt, and the origin of rapid ice how in central Greenland. *Science*, **294**(5550): 2338-2342.

Fahnestock, M., W. Abdalati, S. Luo and S. Gogineni. 2001b. Internal layer tracing and age-depth-accumulation relationships for the northern

Greenland ice sheet. *Journal of Geophysical Research-Atmospheres*, **106**(D24): 33789-33797.

Fastook, J.L. 2005. Embedded Models: Application to the Ross Sea and Amundsen Sea Sectors, Retreat from LGM. *West Antarctic Ice Sheet (WAIS) Workshop*, Sterling, Virginia.

Fishbaugh, K.E. and J.W. Head. 2002. Chasma Boreale, Mars: Topographic characterization from Mars Orbiter Laser Altimeter data and implications for mechanisms of formation. *Journal of Geophysical Research-Planets*, **107**(E3).

Fishbaugh, K.E. and C.S. Hvidberg. 2006. Martian north polar layered deposits stratigraphy: Implications for accumulation rates and flow. *Journal of Geophysical Research-Planets*, **111**(E6).

Fisher, D.A. 1993. If Martian Ice Caps Flow - Ablation Mechanisms and Appearance. *Icarus*, **105**(2): 501-511.

Fisher, D.A. 2000. Internal layers in an "accublation" ice cap: A test for flow. *Icarus*, **144**: 289-294.

Fisher, D.A., M.H. Hecht, S.P. Kounaves and D.C. Catling. 2009. A perchlorate brine lubricated deformable bed could facilitate flow of the North Polar Cap of Mars: possible mechanisms for water table recharging. *Journal of Geophysical Research*.

Fitzsimons, S.J., K.J. Mcmanus and R.D. Lorrain. 1999. Structure and strength of basal ice and substrate of a dry-based glacier: evidence for substrate deformation at sub-freezing temperatures. *Annals of Glaciology*, **28**: 236-240.

Fitzsimons, S.J., K.J. Mcmanus, P. Sirota and R.D. Lorrain. 2001. Direct shear tests of materials from a cold glacier: implications for landform development. *Quaternary International*, **86**(1): 129-137.

Fortezzo, C.M. and K.L. Tanaka. 2006. Unconformity and bedding orientations in Planum Boreum, Mars: Preliminary results and discussion. *4th International Conference on Mars Polar Science and Exploration*.

Fujita, S., H. Maeno, S. Uratsuka, T. Furukawa, S. Mae, and others. 1999. Nature of radio echo layering in the Antarctic ice sheet detected by a two-frequency experiment. *Journal of Geophysical Research-Solid Earth*, **104**(B6): 13013-13024.

Gagliardini, O. and J. Meyssonnier. 2002. Lateral boundary conditions for a local anisotropic ice-flow model. In Wolff, E.W., *ed.*, 503-509.

Glen, J.W. 1955. The Creep of Polycrystalline Ice. *Proceedings of the Royal Society of London Series a-Mathematical and Physical Sciences*, **228**(1175): 519-538.

Goldsby, D.L. 2006. Superplastic flow of ice relevant to glacier and ice-sheet mechanics. In Knight, P.G., *ed. Glacier Science and Environmental Change*, 308-314.

Goldsby, D.L. and D.L. Kohlstedt. 1997. Grain boundary sliding in fine-grained ice I. *Scripta Mater*, **37**(9): 1399-1406.

Goldsby, D.L. and D.L. Kohlstedt. 2001. Superplastic deformation of ice: Experimental observations. *Journal of Geophysical Research*, **106**(B6): 11017-11030.

Gow, A.J., H.T. Ueda and D.E. Garfield. 1968. Antarctic Ice Sheet - Preliminary Results of First Core Hole to Bedrock. *Science*, **161**(3845): 1011-1013.

Greve, R. and R.A. Mahajan. 2005. Influence of ice rheology and dust content on the dynamics of the north-polar cap of Mars. *Icarus*, **174**(2): 475-485.

Greve, R., R.A. Mahajan, J. Segschneider and B. Grieger. 2004. Evolution of the north-polar cap of Mars: a modelling study. *Planetary and Space Science*, **52**(9): 775-787.

Grott, M., J. Helbert and R. Nadalini. 2007. Thermal structure of Martian soil and the measurability of the planetary heat flow. *Journal of Geophysical Research-Planets*, **112**(E9).

Gubbins, D. 2004. *Time Series Analysis and Inverse Theory for Geophysicists*. Cambridge, Cambridge University Press.

Hammer, C.U., H.B. Clausen and C.C. Langway. 1997. 50,000 years of recorded global volcanism. *Climatic Change*, **35**(1): 1-15.

Hansen, P.C. 1987. *Rank-deficient and discrete ill-posed problems: Numerical aspects of linear inversion*. Society for Industrial Mathematics.

Hecht, M.H., S.P. Kounaves, R.C. Quinn, S.J. West, S.M.M. Young, and others. 2009. Detection of Perchlorate and the Soluble Chemistry of Martian Soil at the Phoenix Lander Site. *Science*, **325**(5936): 64-67.

Herkenhoff, K.E. and J.J. Plant. 2000. Surface ages and resurfacing rates of the polar layered deposits on Mars. *Icarus*, **144**: 243-253.

Hindmarsh, R.C.A., G. Vieli, M.J. Raymond and G.H. Gudmundsson. 2006. Draping or overriding: The effect of horizontal stress gradients on internal layer architecture in ice sheets. *Journal of Geophysical Research-Earth Surface*, **111**(F2).

Hooke, R.L. 2005. *Principles of glacier mechanics*. second ed., Cambridge University Press.

Hooke, R.L., B.B. Dahlin and M.T. Kauper. 1972. Creep of ice containing dispersed fine sand. *Journal of Glaciology*, **11**(63): 327.

Hovius, N., A. Lea-Cox and J.M. Turowski. 2008. Recent volcano-ice interaction and outburst flooding in a Mars polar cap re-entrant. *Icarus*, **197**(1): 24-38.

Hudleston, P.J. 1976. Recumbent folding in the base of the Barnes ice cap, Baffin Island, Northwest Territories, Canada. *Geol. Soc. Am. Bull.*, **87**(12): 1684-1692.

Hutter, K. 1983. *Theoretical glaciology*. Dordrecht, D. Reidel Publishing Company.

Huybrechts, P. 2002. Sea-level changes at the LGM from ice-dynamic reconstructions of the Greenland and Antarctic ice sheets during the glacial cycles. *Quaternary Science Reviews*, **21**(1-3): 203-231.

Huybrechts, P., O. Rybak, F. Pattyn, U. Ruth and D. Steinhage. 2007. Ice thinning, upstream advection, and non-climatic biases for the upper 89% of the EDML ice core from a nested model of the Antarctic ice sheet. *Climate of the Past*, **3**(4): 577-589.

Hvidberg, C.S. 2003. Relationship between topography and flow in the north polar cap on Mars. *Annals of Glaciology*, **37**: 363-369.

Hvidberg, C.S., K. Keller, N. Gundestrup and P. Jonsson. 2001. Ice-divide flow at Hans Tausen Iskappe, North Greenland, from surface movement data. *Journal of Glaciology*, **47**(156): 78-84.

Ipcc. 2007. Chapter 4: Observations: Changes in Snow, Ice and Frozen Ground. *Intergovernmental Panel on Climate Change Working group 1: The physical basis for climate change*.

Ivanov, A.B. and D.O. Muhleman. 2000. The role of sublimation for the formation of the northern ice cap: results from the Mars Orbiter Laser Altimeter. *Icarus*, **144**: 436-448.

Jacobel, R.W. and B.C. Welch. 2005a. A time marker at 17.5 kyr BP detected throughout West Antarctica. *Annals of Glaciology*, **41**: 47-51.

Jacobel, R.W. and B.C. Welch. 2005b. A time marker at 17.5 kyr BP detected throughout West Antarctica. In Hamilton, G., *ed.*, 47-51.

Jacobson, H.P. and E.D. Waddington. 2005. Recumbent folding of divide arches in response to unsteady ice-divide migration. *Journal of Glaciology*, **51**(173): 201-209.

Johannesson, T., C. Raymond and E. Waddington. 1989. Time-scale for adjustment of glaciers to changes in mass balance. *Journal of Glaciology*, **35**(121): 355-369.

Joughin, I., W. Abdalati and M. Fahnestock. 2004a. Large fluctuations in speed on Greenland's Jakobshavn Isbrae glacier. *Nature*, **432**(7017): 608-610.

Joughin, I., D.R. Macayeal and S. Tulaczyk. 2004b. Basal shear stress of the Ross ice streams from control method inversions. *Journal of Geophysical Research-Solid Earth*, **109**(B9).

Joughin, I. and S. Tulaczyk. 2002. Positive mass balance of the Ross Ice Streams, West Antarctica. *Science*, **295**(5554): 476-480.

Kieffer, H.H., S.C. Chase, T.Z. Martin, E.D. Miner and F.D. Palluconi. 1976. Martian North Pole Summer Temperatures - Dirty Water Ice. *Science*, **194**(4271): 1341-1344.

Kieffer, H.H., B.M. Jakosky, C.W. Snyder and M.S. Matthews. 1992. *Mars*. The University of Arizona Press.

Knight, P.G. 1997. The basal ice layer of glaciers and ice sheets. *Quaternary Science Reviews*, **16**(9): 975-993.

Kolb, E.J. and K.L. Tanaka. 2006. Accumulation and erosion of south polar layered deposits in the Promethei Lingula region, Planum Australe, Mars. *Mars*, **2**: 1-9.

Koutnik, M., S. Byrne and B. Murray. 2002. South Polar Layered Deposits of Mars: The cratering record. *Journal of Geophysical Research-Planets*, **107**(E11).

Koutnik, M., E. Waddington and D.P. Winebrenner. 2009. A method to infer past surface mass balance and topography from internal layers in martian polar layered deposits. *Icarus*, **204**: 458-470.

Koutnik, M.R., E. Waddington, D.P. Winebrenner and T.A. Neumann. 2008. Was martian ice warmer in the past? *LPSC XXXIX*.

Laird, C.M., W.A. Blake, K. Matsuoka, H. Conway, C.T. Allen, and others. In Press. Deep Ice Stratigraphy and Basal Conditions in Central West Antarctica Revealed by Coherent Radar. *IEEE Geoscience and Remote Sensing Letters*.

Lam, J.K. and J.A. Dowdeswell. 1996. An adaptive-grid finite-volume model of glacier-terminus fluctuations. *Annals of Glaciology*, **23**: 86-93.

Lambeck, K. and J. Chappell. 2001. Sea level change through the last glacial cycle. *Science*, **292**(5517): 679-686.

Lambert, F., B. Delmonte, J.R. Petit, M. Bigler, P.R. Kaufmann, and others. 2008. Dust-climate couplings over the past 800,000 years from the EPICA Dome C ice core. *Nature*, **452**(7187): 616-619.

Larsen, J. and D. Dahl-Jensen. 2000. Interior temperatures of the northern polar cap on Mars. *Icarus*, **144**: 456-462.

Laskar, J., A.C.M. Correia, M. Gastineau, F. Joutel, B. Levrard, and others. 2004. Long term evolution and chaotic diffusion of the insolation quantities of Mars. *Icarus*, **170**(2): 343-364.

Laskar, J., B. Levrard and J.F. Mustard. 2002. Orbital forcing of the martian polar layered deposits. *Nature*, **419**(6905): 375-377.

Levrard, B., F. Forget, F. Montmessin and J. Laskar. 2004. Recent ice-rich deposits formed at high latitudes on Mars by sublimation of unstable equatorial ice during low obliquity. *Nature*, **431**(7012): 1072-1075.

Levrard, B., F. Forget, F. Montmessin and J. Laskar. 2007. Recent formation and evolution of northern Martian polar layered deposits as inferred from a Global Climate Model. *Journal of Geophysical Research-Planets*, **112**(E6).

Leysinger-Vieli, G.J.-M.C. and G.H. Gudmundsson. 2004. On estimating length fluctuations of glaciers caused by changes in climatic forcing. *Journal of Geophysical Research-Earth Surface*, **109**(F1).

Leysinger-Vieli, G.J.-M.C., R. Hindmarsh and M.J. Siegert. 2007. Three-dimensional flow influences on radar layer stratigraphy. *Annals of Glaciology*, **46**: 22-28.

Li, X., D. Iliescu and I. Baker. 2009. On the effects of temperature on the strength of H2SO4-doped ice single crystals. *Journal of Glaciology*, **55**(191): 481-484.

Macayeal, D.R. 1993. A Tutorial on the Use of Control Methods in Ice-Sheet Modeling. *Journal of Glaciology*, **39**(131): 91-98.

Marshall, S.J. and G.K.C. Clarke. 1997. A continuum mixture model of ice stream thermomechanics in the Laurentide Ice Sheet .1. Theory. *Journal of Geophysical Research-Solid Earth*, **102**(B9): 20599-20613.

Marshall, S.J. and K.M. Cuffey. 2000. Peregrinations of the Greenland Ice Sheet divide in the last glacial cycle: implications for central Greenland ice cores. *Earth and Planetary Science Letters*, **179**(1): 73-90.

Martin, C., R.C.A. Hindmarsh and F.J. Navarro. 2006. Dating ice flow change near the flow divide at Roosevelt Island, Antarctica, by using a thermomechanical model to predict radar stratigraphy. *Journal of Geophysical Research-Earth Surface*, **111**(F1).

Martin, C., R.C.A. Hindmarsh and F.J. Navarro. 2009. On the effects of divide migration, along-ridge flow, and basal sliding on isochrones near an ice divide. *Journal of Geophysical Research-Earth Surface*, **114**.

Martin, L.J. and R.W. Zurek. 1993. An analysis of the history of dust activity on Mars. *Journal of Geophysical Research*, **98**: 3221-3246.

Maxwell, D., M. Truffer, S. Avdonin and M. Stuefer. 2008. An iterative scheme for determining glacier velocities and stresses. *Journal of Glaciology*, **54**(188): 888-898.

Menke, W. 1989. *Geophysical data analysis : discrete inverse theory*. San Diego, Academic Press.

Milkovich, S.M. and J.W. Head. 2005. North polar cap of Mars: Polar layered deposit characterization and identification of a fundamental climate signal. *Journal of Geophysical Research-Planets*, **110**(E1).

Milkovich, S.M. and J.J. Plaut. 2008. Martian South Polar Layered Deposit stratigraphy and implications for accumulation history. *Journal of Geophysical Research-Planets*, **113**(E6).

Mischna, M.A. and M.I. Richardson. 2005. A reanalysis of water abundances in the Martian atmosphere at high obliquity. *Geophysical Research Letters*, **32**(3).

Morse, D.L., D.D. Blankenship, E.D. Waddington and T.A. Neumann. 2002. A site for deep ice coring in West Antarctica: results from aerogeophysical surveys and thermo-kinematic modeling. *Annals of Glaciology*, **35**: 36-44.

Morse, D.L., E.D. Waddington, H.P. Marshall, T.A. Neumann, E.J. Steig, and others. 1999. Accumulation rate measurements at Taylor Dome, East Antarctica: Techniques and strategies for mass balance measurements in polar environments. *Geografiska Annaler Series a-Physical Geography*, **81A**(4): 683-694.

Morse, D.L., E.D. Waddington and E.J. Steig. 1998. Ice age storm trajectories inferred from radar stratigraphy at Taylor Dome, Antarctica. *Geophysical Research Letters*, **25**(17): 3383-3386.

Murray, B., M. Koutnik, S. Byrne, L. Soderblom, K. Herkenhoff, and others. 2001. Preliminary geological assessment of the northern edge of ultimi lobe, Mars south polar layered deposits. *Icarus*, **154**(1): 80-97.

Nereson, N.A. and C.F. Raymond. 2001. The elevation history of ice streams and the spatial accumulation pattern along the Siple Coast of West Antarctica inferred from ground-based radar data from three inter-ice-stream ridges. *Journal of Glaciology*, **47**(157): 303-313.

Nereson, N.A., C.F. Raymond, R.W. Jacobel and E.D. Waddington. 2000. The accumulation pattern across Siple Dome, West Antarctica, inferred from radar-detected internal layers. *Journal of Glaciology*, **46**(152): 75-87.

Nereson, N.A. and E.D. Waddington. 2002. Isochrones and isotherms beneath migrating ice divides. *Journal of Glaciology*, **48**(160): 95-108.

Neumann, T.A., H. Conway, S.F. Price, E.D. Waddington, G.A. Catania, and others. 2008. Holocene accumulation and ice sheet dynamics in central West Antarctica. *Journal of Geophysical Research-Earth Surface*, **113**(F2).

NGRIP members. 2004. High-resolution record of Northern Hemisphere climate extending into the last interglacial period. *Nature*, **431**(7005): 147-151.

Nye, J.F. 1960. The Response of Glaciers and Ice-Sheets to Seasonal and Climatic Changes. *Proceedings of the Royal Society of London Series a-Mathematical and Physical Sciences*, **256**(1287): 559-584.

Nye, J.F. 1963. Response of a Glacier to Changes in Rate of Nourishment and Wastage. *Proceedings of the Royal Society of London Series a-Mathematical and Physical Sciences*, **275**(OCT): 87-&.

Nye, J.F. 2000. A flow model for the polar caps of Mars. *Journal of Glaciology*, **46**(154): 438-444.

Oerlemans, J. 1981. Some basic experiments with a vertically-integrated ice-sheet model. *Tellus*, **33**(1): 1-11.

Ohmura, A., P. Calanca, M. Wild and M. Anklin. 1999. Precipitation, accumulation, and mass balance of the Greenland ice sheet. *Zeitschr. Gletscherk. Glazialgeol.*, **35**: 1-20.

Onur, O. and S. Eyi. 2005. Effects of the Jacobian evaluation on Newton's solution of the Euler equations. *International Journal for Numerical Methods in Fluids*, **49**: 211-231.

Paige, D.A. and K.D. Keegan. 1994. Thermal and albedo mapping of the polar-regions of Mars using viking thermal mapper observations 2. South polar-region. *Journal of Geophysical Research-Planets*, **99**(E12): 25993-26013.

Paren, J.G. and G.D. Robin. 1975. Internal reflections in polar ice sheets. *Journal of Glaciology*, **14**(71): 251-259.

Parker, R.L. 1994. *Geophysical inverse theory*. Princeton, N.J., Princeton University Press.

Parrenin, F. and R. Hindmarsh. 2007. Influence of a non-uniform velocity field on isochrone geometry along a steady flowline of an ice sheet. *Journal of Glaciology*, **53**(183): 612-622.

Parrenin, F., R.C.A. Hindmarsh and F. Remy. 2006. Analytical solutions for the effect of topography, accumulation rate and lateral flow divergence on isochrone layer geometry. *Journal of Glaciology*, **52**(177): 191-202.

Patankar, S. 1980. *Numerical heat transfer and fluid flow*. Hemisphere Publishing Company.

Paterson, W.S. 1972. Laurentide Ice Sheet - estimated volumes during late Wisconsin. *Reviews of Geophysics and Space Physics*, **10**(4): 885-&.

Paterson, W.S.B. 1969. The Meighen ice cap, Arctic Canada: Accumulation, ablation and flow. *Journal of Glaciology*, **8**(51): 341-352.

Paterson, W.S.B. 1994. *The physics of glaciers*. 3rd ed. Oxford, England, Pergamon.

Pathare, A.V. and D.A. Paige. 2005. The effects of martian orbital variations upon the sublimation and relaxation of north polar troughs and scarps. *Icarus*, **174**(2): 419-443.

Pathare, A.V., D.A. Paige and E. Turtle. 2005. Viscous relaxation of craters within the martian south polar layered deposits. *Icarus*, **174**(2): 396-418.

Petit, J.R., J. Jouzel, D. Raynaud, N.I. Barkov, J.M. Barnola, and others. 1999. Climate and atmospheric history of the past 420,000 years from the Vostok ice core, Antarctica. *Nature*, **399**(6735): 429-436.

Pettit, E.C. and E.D. Waddington. 2003. Ice flow at low deviatoric stress. *Journal of Glaciology*, **49**(166): 359-369.

Phillips, R.J., M.T. Zuber, S.E. Smrekar, M.T. Mellon, J.W. Head, and others. 2008. Mars north polar deposits: Stratigraphy, age, and geodynamical response. *Science*, **320**(5880): 1182-1185.

Picardi, G., J.J. Plaut, D. Biccari, O. Bombaci, D. Calabrese, and others. 2005. Radar soundings of the subsurface of Mars. *Science*, **310**(5756): 1925-1928.

Pinglot, J.F., J.O. Hagen, K. Melvold, T. Eiken and C. Vincent. 2001. A mean net accumulation pattern derived from radioactive layers and radar

soundings on Austfonna, Nordaustlandet, Svalbard. *Journal of Glaciology*, **47**(159): 555-566.

Plaut, J.J., R. Kahn, E.A. Guinness and R.E. Arvidson. 1988. Accumulation of sedimentary debris in the south polar-region of Mars and implications for climate history. *Icarus*, **76**(2): 357-377.

Plaut, J.J., G. Picardi, A. Safaeinili, A.B. Ivanov, S.M. Milkovich, and others. 2007. Subsurface radar sounding of the south polar layered deposits of Mars. *Science*, **316**(5821): 92-95.

Price, S.F., H. Conway and E.D. Waddington. 2007. Evidence for late pleistocene thinning of Siple Dome, West Antarctica. *Journal of Geophysical Research-Earth Surface*, **112**(F3): -.

Putzig, N.E., R.J. Phillips, B.A. Campbell, J.W. Holt, J.J. Plaut, and others. 2009. Subsurface structure of Planum Boreum from Mars Reconnaissance Orbiter Shallow Radar soundings. *Icarus*.

Raisbeck, G.M., F. Yiou, M. Fruneau, J.M. Loiseaux, M. Lieuvin, and others. 1981. Cosmogenic ^{10}Be concentrations in Antarctic ice during the past 30,000 years. *Nature*, **292**: 825-826.

Rasmussen, S.O., K.K. Andersen, A.M. Svensson, J.P. Steffensen, B.M. Vinther, and others. 2006. A new Greenland ice core chronology for the last glacial termination. *Journal of Geophysical Research-Atmospheres*, **111**(D6).

Raymond, M.J. and G.H. Gudmundsson. 2005. On the relationship between surface and basal properties on glaciers, ice sheets, and ice streams. *Journal of Geophysical Research-Solid Earth*, **110**(B8).

Reeh, N. 1988. A flow-line model for calculating the surface profile and the velocity, strain-rate, and stress-fields in an ice sheet. *Journal of Glaciology*, **34**(116): 46-54.

Reeh, N., H. Oerter and E. Thomsen. 2002. Comparison between ice-margin and ice core oxygen-18 records. *Annals of Glaciology*, **35**: 136-144.

Richardson, M.I. and R.J. Wilson. 2002. A topographically forced asymmetry in the martian circulation and climate. *Nature*, **416**(6878): 298-301.

Rignot, E., G. Casassa, P. Gogineni, W. Krabill, A. Rivera, and others. 2004. Accelerated ice discharge from the Antarctic Peninsula following the collapse of Larsen B ice shelf. *Geophysical Research Letters*, **31**(18).

Rignot, E. and P. Kanagaratnam. 2006. Changes in the velocity structure of the Greenland ice sheet. *Science*, **311**(5763): 986-990.

Ritz, C., V. Rommelaere and C. Dumas. 2001. Modeling the evolution of Antarctic ice sheet over the last 420,000 years: Implications for altitude changes in the Vostok region. *Journal of Geophysical Research-Atmospheres*, **106**(D23): 31943-31964.

Ross, R.G. and J.S. Kargel. 1998. Thermal conductivity of solar system ices, with special reference to Martian polar caps. In Schmitt, B., *ed. Solar system ices*, Dordrecht, Netherlands, Klewer Academic Publishers.

Salathe, E.P., P.W. Mote and M.W. Wiley. 2007. Considerations for selecting downscaling methods for integrated assessments of climate change impacts. *International Journal of Climatology*, **27**: 1611-1621.

Samyn, D., S.J. Fitzsimons and R.D. Lorrain. 2005. Strain-induced phase changes within cold basal ice from Taylor Glacier, Antarctica, indicated by textural and gas analyses. *Journal of Glaciology*, **51**(175): 611-619.

Schorghofer, N. 2008. Temperature response of mars to Milankovitch cycles. *Geophysical Research Letters*, **35**(18).

Seu, R., R.J. Phillips, G. Alberti, D. Biccari, F. Bonaventura, and others. 2007. Accumulation and erosion of Mars' south polar layered deposits. *Science*, **317**(5845): 1715-1718.

Shepherd, A.P., D.J. Wingham, J.A.D. Mansley and H.F.J. Corr. 2001. Inland thinning of Pine Island Glacier, West Antarctica. *Science*, **291**(5505): 862-864.

Siegert, M.J. 2003. Glacial-interglacial variations in central East Antarctic ice accumulation rates. *Quaternary Science Reviews*, **22**(5-7): 741-750.

Siegert, M.J. and A.J. Payne. 2004. Past rates of accumulation in central West Antarctica. *Geophysical Research Letters*, **31**(12).

Sowers, T., M. Bender and D. Raynaud. 1989. Elemental and isotopic composition of occluded O-2 and N-2 in polar ice. *Journal of Geophysical Research-Atmospheres*, **94**(D4): 5137-5150.

Spencer, M.K., R.B. Alley and J.J. Fitzpatrick. 2006. Developing a bubble number-density paleoclimatic indicator for glacier ice. *Journal of Glaciology*, **52**(178): 358-364.

Spikes, V.B., G. Hamilton, S.A. Arcone, S. Kaspari and P.A. Mayewski. 2004. Variability in accumulation rates from GPR profiling on the West Antarctic plateau. *Annals of Glaciology*, **39**: 238-244.

Steen-Larsen, H.C., E. Waddington and M. Koutnik. In Press. Formulating an inverse problem to infer the accumulation-rate pattern from deep internal layering in an ice sheet using a Monte Carlo approach. *Journal of Glaciology*.

Stone, J.O., G.A. Balco, D.E. Sugden, M.W. Caffee, L.C. Sass, and others. 2003. Holocene deglaciation of Marie Byrd Land, West Antarctica. *Science*, **299**(5603): 99-102.

Tanaka, K.L. 2005. Geology and insolation-driven climatic history of Amazonian north polar materials on Mars. *Nature*, **437**(7061): 991-994.

Tanaka, K.L., J.A.P. Rodriguez, J.A. Skinner, M.C. Bourke, C.M. Fortezzo, and others. 2008. North polar region of Mars: Advances in stratigraphy, structure, and erosional modification. *Icarus*, **196**(2): 318-358.

Thorsteinsson, T., J. Kipfstuhl and H. Miller. 1997. Textures and fabrics in the GRIP ice core. *Journal of Geophysical Research-Oceans*, **102**(C12): 26583-26599.

Thorsteinsson, T., E. Waddington and R.C. Fletcher. 2003. Spatial and temporal scales of anisotropic effects in ice-sheet flow. *Annals of Glaciology*, **37**: 40-48.

Touma, J. and J. Wisdom. 1993. The Chaotic Obliquity of Mars. *Science*, **259**(5099): 1294-1296.

Truffer, M. 2004. The basal speed of valley glaciers: an inverse approach. *Journal of Glaciology*, **50**(169): 236-242.

Van Den Berg, J., R.S.W. Van De Wal and J. Oerlemans. 2006. Effects of spatial discretization in ice-sheet modelling using the shallow-ice approximation. *Journal of Glaciology*, **52**(176): 89-98.

Van Der Veen, C. 1999. *Fundamentals of glacier dynamics.* Rotterdam, Taylor & Francis.

Van Der Veen, C. and J. Oerlemans. 1984. *Ice sheets and climate.* Dordrecht/Boston/Lancaster, Reidel.

Van Der Veen, C. and I.M. Whillans. 1989. Force budget: I. Theory and numerical methods. *Journal of Glaciology*, **35**: 53-60.

Vasavada, A.R., J.P. Williams, D.A. Paige, K.E. Herkenhoff, N.T. Bridges, and others. 2000. Surface properties of Mars' polar layered deposits and polar landing sites. *Journal of Geophysical Research-Planets*, **105**(E3): 6961-6969.

Vaughan, D.G., H.F.J. Corr, C.S.M. Doake and E.D. Waddington. 1999. Distortion of isochronous layers in ice revealed by ground-penetrating radar. *Nature*, **398**(6725): 323-326.

Versteeg, H.K. and W. Malalasekera. 1995. *An Introduction to Computational Fluid Mechanics: The Finite Volume Method.* Essex, England, Pearson Education Ltd.

Vialov, S.S. 1958. Regularities of glacial shields movements and the theory of plastic viscous flow. *Physics of the movements of ice*, **47**: 266-275.

Waddington, E. 1982. Accurate modelling of glacier flow. (PhD University of British Columbia.)

Waddington, E.D., J.F. Bolzan and R.B. Alley. 2001. Potential for stratigraphic folding near ice-sheet centers. *Journal of Glaciology*, **47**(159): 639-648.

Waddington, E.D., H. Conway, E.J. Steig, R.B. Alley, E.J. Brook, and others. 2005. Decoding the dipstick: Thickness of Siple Dome, West Antarctica, at the Last Glacial Maximum. *Geology*, **33**(4): 281-284.

Waddington, E.D., T.A. Neumann, M.R. Koutnik, H.P. Marshall and D.L. Morse. 2007. Inference of accumulation-rate patterns from deep layers in glaciers and ice sheets. *Journal of Glaciology*, **53**(183): 694-712.

Ward, W.R. 1992. Long-term orbital and spin dynamics of Mars. In Kieffer, H.H., B.M. Jakosky, C.W. Snyder and M.S. Matthews, *eds. Mars*, Tucson, University of Arizona Press, 298-320.

Weertman, J. 1958. Traveling waves on glaciers. *IASH*, **47**: 162-168.

Whorton, E., E.C. Pettit, E. Waddington and R. Sletten. In Preparation. Debris-rich basal ice layer effects on polar glacier dynamics.

Winebrenner, D.P., M.R. Koutnik, E.D. Waddington, A.V. Pathare, B.C. Murray, and others. 2008. Evidence for ice flow prior to trough formation in the martian north polar layered deposits. *Icarus*, **195**(1): 90-105.

Wunsch, C. 1996. *The ocean circulation inverse problem*. Cambridge University Press.

Appendix A: Constants and symbols

Symbol	**Parameter**	**Value**
g	acceleration of gravity	9.81 m s^{-2}
ρ	density of ice	916 kg m^{-3}
n	flow-law exponent	3
Q	activation energy for creep	
	below -10 °C	42 - 84 kJ mol^{-1}
	above -10 °C	139 kJ mol^{-1}
R	gas constant	8.314 J mol^{-1} K^{-1}

Age	internal-layer age
A_0	temperture-independent ice-softness parameter
$A(T)$	temperature-dependent ice-softness parameter
α	surface slope
a	ablation rate
$\dot{b}$	accumulation rate
c	accumulation rate (Chapter 3)
E	ice-flow enhancement factor
$\dot{\varepsilon}$	strain rate
h	ice thickness
H	maximum ice thickness
ϕ	horizontal velocity shape function
I_p	performance index
L	ice-mass length
m	slope
$\dot{m}$	basal-melt rate
Q_{in}^0	ice-flux initial condition
Q_{geo}	geothermal flux
S_{in}^0	ice-thickness initial condition
S	ice-surface elevation
t	temporal coordinate
T	ice temperature
τ	shear stress

Symbol	**Parameter**
u	horizontal velocity
$\overline{u}$	average horizontal velocity
v	vertical velocity
V	volume
ψ	vertical velocity shape function
W	flowband width
x	horizontal coordinate
$\hat{x}$	normalized horizontal coordinate
z	vertical coordinate
$\hat{z}$	normalized horizontal coordinate

Appendix B: Maps

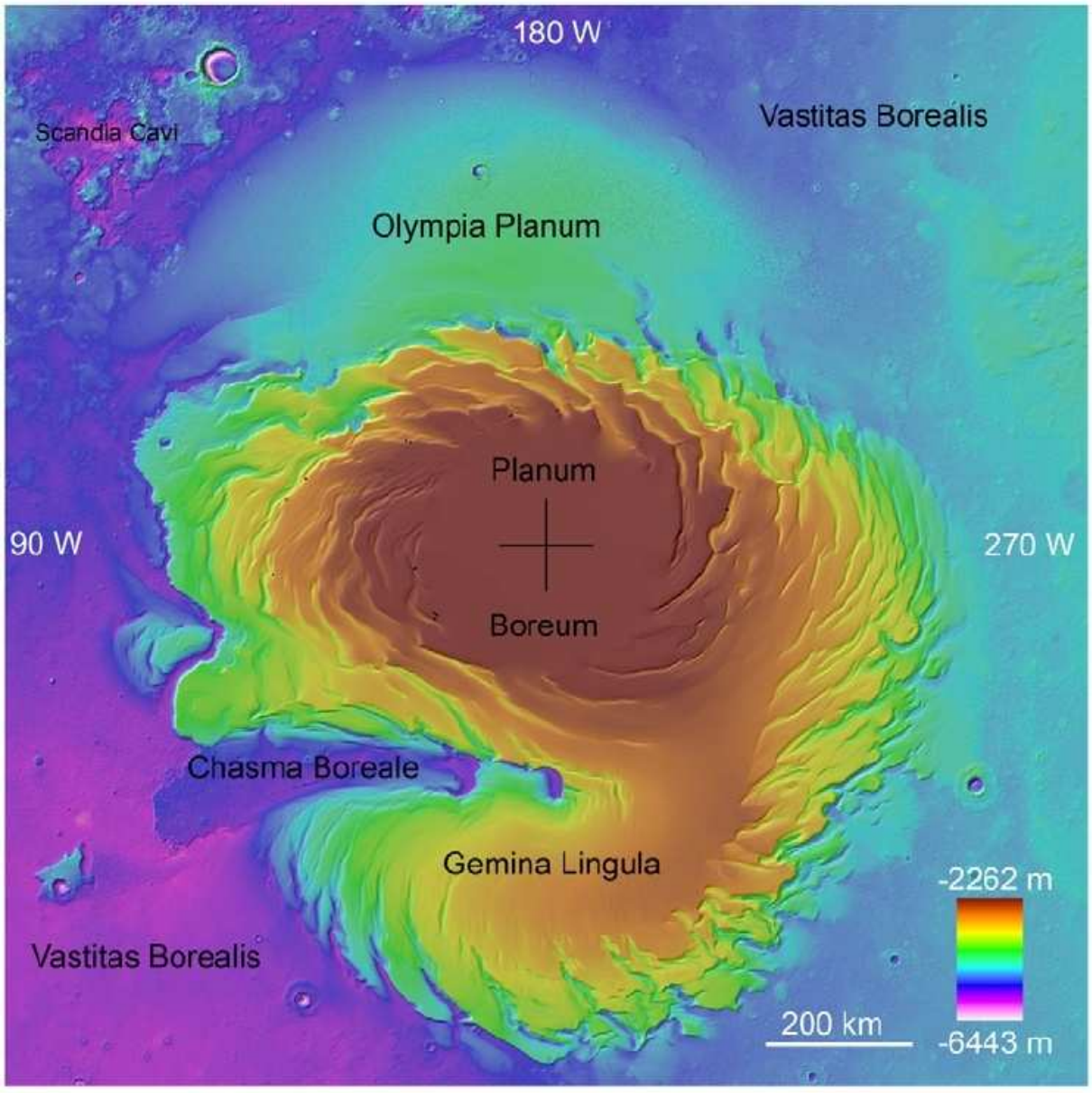

Figure B.1. North Polar Layered Deposits, Mars. Figure from Fishbaugh and others (2008). Image is shaded-relief topography.

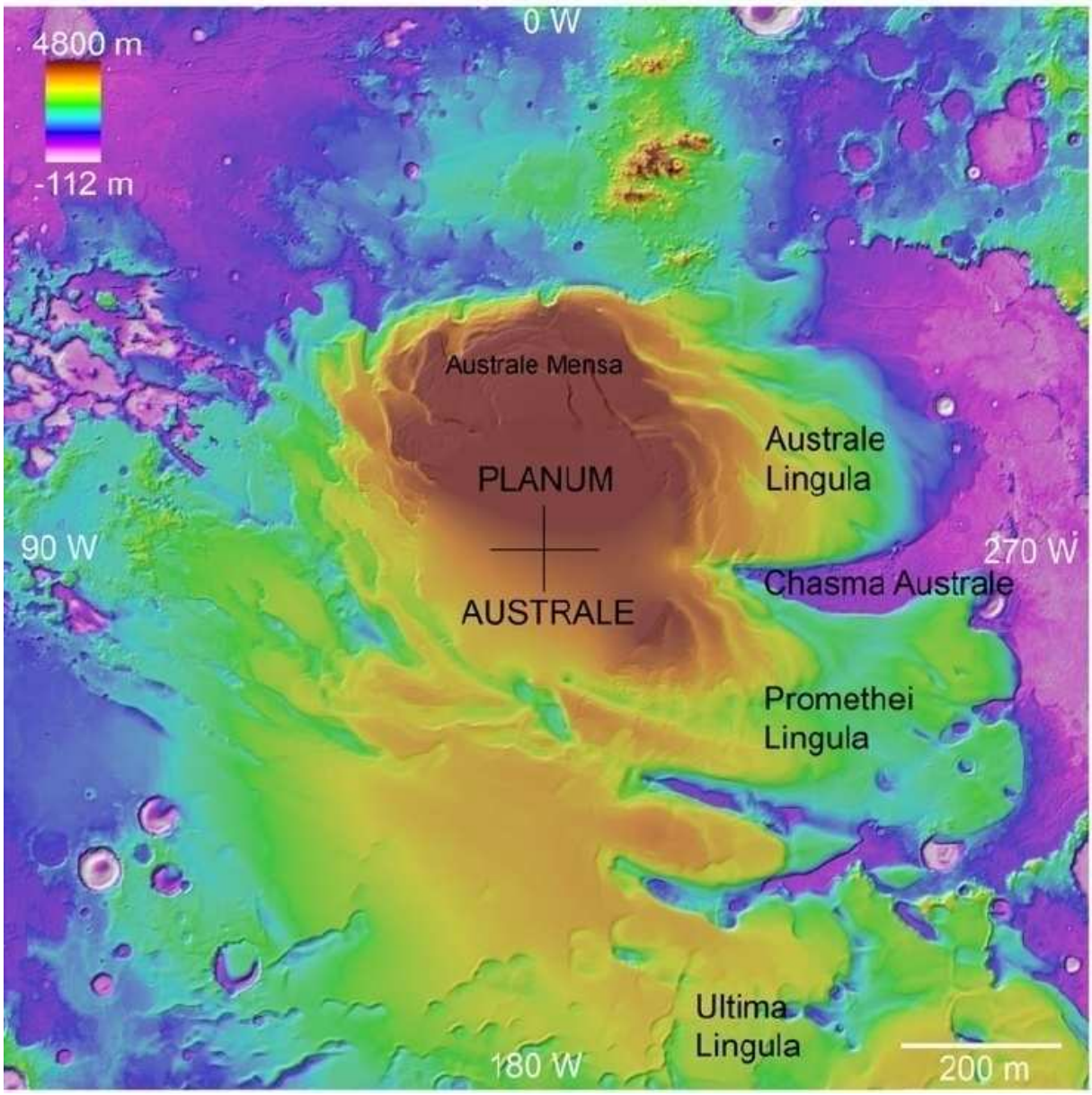

Figure B.2. South Polar Layered Deposits, Mars. Figure from Fishbaugh and others (2008). Image is shaded-relief topography.

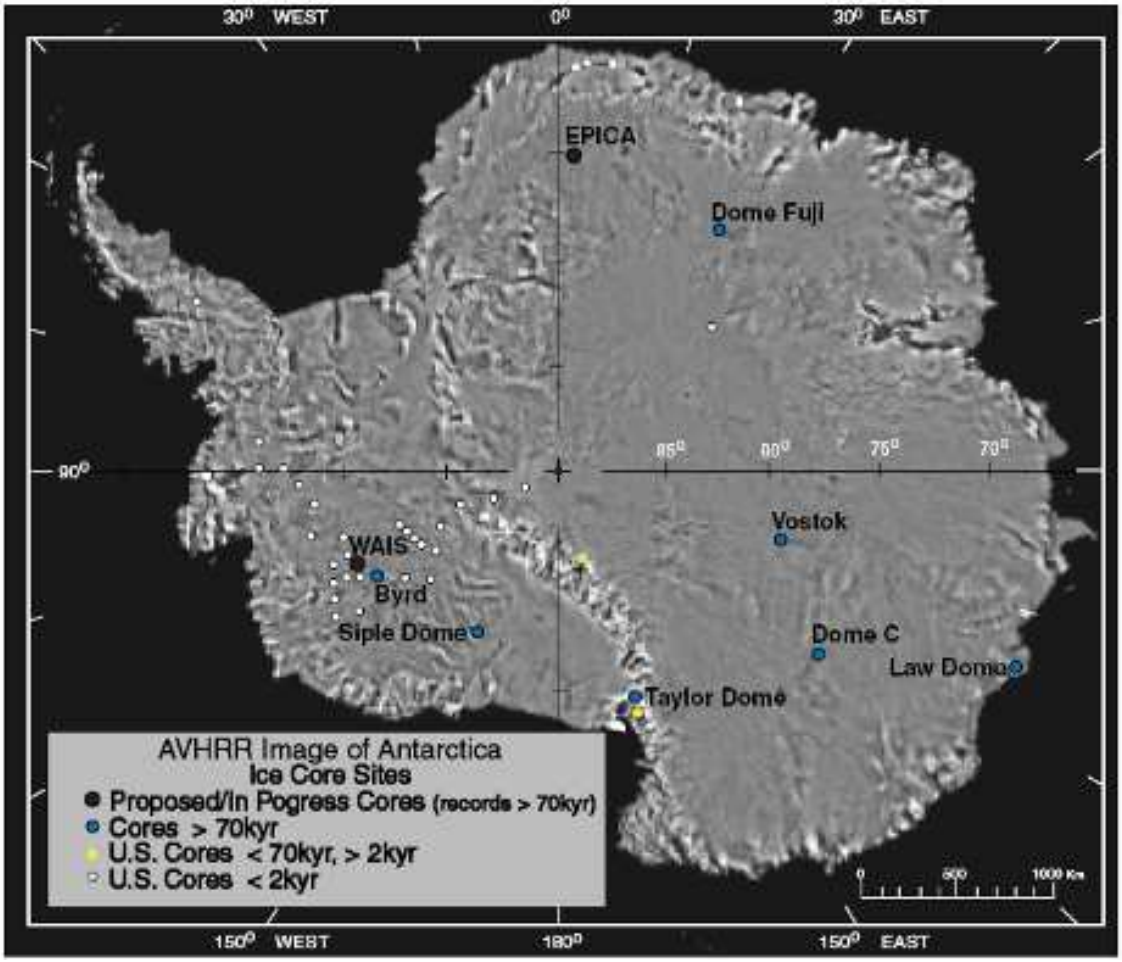

Figure B.3. AVHRR (Advanced Very High Resolution Radiometer) map of Antarctica, including deep ice core sites. Figure from Ice Core Working Group (2003).

Appendix C: Parameters for Earth and Mars

	Earth	**Mars**
Mean radius (m)	6371	3389
Mass (10^{23} kg)	59.736	6.4185
Density (g cm^{-3})	5.515	3.933
Sidereal rotation period (h)	23.93419	24.622962
Equatorial gravity (m s^{-2})	9.78	3.69
Obliquity of axis	23.45 º	25.19 º

Table C1. Geophysical parameters for Earth and Mars (values from *Planetary Sciences*, Imke de Pater and Jack Lissauer 2001, Cambridge Univ. Press).

	Definition	**Earth**	**Mars**
Argument of perihelion (1)	The angle between the ascending node (going north, the point in the orbit where the ecliptic is crossed) and the perihelion measured counter-clockwise along the plane of the orbit	102.8º	336 º
Eccentricity (2)	Shape of the orbit, eccentricity is zero for a circular orbit	0.0167 º	0.093 º
Inclination (3)	The angle between the plane of the orbit and the plane of the ecliptic (plane of the Earth's orbit around the sun)	0 º	1.85 º
Longitude of the Ascending node (4)	The angle between the vernal equinox and the ascending node, measured counter-clockwise	--	49.6
Semimajor axis of orbit (5)	The longer half of the axes of the orbital ellipse	1 AU	1.524 AU

Table C2. Orbital elements for Earth and Mars (values from *Fundamental Astronomy*, Karttunen and others 1996, Springer).

	Effect	**Range of values**	**Periodicity**
Eccentricity of orbit	Strong seasonal effect (e.g. dust storms); small effect on insolation	~0-0.1	99 Kyr, 2.4 Myr
Inclination of orbit	No direct effect on insolation but effects obliquity	~0º -5º	1.2 Myr
Precession of orbit	No direct effect on insolation but can lead to secular spin-orbit resonance	--	72 Kyr
Precession of spin axis	Latitudinal effect on seasonal insolation and can lead to secular spin-orbit resonance	--	51 Kyr
Obliquity of spin axis	Also altered by changes in other parameters, strong latitudinal effect on annual insolation	~13º -48º	120 Kyr, 95 Kyr
"Precession" of the Equinoxes	Not an orbital parameter, but has a strong latitudinal effect on annual insolation	--	150 Kyr

Table C3. Parameter Variations for Mars for the last ~20 Myr (Ward, Mars book 1992; Laskar and others 2002; Fishbaugh, ISSI presentation 2008).

Martian Seasons

Martian seasons are measured by the areocentric longitude of the Sun (L_s), which is the angle between Mars and the Sun measured with respect to the Northern hemisphere at the vernal equinox, where $L_s=0^o$ (e.g. Kieffer and others, 1992; Laskar and others 2004). A Martian day (sol) is 88775.245 seconds, and a Martian year is 668.6 sols. A Martian month spans $L_s=30^o$, and due to the eccentricity of the orbit the length of a month ranges from 46-67 sols.

Month	Ls range	Sol range	Duration	Events
1	0-30	0-61.2	61.2	NH Vernal equinox, $L_s=0$
2	30-60	61.2-126.6	65.4	--
3	60-90	126.6-193.3	66.7	Aphelion at $L_s=71$
4	90-120	193.3-257.8	64.5	NH Summer solstice, $L_s=90$
5	120-150	257.-8-317.5	59.7	--
6	150-180	317.5-371.9	54.4	--
7	180-210	371.9-421.6	49.7	NH Autumnal equinox, $L_s=180$
8	210-240	421.6-468.5	46.9	Perihelion at $L_s=251$
9	240-270	468.5-514.6	46.1	NH Winter solstice, $L_s=270$
10	270-300	514.6-562	47.4	--
11	300-330	562-612.9	50.9	--
12	330-360	612.9-668.6	55.7	--

Table C4. (values from Laskar: http://www-mars.lmd.jussieu.fr/mars/time/solar_longitude.html)

Appendix D: Insolation variations on Mars

Mars' orbital parameters are highly chaotic compared to Earth because of secular spin-orbit resonance between Mars and nearby planetary objects (e.g. Touma and Wisdom, 1993). Due to this chaotic interaction, the obliquity, the eccentricity, and the precession can be reliably reconstructed only over the past 10-20 Myr (e.g. Laskar and others 2004); solutions from further in the past are nonunique. Presently, Mars has an Earth-like obliquity of 25.2°, but over the last 10 Myr, Mars' obliquity reached a minium value of ~14° and a maximum value of ~48°, cycling from higher to lower values every 10^4-10^5 years with an average of ~32° (Touma and Wisdom, 1993; Laskar and others 2004). From ~4-10 Myr ago, obliquity fluctuated about 35°, whereas from ~4 Myr ago to the present, obliquity fluctuated about 25° (Touma and Wisdom, 1993; Laskar and others 2004). As noted by Pathare and Paige (2005), the obliquity variation is severe, and Mars' obliquity remains within 5° of any given value for less than 10,000 years. However, every 2-3 Myr there are periods where obliquity varies only slightly, which has been the situation from 0.5 Myr ago to the present.

The present-day eccentricity is 0.093 (e.g. Ward, 1992) and Mars experiences quasiperiodic variations in eccentricity of 0.04 every ~10^5 years, in addition to a larger variation of 0.1 every ~2 Myr. In addition, over the past 10 Myr, Mars' eccentricity is highest during the few-thousand-year periods when the obliquity varies only slightly. Mars has an argument of perihelion of 251°, describing the direction of the major axis during orbit around the sun. This varies from 90 ° -270° with an ~50,000 year period (Ward, 1992). See Appendix C for a comparison of orbital parameters for Earth and Mars, and the range and periodicity of orbital-parameter variation for Mars.

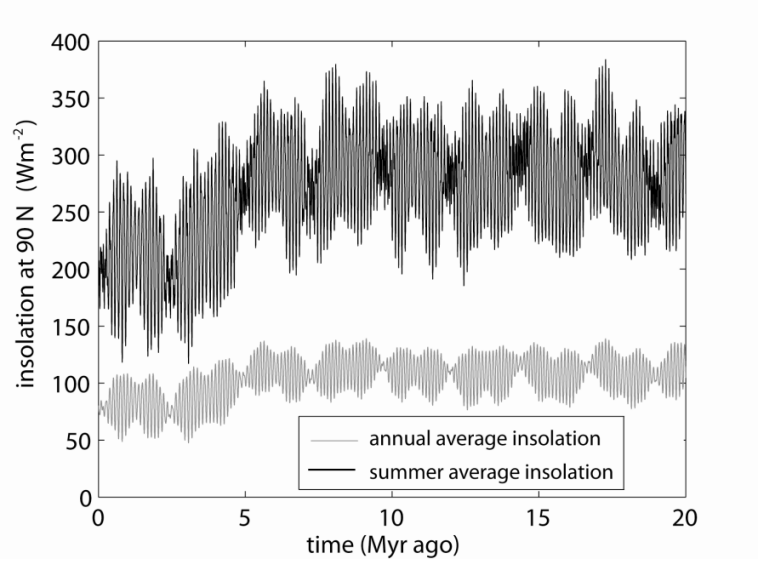

Figure D.1. Annual-average insolation compared to summer-average insolation at 90 N over the past 20 Myr (data from Laskar and others 2004).

The effects of orbital variations on Mars' surface temperature have been calculated (e.g. Pathare and Paige 2005; Levrard and others 2007; Schorghofer 2008), and the annual-average surface temperature at 80-90 º N is always below ~180 K. As shown in Figure D.1, calculated using values from Laskar and others (2004), the summertime insolation at the North Pole is ~2.5 times greater than the annual-average temperature at the North Pole. However, the annual-average temperature remains much lower than the summertime temperature at least in part because the North PLD are covered with carbon dioxide (CO_2) frost during the winter, which has a 7 mbar frost-point temperature of 148 K (Kieffer and others 1976).

Sublimation of water ice at the poles is affected by insolation variations, but how is accumulation of water ice affected by changes in insolation? Richardson and Wilson (2002) showed that due to the inter-hemispheric difference in topography, there is an orbital-independent

atmospheric-circulation bias that favors water-ice deposition at the North Pole compared to the South Pole. While the influence of topography is typically greater than the influence of orbital variations, Montmessin and others (2007) showed that due to the present-day timing of perihelion, localized water-ice deposition is presently favored at the South Pole. Levrard and others (2004) showed that the distribution of polar accumulation is sensitive to obliquity, but the rate of polar accumulation is comparatively insensitive. For example, at an obliquity of 30° there is no water ice accumulation in the South polar region, and only limited accumulation in the North. Whereas, at an obliquity of ~25° there is limited accumulation in the South and moderate accumulation in the North, and at ~15-20° obliquity the accumulation in the North and South are maximized, but the accumulation rate is higher in the North (Levrard and others, 2004). However, for 15-30° obliquity, Levrard and others (2004) found that the accumulation rate at the poles was always ~0.1-2 mm/yr. In order to quantify how insolation variations have affected the PLD, it will be important to incorporate our understanding of global and local patterns of water-ice sublimation and deposition.

To affect the rate of ice flow, changes in surface temperature must propagate to the near-basal ice. The propagation of changes in surface temperature occurs primarily via diffusion, and the characteristic timescale for diffusion is:

$$\tau_d = \frac{H^2}{\kappa(T)} \tag{D.1}$$

where H is the ice thickness and $\kappa(T)$ is the temperature-dependent diffusivity (in m^2yr^{-1}), and $\kappa(T) = K(T)/\rho c(T)$, where $K(T)$ is the temperature-dependent thermal conductivity (e.g. Paterson 1994, pg. 205), ρ is the ice density, and $c(T)$ is the temperature-dependent specific heat

capacity (e.g. Paterson 1994, pg. 205). In Figure D.2a we show how conductivity K, specific heat capacity c, and diffusivity κ change as a function of temperature. Conductivity increases by ~1.7 as temperature increases from 150 to 270 K. Specific heat capacity decreases by ~0.5 as temperature increases from 150 to 270 K. Diffusivity is calculated with a density of 917 kg m^{-3}, and decreases by ~0.3 as temperature increases from 150 to 270 K. Figure D.2b shows how the diffusion timescale changes as a function of near-basal ice temperature for a 2 km thick ice mass with a density of 917 kg m^{-3}, of 1000 kg m^{-3}, and of 1100 kg m^{-3}. For a density of 917 kg m^{-3} and a temperature range of 150-270 K, the diffusion timescale goes from ~100-30 Kyr because colder ice has a higher diffusivity.

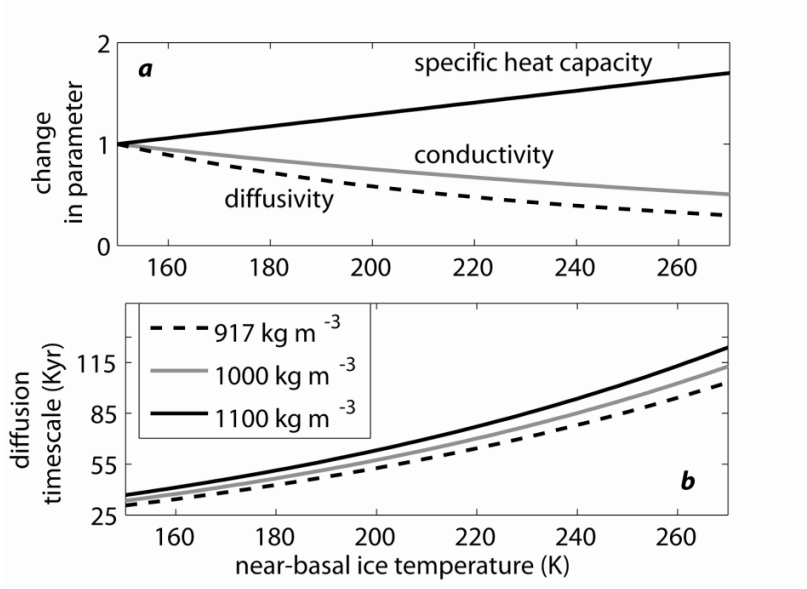

Figure D.2. a) Specific heat capacity, thermal conductivity, and thermal diffusivity as a function of ice temperature, all normalized by their values at 150 K. b) Characteristic timescale for diffusion as a function of near-basal ice temperature for ice density of 917, 1000, and 1100 kg m^{-3}.

Appendix E: Steady-state surface models

The steady-state continuity equation (e.g. Paterson 1994, pg. 256; Chapter 2, Equation A2.1.1) can be solved analytically and numerically for a steady-state ice-surface profile. Simplifying assumptions must be made in order to solve the equation analytically. The simplest surface-profile solution is found by representing the depth-averaged horizontal ice velocity $\bar{u}$ with the 'Shallow Ice Approximation' (e.g. Hutter, 1983 pg. 256; Paterson, 1994, pg. 262; Chapter 2, Section A2.1). Then, an analytical solution can be found to the mass-conservation equation $cx = h(x)\bar{u}$, where c is the accumulation rate, x is the distance along the profile, and $h(x)$ is the ice thickness along the profile (Paterson, 1994, pg. 243). The solution to this differential equation can be nondimensionalized by the length of the profile L and by the ice thickness H_0 at the ice divide at the position x_0. This is called the Vialov solution (Vialov, 1958; Paterson, 1994, pg. 243):

$$\left[\frac{h(x)}{H_0}\right]^{2+1/n} + \left[\frac{x - x_0}{L}\right]^{1+1/n} = 1 \qquad \text{(E.1)}$$

where n is the flow-law exponent. The Vialov solution assumes that the mass-balance pattern consists of accumulation over the entire domain (and that ablation occurs at an infinitely small region at the terminus). While this mass-balance pattern is not always a physically realistic assumption, this surface profile is a good approximation to actual ice-sheet surfaces.

A second analytical solution assumes that the mass-balance pattern consists of uniform accumulation c in the upper zone of the ice sheet, and uniform ablation a in the lower zone of the ice sheet, and the two zones are separated at the equilibrium line R; this is the Paterson solution (Paterson,

1972; Paterson, 1994, pg. 245). The Paterson solution satisfies the steady-state criterion:

$$cR - a(L - R) = 0 \tag{E.2}$$

The Paterson-surface profile is given by (e.g. Paterson, 1994, pg. 245):

$$0 \le x \le R: \qquad \left[\frac{h(x)}{H_0}\right]^{2+\frac{2}{n}} + \left[1+\frac{c}{a}\right]^{\frac{1}{n}}\left[\frac{x}{L}\right]^{1+\frac{1}{n}} = 1 \tag{E.3}$$

$$R \le x \le L: \qquad \left[\frac{h(x)}{H_0}\right]^{2} = \left[1+\frac{a}{c}\right]^{1+\frac{1}{n}}\left[1-\frac{x}{L}\right] \tag{E.4}$$

A surface profile generated using a Vialov model and a surface profile generated using a Paterson model can be compared to a numerical solution of the continuity equation. Figure E.1a compares these three profiles for the case where the maximum ice thickness, the accumulation rate, and the profile length are the same for all profiles. For a mass-balance pattern of uniform accumulation over the entire domain, the numerical solution is equivalent to the Vialov model. However, the Paterson model includes an ablation zone, and with a ratio of accumulation rate to ablation rate c/a=0.1, the Paterson profile is thinner compared to a Vialov profile of the same length. Figure E.1b compares the difference in length that is required for a Paterson profile with c/a=0.1 to match a Vialov profile over most of the domain.

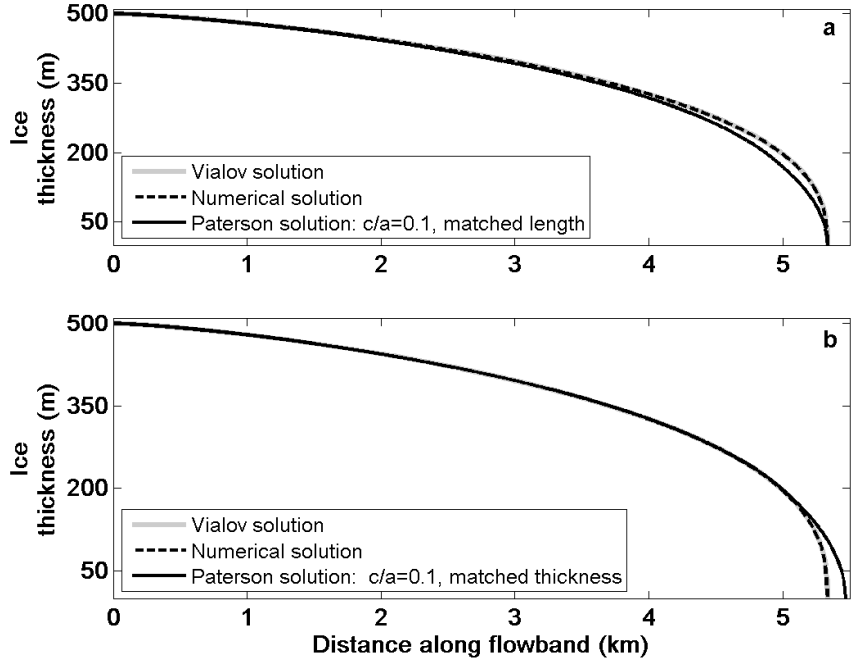

Figure E.1. a) Steady-state-ice-sheet surface profiles with the same full-span length, calculated using a Vialov model, a Paterson model with a mass-balance distribution of c/a=0.1, and solved numerically (see Chapter 2). **b)** A Paterson profile with a surface shape that is matched to the Vialov profile and to the numerical solution over most of the domain.

Appendix F: Kinematic-wave theory and response timescales

Mass-balance changes, ice-flux changes, or local ice-thickness changes drive ice-sheet thickness changes and the development of kinematic waves (Weertman, 1958; Nye, 1960, 1963; Hooke, 2005, pg. 365). Kinematic waves act to restore stability so that ice masses conserve mass. These waves may not be physically recognizable, compared to waves in an ocean, for example; they are waves of constant ice flux moving through the ice mass at a speed which is different from the average speed of the ice. The kinematic-wave equation describes this response as a perturbation from a datum state, in terms of ice flux or ice thickness (e.g. Hooke, 2005, pg. 373). The datum state is the initial condition. For any known accumulation-rate perturbation b_1, the ice flux in the perturbed state q_1 can be found from the ice thickness in the perturbed state h_1 using the kinematic-wave equation. To derive this relationship, we assume that the flux q, at any position x, is a function of ice thickness h and surface slope dS/dx $(=\alpha)$, $q = q(x,h,\alpha)$, and continuity in the perturbed state is

$$\frac{\partial q_1}{\partial t} + \frac{\partial h_1}{\partial t} = b_1 \qquad \text{(F.1)}$$

For small perturbations from the datum state, q_1 at any position x can be given by a series expansion (e.g. Nye, 1960),

$$q_1 = \left(\frac{\partial q}{\partial h}\right)_0 h_1 + \left(\frac{\partial q}{\partial \alpha}\right)_0 \alpha_1 \qquad \text{(F.2)}$$

The coefficients of ice thickness and surface slope are

$$c_0(x) = \left(\frac{\partial q}{\partial h}\right)_0 = (n+2)\frac{q_0}{\alpha_0} \qquad \text{(F.3)}$$

$$D_0(x) = \left(\frac{\partial q}{\partial \alpha}\right)_0 = n\frac{q_0}{\alpha_0} \qquad \text{(F.4)}$$

where n is the exponent in the flow law. The quantity c_0 is the kinematic-wave velocity per unit width, in units (m yr^{-1}). The quantity D_0 is the kinematic-wave diffusivity per unit width, in units (m^2 yr^{-1}). The surface slope can be represented in terms of ice thickness $\alpha = -\partial h / \partial x$. While the idealizations of kinematic-wave theory break down near the ice-sheet terminus, where surface slopes become large, replacing the terminus with a wedge shape addresses this problem (see also Chapter 4). This was suggested by Nye (e.g. 1960, 1963), since c_0 should remain non-zero while D_0 goes to zero at the terminus (Nye, 1963).

Using Equation F.1 in Equation F.2, gives the linearized kinematic-wave equation, derived by Nye (1960):

$$\frac{\partial h_1}{\partial t} = b_1 - \frac{\partial c_0}{\partial x} h_1 - \left(c_0 - \frac{\partial D_0}{\partial x} \right) \frac{\partial h_1}{\partial x} + D_0 \frac{\partial^2 h_1}{\partial x^2} \qquad \text{(F.5)}$$

This shows how the response of ice masses to small perturbations can be determined using linearized kinematic wave theory. Each term describes how ice thickness will change over time due to a perturbation in accumulation, and how the kinematic wave will propagate and diffuse over the ice-mass length. From this solution for a spatially uniform step-change in mass balance, from b_0 (x) to b_0 (x) + b_1, Jóhannesson and others (1989) showed that the response time to approach the new total ice volume (the volume response time) is

$$\tau_V = \frac{V_1}{\bar{b}_1 l_0} \qquad \text{(F.6)}$$

where V_1 is the volume perturbation, $\bar{b}_1$ is the average accumulation perturbation, and l_0 is the length in the datum state. Jóhannesson and others (1989) also formulated a propagation timescale, τ_c:

$$\tau_c = \frac{l_0}{\bar{c}_0} \qquad \text{(F.7)}$$

and a diffusion timescale, τ_D:

$$\tau_D = \frac{{l_0}^2}{\pi^2 \overline{D}_0} \tag{F.8}$$

Hooke (2005, pg. 377) noted that the π^2 term in Equation F.8 arises from the Fourier solution of the diffusion equation. The volume response time is significantly longer than the propagation or diffusion timescales because ice flow can redistribute mass along the surface more quickly than the additional mass in the perturbed state can accumulate or ablate (e.g. Hooke, 2005, pg. 377). All of these response timescales are e-folding timescales; the amount of time calculated is the time it takes to reach approximately two-thirds of the way to the new steady state.

Jóhannesson and others (1989) showed that the volume response time can be simplified by approximating the volume perturbation V_1 as equal to the maximum thickness of the glacier in the datum state $H_{0\max}$ multipled by the change in length ΔL. Then, the annual gain in mass from the perturbation must equal the mass lost at the terminus:

$$\overline{b}_1 L_0 = \left|b(L_0)\right| \Delta L \tag{F.9}$$

where $\left|b(L_0)\right|$ is the absolute value of the ablation rate at the terminus in the datum state (e.g. Jóhannesson and others1989; Hooke 2005, pg. 378). Therefore, the volume perturbation is

$$V_1 = \Delta L h_{0\max} = \frac{H_{0\max} \overline{b}_1 L_0}{\left|b(L_0)\right|} \tag{F.10}$$

and the volume response time is

$$\tau_V = \frac{H_{0\max}}{\left|b_0(L_0)\right|} \tag{F.11}$$

This representation of the volume response can be calculated simply in terms of the maximum ice thickness $H_{0\max}$ and the ablation rate at the

terminus $|b_0(L_0)|$, which are relatively straightforward to calculate or estimate.

A relaxation time for an ice mass can also be derived from a zero-dimensional ice-flow model (Oerlemans, 1981; van der Veen and Oerlemans, 1984; Van der Veen, 1999, pg. 261); the description of the response time associated with this model is given in Van der Veen (1999, pg. 265), and is summarized here. The zeroth-order model is

$$\frac{\partial H}{\partial t} = -\frac{2A}{n+2}(\rho g)^n \frac{H^{2n+2}}{L^{n+1}} + b \qquad \text{(F.12)}$$

Representing the time variation in these values in terms of a perturbation from steady state, i.e. ice thickness $H = H_0 + H'$ and $b = b_0 + b'$, then expanding this equation as a Taylor series, and subtracting the steady-state continuity equation (Equation F.12) from this perturbation equation, gives an equation for the rate of change of perturbations in ice thickness,

$$\frac{\partial H'}{\partial t} = -\frac{H'}{\tau_R} + b' \qquad \text{(F.13)}$$

where the relaxation time τ_R is given by

$$\tau_R = \frac{L^{n+1}(n+2)}{H_0{}^{2n}(2n+2)2A(\rho g)^n}. \qquad \text{(F.14)}$$

Appendix G: Finite Volume Method

The Finite Volume Method (FVM), where the governing equations are solved in the integral form, stands in comparison to the Finite-Difference Method (FDM), where the governing equations are solved in the differential form. The finite-difference approximation of the derivative is a truncated Taylor series expansion (discussed further in Appendix H). In the FDM, the governing equation is satisfied only over the entire domain, and discretization must be performed on a uniform grid, or there must be a coordinate transformation to relate the non-uniform grid to a uniform grid. The FDM is easy to implement, but the quality of the approximation between grid points can be highly dependent on how the derivative is defined and on the order of the approximation (e.g. first-order forward differences compared to second-order centered differences), as well as on the discretization grid size (e.g. van den Berg and others, 2006). The Finite-Element Method (FEM) is another method that, similar to the FVM, solves the governing equations in the integral form. The FEM is designed to facilitate complicated domain geometries.

While all three methods have been used to solve the equations for ice flow (e.g. Van der Veen, 1999, pg. 215; Hooke, 2005, pg. 288; Price and others, 2007), an inevitable aspect of numerical analysis is to find the appropriate balance between accuracy and numerical cost. We chose the FVM because satisfying conservation across each finite volume allows for flexible grid spacing, and the FVM is an efficient low-order discretization scheme that has been thoroughly described and rigorously tested by Patankar (1980) and by Versteeg and Malalasekera (1995).

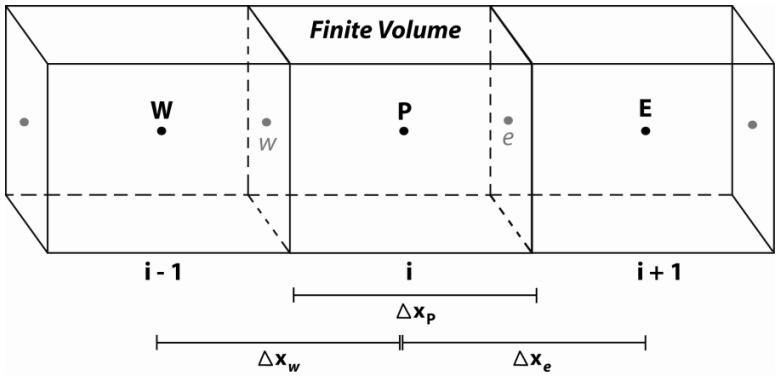

Figure G.1. Sketch illustrating the notation adopted for the finite-volume method (following Patankar, 1980). Centerpoints are denoted by capitals (*P* for center volume, *W* for western volume, and *E* for eastern volume), and edges are denoted by lowercase (*w* for western edge, and *e* for eastern edge). Distances between volume centerpoints, and the finite-volume length is given by the corresponding Δx.

We follow the notation given by Patankar (1980, pg. 32). A given center point is denoted by *P*, the western (upstream) edge point is denoted by *w*, and the eastern (downstream) edge point is denoted by *e*. The adjacent western finite-volume center point is denoted by *W* and the adjacent eastern finite-volume center point is denoted by *E*. There is a discrete distance from each center point to each edge point, and from each center point to each center point. The distance from center point *W* to center point *P* is Δx_w, the distance from center point *P* to center point *E* is Δx_e, and the distance from edge point *w* to edge point *e* is Δx_P. These finite volume relationships are illustrated in Figure G.1.

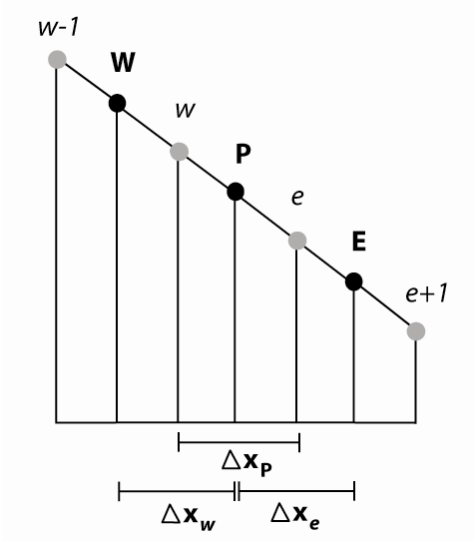

Figure G.2. Sketch of how edge thicknesses and slopes are defined in a finite-volume representation, following Equations G.1 and G.2. Western and eastern values that lie outside the domain must be extrapolated.

Ice thicknesses at the western edges and at the eastern edges are given by the known ice thickness at the neighboring upstream and downstream center points:

$$h_w = \frac{h_P + h_W}{2} \qquad h_e = \frac{h_P + h_E}{2} \tag{G.1}$$

Surface slopes at the western edges and at the eastern edges are similarly interpolated from the known ice thicknesses at the neighboring center points:

$$\frac{dS}{dx}_w = \frac{S_P - S_W}{x_P - x_W} \qquad \frac{dS}{dx}_e = \frac{S_E - S_P}{x_E - x_P} \tag{G.2}$$

However, the western-most and the eastern-most edge values of ice thickness and surface slope must be extrapolated. Figure G.2 illustrates the piecewise-linear relationship between the known ice thickness at the finite-volume center points and the interpolated ice thickness at the finite-volume edge points, expressed by Equations G.1 and G.2.

Appendix H: Explicit, Implicit, and Crank-Nicolson Numerical Schemes

Solving a differential equation by numerical integration involves time marching over discrete time steps, which is different than an analytical integration over a continuous function of time. The analytical and numerical evaluations both require a known initial condition, and the numerical evaluation should yield a similar solution to the same problem solved analytically. Accuracy and stability are essential in numerical analysis, and the numerical scheme is often chosen based on these considerations.

Most numerical integration methods for differential equations can be derived from a Taylor's series expansion, where the time-derivative term is evaluated to find an unknown value at a future time step $t + \Delta t$ in terms of a known value at the current time step t. For example, the ice-thickness profile $h(x)$, at a discrete time $t + \Delta t$, can be expressed as

$$h(x, t + \Delta t) = h(x, t) + \frac{dh(x,t)}{dt}\Delta t + \frac{d^2 h(x,t)}{dx^2}\frac{(\Delta t)^2}{2!} + O(\Delta t)^3 \qquad \text{(H.1)}$$

It is common to truncate the series and use a first-order approximation; this is known as the Euler method, or the explicit method, because it is based on explicit time stepping in terms of known values. Therefore, an explicit scheme assumes that the solution at time $t + \Delta t$ depends on known values at time t, in other words, the known values at time t apply over nearly the entire time step Δt. In comparison, an implicit scheme assumes that the solution at time $t + \Delta t$ depends on values at time $t + \Delta t$, in other words, the (possibly unknown) values at time $t + \Delta t$ apply over nearly the entire

timestep Δt. An alternative is the Crank-Nicolson scheme, which assumes that the solution at time $t + \Delta t$ depends on an equally-weighted linear combination of values at time t and values at time $t + \Delta t$ (Patankar, 1980); other semi-implicit schemes with different weighting factors could also be used, but θ must be between 0 and 1. After Patankar (1980, pg. 56), Figure H.1 sketches the difference between a fully-implicit, a fully-explicit, and a semi-implicit scheme. Choosing the proper numerical scheme depends on the physical response of the modelled system, as well as on the required grid resolution and on computation-time constraints.

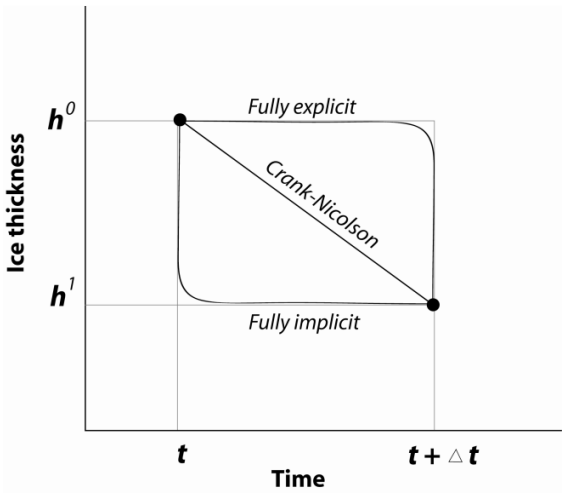

Figure H.1. Sketch showing the relationship between a fully implicit, a fully explicit, and a Crank-Nicolson solution scheme (after Patankar, 1980, pg. 56).

We can represent the mass-conservation equation in the form of a diffusion equation, and directly employ the numerical solution method from Patankar (1980, pg. 55). To do this, we represent $\partial q / \partial x$ as $D \partial h / \partial x$, where D acts like a diffusion coefficient, and is discussed in Appendix I. It is

assumed that the value of D is known at each timestep, and Appendix I also addresses how to iteratively update the estimate of D, because it is a nonlinear function of the ice thickness and surface slope values that we are trying to find.

Following Patankar (1980), the mass-conservation equation is integrated over each finite volume from the western edge x_w to the eastern edge x_e, and over each timestep from t to $t+\Delta t$:

$$\int_{x_w}^{x_e}\int_{t}^{t+\Delta t} \frac{\partial h(\chi,\tau)}{\partial \tau}\, d\tau d\chi = \int_{t}^{t+\Delta t}\int_{x_w}^{x_e}\left(\frac{\partial}{\partial \chi}\left(D\frac{\partial h(\chi,\tau)}{\partial \chi}\right)+\dot{b}(\chi,\tau)\right)d\chi d\tau \qquad \text{(H.2)}$$

This equation is evaluated across each discrete finite volume in the domain, and from this set of equations a linear matrix system can be setup to solve for ice thickness at finite-volume center points at the unknown future timestep $h(x_P, t+\Delta t)$,

$$Ah^{t+\Delta t} = Bh^{t} + S \qquad \text{(H.3)}$$

with the solution for ice thickness given by,

$$h^{t+\Delta t} = A^{-1}(Bh^{t} + S) \qquad \text{(H.4)}$$

In this case, A is a matrix of implicit coefficients, B is a matrix of explicit coefficients, and S is a vector of constant boundary values and source terms. Following Patankar (1980, pg. 55), A is a tridiagonal matrix with coefficients for a western volume a_W, a center volume a_P, and an eastern volume a_E, and B is a matrix of center-point values a_P^0, giving

$$a_P h_P{}^{t+\Delta t} = a_W\left(\theta h_W{}^{t+\Delta t} + (1-\theta)h_W{}^{t}\right) + \left(\theta a_E h_E{}^{t+\Delta t} + (1-\theta)h_E{}^{t}\right) + S \qquad \text{(H.5)}$$

with,

$$a_P{}^0 = \frac{\Delta x_P}{\Delta t} \tag{H.6}$$

$$a_W = \frac{D_w}{\Delta x_w} \tag{H.7}$$

$$a_E = \frac{D_e}{\Delta x_e} \tag{H.8}$$

$$a_P = a_P{}^0 + \theta a_E + \theta a_W \tag{H.9}$$

The subscripts w and e represent values at finite-volume edges, and θ is the scaling factor for explicit and implicit contributions (θ=1 for a fully implicit scheme, θ=0.5 for a Crank-Nicolson scheme, and θ=0 for a fully explicit scheme). The vector of boundary values and source terms depends on the specific problem, and for our mass-flow problem it is given by,

$$S = -\frac{1}{W(x_P)}((1-\theta)(Q_e{}^t - Q_w{}^t)) + ((1-\theta)\dot{b}(x_P,t) + \theta\dot{b}(x_P,t+\Delta t)) \tag{H.10}$$

Equations H.6- H.10 are modified at the boundaries, where the first a_W value and the last a_E value do not exist in the domain because it has a discrete start value and a discrete end value. Therefore, the boundary value of ice thickness, or the boundary ice flux must be known or must be treated as a separate calculation (e.g. using the method described in Chapter 4).

The explicit scheme is the most straightforward scheme because the solution is found explicitly from known values (the values at time t), and for the nonlinear ice-flow problem this is an advantage because the equation for ice thickness can be evaluated directly (see Appendix I). However, the explicit scheme can become numerically unstable, giving a physically unrealistic solution if the timesteps Δt exceed a threshold value (Patankar,

1980, pg. 57). Problems that require extremely small step sizes to remain numerically stable are referred to as stiff, and this method can be severely restricting when solving the stiff problem for ice-thickness evolution (e.g. Hindmarsh and Payne, 1996). In addition to temporal-grid constraints for accuracy and stability, there may also be spatial-grid constraints required to find an accurate and stable solution for the ice-flow problem (e.g. Van den Berg and others, 2006).

Patanakar (1980, pg. 57) and Patankar and Baliga (1978) argue that a fully implicit scheme is more desirable than a Crank-Nicolson scheme. The Crank-Nicolson scheme is often considered to be unconditionally stable, but this does not mean that the solution is unconditionally realistic. Patankar and Baliga (1978) show that as the timestep increases, a scheme split between implicit and explicit values can develop numerical oscillations. In terms of the matrix equations, in particular in Equation H.10, Patankar (1980, pg. 57) shows that these oscillations can occur when $\theta \neq 1$, because the coefficient of hP^t, given by $a_P{}^0 - (1-\theta)(a_E + a_W)$, can become negative unless $\theta = 1$. Therefore, the Crank-Nicolson scheme is mathematically stable, as the oscillations will eventually die out, but the oscillations can still develop, and they are physically unrealistic. This is the primary reason Patankar and Baliga (1978) argue that a fully-implicit scheme better represents reality, particularly for the heat-flow problem; unless the timestep is acceptably small, the assumption that the values will change linearly is not valid where the values change exponentially over the timestep. In the highly non-linear ice-flow problem, we encounter this exact problem. In the semi-implicit scheme, which includes the Crank-Nicolson equal-weighting scheme, whenever the timestep is not small enough, we also find that physical instabilities can develop (as described by Patankar,

1980, pg. 57). However, these oscillations do not form using the fully-implicit scheme.

Since the explicit scheme is more straightforward to implement, and a correctly implemented fully-explicit scheme and a correctly implemented fully-implicit scheme should yield a similar solution, we verify that our fully-implicit solution matches an appropriately time-stepped fully-explicit solution. The timestep size required for the explicit scheme, in combination with our own computational constraints, limit this test to a runtime of a few hundred years. Figure H.2 compares these two solutions for 150 years of ice sheet evolution in response to a step change in accumulation. The explicit scheme uses 0.05 year timesteps, and the implicit scheme uses one year timesteps (two and five year timesteps give nearly the same solution). The fully implicit solution value for ice flux (or ice thickness) at the limited-domain boundary is within a fraction of a percent of the fully explicit solution value for this 150-year calculation of ice-thickness response to an impulse in accumulation. The computation time required for a stable solution with an explicit scheme is approximately two orders of magnitude longer than solving the equivalent problem with an implicit scheme (i.e. an explicit calculation that requires ~1000 seconds could be performed with an implicit calculation in ~10 seconds). We want to minimize the computation time, and we want to avoid unstable and unphysical behavior, so we use a fully-implicit scheme.

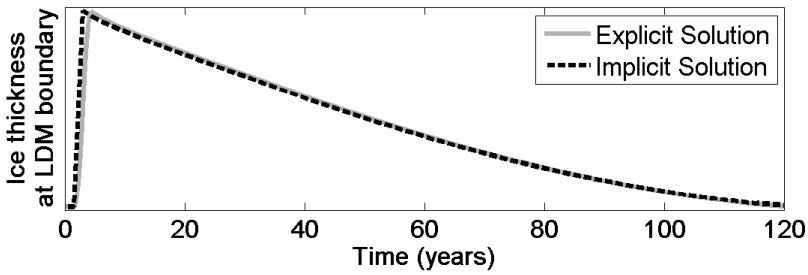

Figure H.2. Comparison of the solution for ice-thickness evolution using an explicit calculation (0.05 year timestep), and using an implicit calculation (2 year timestep). The run is for 150 years in response to an impulsive perturbation in accumulation.

Appendix I: Nonlinearity

In the continuity equation for ice flow, the value of ice flux is a nonlinear function of ice thickness, which means that this governing nonlinear equation cannot be solved directly for the evolution of ice thickness. To linearize our problem, we group the nonlinear terms in the dynamic flux into a coefficient, consisting of the ice thickness and the surface slope, and assume that this coefficient has a known value. Following this step, the mass-continuity equation can be represented in a generic differential-equation form that consists of an unsteady term, a diffusion term, an advection term, and a source term:

$$\frac{\partial S(x,t)}{\partial t} - \frac{\partial B(x,t)}{\partial t} = -\frac{1}{W(x)}\left[(1-\alpha)\frac{\partial}{\partial x}\left(D(x,t)W(x)\frac{\partial S(x,t)}{\partial x}\right) + \alpha\bar{u}(x,t)W(x)h(x,t)\right] + \dot{b}(x,t) \tag{I.1}$$

where α is a weighting factor to split contributions from the diffusion and the advection terms, $\bar{u}(x,t)$ is the depth-averaged horizontal velocity, and *D(x,t)* acts like a diffusion coefficient given by

$$D(x,t) = \frac{2\tilde{A}(T(x,t))}{n+2}(\rho g)^n h(x,t)^{n+2}\left(\frac{dS(x,t)}{dx}\right)^{n-1} \tag{I.2}$$

We considered the case $\alpha \neq 0$, where the discretization equation is solved using an advection term. However, unless this term is necessary to include, Patankar (1980, pg. 41) typically excludes the advection term to facilitate a simpler solution. While it is possible, and often necessary, to include the advection term in the heat-flow problem (e.g. Patankar, 1980, chapter 5), we think including an advection term in the mass-flow problem adds unnecessary complexity, especially because there is no physical requirement to include this term. The schemes described in Patankar (1980, pg. 79-95)

for the heat-flow problem rely on mass continuity to justify that the strength of the advection, given by $F = \rho u$, is equal across eastern and western finite-volume edges $F_e=F_w$; this means that $F_e-F_w=0$. When solving a mass-flow problem, there is no global constraint that can be utililized to justify $F_e=F_w$, and therefore justify $F_e-F_w=0$ in the discretization equation. Since the value of $F_e=F_w$ for the mass-flow problem is a function of the unknown value of the ice thickness, this adds additional complexity. Therefore, we feel that it is unnecessary to include an advection term. We favor a linearization that groups the nonlinearity into a single coefficient $D(x,t)$, giving an equation with a diffusion form (Equation I.1 with $\alpha = 0$; this is the linearization form used by e.g. Waddington, 1982, pg. 239; Van der Veen, 1999, pg. 226).

The numerical solution to Equation I.1 is found by integrating over each finite volume from the west edge x_w to the east edge x_e, and from the current timestep t to the future timestep $t + \Delta t$. Ice thickness $h(x,t)$ and ice-surface elevation $S(x,t)$ are related by $S(x,t) = h(x,t) + B(x_P)$. Ice-surface elevation is calculated at finite-volume centers $S(x_P, t + \Delta t)$:

$$\begin{aligned}&(S(x_P,t+\Delta t)-S(x_P,t))\frac{\Delta x_P}{\Delta t} = \\ &-\left[D(x_e,t+\Delta t)\frac{\partial S(x_e,t+\Delta t)}{\partial x}-D(x_w,t+\Delta t)\frac{\partial S(x_w,t+\Delta t)}{\partial x}\right] \\ &+\dot{b}(x_P,t+\Delta t)\Delta x_P\end{aligned} \qquad \text{(I.3)}$$

where $D(x_w,\ t+\Delta t)$ and $D(x_e,\ t+\Delta t)$ are the values of the diffusion coefficient evaluated at western and eastern finite-volume edges, respectively. The coefficients at finite-volume edges require the values of ice thickness and surface slope there, we linearly extrapolate the ice thickness and we quadratically extrapolate the surface slope from the calculated values at

finite-volume centers. The flux coming in across the edge of one volume is equal to the ice flux going out through the adjacent upstream volume edge. The ice flux at one boundary must be prescribed as a boundary condition, and the ice flux at the other boundary in the domain must be calculated as part of the solution for ice-thickness evolution.

The value of the coefficient $D(x,\ t+\Delta t)$ is a function of $h(x,\ t+\Delta t)$ and $dS/dx\ (x,\ t+\Delta t)$, and at time $t+\Delta t$ these values are of course unknown, since we are solving the problem for $h(x,\ t+\Delta t)$; this is the nonlinearity in our problem. To address this quandary, we follow an iterative approach (e.g. Patankar, 1980, pg. 47). The iterative sequence starts by estimating the coefficient values as function of the known values at time t, so that at the first iteration, $D(x,\ t+\Delta t) = D(x,\ t)$. However, in a transient problem it is unlikely that a solution with this initial estimate will satisfy continuity, so we must iteratively adjust this estimate of the diffusion coefficient so that the solution for $S(x,\ t+\Delta t)$ calculated with $D(x,\ t+\Delta t)$ will satisfy the continuity equation. We iteratively update the estimate of $D(x,\ t+\Delta t)$ using the new estimate of $S(x,\ t+\Delta t)$, until continuity is satisfied. There are two ways to check that mass conservation holds: (1) directly calculate the residual of the continuity equation and iterate until this residual is small, or (2) calculate the difference in the ice-thickness solution from iteration i-1 to iteration i and iterate until this difference is small. We find that both of these approaches yield the same ice-thickness solution, but the second approach requires less computation time.

The degree to which the continuity equation is satisfied at each iteration i, which we call the residual of the continuity equation, is given by

$$r^i = ((S(x_P, t+\Delta t) - S(x_P, t))\Delta x_P$$
$$+\left(D(x_e, t+\Delta t)^i W(x_e) \frac{\partial S(x_e, t+\Delta t)}{\partial x} - D(x_w, t+\Delta t)^i W(x_w) \frac{\partial S(x_w, t+\Delta t)}{\partial x} \right) \qquad \text{(I.4)}$$
$$-\dot{b}(x_P, t+\Delta t)\Delta x_P \Delta t$$

We seek a value of $D(x,t+\Delta t)^i$ that, when calculated using an appropriate $S(x,t+\Delta t)$, will satisfy $r^i=0$. Following Waddington (1981, pg. 241), the Taylor expansion of r^i about zero is a set of equations that can be solved for changes in the ice thickness δh^i at each iteration that will result in a smaller residual of the continuity equation:

$$r^i = \sum_{k=1}^{J} \frac{\partial r^i}{\partial S_k^{t+\Delta t}} \delta S_k \qquad \text{(I.5)}$$

where k is an index over each spatial value of ice thickness. This can be represented in matrix form as

$$r^i = A\delta S^i, \qquad \delta S^i = A^{-1} r^i \qquad \text{(I.6)}$$

The calculated changes δS^i are subtracted from the current estimate of ice thickness,

$$S(x,t+\Delta t)^i = S(x,t+\Delta t)^{i-1} - \delta S^i \qquad \text{(I.7)}$$

and the new $S(x,t+\Delta t)^i$ is used to estimate an updated diffusion coefficient $D(x,t+\Delta t)^{i+1}$, and then a new solution for ice thickness $S(x,t+\Delta t)^{i+1}$. Iterations continue until the residual r^i is small, and we require $r < 10^{-6}$ (see Appendix J)

While we required that our solution satisfy continuity, a simpler approach can be followed that yields the same solution. The second approach is to iterate until changes in ice thickness from iteration i-1 to iteration i are small. In this case the residual r^i is given by

$$r^i = S(x,t+\Delta t)^i - S(x,t+\Delta t)^{i-1} \tag{I.8}$$

The new estimate of $S(x,t+\Delta t)^i$ is used to calculate an updated diffusion coefficient $D(x,t+\Delta t)^{i+1}$, and then a new solution for ice thickness $S(x,t+\Delta t)^{i+1}$. Iterations with this approach continue until the residual r^i is small, and we also require $r^i < 10^{-6}$. This approach requires more iterations to find a solution, but it is faster because it avoids calculating the Jacobian matrix given by Equation I.5. While linearization with this approach facilitates a simpler and faster numerical solution, the mass-flow problem is highly nonlinear and for the numerical scheme to be stable, we must invoke underrelaxation. As described by Patankar (1980, pg. 67), underrelaxation is a way to slow down convergence of the solution by using a weighted contribution of values from previous iterations. For example, we estimate $D(x,t+\Delta t)^{i+1}$ using contributions of ice thickness and surface slope from the current i, and from iteration i-1, using a weighting factor β, giving the weighted value of $S(x,t+\Delta t)^i{}_w$:

$$S(x,\ t+\Delta t)^i{}_w = \beta\ S(x,\ t+\Delta t)^i + (1-\beta)\ S(x,\ t+\Delta t)^{i-1} \tag{I.9}$$

if β=1, only the estimate from the current iteration is used. We found that $\beta \leq 0.1$ stabilized this iterative solution procedure.

Appendix J: Convergence criteria

As discussed in Appendix I, our implicit numerical scheme iteratively solves the nonlinear continuity equation with the flow-law equation for ice-sheet evolution. Iterations for this solution stop when the residual of the continuity equation is small, or when subsequent changes to the ice-thickness profile are negligible. Waddington (1981, pg. 350-353) discussed the appropriate cutoff value to use for a similar iterative procedure, so that the residual error in the solution is acceptable. Following Waddington (1981, pg. 350-353) for flow of a laminar slab with unit width, where slope and flux vary slowly with distance along the flowline, the residual error r is related to the error from solution convergence e_h by,

$$|r| = 10^{-3}|e_h|. \tag{J.1}$$

As pointed out by Waddington (1981, pg. 353), for the ice-thickness solution to be accurate to 10^{-6}, given ice-thickness changes over each timestep of $\sim 10^{-1}$, the residual convergence criterion,

$$|r| < 10^{-4}. \tag{J.2}$$

A convergence criterion is required to calculate the impulse-response functions, where we solve for ice-sheet evolution in response to a small perturbation in one timestep. A convergence criterion is also required to calculate ice-sheet evolution, where we calculate the ice-thickness history in response to centimeter-scale variations in accumulation that occur over each timestep. To reduce computation time while remaining accurate, we use $|r| < 10^{-6}$ in the surface calculation for the impulse-response functions, and we use $|r| < 10^{-5}$ in the calculation of ice-sheet evolution.

Appendix K: Algorithm Flowcharts

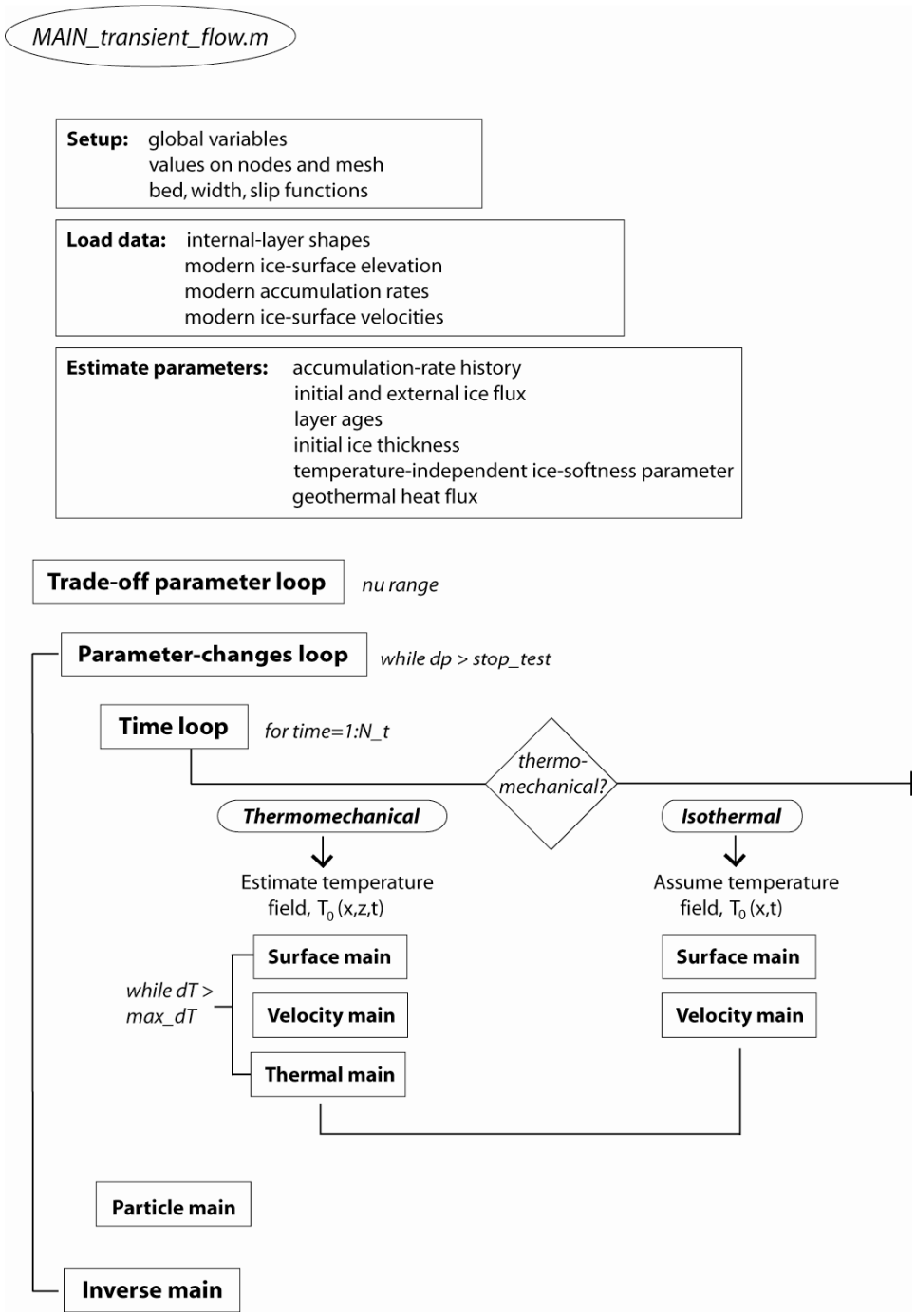

Figure K.1. Main program.

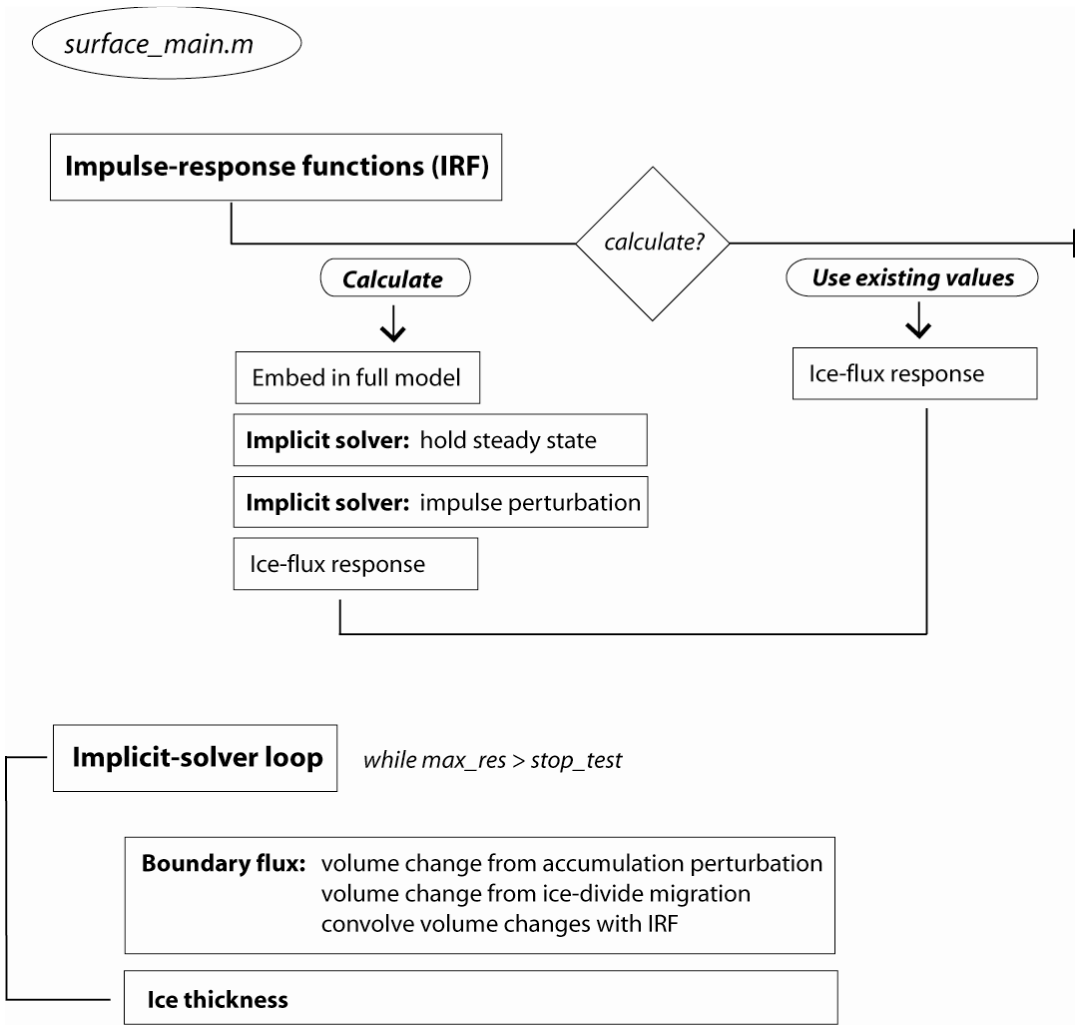

Figure K.2. Surface-evolution calculation.

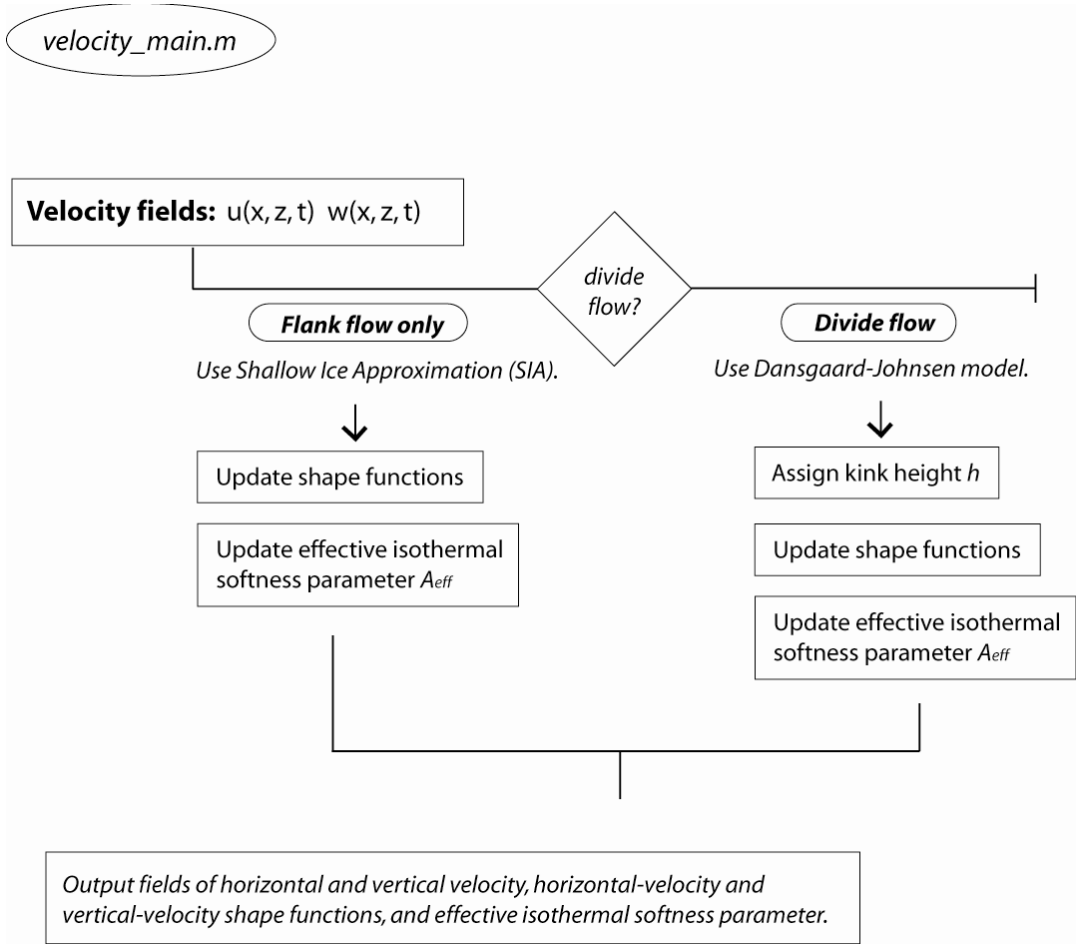

Figure K.3. Velocity-field calculation.

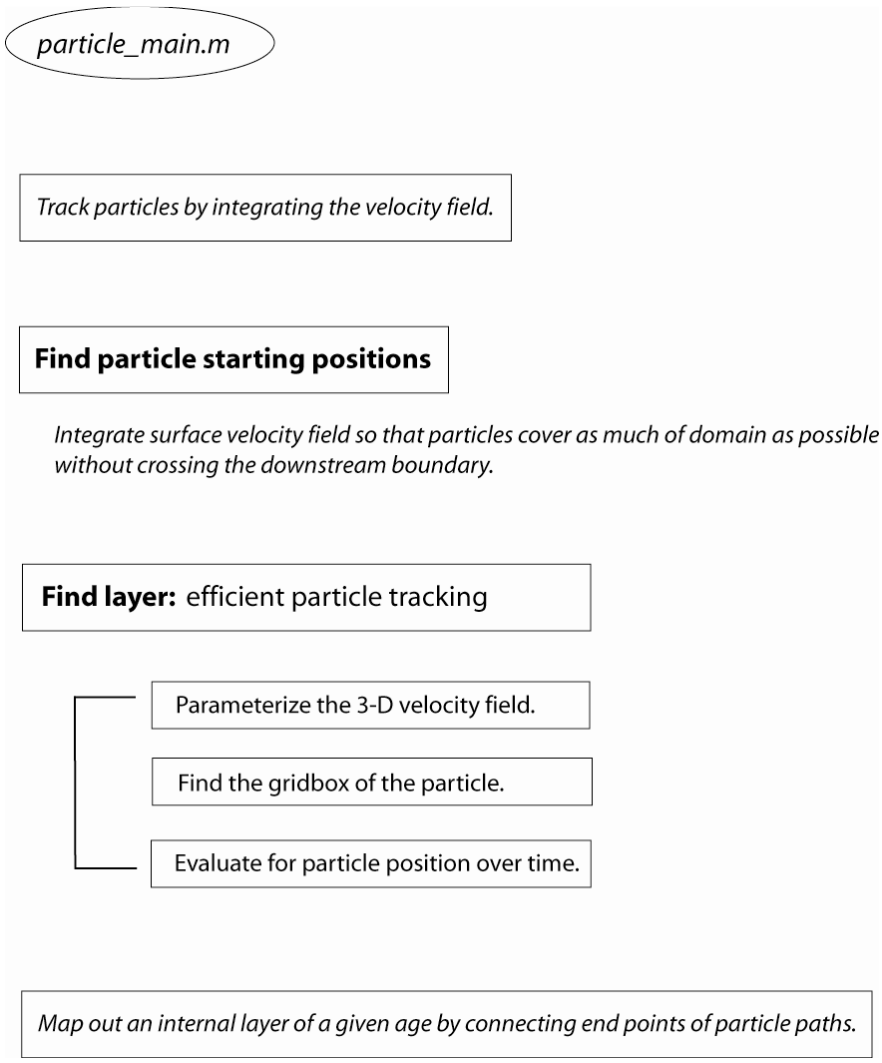

Figure K.4. Particle-tracking module.

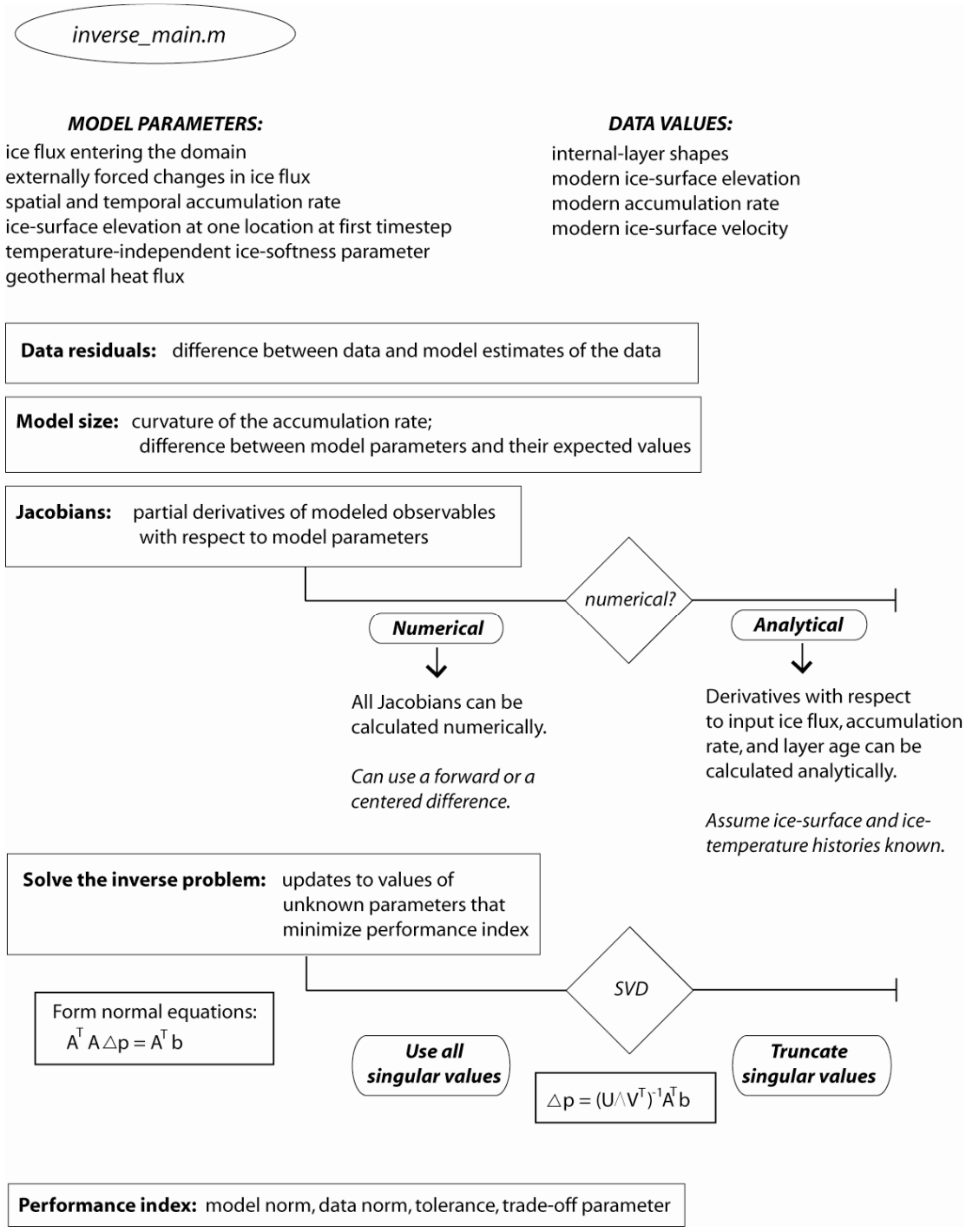

Figure K.5. Inverse algorithm.

Appendix L: Linear interpolating functions

Between any pair of spatial nodes x_i^n and $x^n{}_{i+1}$ separated by $\Delta x_i = x_{i+1}^n - x_i^n$, we define a local non-dimensional position variable X_i, which varies between 0 and 1 in interval i,

$$X_i = \frac{x - x_i^n}{x_{i+1}^n - x_i^n} = \frac{x - x_i^n}{\Delta x_i} \tag{L.1}$$

We define two linear interpolating functions on a generic interval,

$$\begin{aligned} &\gamma_0(X_i) = 1 - X_i && 0 \le X_i \le 1 \\ &\gamma_0(X_i) = 0 && \text{otherwise} \\ &\gamma_1(X_i) = X_i && 0 \le X_i \le 1 \\ &\gamma_0(X_i) = 0 && \text{otherwise} \end{aligned} \tag{L.2}$$

These functions are defined to be zero everywhere outside their interval i. Then, any piecewise-linear function $f(x,t)$ with values $f_i(t)$ at nodes i can be express as

$$\begin{aligned} f(x,t) &= \sum_{i=1}^{N_x - 1} \left[f_i(t)\gamma_0(X_i) + f_{i+1}(t)\gamma_1(X_i) \right] \\ &= \sum_{i=1}^{N_x - 1} f_i(t)\left[\gamma_0(X_i) + \gamma_1(X_{i-1}) \right] \end{aligned} \tag{L.3}$$

with N_x functions $f_i(t)$ at the spatial nodes. We must ensure that $\gamma_0(X_{N_x}) = \gamma_1(X_1) = 0$, because the interpolating functions are not defined there.

We can also explicitly express the time-dependence through piecewise-linear functions expressed in terms of nodal values. Between any pair of temporal nodes t_j^n and $t^n{}_{j+1}$ separated by $\Delta t_j = t_{j+1}^n - t_j^n$, we define a local non-dimensional time variable T_j analogous to X_i, which varies

between 0 and 1 in time-interval j. The same interpolating functions as Equation L.3 can be used to express time-dependent variables at intermediate times

$$\begin{aligned} f(x,t) &= \sum_{j=1}^{N_t-1}\left[f_{ij}\gamma_0(T_j) + f_{i(j+1)}\gamma_1(T_j)\right] \\ &= \sum_{j=1}^{N_t-1} f_{ij}\left[\gamma_0(T_j) + \gamma_1(T_{j-1})\right] \end{aligned} \tag{L.4}$$

Again, we must ensure that $\gamma_0(T_{N_t}) = \gamma_1(T_1) = 0$.

Next, we define integrals of products of the interpolating functions,

$$\Gamma_{mn}(X) = \int_0^X \gamma_m(\chi)\gamma_n(\chi)d\chi \tag{L.5}$$

where m and n can take the values 0 or 1, giving

$$\begin{aligned} \Gamma_{00}(X) &= \frac{1-(1-X)^3}{3} \\ \Gamma_{01}(X) &= \frac{X^2}{2} - \frac{X^3}{3} \\ \Gamma_{11}(X) &= \frac{X^3}{3} \end{aligned} \tag{L.6}$$

Appendix M: Bilinear and trilinear interpolation

Any 2-dimensional grid, with coordinate values x and y, can be parameterized as a 2-dimensional field, and if the coordinate system is chosen such that the four grid points where a function F is known are at (0,0), (0,1), (1,0), (1,1), the function F can be parameterized by the interpolation equation

$$F(x,y) = F(0,0)(1-x)(1-y) + F(1,0)x(1-y) + F(0,1)(1-x)y + F(1,1)xy \quad \text{(M.1)}$$

This can also be represented as

$$F(x,y) = Ax + By + Cxy + D \quad \text{(M.2)}$$

where the coefficients A, B, C, and D are given by A= F (0,0), B= F (1,0)- F (0,0), C= F (0,1)- F (0,0), and D= F (0,0)- F (1,0)- F (0,1)+F(1,1).

Any 3-dimensional grid, with coordinate values x, y, and z, can be parameterized as a 3-dimensional field, and if the coordinate system is chosen such that the nine grid points where the function F is known start at (0,0,0) and span (1,1,1), the function F can be parameterized by the interpolation equation

$$\begin{aligned} F(x,y,z) = {} & F(0,0,0)(1-x)(1-y)(1-z) \\ & + F(1,0,0)x(1-y)(1-z) + F(0,1,0)(1-x)y(1-z) \\ & + F(0,0,1)(1-x)(1-y)z + F(1,0,1)x(1-y)z \\ & + F(0,1,1)(1-x)yz + F(1,1,0)xy(1-z) \\ & + F(1,1,1)xyz \end{aligned} \quad \text{(M.3)}$$

This can also be represented as

$$F(x,y,z) = Ax + By + Cz + Dxy + Exz + Fyz + Gxyz + H \qquad \text{(M.4)}$$

These equations hold if the grid is rectangular, therefore we track particles in a normalized vertical coordinate system $\hat{z}$, given by

$$\hat{z} = \frac{z - B(x)}{S(x,t) - B(x)} \qquad \text{(M.5)}$$

These parameterizations are used in our particle-tracking routine for mapping out an internal layer. In comparison to standard interpolation from known grid values, it is computationally faster to retrieve particle positions from any arbitrary location in the grid by evaluating a parameterized function.

Appendix N: Analytical Jacobians

To solve this nonlinear inverse problem discussed in Chapter 5, we must calculate the Jacobian matrix, which in our case consists of the partial derivatives of each modeled observable (N values) with respect to each model parameter (M values), producing a matrix of size $M \times N$; see Chapter 5, Section A5.3). The modeled observables are estimates of the data values, and this may include the internal-layer shape, the present-day ice velocity, measurements of the accumulation rate, or the ice-surface elevation. The model parameters are the unknown values that we solve for in the inverse problem, and may include the initial condition for the ice flux entering the domain, the changes in ice flux that are from external forcing, the spatial and temporal pattern of accumulation rate, the layer ages, the initial condition for the ice-surface elevation, the temperature-independent ice-softness parameter, or the geothermal flux. One column of the Jacobian matrix describes how each modeled observable changes with respect to one model parameter; the full matrix describes how changes in all the model parameters will result in a better estimate of all the modeled observables.

The Jacobian matrix is expensive to compute numerically. So, if it is possible, we want to calculate components of the Jacobian matrix analytically. To calculate the Jacobians analytically we must represent the modeled observables (e.g. the internal layer) in terms of the model-parameter values (e.g. the accumulation rate), and then derive an analytical expression for the partial derivative of the modeled observable with respect to each parameter value. Analytically evaluating components of the Jacobian matrix can substantially reduce the required computation time. While we can derive expressions for the layer depth, the ice velocity, and the accumulation rate in terms of the model parameters of the accumulation

rate, the ice flux entering the domain, and the layer age, it is not straightforward to represent all components of the Jacobian matrix analytically. In particular, to take these analytical partial derivatives we must hold the ice-thickness history $h(x,t)$ constant; this same assumption cannot be made for the numerical calculations. Therefore, some numerical calculations are always required, and we decided that computational consistency of the Jacobian elements was more important than computational efficiency. In addition, the analytical advantage in this case was not as great because our analytical calculations also required a reasonable computational load.

However, in the event that a numerical calculation is unfeasible, or if it is desirable to solve a different version of this inverse problem, we present analytical expressions for the layer depth, ice flux, ice velocity, and accumulation rate in terms of the model parameters of accumulation rate, ice flux, and layer age. The scheme presented here follows an original derivation by E.D. Waddington (unpublished), and builds on steady-state relationships derived by Waddington and others (2007).

N.1. Layer depth

To represent the depth of an internal layer in terms of the model parameters (e.g. accumulation rate), we must consider transient effects on particle-path position. In steady state, Reeh (1989) noted that at any position x along the ith modeled particle path, which originates on the surface at $x = x_i^s$, the ice flux transported below the depth $h_m(x, t_P)$ of the modeled internal layer at the present time t_P, is equal to the flux $q(x_i^s, t_P)$ at x_i^s, and the ice flux above $h_m(x, t_P)$ is equal to the difference between the total flux $q(x_i^h, t_P)$ and the flux at the surface $q(x_i^s, t_P)$,

$$q_h(x_i^h, t_P) = q(x_i^h, t_P) - q(x_i^s, t_P). \tag{N.1}$$

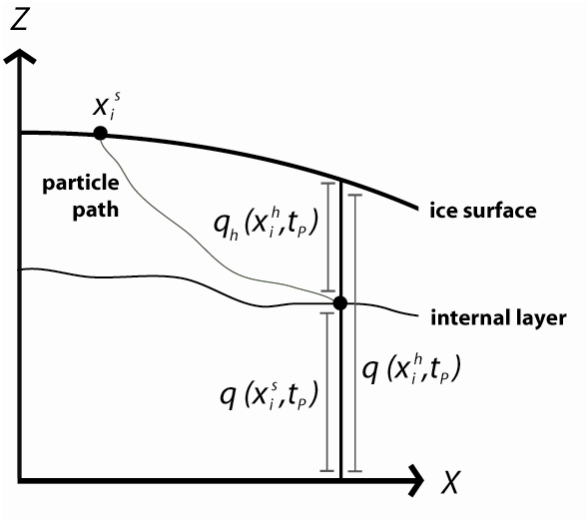

Figure N.1. Sketch of particle-path and ice-sheet geometry.

This is a consequence of mass conservation, and the fact that no flux can cross a streamline in steady state. If x_i^h is the location at which the ith particle path $\mathbf{x}_i^P(t)$ intersects the layer at depth $h_m(x, t_P)$, the partial flux $q_h(x_i^h, t_P)$ that is transported above the depth $h_m(x_i^h, t_P)$ at $x = x_i^h$, at time t_P, can also be written in terms of the velocity and geometry at x_i^h, as

$$q_h(x_i^h, t_P) = \bar{\phi}_h(x_i^h)\bar{u}(x_i^h, t_P)W(x_i^h)h_m(x_i^h, t_P) \tag{N.2}$$

where $\bar{\phi}(x_i^h)$ is the average value of the horizontal-velocity shape function $\phi(x, \hat{z}, t_P)$ between the surface and the path at depth $h_m(x_i^h, t_P)$. Since the shape functions $\phi(x, \hat{z}, t_P)$ and $\psi(x, \hat{z}, t_P)$ are related by vertical integration (see Chapter 5, Section A5.1), and the measured depth of the layer $h_d(x_i^h, t_P)$ is known, $\bar{\phi}(x_i^h)$ can be expressed as

$$\bar{\phi}_h(x_i^h) = \frac{1}{1-\hat{z}_i^h}\int_{\hat{z}_i^h}^{1}\phi(x_i^h,\hat{\zeta},t_P)d\hat{\zeta} = \frac{1-\psi(x_i^h,\hat{z}_i^h,t_P)}{1-\hat{z}_i^h} \tag{N.3}$$

where

$$\hat{z}_i^h = \frac{S(x_i^h,t_P)-h_d(x_i^h,t_P)-B(x_i^h)}{S(x_i^h,t_P)-B(x_i^h)} = 1-\frac{h_d(x_i^h,t_P)}{H(x_i^h,t_P)} \tag{N.4}$$

If we can solve for $q_h(x_i^h, t_P)$ in Equation N.2 in terms of accumulation rate, this is a way to express the layer depth $h_m(x_i^h, t_P)$ in terms of the model parameters. In steady state, this can be evaluated simply, where the modeled layer depth is given by

$$h_m(x_i^h) = \frac{H(x_i^h)}{\bar{\phi}(x_i^h)}\left(1-\frac{q(x_i^s)}{q(x_i^h)}\right) \tag{N.5}$$

However, this must be considered more generally in a transient problem.

If a curve $F_i(x)$ starts on or below the current surface $S(x,t_P)$ at $x = x_i^s$, and ending at depth $h_m(x_i^h, t_P)$ at $x = x_i^h$, $F_i(x)$ can be represented parametrically as a position vector $\mathbf{x}_i^F(s)$, where s measures the distance along the curve, or as $\mathbf{x}_i^F(t)$, where t describes the time at which a particle moving along the curve passes $\mathbf{x}_i^F$. If $\mathbf{x}_i^F(t)$ is not a streamline, then continuity still specifies that no net flux can cross the closed surface of a prism bounded by vertical surfaces defined by the flowband width $W(x)$ on the sides, and by the curve $\mathbf{x}_i^F(t)$ on its upper surface, by vertical faces joining $\mathbf{x}_i^F(t)$ to the bed at its upstream and downstream ends $x = x_i^s$ and $x = x_i^h$, and by the bed $B(x)$ between $x = x_i^s$ and $x = x_i^h$. No flux can cross the sides of $W(x)$, which are defined by streamlines, and we assume that there is no loss or gain of ice along the bed.

We assume that a flux $\psi(x_i^s,\hat{z}_i^s,t_P)q(x_i^s,t_P)$ enters at the upstream end. The factor $\psi(x_i^s,\hat{z}_i^s,t_P)$ accounts for the case that z_i^s may lie below the

present-day surface $S(t_P)$. The flux transported below the curve $\mathbf{x}_i^F(t)$ at the downstream end x_i^h of the prism is then given by the sum of this input flux and any "leakage" of flux into the prism across the curve $\mathbf{x}_i^F(t)$. This output flux is also equal to the difference between the total flux $q(x_i^h, t_P)$ and the partial flux $q_h(x_i^h, t_P)$ that is transported above the depth $h_m(x_i^h, t_P)$ at $x = x_i^h$, at time t_P:

$$q(x_i^h, t_P) - q_h(x_i^h, t_P) = \psi(x_i^s, \hat{z}_i^s, t_P) q(x_i^s, t_P) - \int_{F_i(x)} W(s)\mathbf{u}(\mathbf{x}_i^F(s), t_P) \cdot \hat{\mathbf{n}}(s) ds \tag{N.6}$$

where $\mathbf{u}(\mathbf{x}_i^F(s), t_P)$ is the velocity vector along $F_i(x) = x_i^F(s)$ at time t_P, $\hat{\mathbf{n}}(s)$ is the outward (i.e. upward) unit normal vector to the curve, and s measures the distance along the curve, in the direction of increasing x. The inner product in the integrand can also be written as

$$\mathbf{u}(\mathbf{x}_i^F(s), t_P) \cdot \hat{\mathbf{n}}(s) = [\mathbf{u}(\mathbf{x}_i^F(s), t_P) \times \hat{\mathbf{t}}(s)] \cdot \hat{\mathbf{e}}_y \tag{N.7}$$

where $\hat{\mathbf{t}}(s)$ is the unit tangent vector to $F_i(x)$, and $\hat{\mathbf{e}}_y$ is the horizontal unit vector in the y direction, transverse to the flowband. When the curve $\mathbf{x}_i^F(t)$ is a particle path $\mathbf{x}_i^P(t) = [x_i^P(t), z_i^P(t)]$, its unit tangent vector is:

$$\hat{\mathbf{t}}(\mathbf{x}_i^P(t)) = \frac{\mathbf{u}(\mathbf{x}_i^P(t), t)}{\left|\mathbf{u}(\mathbf{x}_i^P(t), t)\right|} = \frac{[u(x_i^P(t), z_i^P(t), t), w(x_i^P(t), z_i^P(t), t)]}{[u(x_i^P(t), z_i^P(t), t)^2 + w(x_i^P(t), z_i^P(t), t)^2]^{1/2}} \tag{N.8}$$

The surface elevation can change over time due to ice-sheet transients. This means that the position where the path started $\mathbf{x}_i^P(t_i^S) = [x_i^S(t), S(x_i^S, t_i^S)]$ might not fall exactly on the present-day surface $S(x, t_P)$, and the integral along the curve $F_i(x)$ must account for this possibility. If $\mathbf{x}_i^P(t_i^S)$ falls below $S(x, t_P)$, then we just close the surface across which the flux integrates to

zero at that interior point $\mathbf{x}_i^{\mathrm{P}}$ of the ice sheet. If $\mathbf{x}_i^{\mathrm{P}}(t_i^{\mathrm{S}})$ falls above $S(x,t_P)$, then we close the surface across which the flux integrates to zero at the point where the path crosses the present-day surface.

Equation N.2 for the partial flux at the depth of the internal layer can now be expressed as

$$q_h(x_i^h,t_P) = q(x_i^h,t_P) - \psi(x_i^s,\hat{z}_i^s,t_P)q(x_i^s,t_P) + \int_{t_i^s}^{t_P} W(x_i^P(t))[\mathbf{u}(\mathbf{x}_i^{\mathrm{P}}(t),t_P)\times\mathbf{u}(\mathbf{x}_i^{\mathrm{P}}(t),t)]\cdot\hat{\mathbf{e}}_y dt$$

$$= q(x_i^h,t_P) - \psi(x_i^s,\hat{z}_i^s,t_P)q(x_i^s,t_P) +$$

$$\int_{t_i^s}^{t_P} W(x_i^P(t))[u(\mathbf{x}_i^{\mathrm{P}}(t),t_P)w(\mathbf{x}_i^{\mathrm{P}}(t),t) - u(\mathbf{x}_i^{\mathrm{P}}(t),t)w(\mathbf{x}_i^{\mathrm{P}}(t),t_P)]dt \qquad \text{(N.9)}$$

where $\mathbf{u}(\mathbf{x}_i^{\mathrm{P}}(s),t_P)$ is defined by Equation N.7. If the transient particle path $\mathbf{x}_i^{\mathrm{P}}(t)$ is also a streamline at $t=t_P$, the integrand vanishes because $\mathbf{u}(\mathbf{x}_i^{\mathrm{P}}(t),t_P)$ and $\mathbf{u}(\mathbf{x}_i^{\mathrm{P}}(t),t)$ are always parallel; steady state is a special case of this situation. However, if the paths are unaltered, but the speed of particles along a path scales with the contemporary accumulation rate, then the integral also vanishes.

Combining Equation N.2 and Equation N.9 leads to and expression for the depth $h_m(x_i^h)$ of the path at the point x_i^h at which it reaches the correct age of the layer:

$$h_m(x_i^h,t_P) = \frac{H(x_i^h,t_P)}{\bar{\phi}_h(x_i^h)}\left(1 - \frac{\psi(x_i^s,\hat{z}_i^s,t_P)q(x_i^s,t_P)}{q(x_i^h,t_P)} + \frac{1}{q(x_i^h,t_P)}\int_{t_i^s}^{t_P} G(t_P,t)dt\right) \qquad \text{(N.10)}$$

where

$$G(t_P,t) = W(x_i^P(t))[u(\mathbf{x}_i^{\mathrm{P}}(t),t_P)w(\mathbf{x}_i^{\mathrm{P}}(t),t) - u(\mathbf{x}_i^{\mathrm{P}}(t),t)w(\mathbf{x}_i^{\mathrm{P}}(t),t_P)] \qquad \text{(N.11)}$$

To calculate the depth of the kth layer, each particle is tracked from the starting point on the surface $[x_i^s, \mathrm{S}(x_i^s, t_i^s)]$ at time $t_i^s = t_P - Age_k$, to its

position [x_i^h, S(x_i^h, t_P) - $h_m(x_i^h)$] at $t=t_P$. In order to find each partial derivative with respect to one parameter, with the other parameters held constant, we must be sure to stay at the same Age_k and at the same $x=x_i^h$, as the parameters are perturbed. Conceptually, this means that we must move to different paths as the upstream accumulation rates or ice flux entering the domain are perturbed. To allow this, we must consider the starting position x_i^s to also be an implicit function of the parameter values. Following this requirement, differentiating Equation N.10 with respect to each parameter p_j (e.g. the accumulation rate, the incoming ice flux, and the layer age), gives

$$\frac{\partial h_m(x_i^h)}{\partial p_j} = -\frac{h(x_i^h,t_P)}{\bar{\phi}_h(x_i^h)q(x_i^h,t_P)}\times$$
$$\left[\begin{array}{l}\psi(x_i^s,\hat{z}_i^s,t_P)\left(\dfrac{\partial q(x_i^s,t_P)}{\partial p_j}+\dfrac{\partial q(x_i^s,t_P)}{\partial x_i^s}\dfrac{\partial x_i^s}{\partial p_j}-\dfrac{q(x_i^s,t_P)}{q(x_i^h,t_P)}\dfrac{\partial q(x_i^h,t_P)}{\partial p_j}\right)\\ -\dfrac{1}{q(x_i^h,t_P)}\dfrac{\partial q(x_i^h,t_P)}{\partial p_j}\int_{t_i^s}^{t_P}G(t_P,t)dt-G(t_P,t_i^s)\dfrac{\partial t_i^s}{\partial p_j}-\int_{t_i^s}^{t_P}\dfrac{\partial G(t_P,t)}{\partial p_j}dt\end{array}\right] \quad \text{(N.12)}$$

The average horizontal-velocity shape function $\bar{\phi}(x,\hat{z},t)$ and the ice thickness $h(x,t)$ are evaluated at x_i^h at time t_P, and the vertical-velocity shape function $\psi(x,\hat{z},t)$ is evaluated at x_i^h. The ice flux $q(x,t)$ is calculated using Equation N.2, and is evaluated at the particle-path starting positions x_i^s and the particle-path ending positions x_i^h. In Equation N.12, there are five additional derivatives that must be evaluated.

First, the partial derivatives of ice flux with respect to the parameters $\partial q(x,t)/\partial p_j$ are given by Equation N.43 – Equation N.44.

Second,

$$\frac{\partial q(x_i^s, t_P)}{\partial x_i^s} = \dot{b}(x_i^s, t_P) W(x_i^s) \tag{N.13}$$

Third, starting with the known particle path [x_i^{P}(t), z_i^{P} (t)] between x_i^s and x_i^h, where x_i^s is defined by

$$x_i^s = x_i^h - \int_{t_i^s}^{t_P} u(x_i^{\mathrm{P}}(t), z_i^{\mathrm{P}}(t), t) dt \tag{N.14}$$

Differentiating with respect to parameters p_j, gives

$$\frac{\partial x_i^s}{\partial p_j} = -\frac{\partial t_i^s}{\partial p_j} u(x_i^{\mathrm{P}}(t), z_i^{\mathrm{P}}(t), t_i^s) - \int_{t_i^s}^{t_P} \frac{\partial u(x_i^{\mathrm{P}}(t), z_i^{\mathrm{P}}(t), t)}{\partial p_j} dt$$
$$- \int_{t_i^s}^{t_P} \left(\frac{\partial u(x_i^{\mathrm{P}}(t), z_i^{\mathrm{P}}(t), t)}{\partial x^{\mathrm{P}}} \frac{\partial x^{\mathrm{P}}}{\partial p_j} + \frac{\partial u(x_i^{\mathrm{P}}(t), z_i^{\mathrm{P}}(t), t)}{\partial z^{\mathrm{P}}} \frac{\partial z^{\mathrm{P}}}{\partial p_j} \right) dt \tag{N.15}$$

where the first term in Equation N.15 gives the rate at which the path from $\mathbf{x}_i^s$ lengthens as we seek an older layer. To see this, note that $t_i^s = t_P - Age_k$. When $p_j = Age_k$, where Age_k is the age of the layer reached by path i, this term is just the negative value of the horizontal velocity u($\mathbf{x}_i^s(t_i^s)$, t_i^s) at the starting point $\mathbf{x}_i^s(t_i^s)$ for the path. This term is identically zero if parameter p_j is not Age_k.

The second term in Equation N.15 expresses how the velocity along the reference path changes as the parameters change. The integrand in this term can be written as

$$\frac{\partial u(x,z,t)}{\partial p_j} = \frac{\phi(x,\hat{z},t)}{h(x,t)W(x)} \frac{\partial q(x,t)}{\partial p_j} \tag{N.16}$$

which can be integrated numerically because the ith path [x_i^{P}(t), z_i^{P} (t)] is known. The last term in Equation N.15 expresses how the velocity changes as we move through the velocity gradient to an adjacent path, in order to always be on a path that reaches Age_k at position x_i^h as the parameters p_j are perturbed. Equation N.15 contains $\partial x^P / \partial p_j$, which comprises all

intermediate values of $\partial x_i^s / \partial p_j$ along the path. It also contains $\partial z^P / \partial p_j$, which expresses the rate at which we have to move vertically to stay on a path that reaches Age_k at position $x=x_i^h$ as the parameters p_j are perturbed. This means that we need solve simultaneously for both $\partial x^P / \partial p_j$ and $\partial z^P / \partial p_j$. The corresponding equation for rates of vertical path-hopping is

$$\frac{\partial z_i^s}{\partial p_j} = -\frac{\partial t_i^s}{\partial p_j} w(x_i^{\mathrm{P}}(t), z_i^{\mathrm{P}}(t), t_i^s) - \int_{t_i^s}^{t_P} \frac{\partial w(x_i^{\mathrm{P}}(t), z_i^{\mathrm{P}}(t), t)}{\partial p_j} dt$$
$$- \int_{t_i^s}^{t_P} \left(\frac{\partial w(x_i^{\mathrm{P}}(t), z_i^{\mathrm{P}}(t), t)}{\partial x^{\mathrm{P}}} \frac{\partial x^{\mathrm{P}}}{\partial p_j} + \frac{\partial w(x_i^{\mathrm{P}}(t), z_i^{\mathrm{P}}(t), t)}{\partial z^{\mathrm{P}}} \frac{\partial z^{\mathrm{P}}}{\partial p_j} \right) dt \qquad \text{(N.17)}$$

The first term in Equation N.17 describes the rate at which depth must be increased to find a new path that reaches the correct Age_k at position $x=x_i^h$ as the parameters are perturbed (or alternatively, it represents the height above or below the surface from which the path must start at x_i^s in order to reach the "correct" depth $h_m(x_i^h)$ at $x=x_i^h$). The second term shows how changes in vertical velocity along the reference path contribute to the rate of change of the path with depth with changing parameters. Differentiating the vertical-velocity field (e.g. Chapter 5, Equation 5.9), the first integrand in Equation N.17 can be expressed as

$$\frac{\partial w(x,z,t)}{\partial p_j} = \frac{\partial \dot{b}(x,t)}{\partial p_j} \psi(x,\hat{z},t)$$
$$+ \frac{\partial q(x,t)}{\partial p_j} \left[\frac{\phi(x,\hat{z},t)}{h(x,t)W(x)} \left(\hat{z} \frac{dS}{dx} + (1-\hat{z}) \frac{dB}{dx} \right) - \frac{1}{W(x)} \int_0^{\hat{z}} \frac{\partial \phi(x,\hat{\zeta},t)}{\partial x} d\hat{\zeta} \right] \qquad \text{(N.18)}$$

where $x = x_i^P(t)$ and $\hat{z} = \hat{z}_i^P(t)$ are known functions of time t. The final term in Equation N.17 expresses how the vertical velocity changes as we move through the gradients of vertical velocity $w(x,z)$ to find a new path. The velocity gradients $\partial u/\partial x$, $\partial u/\partial z$, $\partial w/\partial x$, $\partial w/\partial z$ can be found numerically or analytically. The analytical expressions can be complex, especially when

the shape functions are complicated, for example when they vary in both x and z (i.e. due to a strong or variable temperature gradient). The numerical calculation is not overly computationally expensive, so the numerical evaluation is used here. The velocity gradients are found by differencing velocities at nearby points. The coupled Equations N.15 and N.17 are found by integrating from $t = t_i^s$ to $t = t_P$, and starting from the initial conditions:

$$\frac{\partial x_i^s}{\partial p_j} = -\frac{\partial t_i^s}{\partial p_j} u(x_i^{\mathrm{P}}(t_i^s), z_i^{\mathrm{P}}(t_i^s))$$

$$\frac{\partial z_i^s}{\partial p_j} = -\frac{\partial t_i^s}{\partial p_j} w(x_i^{\mathrm{P}}(t_i^s), z_i^{\mathrm{P}}(t_i^s)) \tag{N.19}$$

Fourth, in Equation N.12**,** for paths that lead to the layer of age Age_k, and $t_i^s = t_P - Age_k$, and Age_k is, for example, parameter m, then

$$\frac{\partial t_i^s}{\partial p_j} = -\frac{\partial Age_k}{\partial p_j} = -\delta_{mk} \tag{N.20}$$

where δ is the kronecker delta function. We treat time t_i^s, which can depend on some parameters, as the variable that determines the location x_i^s (rather than the other way around).

Fifth, in Equation N.12, $G(t_P,t)$ is a function of the velocity components along the particle paths using Equation N.11, and the derivative with respect to parameters is given by,

$$\frac{\partial G(t_P,t)}{\partial p_j} = W(x_i^{\mathrm{P}}(t)) \cdot \left(u(\mathbf{x}_i^{\mathrm{P}}(t), t_P) \frac{\partial w(\mathbf{x}_i^{\mathrm{P}}(t), t)}{\partial p_j} + w(\mathbf{x}_i^{\mathrm{P}}(t), t) \frac{\partial u(\mathbf{x}_i^{\mathrm{P}}(t), t_P)}{\partial p_j} \right)$$

$$+ u(\mathbf{x}_i^{\mathrm{P}}(t), t) \frac{\partial w(\mathbf{x}_i^{\mathrm{P}}(t), t_P)}{\partial p_j} + w(\mathbf{x}_i^{\mathrm{P}}(t), t_P) \frac{\partial u(\mathbf{x}_i^{\mathrm{P}}(t), t)}{\partial p_j} \tag{N.21}$$

This representation of changes in layer depth with respect to changes in parameter values holds for flank flow, and for ice sheets that experience

minimal divide migration. However, if there has been significant divide migration, there is a chance that particle paths will change direction and cross in the vicinity of the divide; this scenario is sketched in Figure N.2. Therefore, we also provide a generalized formulation of the partial derivative of layer depth with respect to parameter values, following an original derivation by E.D. Waddington (unpublished).

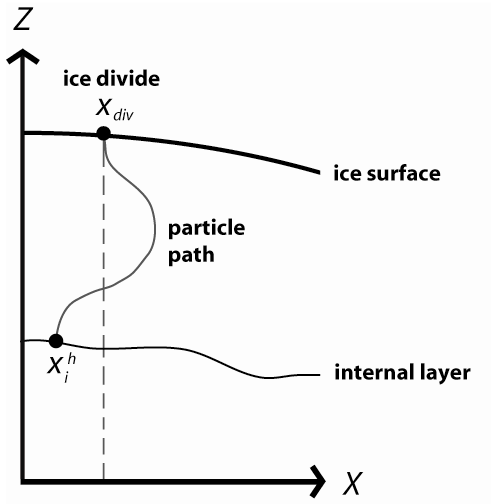

Figure N.2. Sketch of the scenario of particle-path crossing, which may occur in the vicinity of ice divides where there has been significant divide migration.

Instead of representing the particle path parametrically with time as

$$x_i^P(t) = x_i^s(t^s) + \int_{t_i^s}^{t} u(x_i^P, z_i^P, \tau)\, d\tau \tag{N.22}$$

$$z_i^P(t) = z_i^s(t^s) + \int_{t_i^s}^{t} w(x_i^P, z_i^P, \tau)\, d\tau \tag{N.23}$$

we could describe the path in differential equation form rather than integral form:

$$\frac{dx_i^P}{dt} = u(x_i^P(t), z_i^P(t)) \tag{N.24}$$

$$\frac{dz_i^P}{dt} = w(x_i^P(t), z_i^P(t)) \tag{N.25}$$

Then, instead of taking the partial derivative of N.22 and N.23 with respect to parameters p_j, as done in Equation N.15 and N.17, we could differentiate Equations N.24 and N.25. For horizontal velocity,

$$\frac{\partial}{\partial t}\left(\frac{dx_i^P}{dp_j}\right) = \left.\frac{\partial u}{\partial p_j}\right|_{(\mathbf{x}^P,t)} + \left.\frac{\partial u}{\partial x}\right|_{(\mathbf{x}^P,t)}\left[\frac{\partial x_i^P}{\partial p_j}\right] + \left.\frac{\partial u}{\partial z}\right|_{(\mathbf{x}^P,t)}\left[\frac{\partial z_i^P}{\partial p_j}\right] \tag{N.26}$$

and for vertical velocity,

$$\frac{\partial}{\partial t}\left(\frac{dz_i^P}{dp_j}\right) = \left.\frac{\partial w}{\partial p_j}\right|_{(\mathbf{x}^P,t)} + \left.\frac{\partial w}{\partial z}\right|_{(\mathbf{x}^P,t)}\left[\frac{\partial z_i^P}{\partial p_j}\right] + \left.\frac{\partial w}{\partial x}\right|_{(\mathbf{x}^P,t)}\left[\frac{\partial x_i^P}{\partial p_j}\right] \tag{N.27}$$

These two coupled equations can be solved numerically, for example with a Runge-Kutta method. For example,

$$\frac{\partial}{\partial t} f_1 = g_1(t) + k_1(t) f_1 + m_1(t) f_2 \tag{N.28}$$

$$\frac{\partial}{\partial t} f_2 = g_2(t) + k_2(t) f_1 + m_2(t) f_2 \tag{N.29}$$

where

$$f_1 = \left[\frac{\partial x_i^P}{\partial p_j}\right], \qquad f_2 = \left[\frac{\partial z_i^P}{\partial p_j}\right] \tag{N.30}$$

and

$$g_1(t) = \left.\frac{\partial u}{\partial p_j}\right|_{(\mathbf{x}^P,t)}, \qquad g_2(t) = \left.\frac{\partial w}{\partial p_j}\right|_{(\mathbf{x}^P,t)} \tag{N.31}$$

and Equations N.30 and N.31 are given by N.16 and N.18, respectively. Then,

$$k_1(t) = \left.\frac{\partial u}{\partial x}\right|_{(\mathbf{x}^P,t)}, \qquad k_2(t) = \left.\frac{\partial w}{\partial x}\right|_{(\mathbf{x}^P,t)} \tag{N.32}$$

and

$$m_1(t) = \left.\frac{\partial u}{\partial z}\right|_{(\mathbf{x}^P,t)}, \qquad m_2(t) = \left.\frac{\partial w}{\partial z}\right|_{(\mathbf{x}^P,t)} \tag{N.33}$$

These derivatives can be calculated using finite differences along each path *i*. To solve for [$f_1(t)$, $f_2(t)$], the initial conditions are

$$f_1(t_P) = \frac{\partial x_i^h}{\partial p_j} = 0 \tag{N.34}$$

$$f_2(t_i^s) = \frac{\partial z_i^s}{\partial p_j} = \frac{\partial S(x_i^s, t_i^s)}{\partial p_j} = \left.\frac{\partial S}{\partial x}\right|_{(\mathbf{x}^s,t_i^s)} \frac{\partial x_i^s}{\partial p_j} + \left.\frac{\partial S}{\partial t}\right|_{(\mathbf{x}^s,t_i^s)} \frac{\partial t_i^s}{\partial p_j} \tag{N.35}$$

To solve these coupled equations, the boundary condition at the end of each path must be estimated, and iteratively updated. For example, guess that $\partial x_i^s / \partial p_j = 0$, and iteratively update this value until Equation N.34 is satisfied. This formulation numerically calculates the velocity gradients along the path, and the path displacement rates along the paths with changes in parameters p_j.

Internal-layer depth is given by the difference between the present surface at x_i^h and the present elevation of the particle on path *i*:

$$h_m(x_i^h) = S(x_i^h, t_P) - z_i^P\left(x_i^h(t_P)\right) \tag{N.36}$$

To find the changes in layer depth with respect to changes in parameters, take the partial derivative of Equation N.36 with respect to p_j with the surface history and layer depth fixed, using Equation N.23 and Equation N.36. Compared to Equation N.12, this is given by

$$\frac{\partial h_m}{\partial p_j} = \frac{\partial S(x_i^h, t_P)}{\partial p_j} - \frac{\partial z_i^s(t_i^s)}{\partial p_j} - \frac{\partial}{\partial p_j}\left\{\int_{t_i^s}^{t^P} w\left(x_i^P(\tau), z_i^P(\tau)\right) d\tau\right\} \tag{N.37}$$

The first term is equal to zero because the surface is not adjusted with respect to parameters, and the second term is found by solving the coupled Equations N.28 and N.29. The last term in Equation N.37 is given by

$$\frac{\partial}{\partial p_j}\left\{\int_{t_i^s}^{t^P} w\left(x_i^P(\tau), z_i^P(\tau)\right) d\tau\right\} = \frac{\partial t_i^P}{\partial p_j} w\left(x_i^P(t_i^P), z_i^P(t_i^P)\right) - \frac{\partial t_i^s}{\partial p_j} w\left(x_i^s(t_i^s), z_i^s(t_i^s)\right) + \int_{t_i^s}^{t_i^P} \frac{\partial}{\partial p_j}\left\{w\left(x_i^P(t_i^P), z_i^P(t_i^P)\right)\right\}\Big|_{S(x,t), x_i^h} d\tau \tag{N.38}$$

The first term in Equation N.38 is equal to zero because the present time along the path is held constant. The second term is non-zero only when the parameter pj is the layer age. To integrate along the path and solve for the third term in Equation N.38, we need to express

$$\left.\frac{\partial w}{\partial p_j}\right|_{S(x,t), x_i^h} = \left.\frac{\partial w}{\partial p_j}\right|_{(x_i^P, z_i^P, t)} + \left.\frac{\partial w}{\partial x}\right|_{x_i^P, z_i^P, t} \left.\frac{\partial x_i^P}{\partial p_j}\right|_{x_i^P, z_i^P, t, S(x,t)} + \left.\frac{\partial w}{\partial z}\right|_{x_i^P, z_i^P, t} \left.\frac{\partial z_i^P}{\partial p_j}\right|_{x_i^P, z_i^P, t, S(x,t)} \tag{N.39}$$

where the first term represents the change in speed along path i when p_j is changed, the second term represents the change in speed due to shifts in the path position x at time t, and the last term represents the change in speed

due to shifts in the path position z at time t. The first term is given by N.18, and the velocity gradients along the path have been evaluated numerically from the velocity solutions as the particle moves along the path i (Equations N.32 and N.33).

N.2. Ice flux

Ice flux, when expressed kinematically (e.g. Chapter 5, Equation 5.4), is a function of the model parameters. To analytically evaluate the integral in this kinematic expression, we use linear interpolating functions (see Appendix L). The ice flux *q(x,t)* can be expressed in terms of the parameters by

$$q(x,t) = Q_{in}(t) - \int_{x_{in}}^{x} \dot{h}(\chi,t)W(\chi)d\chi + \int_{x_{in}}^{x}\left[\sum_{i=1}^{N_x-1}\left(\dot{b}_i(t)\gamma_0(X_i(\chi)) + \dot{b}_{i+1}(t)\gamma_1(X_i(\chi))\right)\right] \times\left[\sum_{j=1}^{N_x-1}\left(W_j\gamma_0(X_j(\chi)) + W_{j+1}\gamma_1(X_j(\chi))\right)\right]d\chi \quad \text{(N.40)}$$

when the integrals are evaluated with the appropriate products of the linear interpolating functions, this gives

$$q(x,t) = Q_{in}(t) - \int_{x_{in}}^{x} \dot{h}(\chi,t)W(\chi)d\chi + \sum_{i=1}^{N_x-1}\Delta x_i\begin{bmatrix}\dot{b}_i(t)W_i\Gamma_{00}(X_i^e) \\ +(\dot{b}_{i+1}(t)W_{i+1} + \dot{b}_i(t)W_i)\Gamma_{01}(X_i^e) \\ +\dot{b}_{i+1}(t)W_{i+1}\Gamma_{11}(X_i^e)\end{bmatrix} \quad \text{(N.41)}$$

where X_i^e is the endpoint of integration within the integral i. When $x^n{}_{i+1} \le x$, the integration covers the entire interval $[x^n{}_i, x^n{}_{i+1}]$ and X_i^e=1 (see Appendix L). Only the single summation had to be retained because the interpolating functions are defined to be zero outside their respective intervals.

Ice thickness *h(x,t)* is calculated on a different set of spatial and temporal nodes than the accumulation-rate parameter values, and so this integral is complicated to represent in terms of the nodal values of its piecewise-linear integrand components *W(x)* and $\dot{h}(x,t)$. Fortunately, the integral $\int \dot{h}(\chi,t)W(\chi)d\chi$ does not need to be calculated in our evaluation of ice flux in terms of model parameters. While the ice-thickness change over time is physically a function of the accumulation-rate history, we assume that the ice-thickness history is known at each iteration of the inverse problem (i.e. from a previous iteration); the integral $\int \dot{h}(\chi,t)W(\chi)d\chi$ is not considered a function of the model parameters. By replacing the dummy index *i* by *i-1* in the $b_{i+1}(t)$ terms, *q(x,t)* can be expressed as a function of $b_i(t)$ only, rather than $b_i(t)$ and $b_{i+1}(t)$,

$$q(x,t) = \sum_{j=1}^{N_t} Q_{in}\left[\gamma_0(T_j) + \gamma_1(T_{j-1})\right] - \sum_{i=1}^{N_x-1}\left(\sum_{j=1}^{N_t} \dot{b}_{ij}\left[\gamma_0(T_j) + \gamma_1(T_{j-1})\right]\right) \times \left(\Delta x_i\left[W_i\Gamma_{00}(X_i^e) + W_{i+1}\Gamma_{01}(X_i^e)\right] + \Delta x_{i-1}\left[W_{i-1}\Gamma_{01}(X_{i-1}^e) + W_i\Gamma_{11}(X_{i-1}^e)\right]\right) \quad \text{(N.42)}$$

Equation N.42 can be differentiated to find the partial derivatives of ice flux with respect to the model parameters $\partial q(x,t)/\partial p_j$, where $x_i^n \le x_k^b \le x_{i+1}^n$, and $t_i^n \le t_k^b \le t_{i+1}^n$, so that the point *(x,t)* is in the grid box *(k,l)*, giving

$$\frac{\partial q(x,t)}{\partial q_{in}} = (1-T_l)\delta_{nl} + T_l\delta_{n(l+1)}, \qquad T_l = \frac{t-t_l^n}{t_{l+1}^n - t_l^n} \quad \text{(N.43)}$$

$$\frac{\partial q(x,t)}{\partial \dot{b}_{mn}} = \left[(1-T_l)\delta_{nl} + T_l\delta_{n(l+1)}\right] \times \left[\Delta x_m(W_m\Gamma_{00}(X_m^e) + W_{m+1}\Gamma_{01}(X_m^e)) + \Delta x_{m-1}(W_{m-1}\Gamma_{01}(X_{m-1}^e) + W_m\Gamma_{11}(X_{m-1}^e))\right] \quad \text{(N.44)}$$

where X_j^e, which is the nondimensional endpoint for integration in the interval j (Appendix L) contains information about the spatial position k.

N.3. Ice velocity

The horizontal velocity at the surface at any location x_j^u where the velocity has been measured at time t, is described by

$$u_m^s(x_j^u,t) = u(x_j^u, S(x_j^u,t), t) = \bar{u}(x_j^u,t)\phi(x_j^u,1,t)$$
$$= \frac{\phi(x_j^u,1,t)}{h(x_j^u,t)W(x_j^u)} q(x_j^u,t) \tag{N.45}$$

where $\hat{z} = 1$ at the surface $S(x,t)$, and the ice flux $q(x_j^u,t)$ is given by Equation N.42. By differentiating Equation N.45, the partial derivatives at the location x_i^s of the ith measured surface velocity are

$$\frac{\partial u_m^s(x_i^u,t)}{\partial p_j} = \frac{\phi(x_i^u,1,t)}{h(x_i^u,t)W(x_i^u)} \frac{\partial q(x_i^u,t)}{\partial p_j} \tag{N.46}$$

where the derivatives of ice flux with respect to the model parameters $\partial q(x_i^u,t)/\partial p_j$ are given by Equation N.43 and Equation N.44.

N.4. Accumulation rate

When the accumulation rate $\dot{b}_d(x_k^b,t)$ is measured at x_k^b within the interval $[x^n_i, x^n_{i+1}]$ at time t, the corresponding modeled value $\dot{b}_m(x_k^b,t)$ is interpolated from $b_i(t)$ and $b_{i+1}(t)$, i.e.

$$\dot{b}_m(x_k^b,t) = \dot{b}_i(t)(1 - X_i^b) + \dot{b}_{i+1}(t)X_i^b \tag{N.47}$$

where

$$X_i^b = \frac{x_k^b - x_i^n}{x_{i+1}^n - x_i^n} \tag{N.48}$$

If t is not a time node, then $b_i(t)$ and $b_{i+1}(t)$ must be expressed in terms of the earlier and later nodal values, as in Appendix L.

The partial derivative of the kth measurement of accumulation is zero for all parameters except the accumulation rates at the spatial nodes upstream and downstream from x_k^b, and at the time nodes that bracket t_k^b. When $x_i^n \le x_k^b \le x_{i+1}^n$, and $t_i^n \le t_k^b \le t_{i+1}^n$, differentiating Equation N.47 gives

$$\frac{\partial \dot{b}_m(x_k^b, t_k^b)}{\partial \dot{b}_j(t_k^b)} = \delta_{ij}(1 - X_i^b) + \delta_{(i+1)j} X_i^b \tag{N.49}$$

and the derivatives with respect to all other parameters are equal to zero.